UNIVERSITY OF NIŠ

ISSN 0354-4605 (Print)
ISSN 2406-0860 (Online)
COBISS.SR-ID 98807559

FACTA UNIVERSITATIS

Series
ARCHITECTURE AND CIVIL ENGINEERING
Vol. 16, Nº 1, 2018

16 | 1

Scientific Journal **FACTA UNIVERSITATIS**
UNIVERSITY OF NIŠ
Univerzitetski trg 2, 18000 Niš, Serbia
Phone: +381 18 257 095 Telefax: +381 18 257 950
e-mail: facta@ni.ac.rs http://casopisi.junis.ni.ac.rs/

Scientific Journal FACTA UNIVERSITATIS publishes original high scientific level works in the fields classified accordingly into the following periodical and independent series:

Architecture and Civil Engineering
Automatic Control and Robotics
Economics and Organization
Electronics and Energetics
Law and Politics
Linguistics and Literature
Mathematics and Informatics
Mechanical Engineering
Medicine and Biology
Philosophy, Sociology, Psychology and History
Physical Education and Sport
Physics, Chemistry and Technology
Teaching, Learning and Teacher Education
Visual Arts and Music
Working and Living Environmental Protection

SERIES **ARCHITECTURE AND CIVIL ENGINEERING**

Editor-in-Chief: **Dragoslav Stojić**, e-mail: *dragoslav.stojic@gmail.com*

Section Editors: **Milena Dinić Branković**, e-mail: *milena.dinic@gaf.ni.ac.rs*
Miomir Miljković, e-mail: *miomir.miljkovic@hotmail.com*
University of Niš, Serbia, Faculty of Civil Engineering and Architecture
18000 Niš, Aleksandra Medvedeva 14, 18000 Niš
Phone: +381 18 588 181, Fax: +381 18 588 181

Technical Assistance: **Vladan Nikolić**, **Vojislav Nikolić**, e-mail: *fuacets@junis.ni.ac.rs*
University of Niš, Serbia, Faculty of Civil Engineering and Architecture

Proofreading: **Goran Stevanović**, University of Niš, Faculty of Civil Engineering and Architecture
UDC Classification Associate: **Ana Mitrović**, Library of Faculty of Civil Engineering and Architecture, Niš
Secretary: **Olgica Davidović**, University of Niš, e-mail: *olgicad@ni.ac.rs*
Computer support: **Mile Ž. Randelović**, University of Niš, e-mail: *mile@ni.ac.rs*
Miloš Babić, University of Niš, e-mail: *milosb@ni.ac.rs*

Publication frequency – one volume, three issues per year.
Published by the University of Niš, Serbia

Financial support: Ministry of Education, Science and Technological Development of the Republic of Serbia
Printed by "UNIGRAF-X-COPY" – Niš, Serbia

ISSN 0354 – 4605 (Print)
ISSN 2406 – 0860 (Online)
COBISS.SR-ID 98807559

FACTA UNIVERSITATIS

SERIES **ARCHITECTURE AND CIVIL ENGINEERING**
Vol. 16, N^{o} 1, 2018

UNIVERSITY OF NIŠ

INSTRUCTIONS FOR CONTRIBUTORS

Contributions should be (preferably) in English, French or German.
Under the paper title, the name(s) of the author(s) should be given while the full name, official title, institute or company affiliation and the like should be placed at the end of the paper together with the exact mail and e-mail address, as well as short (running) title of paper.
Manuscript format. A brief abstract of approximately 100 to 150 words in the same language and a list of up to six key words should precede the text body of the manuscript. All the authors apart from foreign ones should also submit a complete manuscript in Serbian. Manuscripts should be prepared as doc. file, Word version 6.0 or higher. Manuscript should be prepared using a Word template (downloaded from web address http://casopisi.junis.ni.ac.rs/index.php/FUArchCivEng/about/submissions#onlineSubmissions).
Manuscript length. Brief articles and discussions (10 pages or less) are encouraged. Otherwise, papers should present well-focused arguments of approximately 16 pages.
Style requirements. **Letters, figures and symbols** should be clearly denoted.
Equations should be typewritten and, with the number, placed in parentheses at the right margin. References to equations should be in the form "Eq. (2)" or simply (2). For equations that cannot be entered in a single line, use the Equation Editor in MS Word. In equations and in the text, *italicize* symbols that are used to represent variables or parameters, including subscripts and superscripts. Only use characters and symbols that are available in the Equation Editor, in the *Symbol font* or in *Times New Roman*.
All illustrations (figures, photographs, line drawings, graphs) should be numbered in series and all legends should be included at the bottom of each illustration. All figures, photographs, line drawings and graphs, should be prepared in electronic form and converted in TIFF or JPG (max quality) file types, in 300 dpi resolution, for superior reproduction. Figures, line drawings and graphs prepared using elements of MS Drawing or MS Graph must be converted in form of pictures and unchangeable. All illustrations should be planned in advance so as to allow reduction to 12.75 cm in column width. Please review all illustrations to ensure that they are readable.
All **tables** should be numbered with consecutive Arabic numbers. They should have descriptive captions at the top of each table and should be mentioned in the text.
The **references** should be numbered in the order in which they appear in the text, at the end of the manuscript, in the same way as the following examples:

1. Kollbruner C. F., Hajdin N., Stipanić B.: *Contribution to the Analysis of Cable-Stayed Bridges* N. 48, Schulthess Verlag, Zürich, 1980, pp. 66-77.
2. Đuranović P.: Organizacija upravljanja projektima, Izgradnja N^{o} 1/96, Beograd, 1996, str. 45-52.
3. Živković D.: Influence of front excavation on the state and deformity of montage lining of hydraulic pressure tunnels, Ph. D. University of Niš, 1988, pp. 95-108.
4. Kurtović-Folić N.: Typology of Architectural Forms-Strong and Weak Typological Characteristics, Facta Universitatis, University of Niš, Vol. 1, N^{o} 2, 1995, pp. 227-235.

References should be quoted in the text by the corresponding number in square brackets.

Electronic submission. Papers for consideration should be submitted to the Series Editor in electronic form via the Journal's home page: http://casopisi.junis.ni.ac.rs/index.php/FUArchCivEng/index.

FACTA UNIVERSITATIS
Series: **Architecture and Civil Engineering** Vol. 16, No 1, 2018, pp. 1-16
https://doi.org/10.2298/FUACE160514001B

TORSIONAL BEHAVIOUR OF NORMAL STRENGTH RCC BEAMS WITH FERROCEMENT "U" WRAPS

UDC 624.072.2

Gopal Charan Behera[1], Manoranjan Dhal[2]

[1]Civil Engineering Department, Gandhi Engineering College, Bhubaneswar, Odisha, India
[2]Civil Engineering Department, BIET, Barapada, Bhadrak, Odish-756114, India

Abstract. *Wrapping technology is one of the effective ways of strengthening concrete elements. Several researchers reported the effectiveness of Glass fiber reinforced polymers and carbon fiber reinforced polymers for improving the strength of the concrete elements. Wrapping on three sides is one of the effective methods for strengthening the beams supporting slabs. Scant literature is available on the strength enhancement of "U" wrapped concrete elements subjected to torsional loads. In this investigation an attempt is made to quantify the improvement in the behaviour of "U" wrapped rectangular concrete members subjected to torsional loads "U" wraps. Ferrocement is taken here as wrapping material. Beams were cast with different number of mesh layers with different torsional reinforcement. The beams were analyzed with MARS. The predictions are in good agreement with experimental test results.*

Key words: *ferrocement, U wrap, Ultimate Torque, MARS: ferrocement.*

1. INTRODUCTION

A reinforced concrete (RC) structural element such as peripheral beams, ring beams at bottom of circular slab, beams supporting canopy and other types of beams are subjected to torsional loading. Strengthening or upgrading becomes necessary for these beams when they are unable to provide the resistance. Increased service loading, diminished capacity through aging and degradation and more stringent updates in code regulations have also necessitated for the retrofitting of existing structures (Rao and Seshu, 2005; Hii and Riyad, 2007). Repair and strengthening of RC members can be done by epoxy repair, steel jacketing or by fibre-reinforced polymer (FRP) composite. Each technique requires a different level of artful detailing. Availability of labour, cost and disruption of building occupancy plays major role in deciding about type of repair (Karayannis *et al.*, 2008). FRPs can be effectively used to upgrade such structural deficient reinforced concrete structures. Torsional retrofitting using

Received May 14, 2016 / Accepted July 2, 2016
Corresponding author: Nebojša S. Gadžić
1Civil Engineering Department, Gandhi Engineering College, Bhubaneswar, Odisha, India
E-mail: beheragb@gmail.com

FRP has received less attention (Ghobarah *et al.*, 2002; Ming *et al.*, 2007; Santhakumar and Chandrasekharan, 2007). Strengthening structures with FRP increases the strength in flexure, shear and torsion capacity as well as changes the failure mode and failure plane (Deifalla and Ghobarah, 2010.a). In practice it is seldom possible to fully wrap the beam cross section due to the presence of either a floor slab, or a flange. However, most of the research on FRP strengthened RC members investigated rectangular section fully wrapped with FRP (Ghobarah *et al.*, 2002; Panchacharam and Belarbi, 2002; Salom *et al.*,2004; Hii and Riyad, 2007; Ameli and Ronagh, 2007) with the exception of a few studies that investigated T-beams with U-jacket (Panchacharam and Belarbi, 2002; Chalioris, 2008). Few studies regarding torsion strengthening using FRP have shown that the continuous wrapping is much more effective than using the strips (Ghobarah *et al.*, 2002; Panchacharam and Belarbi, 2002; Chalioris, 2008; Deifalla and Ghobarah, 2010b). Recent studies have shown that the basic deformation of the torsionally strengthened beams is similar to unstrengthened ones, however, the external bonding limits the crack formation, propagation, widening and spacing between cracks (Hii *et al.*, 2007; Ameli and Ronagh, 2007; Chalioris, 2008).

Retrofitting by FRP is restricted to developed countries and urban areas of developing countries due to their high cost and skilled workmanship for its application (Bansal *et al.*, 2007). It is well-known that although common concrete jackets enhance the strength, stiffness and toughness and improve the overall performance, they exhibit substantial shortcomings. These disadvantages are (a) the required labour-intensive procedures and (b) the increase of the member sizes, which reduces the available floor space, increases mass, change in stiffness and alters the dynamic characteristics of the building. Steel jacketing and FRP wrapping have the advantage of high strength and eliminate some of the limitations of concrete jacketing. However, they have poor fire resistance due to strength degradation of resin under moderate temperature. With due consideration on simplicity and constructability, a rehabilitation method for beam–column joints using ferrocement jackets with embedded diagonal reinforcements is proposed. Tests on reinforced concrete columns and beams strengthened by ferrocement have shown significant enhancement in strength (Li *et al.*, 2013). From cost effective point of view and also from strength point of view ferrocement may be a substitute for FRP as it possesses high tensile strength, water tightness and is easy for application (ACI Committee 549,1979).

Ferrocement laminates in the form of Welded Wire Mesh (WWM) when encapsulated with a properly designed thin mortar layer can provide good alternative and low-cost technique in strengthening and repairing different structural elements for enhancing their load carrying capacities and ductility. Ferrocement meets the criteria of flowability and strength in addition to impermeability, sulfate resistance, corrosion protection and in some cases frost durability. Such performance is made possible by reducing porosity, inhomogeniety, and microcracks in the cement matrix and the transition zone Shannag and Mourad, (2012). The study by (Kumar *et al*., 2007) under three different axial load ratios confirmed that confining columns using ferrocement jackets resulted in enhanced stiffness, ductility, and strength and energy dissipation capacity. The mode of failure could be changed from brittle shear failure to ductile flexural failure. Experimental and analytical study of thin concrete jacketing with self compacting concrete and “U” shaped stirrup was found to be beneficial in changing stiffness and altering the dynamic characteristics of the beam (Chalioris *et al*., 2014).

1.1. Significance of present Investigation

Torsion, due to its circulatory nature, can be well retrofitted by closed form of wrap. Few analytical and experimental studies are found to quantify the torsional strength of FRP bonded full wrap (Ming *et al*., 2006; Hii and Riyad, 2006; Salom *et al.,* 2004; Ameli and Ronagh, 2007; Chalioris, 2007). But inaccessibility and extension of flanges over the web has necessitated strengthening the beams by "U" wrap rather than full wrap (Behera *et al., 2008).* For quantification of torsional strength of "U" wrapped beams very few attempts have been made by (Panchacharam and Belarbi, 2002; Deifalla *et al.,* 2013). U-jacketed flanged beams exhibited premature debonding failure at the concrete and the FRP sheet adhesive interface Chalioris (2008). From the above points, it is clear that the "U" wrapped beams cannot perform in the same manner as that of full wrapped beams under torsional loading as it lacks one torsion resisting element(reinforcement) on un-wrapped face.

The mentioned literature in the introduction substantially recommends ferrocement as a retrofitting substitution for FRP. Few studies are available to quantify the torsional strength of ferrocement "U" wrapped beams. Experimental and analytical estimation of torsional strength of "U" wrapped RC beams reported by the author earlier was limited to plain beams only (Behera *et al.,* 2008).

This paradigm was a motivation to take up the present investigation. The torque-twist response of reinforced beams is characterized by different salient stages such as elastic, cracking and ultimate stages (Chalioris, 2006; Behera *et al.,* 2008)**.** Elastic and cracking torque of a beam is dependent upon its constituent materials and cross sectional area (ACI committee 318,2002; Chalioris, 2006; Nei *et al*., 2009). The reinforcement provided in longitudinal and transverse direction controls the torque twist response in the post cracking stage (Liang-Jenq, Leu. and Yu-Shu, 2000; Rao *et al*., 2003; 2005; 2006; Chalioris, 2006). Literature review reveals that the torsional response of a wrapped beam is dependent on aspect ratio, constituent materials of core and wrapping material (Salom *et al*.2003; Rita *et al*., 2003; Ming and Grunberg, 2006). A beam if wrapped with ferrocement "U" wrap, then its torque twist response is influenced by ferrocement wrap (ferrocement matrix strength and number of layers along with reinforcement in the core) and states of torsion. The six possible states of torsion (arrangement of reinforcement in longitudinal and transverse direction that can be arranged in a beam) are as follows

I Only longitudinally reinforced
II Only transversely reinforced
III Under Reinforced Beams
IV Longitudinally over reinforced and transversely under reinforced.
V Longitudinally under reinforced and transversely over reinforced
VI Completely over reinforced.

The objective of the present experimental study is to evaluate the ultimate torque of a wrapped ferrocement "U" wrap beam using soft computing method MARS.

1.2. Soft Computing by MARS

Here soft computing method is employed for the calculation of ultimate Torque, twist, stiffness and toughness using MARS. This method is also known as the dark box method as finally the method of calculations is unknown and only end results were found out by this method.

2. EXPERIMENTAL PROGRAM

To study the above mentioned parameters, beams are cast and tested under pure torsional loading. The variations considered are the number mesh layers in the ferrocement 'U' wrap, size aspect ratio, mortar strength, concrete strength and the state of torsion. To study the effect of number of mesh layers on torsional strength of four possible cases of states of torsion, the number of mesh layers is varied as 3, 4 and 5.

Torsional loading induces spiral cracking approximately inclined at 45^0 to the longitudinal direction of the beam. To allow this pattern of cracking and to form two complete spirals in the central test region of the beam, a length 1500 mm is required. In order to hold the specimen and to apply the torque, the end zones are heavily reinforced for a length of 250 mm on either side of the beam. Thus, the total length of the beam is fixed as 2000 mm. In under reinforced section the amount of reinforcement provided in longitudinal and transverse direction is less than that required for torsionally balanced section. In longitudinally over reinforced sections lower amount of reinforcement in transverse direction and higher amount of reinforcement in the longitudinal direction than the reinforcement required for torsionally balanced sections are provided. In transversely over reinforced sections higher amount of reinforcement in transverse direction and lower amount of reinforcement in the longitudinal direction than the reinforcement required for torsionally balanced sections are provided. In completely over reinforced sections higher amount of reinforcement in transverse direction and longitudinal direction than the reinforcement required for torsionally balanced sections are provided. All details of the beams tested in this investigation are presented in Table 1. Figures of beams cast were shown in Behera *et al.* (2008).

Table 1 Details of Beams

Sl. No.	Series	Designation	Dimensions (mm)	Compressive strength		Reinforcement Details				
						Core Reinforced Concrete				Outer Wrap
						Longitudinal Steel		Transverse steel		
				Ferrocement matrix (MPa)	Concrete (MPa)	Diameter, No. of bars	Yield Strength (MPa)	Diameter, Spacing	Yield Strength (MPa)	No. of mesh layers
1		BQ4N	125 x 250	40	35					
2		BQ3N	125 x 250	40	35					
3		BQ5N	125 x 250	40	35					
4	Only Longitudinal	L3N	125 x 250	40	35	12 mm, 4 nos.	440			3
5		L4N	125 x 250	40	35	12 mm, 4 nos.	440			4
6		L5N	125 x 250	40	35	12 mm, 4 nos.	440			5
7	Only Transverse	T3N	125 x 250	40	35			8mm @ 100 mm c/c	465	3
8		T4N	125 x 250	40	35			8mm @ 100 mm c/c	465	4
9		T5N	125 x 250	40	35			8mm @ 100 mm c/c	465	5
10	U	U3N	125 x 250	40	35	6 mm, 4 nos.	350	6mm @ 100 mm c/c	350	3
11		U4N	125 x 250	40	35	6 mm, 4 nos.	350	6mm @ 100 mm c/c	350	4
12		U5N	125 x 250	40	35	6 mm, 4 nos.	350	6mm @ 100 mm c/c	350	5
13	L	Lo3N	125 x 250	40	35	12 mm, 4 nos.	440	6mm @ 100 mm c/c	350	3
14		Lo4N	125 x 250	40	35	12 mm, 4 nos.	440	6mm @ 100 mm c/c	350	4
15		Lo5N	125 x 250	40	35	12 mm, 4 nos.	440	6mm @ 100 mm c/c	350	5
16	T	To3N	125 x 250	40	35	6 mm, 4 nos.	350	8mm @ 100 mm c/c	465	3
17		To4N	125 x 250	40	35	6 mm, 4 nos.	350	8mm @ 100 mm c/c	465	4
18		To5N	125 x 250	40	35	6 mm, 4 nos.	350	8mm @ 100 mm c/c	465	5
19	C	Co3N	125 x 250	40	35	12 mm, 4 nos.	440	8mm @ 100 mm c/c	465	3
20		Co4N	125 x 250	40	35	12 mm, 4 nos.	440	8mm @ 100 mm c/c	465	4
21		Co5N	125 x 250	40	35	12 mm, 4 nos.	440	8mm @ 100 mm c/c	465	5
23		BH	125 x 250		60					
24		BO4H	125 x 250	55	60					4
25		L4H	125 x 250	55	60	12 mm, 6 nos.	440			4
26		T4H	125 x 250	55	60			10mm @ 70 mm c/c	445	4
27	U	U4H	125 x 250	55	60	6 mm, 6 nos.	350	6mm @ 70 mm c/c	350	4
28	L	Lo4H	125 x 250	55	60	12 mm, 6 nos.	440	6mm @ 70 mm c/c	350	4
29	T	To4H	125 x 250	55	60	6 mm, 6 nos.	350	10mm @ 70 mm c/c	445	4
30	C	Co4H	125 x 250	55	60	12 mm, 6 nos.	440	10mm @ 70 mm c/c	445	4

Co5N represents a beam of size (125 mm X 250 mm), Co stands for completely over reinforced, numeric 5 represents number of mesh layer and N stands for concrete of strength 35 MPa. So, Co5N represents a completely over reinforced beam with 5 numbers of mesh layers in ferrocement zone with mortar grade 40 MPa and concrete of 35 MPa in the core.

The materials used, casting and testing procedure of beams is presented in Behera *et al*. (2014). The experimental results of beams are presented in Table 2.

3. Soft Computing Method: Multivariate Adaptive Regression Spline (MARS)

MARS is an adaptive procedure because the selection of basis functions is data-based and specific to the problem at hand. This algorithm is a nonparametric regression procedure that makes no specific assumption about the underlying functional relationship between the dependent and independent variables. It is very useful for high dimensional problems. For this model an algorithm was proposed by Friedman (1991) as a flexible approach to high dimensional nonparametric regression, based on a modified recursive partitioning methodology. MARS uses expansions in piecewise linear basis functions of the form Equation (1)

$$c^{+}(x,\tau)=[+(x-\tau)]_{+},\ c^{-}(x,\tau)=[-(x-\tau)]_{+} \tag{1}$$

where, $[q]=\max\{0,q\}$ and τ is an univariate knot. Each function is piecewise linear, with a knot at the value τ, and it is called a reflected pair. The points in Figure 4 illustrate the data (x_i, y_i) (i = 1, 2,...*N*), composed by a p-dimensional input specification of the variable x and the corresponding 1-dimensional responses, which specify the variable y.

Let us consider the following general model Equation (5) on the relation between input and response:

$$Y = f(X)+\varepsilon \tag{2}$$

Where, Y is a response variable, $X=(X_1, X_2, \ldots\ldots X_n)^T$ is a vector of predictors and ε is an additive stochastic component, which is assumed to have zero mean and finite variance.

The goal is to construct reflected pairs for each input x_j (j=1,2……p) with p-dimensional knots $\tau_i = (\tau_{i,1}, \tau_{i2},\ldots., \tau_{i,p})^T$. Actually, we could even choose the knots $\tau_{i,j}$ more distant from the input values $x_{i,j}$, if any such a position promises a better data fitting.

After these preparations, our set of basis functions is Equation (6):

$$\delta := \{(X_j-\tau)_+, (\tau-X_j)_+ \mid \tau\in\{x_{1,j}, x_{2,j}, \ldots\ldots, x_{N,j}\},\ j\in\{1,2,\ldots\ldots, p\}\} \tag{3}$$

If all of the input values are distinct, there are 2Np basis functions altogether. Thus, we can represent f (X) by a linear combination, which is successively built up by the set δ and with the intercept θ_0, such that Equation (3) takes the form

$$Y=\theta_0+\sum_{m=1}^{M}\theta_m\psi_m(X)+\varepsilon. \tag{4}$$

All the beams tested in the experimental program are analyzed by MARS for obtaining the ultimate torque, ultimate twist, secant stiffness at ultimate and toughness. The values are presented below.

a) For Ultimate Torque

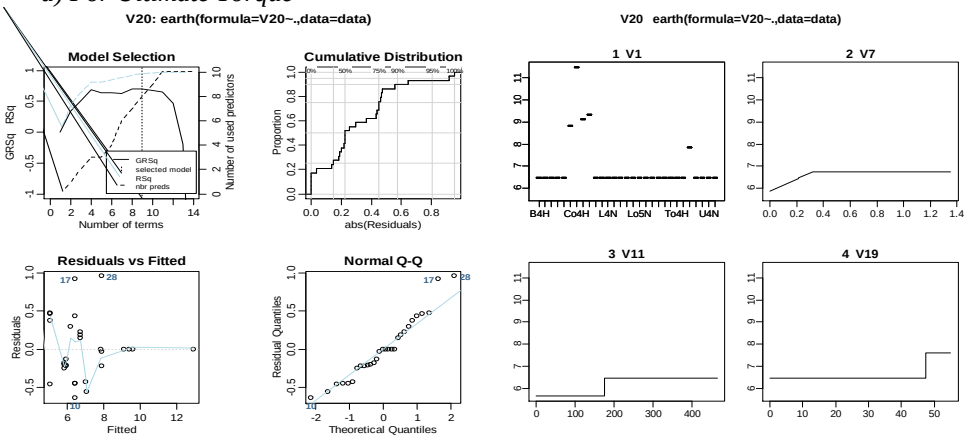

V1Co4H	8	100.0	100.0
V7	6	72.4	71.3
V11	6	52.7	56.9
V19	4	31.3	37.3
V1Co3N	3	29.0	31.2
V1Co4N	3	29.0	31.2
V1Co5N	3	29.0	31.2
V1To5N	1	10.3	15.1

coefficients	
(Intercept)	6.7528209
V1Co3N	2.3521791
V1Co4H	5.0055965
V1Co4N	2.6731791
V1Co5N	2.8671791
V1To5N	1.3965373
h(0.322651-V7)	-2.7323212
h(350-V11)	-0.0022761
h(V19-40)	0.0767722

$$T = 6.752 - maximum[0,0.32265 - spacing\ of\ longitudinal\ reinforcement] * 2.7323 - maximum[0,350 - Fty] * 0.002276 + maximum[0, Mortar\ strength - 40] * 0.07677$$

Table 2. Experimental and Predicted Values of Ultimate Torque by MARS

Ultimate Torque(kNm)			Ultimate Torque(kNm)		
Beams	Expt	MARS	Beams	Expt	MARS
BQ3N	5.443	5.074	To3N	6.899	6.463
BQ4N	5.546	5.074	To4N	7.38	6.463
BQ5N	5.54	5.074	To5N	7.86	7.86
L3N	5.73	5.956	Co3N	9.105	9.105
L4N	5.74	5.956	Co4N	9.426	9.426
L5N	5.82	5.956	Co5N	9.62	9.62
T3N	5.62	5.871	BH	4.612	5.074
T4N	5.67	5.871	B4H	6.52	6.226
T5N	5.69	5.871	L4H	6.55	7.107
U3N	5.816	6.458	T4H	6.59	7.022
U4N	6.01	6.458	U4H	7.68	7.904
U5N	6.01	6.458	Lo4H	7.87	7.904
Lo3N	6.899	6.752	To4H	8.86	7.904
Lo4N	6.939	6.752	Co4H	12.91	12.91
Lo5N	6.979	6.752			

4. Interpretation of Test Results

In this phase of investigation, the experimental results obtained were analyzed and compared with the results of obtained by MARS.

4.1. Torsional Behavior of Normal Strength Beams

In this section, the torque-twist response of normal strength concrete beams with ferrocement "U" wrap, (plain beams and reinforced concrete beams) tested were discussed.

4.1.1. Torsional Behavior of Plain Normal Strength Beams

Normal strength plain "U" wrap beam with core concrete strength 35 MPa, mortar strength 40 MPa, aspect ratio 2.0 and with 3,4 and 5 numbers of wire mesh layers in ferrocement shell was cast and tested. The beams were designated as BQ3N, BQ4N AND BQ5N.

4.1.1.1. General Torsional Behavior of Plain Normal Strength Beams

The ultimate torque of the plain beams with jacketing was presented in the Table- 2. A comparison of experimental torque with that of predicted by MARS of plain concrete beams in column shows that experimental are higher than the predicted values 6.76%, 8.50% and 8.40 % for BQ3N, BQ4N and BQ5N respectively. This shows that the predicted values are well in agreement with experimental values for plain "U" wrapped beams.

4.1.1.2. Effect of Number of Layers:

In ferrocement wrapped concrete beams, the most important parameters influencing the torque-twist response are number of mesh layers and strength of ferrocement mortar matrix. To study the effect of number of layers, the aspect ratio is kept as 2.0; core concrete and mortar matrix are taken as 35 MPa and 40 MPa respectively. When it is analyzed with

layers from 3, 4 and 5, the ultimate torques are found to be 5.07 kNm for all beams without any variation. This is due to the fact that the crack is initiated on un-wrapped face for 3 layers also. Increasing the number of layers beyond three layers only increases the tensile strength of ferrocement, but unable to change the failure plane. The ultimate torque of these beams were found to be experimentally 5.415 kNm, 5.415 kNm and 5.49 kNm respectively for 3, 4 and 5 numbers of mesh layers against the predicted value of 5.07 kNm for all beams. The variation of ultimate torque with number of layers was shown in Fig. 1.

From the literature it is found strengthening of the longer faces improve the torque carrying capacity. But this way of strengthening shifts the failure plane from longer face to un-wrapped shorter face. Thus any further strengthening of longer face beyond this limit will not improve the capacity of the section. If the grade of core concrete, mortar of the wrapping and the aspect ratio of the cross section are constant, then the increase in the number of layers beyond certain limit may not enhance the torque carrying capacity of wrapped beams. The similar behavior is noticed in the predicted values also. Increase in the number of layers would be more effective for higher aspect ratio, high strength core concrete and for reinforced concrete sections in the post cracking stage (when the un-wrapped portion contains high strength materials).

4.1.2. Torsional Behavior of RCC Normal Strength Beams

In this phase, the response of ferrocement "U" wrapped reinforced concrete beams with normal strength core concrete is discussed. In a reinforced concrete beam the states of torsion influences the torque-twist diagram. For a wrapped beam the states of torsion and ferrocement influence the torsional behavior. The number of layers present in the ferrocement influences its torsional behavior. So, the variables in this study were taken as states of torsion with respect to one grade of concrete and the number of mesh layers on ferrocement "U" wrap. The longitudinal reinforcement and transverse reinforcement were varied in such a way that all possible six states of torsion to occur.

To study the effect of number of layers on all possible arrangements of reinforcement in a reinforced concrete member for torsion, the layers are varied as three, four and five on each possible state of torsion. The aspect ratio, concrete strength and ferrocement matrix strength of the beams were fixed as 2.0, 35 MPa and 40 MPa respectively. So, in this phase total eighteen numbers of beams were tested.

4.1.2.1. General Behavior of RCC Normal Strength Beams

All beams in this phase were similar to beams of BQ3N, BQ4N and BQ5N with different amount of reinforcement in core concrete.

4.1.2.2. Beams with Only Longitudinal Reinforcement

A reinforced concrete member when subjected to torsion, longitudinal reinforcement, transverse reinforcement and the concrete present in the diagonal strut resist the load. For a single type of reinforcement, as one of the load resisting elements is absent, the load carrying capacity is limited to plain beams only. Thus the beams with single type of reinforcement with ferrocement "U" wrap can be analyzed as plain ferrocement "U" wrapped beams. The beams L3N, L4N and L5N were cast to reflect the effect of layers on torque-twist response of "U" wrapped beams with longitudinal steel alone. The beams L3N, L4N and L5N were similar to the beams BQ3N, BQ4N and BQ5N respectively if the later beams were provided with only longitudinal steel. The ultimate torque of these beams L3N,

L4N and L5N were found 5.69 kNm, 5.73 kNm and 5.73 kNm respectively which indicates that there was no such improvement in ultimate torque. The predicted torque of the beams was found to be 5.956 kNm for all the three beams. The predicted values are found to be 3.94%, 3.766% and 2.34% more for beams L3N, L4N and L5N respectively as shown in Fig. 2.

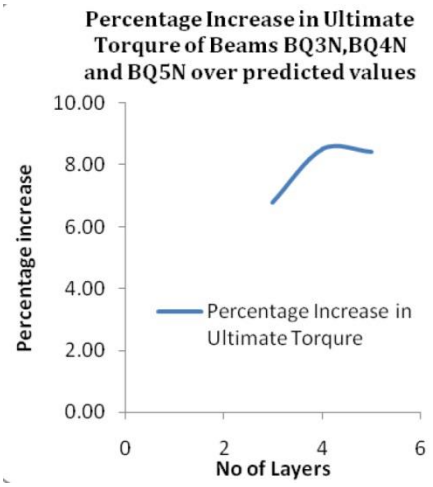

Fig. 1 Percentage Increase in Ultimate Torque and Twist of Experimental Values over Predicted Values

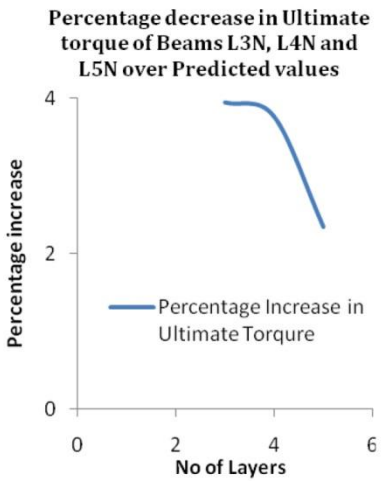

Fig. 2 Percentage variation of torque, twist and Stiffness of only Longitudinally reinforced beams

4.1.2.3. Beams with Only Transverse Reinforcement

To observe the effect of number of layers on the beams those were provided with only transverse reinforcement, three beams were analyzed, designated as T3N, T4N and T5N and tested under pure torsional loading. The difference in beams T3N, T4N and T5N to that of plain ferrocement "U" wrapped beams BQ3N, BQ4N and BQ5N was that the latter were provided with 8 mm diameter bars with 100 mm c/c.

The cracking and ultimate torsional strength of all these beams were found to be 5.62 kNm, 5.67 kNm and 5.69 kNm experimentally. The predicted ultimate torques of all these beams is found to be 5.871 kNm for all these beams as shown in Fig.3. The torque increased by 3.25%, 2.24% and 2.71% for beams T3N, T4N and T5N over their plain "U" wrapped beams BQ3N, BQ4N and BQ5N respectively. This shows that the improvement is very marginal.

The "U" wrapping beams with single type of reinforcement i.e., transverse reinforcement or longitudinal reinforcement alone cannot enhance the torsional capacity of beams to a substantial amount, but are able to increase the toughness to a considerable amount with respect to plain "U" wrapped beams. Similar observations were reported by earlier researchers for reinforced concrete beams and for steel fiber reinforced beams T.D.G Rao and D.R.Seshu [2006].

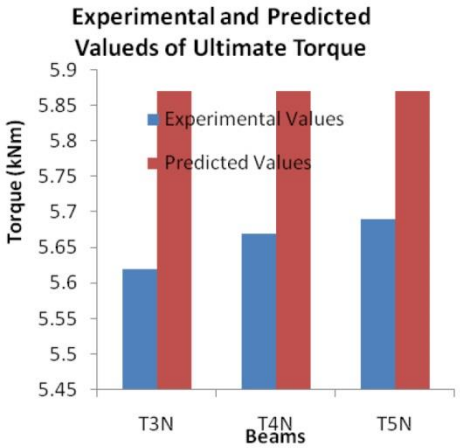

Fig. 3 Percentage variation of torque of only Transverse reinforced beams

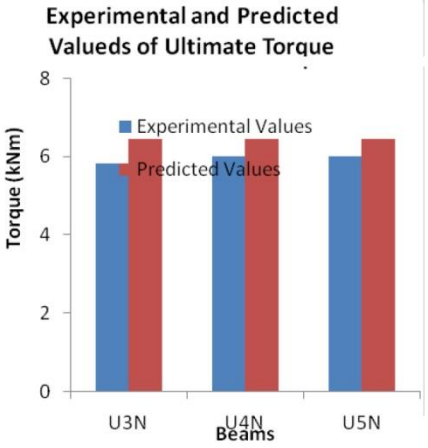

Fig. 4 Experimental and Predicted values of Torque for under reinforced beams

4.1.2.4. Under Reinforced Beams

To study torque-twist response of under reinforced beams with different numbers of mesh layers in the ferrocement "U" wrap, three beams were analyzed and experimental data are compared. Three beams were cast with three, four and five layers of mesh reinforcement and the main reinforcement (longitudinal and transverse) provided is lower than the balanced reinforcement. The beams were designated as U3N, U4N and U5N. The aspect ratio, ferrocement matrix mortar strength and core concrete strength of these beams were kept as 2.0, 40 MPa and 35 MPa respectively. The companion specimens for these reinforced beams are BQ3N, BQ4N and BQ5N. Henceforth these beams will be called as U series beams. The experimental ultimate torque values were found to be 5.816 kNm, 6.01 kNm and 6.01 kNm against predicted values of 6.45 KNm for three, four and five layers respectively as shown in Fig.4. The predicted value overestimates by 7.31% for beam U5N.

4.1.2.5. Longitudinally Over Reinforced Beams

The beams in this series were cast to study the torsional response of longitudinally over reinforced beams with three, four and five number of mesh layers in the wrapping portion, keeping the aspect ratio, mortar strength and concrete grade as 2.0, 40 MPa and 35 MPa respectively. The beams were designated as Lo3N, Lo4N and Lo5N and henceforth will be called as "L" series beams for normal strength beams. The experimental and predicted values are shown in Table 2. The ultimate torques of the beams was found to be 6.899 kNm, 6.939 kNm and 6.979 kNm for beams Lo3N, Lo4N and Lo5N respectively against the predicted values 6.752 kNm for all the three beams. As there is shortage of reinforcement in transverse direction on the unwrapped face, increase the number layers cannot enhance the ultimate torque. The same was revealed from the soft computing method MARS. The predicted values are well in agreement with experimental values as shown in Fig.5.

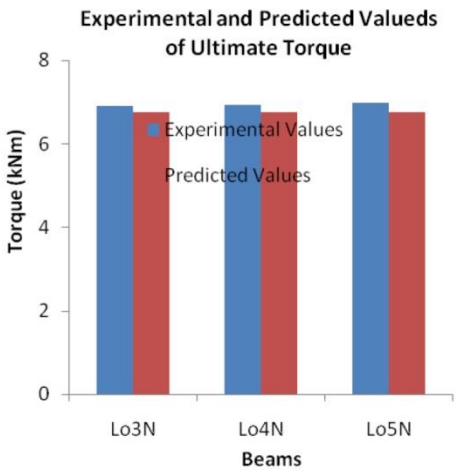

Fig. 5 Experimental and Predicted Torque variation of longitudinally over reinforced beams

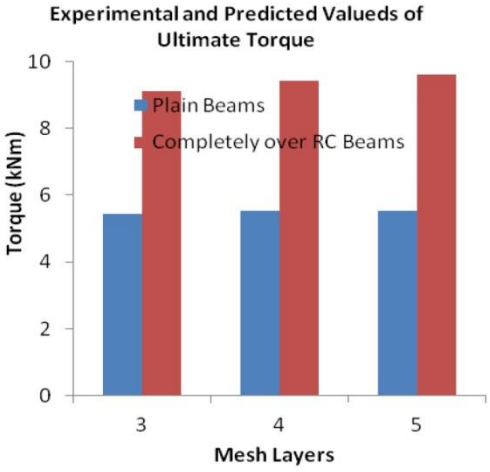

Fig. 6 Torque of Plain and over reinforced beams for different layers

4.1.2.6. Transversely Over Reinforced Beams

To examine transversely over reinforced beams, three beams, designated as To3N, To4N and To5N were analyzed and verified with experimental results. The material properties of core and wrap were mentioned in experimental section. The beams henceforth will be referred to as "T" series beams. The torque-twist responses of individual beams, both experimental and predicted are presented below. The ultimate torque of these beams To3N, To4N and To5N was found to be 6.899 kNm, 7.38 kNm and 7.86 kNm. The increases in ultimate torque of these beams To3N, To4N and To5N over their companion beams BQ3N, BQ4N and BQ5N were found to be 27.35%, 36.41% and 43.16% respectively. This shows there was a noticeable amount of increase in ultimate torque. The ultimate torque of beam To4N was 7.11% more than that of To3N and To5N was more than 14.07% of beam To3N. The rate of enhancement of ultimate torsional strength of this series with respect to number of mesh layers was more in comparison to other states of torsion. The predicted values are found to be 6.463 kNm,6.463 kNm and 7.86 kNm respectively. The predicted values are lower by 6.32%, 12.42 % and 0 % than their experimental values.

4.1.2.7. Completely over reinforced

To observe the effect of number of layers on completely over reinforced beams, three over reinforced beams were analyzed. The beams in this series were designated as Co3N, Co4N and Co5N. The main reinforcement was designed in such a way that there would be no yielding of reinforcement and failure would be due to crushing of concrete**.** The material details of these beams were presented in Table 1. The ultimate torques of these beams was 9.015 kNm, 9.426 kNm and 9.62 kNm respectively for beams Co3N, Co4N and Co5N over the same predicted values. The increase in ultimate torque of these beams Co3N, Co4N and Co5N with respect to their companion beams BQ3N, BQ4N and BQ5N were found to be 66.38%, 74.23% and 75.22% respectively. The experimental values are presented in Fig. 6 for these beams. These beams showed maximum increase in ultimate torque over their respective plain "U" wrapped beams BQ3N, BQ4N and BQ5N in

comparison to all states of torsion. The increase in ultimate torque of Co4N over Co3N was 4.5% while the same was 6.71% for Co5N over the beam Co3N. Here absolutely the predicted values are exactly equal to the experimental values.

4.2. Torsional Behavior of High Strength Beams

Torsional behavior of High strength concrete beam differs from the normal strength concrete beams in respect of brittleness and toughness. Also due to change of tensile strength and softening co-efficient factors, the torsional behavior of high strength concrete beams should be treated separately. Thus high strength concrete beams containing plain concrete and reinforced concrete beams are analyzed in this section.

4.2.1. Torsional Behavior Plain High strength beams

The torsional behavior of a plain ferrocement "U" wrapped beam is influenced by its core material properties and shell ferrocement material properties. The aspect ratio and core concrete tensile strength are the important factors for core material which influence the torsional behavior of a plain wrapped beam. The number of layers and mortar strength in ferrocement shell are the other important parameters to govern the torsional strength of ferrocement "U" wrapped plain beams. In this section BH and B4H were analyzed.

The ultimate torque of the two beams BH and B4H was found to be 4.612 kNm and 6.52 kNm respectively. Beam BH is a plain beam without wrapping while B4H has a ferrocement wrap of 4 layers of mesh without any conventional reinforcement. The increase in ultimate torque of B4H is 41.37% over beam BH. This is due to wrapping. This shows even the wrapping is on three sides, the torsional strength increases a lot.

A plain beam with aspect ratio 2.0 and core concrete strength 60 MPa was cast and tested. The ultimate torque and twist were found to be 4.61 kNm and 0.0028 rad/m respectively. The same calculated by skew bending theory was found 4.34 kNm and 0.003468 rad/m. When the similar beam was provided with a ferrocement "U" wraps with four layers of mesh and even with ferrocement matrix of lower strength (55 MPa) than that of core concrete, the torsional strength was found to be 6.50 kNm. This shows that the beams with "U" wraps have more strength than that of plain beams and their strength cannot be estimated by skew bending theory.

4.2.2. Torsional Behavior of RCC High Strength Beams

Reinforcement gets activated beyond cracking. So, torque-twist response of a reinforced concrete beam beyond cracking is influenced by the reinforcement present in the beam. The post cracking torque-twist response of a ferrocement "U" wrapped beam is characterized by the reinforcement present in the core concrete and the mesh layers in the ferrocement shell.

Out of six possible arrangements of reinforcement in the core concrete, the last four types are related to states of torsion. After cracking, the torsional resistance is due to longitudinal reinforcement, transverse reinforcement and the concrete present between the diagonal strut. As the first two categories lack one of the resisting components, they can be analyzed as plain beams. In normal strength "U" wrapped concrete beams; it was proved that the beams with single type of reinforcement were unable to increase the torsional strength over plain beams but capable of increasing the toughness to some extent. To examine the effect of "U" wrapping on the torsional strength of beams containing single type of reinforcement i.e. either only longitudinal or transverse reinforcement with high

strength concrete, two beams were cast and tested in third phase of the work. The aspect ratio, core concrete compressive strength and ferrocement mortar matrix of the beams were kept constant as 2.0, 60 MPa and 55 MPa.

4.2.2.1. Beams with only Longitudinal Reinforcement

A beam was cast with six numbers of 12 mm diameter bars as longitudinal reinforcement provided in the core area without any transverse reinforcement and four numbers of mesh layers in the ferrocement shell. The beam was designated as L4H.

Ultimate torque of beam L4H was found to be 6.55 kNm. The increase in torque of beam L4H over its plain "U" wrap beam B4H is 4.46%. The predicted value 8.51% more than the experimental values.

4.2.2.2. Beams with only Transverse Reinforcement

To investigate the effect of only transverse reinforcement on torque-twist response of ferrocement "U" wrapped concrete beam, T4H was cast and tested. T4H was cast with stirrups of 10 mm diameter bars at a spacing of 70 mm c/c without longitudinal reinforcement in the test region. The ultimate torque of the beam was found to be 6.59 kNm against the predicted value of 7.02 kNm. The increase in cracking torque over the beam B4H was 1.38% only.

4.2.2.3. Effect of Number of Layers on different States of Torsion

To study the effect of a particular mesh layer on different states of torsion, aspect ratio, ferrocement mortar matrix and concrete strength of beams were kept as 2.0, 55 MPa and 60 MPa, mesh layer was kept as 4 and beams were U4H, Lo4H, To4H and Co4H. The designations of the beams were already explained earlier. The beams U4H, Lo4H, To4H and Co4H have ultimate torque of 7.68 kNm, 7.87 kNm, 8.86 kNm and 12.91 kNm respectively. The predicted values are 7.68 % less, 2.91 % more, and 0.43 % more and exactly same with their experimental values for the beams U4H, Lo4H, To4H and Co4H respectively. A comparison of normal strength and high strength beams shown in Fig.8.

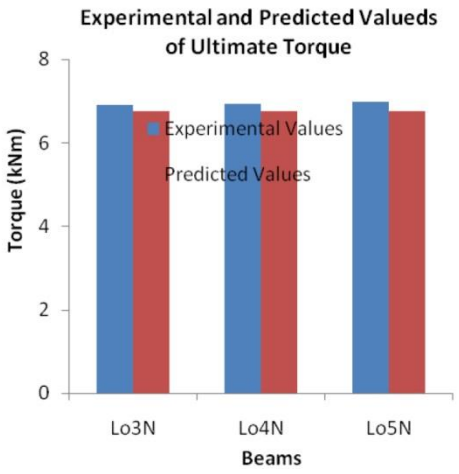

Fig. 7 Comparison of Torque between Experimental and Predicted Values for high strength Beams

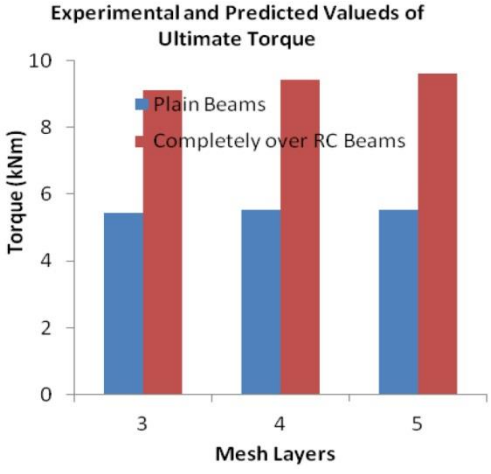

Fig. 7 Comparison of Torque between normal strength and high strength Beams for 4 layers

5. CONCLUSIONS

From the soft computing model MARS and experimental study for torsional behavior of "U" wrapped plain and reinforced concrete beams, the following conclusions were drawn.

Plain "U" Wrapped Beams

1. A significant increase in torsional strength is observed with ferrocement "U" wrapped normal and high strength concrete beams over their plain concrete beams.
2. Ultimate torque is dependent upon the core concrete, mortar strength, mesh layers and aspect ratio combinedly.
3. The "U" wrap can increase the torsional capacity of a plain beam. This proves the effectiveness of "U" wrapped beams.

"U" Wrapped Reinforced Concrete Beams

1. The increase in torsional strength over the number of layers for any state of torsion is very less.
2. Single type of reinforcement either longitudinal or transverse reinforcement is ineffective in enhancing the torsional strength.
3. Transversely over reinforced concrete beams showed overall increase in torque over longitudinally over reinforced beams.
4. Soft computing model and the experimental results reveal that the torque twist response of a ferrocement "U" wrap beam is more influenced by the state of torsion than the amount of ferrocement reinforcement.
5. The results of soft computing by MARS are well in agreement with experimental results.

REFERENCES

1. ACI committee 318, (2002). Building code requirements for structural concrete and commentary, *ACI 318R-02*: Farmington Hills, Michigan.
2. ACI Committee 549. (1979). Ferrocement-Materials and Applications. ACI Symposium Proceedings SP-61: *American Concrete Institute* 549, Farmington Hills, Michigan.
3. Ameli, M., and Ronagh,H.(July-Aug 2007). "Analytical model for evaluating torque of FRP strengthened reinforced concrete beams." *Journal of Composites for construction*, pp. 384-390.
4. Bansal,P.P., Kumar, M. and Kaushik,S. K.(2007). " Effect of mesh orientation on strength of beams retrofitted using ferrocement jacket." *International Journal of Engineering*, Vol- 20 Issue-(1),pp.8-19.
5. Behera, G. C. Rao, T. D. G. & Rao, C. B. K. (August-2008). " Torsional Capacity of High Strength Concrete Beams jacketed with ferrocement U wraps." *Asian Journal of Civil Engineering*, Volume -9 Number 4, pp. 411-422.
6. Behera, G. C. Rao, T. D. G. & Rao, C. B. K"A study on post cracking torsional behaviour of high strength reinforced concrete beams with ferrocement "u" wraps" Vol. 22, 2014, No. 3, DOI: 10.2478/sjce-2014-0012, Slovak Journal of Civil Engineering,pp.1 – 12.
7. Behera, G. C. Rao, T. D. G. & Rao, C. B. K **"**Analytical model for torsional response of RC beams strengthened with ferrocement U-Wraps" DOI: 10.2749/101686614X13854694314847, SEI Vol.24, No.4, Nov-2014, IABSE Structural Engineering International, pp.509-520.
8. Chalioris, C.E.(2006). "Experimental Study of the Torsion of Reinforced Concrete Members." *Structural Engineering and Mechanics*, Vol. 23, No. 6, pp. 713-737.
9. Chalioris, C.E.(2007). "Analytical Model for the Torsional Behaviour of Reinforced Concrete Beams Retrofitted with FRP Materials." *Engineering Structures*, Vol. 29, No. 12, pp. 3263-3276.
10. Chalioris, C.E.(2008). "Torsional Strengthening of Rectangular and Flanged Beams using Carbon Fibre-Reinforced-Polymers - Experimental Study." *Construction and Building Materials*, Vol. 22, No. 1, pp. 21-29, 2008.

11. Chalioris C.E., Thermou, G.E. and Pantazopoulou, S.J. (2014). "Behaviour of Rehabilitated RC Beams with Self-Compacting Concrete Jacketing - Analytical Model and Test Results." *Construction and Building Materials*, Vol. 55, pp. 257-273.
12. Deifalla, A., Awad, A. and Elgarhy, M. (2013). " Effectiveness of externally bonded CFRP strips for strengthening flanged beams under torsion; An experimental study."*Engineering structure* (56),pp.2065-2075.
13. Deifalla, A. and Ghobarah, A.(2010 a). "Full Torsional Behavior of RC Beams Wrapped with FRP: Analytical Model." *Journal of Composites for Construction*, Vol.14,No.3,pp.289-300.
14. Deifalla, A. and Ghobarah, A.(2010 b). " Strengthening RC T-beams Subjected to Combined Torsion and Shear using FRP Fabrics: Experimental study.", *Journal of Composites for Construction*, Vol. 14, No. 3, pp. 301-311.
15. Ghobarah, A. Ghorbel, M. N. and Chidiac, S. E.(November-2002). " Upgrading Torsional Resistance of Reinforced Concrete Beams Using Fiber-Reinforced Polymer." *ASCE Journal of composites for Construction*, Vol- 6 No.4, pp. 257-263.
16. Hii A, K. Y. and Riyad, A.M.(2006)."An experimental and numerical investigation on torsional strengthening of solid and box- section RC beams using CFRP laminates." *Composite structures*,vol.75, pp. 213-221.
17. Hii, A.K.Y. and Riyad, A. M. (Jan-Feb 2007). "Torsional capacity of CFRP Strengthened reinforced concrete beams." *Journal of Composites for construction ASCE*, pp. 71-80.
18. Karayannis, C.G., Chalioris, C.E.and Sirkelis, G.M.(2008). " Local Retrofit of Exterior RC Beam-Column Joints using Thin RC Jackets - An Experimental Study." *Earthquake Engineering and Structural Dynamics*, Vol. 37, No. 5, pp. 727-746.
19. Kumar, P.R., Oshima, T, M. and Yamazaki, T.(2007). " Studies on RC and ferrocement jacketed columns subjected to simulated seismic loading" *Asian Journal of Civil Eng (Build Housing)*, Vol.8(2), pp.215–225.
20. Li, B.,Lam, E.S.S., Wu, B. and Wang, Y.-Y.(2013). " Experimental Investigation on Reinforced Concrete Interior Beam-Column Joints Rehabilitated by Ferrocement Jackets," *Engineering Structures*, Vol. 56, pp. 897-909.
21. Liang-Jenq, Leu. and Yu-Shu, Lee.(February 2000). " Torsion design charts for reinforced concrete rectangular members." *journal of structural engineering ASCE*,pp.210-218.
22. Ming, J. and Grunberg, J.(2006). "Mechanical analysis of reinforced concrete box beam Strengthened with carbon fiber sheets under combined actions." *Composite Structures*, vol.73,pp. 488-494.
23. Ming, J., Werasak, R. and Zhongxian, Li.(2007). "Torsional strengthening of reinforced concrete box beams using carbon fiber reinforced polymer." *Science Direc, Composite structures*,Vol.78, pp.264-270.
24. Nie, J., Liang, T. and Cai,S. C.(2009). " Performance of steel- concrete composite beams under combined bending and torsion". *journal of structural* Engineering,ASCE,pp.1049-1057.
25. Panchacharam,S. and Belarbi,A.(13-19 October 2002)."Torsional Behavior of Reinforced Concrete Beams Strengthened with FRP Composites." In *Proceedings of First FIB Congress*, Osaka, Japan, pp. 1-11.
26. Rao, T. D. G. and Seshu, D.R. (2005). " Analytical model for torsional response of steel fiber reinforced concrete members under pure torsion." *Concrete and Cement Composites*, Vol. 27,pp.493-501.
27. Rao, T. D. G. and Seshu, D.R.(2006). " Torsional Response of fibrous reinforced concrete beams; Effect of single type reinforcement." *Construction and Building materials*, Vol.20,pp.187-192.
28. Rao,T. D. G. and Seshu, D.R. (2003). "Torsion of steel fiber reinforced concrete members." *Cement and Concrete Research*, pp. 1783-1788.
29. Rita, S. Y., Wong, F. and Vecchio, J. (January-Feb-2003). "Towards Modeling of Reinforced Concrete Members with Externally Bonded Fiber-Reinforced Polymer Composites." *ACI Structural Journal*, pp.47-55.
30. Salom, P.R., Gergely, J., and Young, D.T.(January 2003). "Torsional retrofit of Spandrel Beams with composite Laminates." In: *Proceedings of Institution of Civil Engineers, Structures and Buildings*, 157 Issues SBI,pp. 69-76.
31. Salom,P.R., Greeley, J.R. and David,Y.T.(March-April 2004)."Torsional Strengthening of Spandrel Beams with Fiber-Reinforced Polymer Laminates."*Journal of composites for construction, ASCE*, pp.157-162.
32. Santhakumar, D. R. and Chandrasekharan, E.(2007). "Behaviour of reinforced concrete beams under combined bending and torsion: A numerical study." *Electronic Journal of structural Journal*, pp. 1-7.
33. Shannag, M.J. and Mourad, S.M.(2012). "Flowable high strength cementitious matrices for ferrocement applications." *Construction and Building Materials*, Vol. 36, pp. 933-939.

TORZIONO PONAŠANJE GREDA OD ARMIRANOG BETONA OJAČANIH ZAŠTITNIM OBLOGAMA U OBLIKU „U“ KOŠULJICA

Tehnologija oblaganja je jedan od efikasnih načina za ojačanje betonskih elemenata. Više istraživača je izveštavalo o ojačavanj betonskih elemenata polimerima of fiberglasa ili ugljeničnih vlakana. Oblaganje sa tri strane je jedan od efikasnih metoda za ojačavanje greda koje nose međuspratne konstrukcije. Dostupno je malo literature koja se bavi ojačavanjem betonskih elemenata oblogama "U" oblika koji su izloženi torzionim opterećenjima. U ovom istraživanju, pokušano je da se kvantifikuje napredak u ponašanju četvorouglih betonskih elemenata obloženih "U" košuljicama a koji su izloženi torzionom opterećenju. Ferocement je uzet za material obloge. Grede su izlivene sa različitim brojem mrežnih slojeva i različitim torzionim ojačanjima. Grede su analiziranje korišćenjem MARS-a. Dobijeni rezultati se slažu sa rezultatima eksperimentalnog ispitivanja.

Ključne reči: *ferocement: „U“ obloga, Moment loma, MARS, ferocement*

FACTA UNIVERSITATIS
Series: **Architecture and Civil Engineering** Vol. 16, No 1, 2018, pp. 17-27
https://doi.org/10.2298/FUACE160609002Z

COMPARATIVE ANALYSIS OF USING DEGREE OF RIGIDITY AND ROTATIONAL STIFFNESS OF CONNECTIONS IN STRUCTURAL DESIGN

UDC 624.046.4

Srđan Živković, Marija Spasojević Šurdilović, Dragana Turnić, Marko Milošević

University of Niš, Faculty of Civil Engineering and Architecture, Niš, Serbia

Abstract. *Using classical formulation of stiffness method, impact of semi-rigid connections on the stresses and strains can be analyzed by the degree of rigidity or by rotational stiffness of connections. In this paper, functional dependence between the degree of rigidity and rotational stiffness of connections is formulated and the comparative analysis of these two approaches in the analysis of semi-rigid connections behavior of members in real structures, is implemented.*

Key words: *semi-rigid connections, rotational stiffness of connection, degree of rigidity of connection*

1. INTRODUCTION

1.1. Mathematical model of a semi-rigid connection

Generally, the semi-rigid connection of two members allows a certain degree of additional relative displacement in the plane of the connection, in the direction of all generalized displacements, which, for the linear element in plane means a relative horizontal and vertical displacement and rotation of the cross-section at the joint location (Figure 1). As for the majority of frame structures, vertical and horizontal displacements (slipping) of the joints are negligible in comparison to the relative rotation of the cross section at the joint location, the influence of semi-rigid connections can be modeled with an elastic spring with rotational stiffness S_{ik}. This coefficient includes the impact of rotational stiffness of the connection on the change of static and deformation parameters in the structure. The numerical value of rotational stiffness of the connections of the member „*ik*“ at *i*, and *k*, nodes is determined by the expressions:

Received June 9, 2016 / Accepted April 12, 2017
Corresponding author: Srđan Živković
Faculty of Civil Engineering and Architecture, University of Niš, 18000 Niš, Aleksandra Medvedeva 14, Serbia
E-mail: srdjan.zivkovic@gaf.ni.ac.rs

$$S_i = \frac{M_i}{\phi_i}, S_k = \frac{M_k}{\phi_k} \tag{1}$$

where:

M_i, M_k – is the bending moment at the location of the connection in the node *i*, that is, *k*,

Φ_i, Φ_k – relative rotation of the connection in node *i*, that is, *k*.

Rotational stiffness of the connection, in the geometrical terms, represents the angle which is constituted by the tangent and abscissa on the moment-rotation curve of the connection that is the gradient of the $M - \Phi$ connection curve (Figure 2).

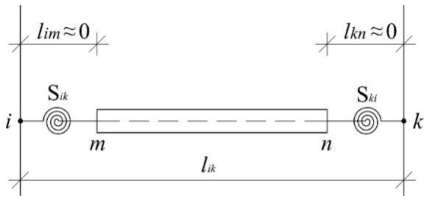

Fig. 1 Hybrid beam element

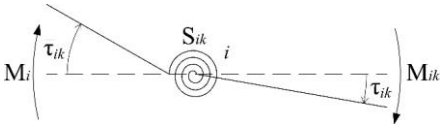

Fig. 2 Elastic spring deformation

1.2. Basic strain parameters of a straight member according to the first order theory

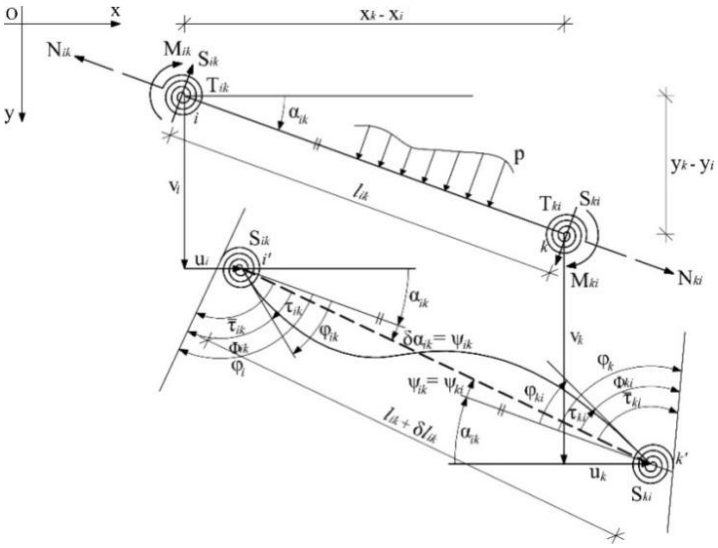

Fig. 3 Straight member with semi-rigid connections at the ends *i* and *k*, before and after deformation

Let the member be decomposed from the given structural system (Figure 3), which is connected to the rest of the structure on its nodes. The isolated member, under the arbitrary load *p* and unknown intersecting forces in the node *i*: N_{ik}, T_{ik} and M_{ik}, and in the node *k*: N_{ki}, T_{ki} and M_{ki}, is in equilibrium.

Due to the deformability of connections, the rotation of the end cross sections of the member φ_{ik}, that is φ_{ki}, is not equal to the rotation of nodes φ_i, that is φ_k, but it is:

$$\begin{gathered}\varphi_i - \varphi_{ik} = \bar{\tau}_{ik} - \tau_{ik} = \Phi_{ik}, \text{ and} \\ \varphi_k - \varphi_{ki} = \bar{\tau}_{ki} - \tau_{ki} = \Phi_{ki}\end{gathered} \tag{2}$$

If the angles of tangent rotations are designated with $\alpha_{ik}^{(o)}$ and $\alpha_{ki}^{(o)}$ on the nodes *i* and *k* of a *simple beam*, due to the applied load *p*; with $\alpha_{ik}^{(\Delta t)}$ and $\alpha_{ki}^{(\Delta t)}$ the same rotation angles due to temperature differences $\Delta t°$; and with α_{ik} and β_{ik}, that is α_{ki} and β_{ki}, the slope angles due to unit bending moments $M_{ik} = 1$ and $M_{ki} = 1$ (Figure 4), then on the basis of the equations (1) and (2), and the principle of superposition, the expressions for the moments on the ends *i* and *k*, of the member „*ik*" can be obtained:

$$\begin{aligned}M_{ik} &= \bar{a}_{ik} \cdot \varphi_i + \bar{b}_{ik} \cdot \varphi_k - \bar{c}_{ik} \cdot \psi_{ik} + \bar{m}_{ik}^{(o)} + \bar{m}_{ik}^{(\Delta t)}, \\ M_{ki} &= \bar{b}_{ki} \cdot \varphi_i + \bar{a}_{ki} \cdot \varphi_k - \bar{c}_{ki} \cdot \psi_{ik} + \bar{m}_{ki}^{(o)} + \bar{m}_{ki}^{(\Delta t)};\end{aligned} \tag{3}$$

where the following designations are introduced:

$$\bar{a}_{ik} = \frac{\alpha_{ki} + \frac{1}{S_{ki}}}{D}, \quad \bar{a}_{ki} = \frac{\alpha_{ik} + \frac{1}{S_{ik}}}{D}, \quad \bar{b}_{ik} = \frac{\beta_{ik}}{D} = \bar{b}_{ki},$$

$$D = \left(\alpha_{ik} + \frac{1}{S_{ik}}\right) \cdot \left(\alpha_{ki} + \frac{1}{S_{ki}}\right) - \beta_{ik}^2$$

$$\bar{c}_{ik} = \bar{a}_{ik} + \bar{b}_{ik}, \quad \bar{c}_{ki} = \bar{a}_{ki} + \bar{b}_{ki},$$

$$\bar{m}_{ik}^{(o)} = -\left(\bar{a}_{ik} \cdot \alpha_{ik}^{(o)} - \bar{b}_{ik} \cdot \alpha_{ki}^{(o)}\right), \quad \bar{m}_{ki}^{(o)} = -\left(\bar{a}_{ki} \cdot \alpha_{ki}^{(o)} - \bar{b}_{ik} \cdot \alpha_{ki}^{(o)}\right)$$

$$\bar{m}_{ik}^{(\Delta t)} = -\left(\bar{a}_{ik} \cdot \alpha_{ik}^{(\Delta t)} - \bar{b}_{ik} \cdot \alpha_{ki}^{(\Delta t)}\right), \quad \bar{m}_{ki}^{(\Delta t)} = \bar{a}_{ki} \cdot \alpha_{ki}^{(\Delta t)} - \bar{b}_{ik} \cdot \alpha_{ik}^{(\Delta t)}.$$

In the general case, the values in the equation (3), for the member with $EI_{ik} = const$ are $\bar{a}_{ik} \neq \bar{a}_{ki}$, $\bar{b}_{ik} = \bar{b}_{ki}$ and $\bar{c}_{ik} \neq \bar{c}_{ki}$. Since the parameters $\bar{a}_{ik}, \bar{b}_{ik}, \bar{c}_{ik}, \bar{a}_{ki}, \bar{b}_{ki}, \bar{c}_{ki}$, do not depend only on the geometrical characteristics of the cross-sections and mechanical properties of the basic material of the member, but also on the characteristics of the connections on the nodes of the member, and they are therefore named the constants of the member with semi-rigid connections.

On the basis of the conducted analysis, it can be concluded that, in the further analysis all the members of any type can be treated as a single type of members with semi-rigid connections at their nodes, with their appropriately calculated rotational stiffness of connections, which simplifies and standardizes the calculation, and is particularly important for application of structural design software.

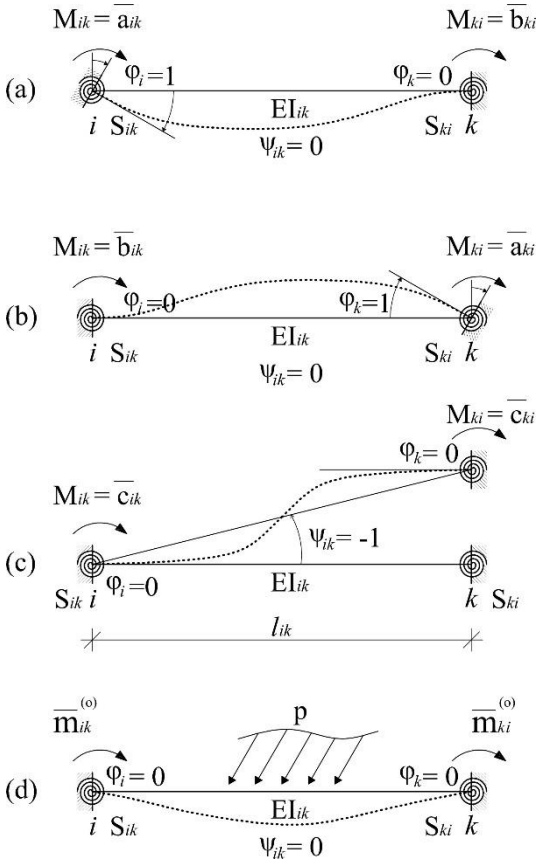

Fig. 4 Physical meaning of beam constants and the initial bending moments at the ends of a beam with semi-rigid connections

2. MEMBER STIFFNESS MATRIX IN THE CASE OF USING THE ROTATIONAL STIFFNESS OF CONNECTIONS

A large number of general and specialized software were developed for analysis and calculation of the structures, practically covering all the areas of analysis of stress-strain state of structures. The stiffness method presented in the matrix form is, almost regularly, the basis for production of contemporary computer software for linear system structural analysis, due to its general character, simplicity and significant automatism in calculation.

Regarding that the contemporary stress-strain analysis of complex engineering structures, cannot be imagined without the matrix formulation and application of electronic computers. The corrected member stiffness matrix will be used for the members semi-rigidly connected at the nodes, starting from the previously defined classic stiffness method, for the calculation of the system with semi-rigid connections of members.

Axial strain and bending of elements, represent two independent theories within the first order theory, so they can be considered independently. This can be concluded based on the structure of the stiffness matrix for the „*k*" type member, from which it can be seen that the members characterizing the axial rigidity, depend exclusively on the displacement in the direction of the element axis. The correction of stiffness matrix to take into account the deformability of the member connections, are performed only on the part of matrix, which refers to the bending issue. The terms of the stiffness matrix, referring to the axial load, remain unchanged, for the case of the members with deformable connections.

The stiffness matrix of the member with semi-rigid connections can be obtained starting from the basic stiffness matrix. For this purpose, it is necessary to establish relation between the basic deformation parameters and displacement parameters of the member, and the relation between the generalized forces and basic static parameters of the member.

In figure 3, a straight member with the semi-rigid connections on its nodes *i* and *k*, is presented, before and after the deformation. Assuming that those are small displacements and holding that $\alpha_{ik} = 0$, in the figure 3 the following interdependencies between the basic deformation and displacement parameters are obvious:

$$\begin{aligned} \bar{\tau}_{ik} &= \varphi_i - \psi_{ik} = \varphi_i - \frac{1}{l}(v_k - v_i), \\ \bar{\tau}_{ki} &= \varphi_k - \psi_{ik} = \varphi_k - \frac{1}{2}(v_k - v_i); \end{aligned} \tag{4}$$

which can be presented in the following matrix form:

$$\begin{bmatrix} \bar{\tau}_{ik} \\ \bar{\tau}_{ki} \end{bmatrix} = \begin{bmatrix} \frac{1}{l} & 1 & -\frac{1}{l} & 0 \\ \frac{1}{l} & 0 & -\frac{1}{l} & 1 \end{bmatrix} \cdot \begin{bmatrix} v_i \\ \varphi_i \\ v_k \\ \varphi_k \end{bmatrix} \tag{5}$$

where:

$$\begin{bmatrix} \frac{1}{l} & 1 & -\frac{1}{l} & 0 \\ \frac{1}{l} & 0 & -\frac{1}{l} & 1 \end{bmatrix} = [C] \tag{6}$$

is the matrix defining the relation between the basic deformation parameters of the „*ik*" member and generalized displacements.

The relation between the basic stiffness matrix and stiffness matrix [4], can be written in the following way:

$$[K] = [C]^T [K_0][C] \tag{7}$$

where:

$[K_0]$ – is the basic stiffness matrix,

$[C]^T$ – transposed matrix, of the matrix $[C]$, which defines the relation between the basic static parameters and generalized forces, and

$[C]$ – the matrix defining the relation between the basic deformation parameters of the member and generalized displacements.

The basic stiffness matrix is equal to the inverse flexibility matrix - $[D_0]$, i.e.:

$$[K_0] = [D_0]^{-1} = \frac{1}{\det[D_0]} \cdot adj[D_0] \tag{8}$$

The flexibility matrix $[D_0]$, represents the relation between the basic deformation and statically independent parameters of the member:

$$\{\delta\} = [D_0]\{X\} \tag{9}$$

where:
$\{\delta\}$ – vector of deformation parameters of the member,
$[D_0]$ – flexibility matrix, and
$\{X\}$ – vector of statically independent parameters of the member.

From the equation (8) [5], the basic matrix or stiffness is:

$$[K_0] = [D_0]^{-1} = \begin{bmatrix} a_{ik}\cdot\eta_1 & b_{ik}\cdot\eta_2 \\ b_{ik}\cdot\eta_2 & a_{ki}\cdot\eta_3 \end{bmatrix} = \begin{bmatrix} \bar{a}_{ik} & \bar{b}_{ik} \\ \bar{b}_{ik} & \bar{a}_{ki} \end{bmatrix} \tag{10}$$

The member stiffness matrix, with partially rigid connections, according to the expression (7) [5], has the following form:

$$[K] = \begin{bmatrix} \frac{\bar{c}_{ik}+\bar{c}_{ki}}{l^2} & \frac{\bar{c}_{ik}}{l} & -\frac{\bar{c}_{ik}+\bar{c}_{ki}}{l^2} & -\frac{\bar{c}_{ik}}{l} \\ \frac{\bar{c}_{ik}}{l} & \bar{a}_{ik} & \frac{\bar{c}_{ik}}{l} & \bar{b}_{ik} \\ -\frac{\bar{c}_{ik}+\bar{c}_{ki}}{l^2} & -\frac{\bar{c}_{ik}}{l} & \frac{\bar{c}_{ik}+\bar{c}_{ki}}{l^2} & -\frac{\bar{c}_{ki}}{l} \\ \frac{\bar{c}_{ik}}{l} & \bar{b}_{ik} & -\frac{\bar{c}_{ki}}{l} & \bar{a}_{ki} \end{bmatrix} \tag{11}$$

Expression reduction yields to the member stiffness matrix which is semi-rigidly connected at the node i, and hinged at the other end, having the following form [5]:

$$[K] = \begin{bmatrix} 3\frac{EI}{l^3}\bar{\eta}_1 & 3\frac{EI}{l^2}\bar{\eta}_1 & -3\frac{EI}{l^3}\bar{\eta}_1 \\ 3\frac{EI}{l^2}\bar{\eta}_1 & 3\frac{EI}{l}\bar{\eta}_1 & -3\frac{EI}{l^2}\bar{\eta}_1 \\ -3\frac{EI}{l^3}\bar{\eta}_1 & -3\frac{EI}{l^2}\bar{\eta}_1 & 3\frac{EI}{l^3}\bar{\eta}_1 \end{bmatrix} \tag{12}$$

It should be noticed that, as opposed to the member stiffness matrix for the members with semi-rigid connections on both nodes, where the influence of semi-rigid connections on the ends is covered by three different parameters, this influence is covered by one parameter only, when the matrix of the member with semi-rigid connection at one node, and hinge of the other, is concerned.

The stiffness matrices, determined by the basic stiffness matrix, excluding the differences in marking are completely equivalent to the stiffness matrices derived in the papers by D. Stojić, D. Bašić and E. Mešić [5], [6], [7], as well as with the stiffness matrices given in ECCS, „Analysis and Design of Steel Frames with Semi-Rigid Joints“, published in London in 1992.

3. Member Stiffness Matrix in the Case of Using the Degree of Rigidity of Connections

In the papers [1] [2] [3], using the classical formulation of the stiffness method, the influences of semi-rigid connections at the nodes of the members, are introduced through the degree of rigidity of connection:

$$\mu_{ik} = \frac{\varphi_{ik}^*}{\varphi_i}, \quad \mu_{ki} = \frac{\varphi_{ki}^*}{\varphi_k}; \tag{13}$$

where:

φ_i and φ_k – are the rotation angles of node „*i*“, that is „*k*“, and

φ_{ik}^* and φ_{ki}^* – are the rotation angles of end cross sections of the member „*ik*“.

By introducing the designations, according to the equation (2) and the figure 3, the degree of rigidity of connection can be expressed in the function of rotation of end cross-sections of the member „*ik*“ and relative rotation of the connections at the nodes of the member *ik*:

$$\mu_{ik} = \frac{\varphi_{ik}}{\varphi_i} = \frac{\varphi_{ik}}{\varphi_{ik}+\Phi_{ik}}, \quad \mu_{ki} = \frac{\varphi_{ki}}{\varphi_k} = \frac{\varphi_{ki}}{\varphi_{ki}+\Phi_{ki}}; \tag{14}$$

or, in the function of rotation of node „*i*“, i.e., „*k*“ and relative rotation of the connection at the nodes of the member „*ik*“:

$$\mu_{ik} = \frac{\varphi_{ik}}{\varphi_i} = \frac{\varphi_i-\Phi_{ik}}{\varphi_i}, \quad \mu_{ki} = \frac{\varphi_{ki}}{\varphi_k} = \frac{\varphi_k-\Phi_{ki}}{\varphi_k}; \tag{15}$$

That is:

$$\mu_{ik} = 1 - \frac{\Phi_{ik}}{\varphi_i}, \quad \mu_{ki} = 1 - \frac{\Phi_{ki}}{\varphi_k}; \tag{16}$$

The same authors derived the basic stiffness matrix, whose general form is, [3]:

$$[K_0] = \begin{bmatrix} \bar{a}_{ik}^* & \bar{b}_{ik}^* \\ \bar{b}_{ik}^* & \bar{a}_{ki}^* \end{bmatrix} \tag{17}$$

For the member with $EI = const.$ written in a derived form, it is:

$$[K_o] = \begin{bmatrix} \mu_{ik}(3+\mu_{ki})\frac{EI}{l} & 2\mu_{ik}\mu_{ki}\frac{EI}{l} \\ 2\mu_{ik}\mu_{ki}\frac{EI}{l} & \mu_{ki}(3+\mu_{ik})\frac{EI}{l} \end{bmatrix} \tag{18}$$

4. Functional Dependence between Degree of Rigidity and Rotational Stiffness of Connections

Analyzing under which conditions the basic stiffness matrix (18) will be identical to the basic stiffness matrix derived in this paper (10), a system of three independent non-linear equations is obtained, which in the matrix form are:

$$\begin{bmatrix} \mu_{ik}(3+\mu_{ki})\frac{EI}{l} & 2\mu_{ik}\mu_{ki}\frac{EI}{l} \\ 2\mu_{ik}\mu_{ki}\frac{EI}{l} & \mu_{ki}(3+\mu_{ik})\frac{EI}{l} \end{bmatrix} = \begin{bmatrix} \frac{4EI}{l}\cdot\eta_1 & \frac{2EI}{l}\cdot\eta_2 \\ \frac{2EI}{l}\cdot\eta_2 & \frac{4EI}{l}\cdot\eta_2 \end{bmatrix} \tag{19}$$

4.1. The case when the member is semi-rigidly connected at one node, and connected with ideal hinge at the other node, $\mu_{ik} \neq 0$ and $\mu_{ki} = 0$, i.e. $\Psi_{ik} \neq 0$ and $\Psi_{ki} \to \infty$

Fig. 5 Semi rigid connection at left node and connection with ideal hinge at right node

The system of equations (19) represents a system of three independent equations where only one unknown parameter μ_{ik} is present. By solving this system of equations according to the unknown parameter μ_{ik}, the following is obtained:

$$\mu_{ik} = \frac{4}{3} \cdot \eta_1 = \frac{4}{3} \cdot \lim_{\Psi_{ki} \to \infty} \frac{1+3\Psi_{ki}}{1+4(\Psi_{ik}+\Psi_{ki})+12\Psi_{ik}\Psi_{ki}} = \frac{4}{3} \cdot \frac{3}{4+12\Psi_{ik}} \tag{20}$$

That is:

$$\begin{aligned} \mu_{ik} &= \frac{1}{1+3\Psi_{ik}}, \qquad \mu_{ki} = 0; \\ \Psi_{ik} &= \frac{1-\mu_{ik}}{3\mu_{ik}}, \quad \Psi_{ki} \to \infty \quad (S_{ki} = 0); \end{aligned} \tag{21}$$

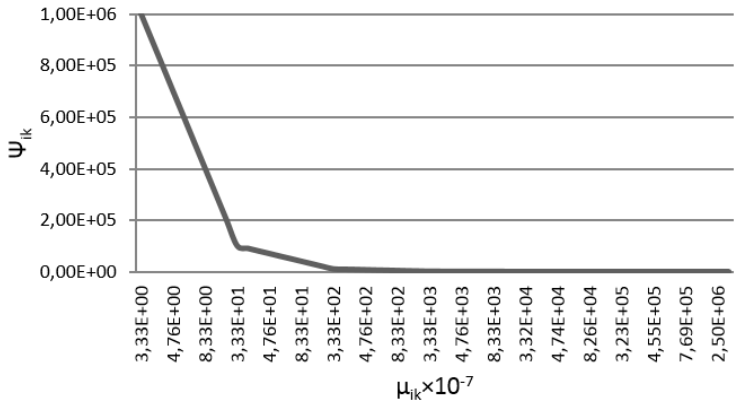

Fig. 6 Functional dependence between μ_{ik} and ψ_{ik} for the case shown in figure 5

4.2. The case when the member is semi-rigidly connected at one node, and ideally rigidly connected at the other node, $\mu_{ik} \neq 0$ and $\mu_{ki} = 1$, i.e. $\Psi_{ik} \neq 0$ and $\Psi_{ki} = 0$

Fig. 7 Semi rigid connection at left node and ideally rigid connection at right node

The system of equations (19) represents a system of three independent equations where only one unknown parameter $\mu_{ik}$is present. By solving this system of equations according to the unknown parameter μ_{ik}, the following is obtained:

$$\begin{aligned} \mu_{ik} &= \frac{1}{1+4\Psi_{ik}}, \qquad \mu_{ki} = 0; \\ \Psi_{ik} &= \frac{1-\mu_{ik}}{4\mu_{ik}}, \quad \Psi_{ki} \to \infty \quad (S_{ki} = 0); \end{aligned} \tag{22}$$

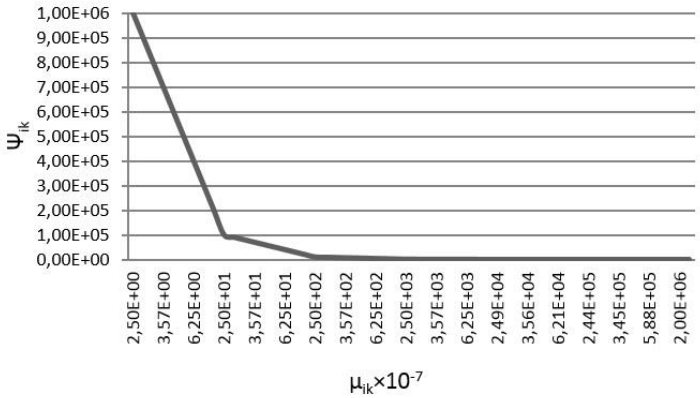

Fig. 8 Functional dependence between μ_{ik} and ψ_{ik} for the case shown in figure 7

It should be emphasized that these dependencies could also be obtained through the geometrical-static interpretation.

For these two special cases of member connections, there is a direct functional dependence between the rotational stiffness and the degree of rigidity of connection, meaning that one can easily calculate their rotational stiffness, if the degree of rigidity of connection of such members is known, or vice versa.

In the case of member with elastic connections at its both ends, it is possible to find only approximate solution that gives dependence between the degree of rigidity and rotational stiffness as a real parameter of connection. One of such solutions, giving the approximate value in a particular domain of the accuracy (1), can be determined by solving the system of

equations (19) using the method of elimination. The solutions of the system of equations are given in the following form:

$$\mu_{ik} \approx \frac{1+4\Psi_{ki}}{1+4(\Psi_{ik}+\Psi_{ki})+12\Psi_{ik}\Psi_{ki}}$$
$$\mu_{ki} \approx \frac{1+4\Psi_{ik}}{1+4(\Psi_{ik}+\Psi_{ki})+12\Psi_{ik}\Psi_{ki}} \tag{23}$$

These solutions meet the first and third equation in the system, while the second equation is just approximately satisfied.

It is obvious that prior obtained exact solutions for two special cases, are derived from this approximate solution .

5. CONCLUSION

In the papers [1] [2] [3], using the classical formulation of deformation method, the influence of semi-rigid connections of members is introduced through the degree of rigidity of connections μ_{ik} and μ_{ki}. In this paper is also applied the classic formulation of the deformation method for the analysis of stress and strain fields of structures with semi-rigid connections of members, but the influence of semi-rigid connections of members is included by the rotation stiffness of connections S_{ik} and S_{ki}.

Based on the comparative analysis of these two approaches, which in different ways introduce into the calculus the influence of connection deformation (μ that is S) on the variation of the stress and strain field of the structure, the following conclusions can be drawn:

- For determination of the degree of rigidity of the semi-rigidly connected member, using its definition (13), (14) or (15), it is necessary to know two parameters, those being:
  - Node „*i*“, that is „*k*“, rotation angles φ_i and φ_k, and rotation angles of end cross sections of the member „*ik*“ - φ_{ik} and φ_{ki}, or
  - rotation angles of end cross sections of the member „*ik*“ φ_{ik} and φ_{ki}, and relative nodal rotation angles of the member „*ik*“ due to connection deformation Φ_{ik} and Φ_{ki}, or
  - rotation angles of node „*i*“, that is „*k*“, - φ_i and φ_k, and relative nodal rotation angles of the member „*ik*“ due to the connection deformation Φ_{ik} and Φ_{ki}.

The degree of rigidity of connection depends not only on deformation of semi-rigid connections at the nodes of the member, but also on deformation parameters which relate to the deformation of nodal cross-sections of the member or deformation of nodes where the member is connected to the other structural members by semi-rigid connections. *For one and the same designed connection, the degree rigidity of connection will not have the same numerical value, so it cannot be adopted as a parameter characterizing the behavior of the very connection, as opposed to the rotational stiffness of the connection characterizing the connection itself.*

- The value of the degree of rigidity of connection depends on type of stress and strain analysis of the structure. Namely, the value of the degree of rigidity of connection for structural analysis, *according to the First order theory, does not have the same numerical value as when such structure with the same, designed connections, would be calculated according to the Second order theory*, which

additionally complicates and limits its application. As opposed to the degree of rigidity, the rotational stiffness of the connection, for the stress and strain field in the elastic domain, has the constant value, irrespective of whether the calculation is done according to First or Second order theory.

- Rotational stiffness of the connection changes depending on the intensity of the connection bending moment, and once calculated for one and same connection, it can be applied for the analysis of the stress and strain field in the elastic, elasto-plastic or plastic domain.

REFERENCES

1. M. Milićević, S. Zdravković, D. Zlatkov, B. Kostadinov: "Matrix Formulation of Design and Testing of Structures with Semi-Rigid Connections", SEWC-Structural Engineers World Congress, July 19-23, 1998., San Francisko, California, 1998., str. 266.
2. D. Zlatkov, S. Zdravković, T. Igić, B. Mladenović: Design of systems with semi-rigid connections by deformation method according to the second-order theory, The 3rd international congress of Serbian Society of Mechanics, Vlasina, 2011, ISBN 978-86-909973-2-9, str. C-60-170.
3. D. Zlatkov, S. Zdravković, B. Mladenović, R. Stojić: Matrix formulation of dynamic design of structures with semi-rigid connections, FACTA UNIVERSITATIS, series: architecture and civil engineering, Vol.9, No 1, 2011, ISSN 0354-4605, UDC 004+624.042.8:624.071.3=111, DOI: 10.2298/fuace1101089z, 2011, pp. 89 – 104.
4. Živković S.: Prilog proračunu čeličnih okvirnih konstrukcija sa deformabilnim vezama štapova, Magistarski rad, Građevinsko-arhitektonski fakultet, Univerzitet u Nišu, 2008.
5. Bašić D., Mešić E., Stojić D.: Damping distribution over the flexible connections in the frame structures, Facta Universitatis, Vol 1, N0 2, Niš, 1995., str. 145-151.
6. Bašić D., Mešić E., Stojić D.: Flexible connections as the discrete dampers, ABSE Colloquium, Istanbul, 1996., str. 153-159.
7. Bašić D., Mešić E., Stojić D.: Flexible joint Connection in Structures: Methods of Computations and Effects, Facta Universitatis, Vol 1, N0 1, Niš, 1994., str. 35-46.

KOMPARATIVNA ANALIZA KORIŠĆENJA STEPENA UKLJEŠTENJA I ROTACIONE KRUTOSTI VEZA U PRORAČUNU KONSTRUKCIJA

Primenom klasične formulacije metode deformacija, uticaj polukrutih veza štapova na polje napona i deformacija može se analizirati korišćenjem stepena uklještenja ili rotacione krutosti veza. U ovom radu formulisana je funkcionalna zavisnost između stepena uklještenja i rotacione krutosti veza i izvršena komparativna analiza ova dva pristupa pri analizi ponašanja polukrutih veza štapova u realnim konstrukcijama.

Ključne reči: *polukrute veze, rotaciona krutost veze, stepen uklještenja*

FACTA UNIVERSITATIS
Series: **Architecture and Civil Engineering** Vol. 16, No 1, 2018, pp. 29-43
https://doi.org/10.2298/FUACE160923003I

RAINFALL–RUNOFF SIMULATION FOR DESIGN FLOOD ESTIMATION IN SMALL RIVER CATCHMENTS

UDC 556.166

Aleksandra Ilić[1], Jasna Plavšić[2], Dragan Radivojević[1]

[1]University of Niš, Faculty of Civil Engineering and Architecture, Niš, Serbia
[2]University of Belgrade, Faculty of Civil Engineering, Belgrade, Serbia

Abstract. *This paper presents development and application of the model aimed at simulating peak flood runoff from the small river basin Obnica in Serbia (having an area of 185 km^2) with an aim to estimate design floods using different approaches. The model is developed using the HEC-HMS software (The United States Army Corps of Engineers (USACE) Hydrologic Centre's Hydrologic Modelling System). The model is calibrated against eight events with observed hydrographs and corresponding rainfall, and verified with a separate set of events. Flood hydrographs are simulated with the constant intensity design storms of various durations and with the 24-hour design storm with design hyetograph determined using the alternating block method. All design floods obtained from the simulated hydrograph peaks are compared with the design floods estimated by statistical analysis of annual maximum flows. The results have shown that the temporally distributed 24-hour storms yield the design floods that are the closest to the statistically derived design flows, while the constant intensity storms cannot reproduce the statistically derived design flows.*

Key words: *design floods, design storms, rainfall-runoff, simulation, HEC-HMS, flood hydrograph*

1. INTRODUCTION

Flood runoff assessment procedure depends on whether hydrological measurements are available on a given watercourse and if they have required scope and quality. Availability of hydrological data of satisfactory quality usually leads to the flood assessment procedure based on the statistical analysis that includes choice of the probability distribution for the observed floods, estimation of the distribution parameters and calculation of the design flood hydrograph characteristics (usually the peak flow) of a certain return period. If the flood

Received September 23, 2016 / Accepted April 11, 2017
Corresponding author: Aleksandra Ilić
Faculty of Civil Engineering and Architecture, University of Niš, 18000 Niš, Aleksandra Medvedeva 14, Serbia
E-mail: aleksandra.ilic@gaf.ni.ac.rs

measurements are not available, the flood assessment relies on the methods which are based on the rainfall-runoff transformation for the ungauged catchments.

For the catchments where rainfall and runoff data are available, a rainfall-runoff model may be developed. Once calibrated, such a model can be used to estimate design floods from either design or observed rainfall storms. There are several software packages that allow modelling of the rainfall–runoff process, and one of them is the HEC-HMS (Hydrologic Centre's Hydrologic Modelling System) by US Army Corps of Engineers [14]. The HEC-HMS model can be used for either event based or continuous modelling of the rainfall-runoff process and consists of a variety of methods for assessing various processes in a catchment (interception, surface depression storage, infiltration losses, runoff transformation, baseflow and hydrograph propagation). The flood hydrograph assessment is usually based on the event modelling, when the processes such as interception and evapotranspiration can be neglected in comparison to flood runoff during a relatively short simulation period covering rainfall and runoff duration. Moreover, the baseflow characterization is usually not important for the purpose of defining the design flood flows and therefore there is no need to employ the model in a continuous mode in order to compute baseflow.

Developing a rainfall-runoff model for the ungauged catchments is impossible and the usual procedure for determining the design relies on the regional relationships between the flood flows and physiographic catchment characteristics (e.g. catchment size, stream length slope, etc). Typically, synthetic unit hydrographs are developed for the ungauged catchments based on their physiographic characteristics, which are used in conjunction with the synthetic design storms to obtain the design flood hydrographs. Since the ungauged catchments are usually small, a question of the most critical design storm duration is usually resolved by trial and the storm duration producing the greatest peak flood flow is then adopted for further analysis. However, such a customary engineering practice sometimes overlooks some basic assumptions underlying the engineering methods applied in this procedure.

In this paper, the goal is to evaluate the typical procedures for design flood assessment at ungauged catchments in Serbia by comparing the traditional design flood estimates with alternative ones. To this end, in this paper a gauged small catchment (the Obnica River basin) in Serbia is selected, which is treated as an ungauged catchment and for which the design floods are estimated based on the design storms and synthetic unit hydrographs. Instead of developing a synthetic unit hydrograph based on the catchment's physiographic characteristics, a rainfall-runoff model is developed for the selected catchment in HEC-HMS based on the available observed events that served for model calibration and verification. This model was applied with the same design storms to obtain the design floods under different assumptions about the most critical design storms. Also, the design flood flows at the catchment outlet that are estimated using statistical analysis of the observed annual maximum flows provide a ground for verification of the other methods of flood flow estimation.

2. MODELLING FLOOD HYDROGRAPHS IN HEC-HMS

2.1. Model description

The way of simulating the runoff process with a mathematical model depends on the problem we need to solve. HEC-HMS schematizes the hydrological cycle as shown in Fig. 1 in a way that is suitable for most problems [8]. Three main components of the model should

be defined first: basin model, meteorological model and control specifications. The basin model represents the catchment and the methods of computing different catchment processes, meteorological model describes the precipitation input and the methods for calculating snow melt and evapotranspiration, and the control specifications define the modelling time frame and time step.

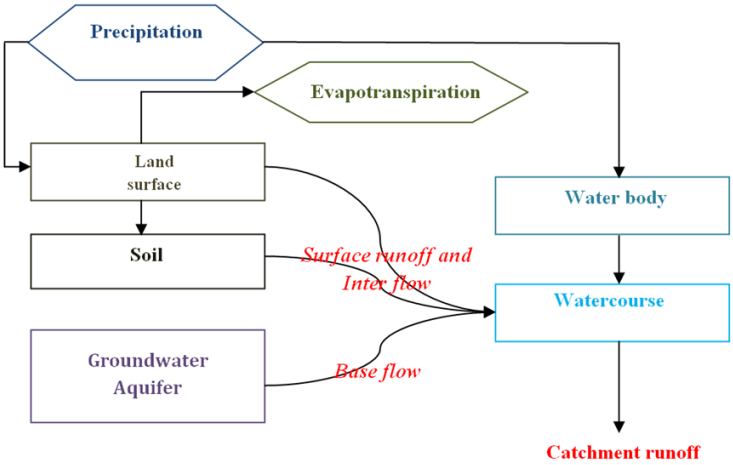

Fig. 1 The hydrologic cycle in HEC-HMS software

In HEC-HMS, a basin model is comprised of a number of elements such as sub-basins, river reaches, junctions, retention, springs, estuaries, reservoirs and diversions (relief) [13] [14] [17]. A sub-basin is the element where the methods for the runoff modelling are defined. For the event modelling, the following methods are important: the loss method, the runoff transform method and the baseflow method. Other methods are related to interception and surface depression storage. River reaches are the elements in which hydrograph routing is performed, and is necessary when a basin needs to be decomposed into sub-basins to route hydrographs from the sub-basins to the basin outlet.

There are seven methods for modelling losses in HEC-HMS: deficit and constant, initial and constant, Green-Ampt, SCS-CN, soil moisture accounting (SMA) method, exponential losses, Smith-Parlange method.

The transformation of excess rainfall into runoff can be obtained by using one of the seven methods: Clark's unit hydrograph, kinematic wave, modified Clark's method, SCS unit hydrograph, Snyder's unit hydrograph, user specified S-graph and a user specified unit hydrograph.

The base flow can be modelled by the following methods: bounded recession, constant monthly, linear reservoir, the Boussinesq equation (non-linear) and the recession method.

Several methods are available for the hydrograph routing, including the simple lag method, the modified pulse method, the Muskingum method, but also the kinematic wave and the Muskingum-Cunge methods for detailed hydraulic computations.

The meteorological model defines type of the rainfall input, for which a range of options are available. The simplest method is the user specified hyetograph. The SCS daily storm distribution is also available for a specified total rainfall depth. Other two

methods (frequency storm and the standard design storm) are also available as the design storm methods. There are three methods for calculating rainfall over the catchment from multiple gauges: gage weights, inverse distance, and gridded rainfall.

2.2. Direct runoff modelling: Snyder's synthetic unit hydrograph

In order to estimate direct runoff from small ungauged catchments or urban areas, the synthetic unit hydrograph (SUH) concept is commonly used. In this study, direct runoff simulation in HEC-HMS is performed with Snyder's SUH.

In 1938 Snyder, according to [1], was the first who developed method for SUH determination. Construction of such a UH involves estimating a number of parameters including basin lag time, hydrograph time base, storm duration, peak flow, hydrograph widths at discharges equal to 50% and 75% of the peak discharge.

The basin lag time t_p is defined as time from the centroid of excess rainfall hyetograph to the maximum ordinate of direct runoff hydrograph [10]. Snyder introduced the standard unit hydrograph on the basis of data from catchments in the north-eastern USA with areas ranging from 30 to 30000 km^2. The standard synthetic unit hydrograph has a ratio 5.5 between the basin lag time and "standard" excess rainfall duration t_k [7]:

$$t_p = 5.5 \cdot t_k \tag{1}$$

Based on the basin geomorphologic characteristics, Snyder came to the following expression for the basin lag in hours:

$$t_p = 0.75 \cdot C_t \cdot (L \cdot L_c)^{0.3} \tag{2}$$

where C_t is the coefficient obtained from regional analysis of the selected unit hydrographs and usually ranges from 1.8 to 2.2, L is the main stream length from the catchment divide to the outlet (in km), and L_c is the distance from the outlet to the point on the main stream which is closest to the catchment centroid (in km). The "standard" excess rainfall duration t_k is therefore a duration that satisfies equation (1).

The peak flow of the standard unit hydrograph is computed using the following relation:

$$Q_p = \frac{2.75 C_p A}{t_p} \tag{3}$$

where C_p is the peak flow coefficient (higher C_p values are associated with lower values of C_t), and A is the catchment area in km^2.

Once the elements of the standard unit hydrograph are computed, the unit hydrograph for another required rainfall duration t_k' can be derived from it. The basin lag time t_p' for the required duration t_k' is modified according to:

$$t_p' = t_p + 0.25(t_k' - t_k) \tag{4}$$

where all lags and durations are in hours. The peak flow of the required unit hydrograph is then computed from the relationship:

$$Q'_p = \frac{Q_p t_p}{t'_p} \tag{5}$$

Since the area under the unit hydrograph is equal to the runoff volume from the unit excess rainfall, the hydrograph time base T_b is obtained by assuming the triangular shape of the unit hydrograph.

In HEC-HMS, application of the Snyder's SUH method requires specifying two parameters: the basin lag t_p for the standard unit hydrograph and the coefficient C_p in equation (3). HEC-HMS then estimates the required unit hydrograph by setting rainfall duration equal to the computational time step, and computing the basin lag and peak unit flow from equations (4) and (5). However, HEC-HMS then estimates the hydrograph time base and the ordinates by finding a Clark's SUH with the equivalent peak flow and time to peak [14].

2.3. Base flow modelling

In this study, the recession method in HEC-HMS is used to model base flow. The recession method assumes the exponential decay of base flow Q_b from an initial value InQ_b [14]:

$$Q_b = InQ_b \cdot k^t \tag{6}$$

where t is time elapsed from occurrence of InQ_b, and k is the recession constant. The initial condition can be specified as initial flow value or as initial flow value per unit catchment area.

The recession model (6) is applied at the start of runoff simulation to simulate recession limb of previous flood event, and after the direct runoff peak time when the direct runoff decreases to the threshold value specified by the user. At the time of occurrence of the threshold value, total flow is defined by (6). The threshold value can be specified as the flow rate or the ratio of the flow to the computed peak flow (R).

2.4. Excess rainfall

The SCS method for modelling excess rainfall is widespread, simple and often used for assessment of direct runoff at ungauged catchments. The Curve Number (CN) parameter of this method varies in a wide range for different soil types and land use and can be found in comprehensive tables developed by former Soil Conservation Service (SCS), now National Resources Conservation Service of the US Department of Agriculture [16].

The excess rainfall is obtained from the following relationship:

$$\begin{aligned} Q &= \frac{(P - I_a)^2}{P - I_a + S} \quad \text{for} \quad P > I_a \\ Q &= 0 \quad \text{for} \quad P \le I_a \end{aligned} \tag{7}$$

where P is cumulative rainfall depth (mm) at given time step, I_a is initial abstraction (mm), Q is cumulative excess rainfall at given time step (mm), and S is potential maximum soil retention (mm). Based on the assumption that the initial abstraction is a fraction of the potential maximum retention:

$$I_a = \lambda S \tag{8}$$

equation (7) becomes:

$$Q = \frac{(P - \lambda S)^2}{P + (1 - \lambda)S} \tag{9}$$

The potential retention S in mm is expressed in terms of the curve number CN:

$$S = \left(\frac{1000}{CN} - 10 \right) \cdot 25.4 \tag{10}$$

The curve number CN ranges from 0 when $S \to \infty$, to 100 when $S = 0$.

When rainfall-runoff data are available, they can be directly used to estimate the potential retention S [16]:

$$S = \frac{P}{\lambda} + \frac{(1-\lambda)Q - \sqrt{(1-\lambda)^2 Q^2 + 4\lambda PQ}}{2\lambda^2} \tag{11}$$

According to equations (10) and (11), the event value of CN can be obtained from:

$$CN = \frac{25400}{\frac{P}{\lambda} + \frac{(1-\lambda)Q - \sqrt{(1-\lambda)^2 Q^2 + 4\lambda PQ}}{2\lambda^2} + 254} \tag{12}$$

2.5. Model calibration and verification

Adjusting model parameters so that the simulated hydrograph matches the observed hydrograph as closely as possible is called model calibration. This process is an optimization process with an objective function that measures the degree of agreement between the computed and the observed hydrograph. The process effectively searches for the minimum value of the objective function. Usually, model parameters are estimated through calibration if they cannot be obtained by observation and measurement, or they do not have physical meaning.

Calibration can be performed manually or automatically. Manual calibration employs the knowledge on the physical characteristics of the catchment and modeller's experience, while in the automatic iterative estimation procedure the parameters are adjusted until the minimum of the selected objective function is reached. HEC-HMS version 4.0 features an optimization manager that enables automatic calibration. There are five possible objective functions [4]: peak-weighted root mean square error (PWRMSE), sum of squared residuals (SSR), sum of absolute residuals (SAR), percent error in peak flow (PEPF) and percent error in volume (PEV).

In the flood runoff hydrograph modelling, PWRMSE is an appropriate objective function, with a weighting factor that gives greater weight to the errors around the value of the hydrograph peak:

$$PWRMSE = \sqrt{\frac{\sum_{t=1}^{N}(O(t)-M(t))^2 \frac{O(t)-\overline{O}}{2\overline{O}}}{N}}; \qquad \overline{O} = \frac{1}{N}\sum_{t=1}^{N} O(t) \tag{13}$$

where $O(t)$ and $M(t)$ are the observed and the modelled flow at time t, and $\overline{O}$ is the average observed flow.

To minimize the objective function, HEC-HMS uses two search methods [4]:

- the univariate gradient (UG) method, which optimizes only one parameter while the others remain constant;
- the Nelder and Mead (NM) method, which is based on the simultaneous optimization of all parameters (SIMPLEX method).

The initial parameter values are set at the beginning of the optimization procedure. HEC-HMS has built-in parameter constraints that have physical meaning. Fine bounds can be defined by user in order to achieve greater efficiency.

Model performance can be evaluated by different model efficiency measures. In addition to PWRMSE as an objective function given by equation (13), some of these measures are described below.

The percent error in peak flow (PEPF) considers only the peak value and disregards the hydrograph volume and time to peak:

$$PEPF = 100\left|\frac{O(peak)-M(peak)}{O(peak)}\right| \tag{14}$$

where $O(peak)$ and $M(peak)$ are the observed and the modelled peak values, respectively.

The correlation coefficient between modelled and measured flows (CORR) is obtained using the expression:

$$CORR = \frac{\sum_{t=1}^{N}(O_t-\overline{O})\times(M_t-M)}{\sqrt{\left[\sum_{t=1}^{N}(O_t-\overline{O})^2 \times \sum_{t=1}^{N}(M_t-\overline{M})^2\right]}} \tag{15}$$

where O_t and M_t are the observed and the modelled flow at time t, $\overline{O}$ and $\overline{M}$ are corresponding means over the calibration period, and N is the number of data.

The root mean standard error is obtained as:

$$RRMSE = 100 \times \sqrt{\frac{1}{N}\sum_{t=1}^{N}\left(\frac{M_t-O_t}{O_t}\right)^2} \tag{16}$$

The Nash-Sutcliff efficiency E is defined by [5]:

$$E = 1 - \frac{\sum_{t=1}^{N} (O_t - M_t)^2}{\sum_{t=1}^{N} (O_t - \overline{O})^2} \tag{17}$$

Model verification is the process of testing the model on the basis of data that were not used for calibration. During the verification process, the parameter values are not changed. Model performance is evaluated again in the verification process to check the adopted parameter values. If the model is well calibrated, its performance with the verification data should be similar to that with the calibration data.

3. DESIGN STORMS

Design storm that produces maximum runoff on a small ungauged rural or urban basin, where time of concentration ranges from several minutes to several hours, is usually selected from the depth-duration-frequency (DDF) relationships. The greatest problem in estimating rainfall of duration shorter than one day in Serbia is lack of representative DDF relationships for a given catchment due to sparse recording raingauge network. The hydrologists are therefore forced to transpose the design storms from the nearest recording raingauges to the location of the study by using data on daily rainfall from the non-recording gauges within the basin or close to it. The transposition is made by assuming that the ratio of the short duration rainfall to the daily rainfall at the gauge location is also valid for the studied basin. The short duration rainfall for the basin is therefore calculated as:

$$P_{BASIN}(t_k, T) = \frac{P_{GAUGE}(t_k, T)}{P_{GAUGE,daily}(T)} P_{BASIN,daily}(T) \tag{18}$$

where t_k denotes storm duration and T denotes return period.

Daily design rainfall for the basin is obtained by finding the areal average from the design daily rainfall at the non-recording gauges. In this study we applied the Thiessen polygon method as a frequently applied method for averaging rainfall. The maximum daily rainfall depth for the return period T is then [9]:

$$P_{BASIN,daily}(T) = \sum_{i=1}^{n} \frac{a_i \cdot P_i(T)}{A} \tag{19}$$

where a_i is the Thiessen polygon area for i^{th} gauge (km^2), $P_i(T)$ is the maximum daily rainfall for return period T at i^{th} gauge (mm), A is the catchment area (km^2), and n is the number of considered non-recording gauges.

The last step in defining design storms is to develop the design hyetograph. The short duration rainfall is generally not distributed uniformly in time and the shape of the runoff hydrograph is strongly affected by the hyetograph shape. In typical engineering applications in Serbia, temporal distribution of design storms is not considered and constant intensity hyetograph shape is usually adopted (so called block storm method). Temporal distribution

of design storms can be developed either statistically or synthetically. In this study, two types of design storms are used as the input to the rainfall-runoff model:

- design storms of constant intensity with different durations (block storms), and
- 24-hour design storms with temporally varying intensity.

The synthetic design rainfall hyetographs for the 24-hour storms are obtained by the alternating block method [3], following the steps below:

a. For the design storm of return period T and duration t_k, design rainfall depths for all durations in Δt increments are taken from the DDF curve for the same return period;
b. Incremental rainfall depths are calculated from the design rainfall depths for all durations in Δt increments;
c. The highest incremental value is placed in the middle of hyetograph. The second highest block is placed to the right of the maximum block and the third highest to the left. The fourth highest rainfall increment is placed to the right of the maximum block after second block and so on until the last one.

4. Data and Results

4.1. Basin model

The rainfall-runoff model for the Obnica River basin, shown in Fig. 2, is developed in HEC-HMS software as the lumped model. The basin is a typical mountainous basin with an area of 185 km^2. The flow is measured at hydrological station Belo Polje at the catchment outlet. As described in section 2, Snyder's SUH is selected for direct runoff computation and rainfall excess is assessed applying the SCS-CN method. Base flow is modelled by the recession method.

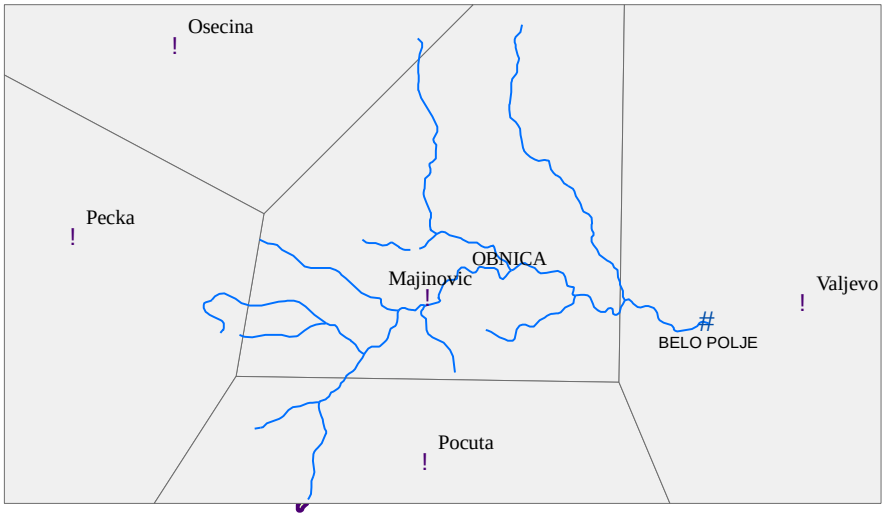

Fig. 2 The Obnica River basin with hydrological station (blue triangle), rain gauges (violet dots) and Thiessen polygons for the rain gauges

Geomorphologic characteristics of the catchment needed for the basin lag time estimation are shown in Table 1, and were determined using GIS software on the basis of digitized 1: 25,000 topographic maps.

For the rainfall excess assessment, initial value of *CN* is estimated using Corine Land Cover database [2], taking into account runoff conditions (land use and soil hydrogeological characteristics) and literature [9].

Table 1 Geomorphologic characteristics of Obnica River Basin

River	Obnica
Station	Belo Polje
Catchment area (km^2)	185
Catchment length (km)	28.1
Weighted channel slope (%)	1.11
Absolute channel slope (%)	2.61
Average catchment slope (%)	18.26
Distance to centre of gravity (km)	14.5
Average catchment elevation (m.a.s.l.)	401

4.2. Model calibration and verification

The model calibration was performed using eight recorded hydrographs and the corresponding rainfall events in the Obnica River basin [9] using the PWRMSE objective function as the criterion. Computational time step was 30 minutes in accordance with the available rainfall and flow data. Table 2 provides an overview of the parameters of the selected modelling methods and explains how they are calibrated. Calibration was performed with both search methods described in section 2.5, namely one parameter optimization (UG) and the simultaneous optimization of all parameters (NM).

Table 2 Parameters subject to calibration

Modelling method	Parameter	Comment
Loss method: SCS-CN	Curve number CN	Initial value based on Corine Land Cover [2]
	Initial abstraction I_a	
Transform method: Snyder's UH	Standard basin lag t_p	Calibration of parameter C_t in Eq. (2)
	Peaking coefficient C_p	Calibration of parameter C_p in Eq. (3)
Baseflow method: Recession	Initial baseflow InQ_b	Manually calibrated, initial values are adopted as described in section 2.3
	Inflection point to peak ratio R	
	Recession constant k	

The calibration results with two optimization methods showed similar correlation coefficients between the observed and simulated hydrograph characteristics. The parameter values obtained by the UG optimization method were adopted because the values of *CN* and initial abstraction vary in a narrow range across the calibration events (Table 3). The correlation coefficient between the observed and modelled hydrograph volumes is *CORR* = 0.987, while the correlation coefficient between the observed and modelled flow peaks is *CORR* = 0.947. Base flow parameters were calibrated manually according to minimum difference between runoff volumes of the measured and modelled

hydrograph. Calibration results are given in Table 3. Adopted values of the parameters are shown in the last row of Table 3.

Table 3 Values of calibrated model parameters and calibration efficiencies

Event No.	Parameter							Efficiency		
	SCS CN		Snyder's UH		Recession					
	I_a mm	CN	t_p h	C_p	InQ_b m^3/s	R	k	E	RRMSE %	PEPF %
103	7.16	89.3	9.22	0.75	4.97	0.484	0.485	0.985	1.0	0.8
95	7.14	93.2	12.56	0.99	20.01	0.928	0.073	0.745	10.3	6.6
79	7.69	77.9	4.78	0.48	0.23	0.025	1.000	0.845	1.3	0.7
71	7.63	87.0	10.40	0.73	1.50	0.161	0.791	0.927	2.0	1.2
67a	11.42	98.9	10.63	0.71	1.02	0.188	0.861	0.935	1.8	1.1
63	7.70	83.7	10.96	0.47	0.98	0.161	1.000	0.912	1.2	0.9
60	7.64	83.2	10.74	1.00	1.57	0.168	0.785	0.921	4.1	2.8
59	7.01	88.4	12.31	0.83	2.27	0.336	0.747	0.785	2.0	1.0
Adop.	7.9	87.7	10.2	0.70	1.88	0.246	0.770			

The model was verified with a separate set of events. The results of the verification are given in Table 4 by comparing the observed and simulated peak flows, times of peak and total runoff volumes. The model performance indicators shown in Table 4 justify the parameter values adopted in the calibration process.

Table 4 Model verification results (peak flow Q, time of peak t, runoff volume V; subscript "o" denotes observed values and "s" simulated values) and corresponding efficiencies

Event No.	Q_o m^3/s	Q_s m^3/s	t_o h	t_s h	V_o mm	V_s mm	E	$RRMSE$ %	$PEPF$ %
70	29.10	15.00	06/06/1980 00:00	05/06/1980 23:30	9.64	6.31	0.447	-3.3	3.4
75	18.10	19.50	18/06/1981 05:30	18/06/1981 06:00	9.31	12.98	0.201	3.3	1.6
86	113.90	67.70	18/04/1985 02:00	18/04/1985 02:30	79.09	57.49	0.763	15.2	8.7
94a	61.10	41.10	21/05/1987 14:30	21/05/1987 14:30	44.88	35.32	0.791	5.7	3.0
100	34.70	38.80	17/06/1989 06:00	17/06/1989 23:30	30.35	35.53	0.758	4.4	3.0

4.3. Development of design storms

Maximum daily rainfall for the Obnica River basin was determined by the Thiessen polygons method based on the statistical analysis of maximum daily rainfall at five rain gages: Majinović, Poćuta, Pecka, Osečina and Valjevo. Processing period was 1946-2006 [5] [11].

Short duration rainfall depths and intensities (DDF and IDF curves) were available for the Valjevo rain gage station. The study included the annual maximum intensities for the following durations: 10, 20, 30, 60, 120, 180, 360, 720 and 1440 minutes. Design rainfall depths of different durations for the Obnica basin were calculated using the DDF curves for the Valjevo station multiplied by the ratio of maximum daily rainfall depths for the basin and at Valjevo [11]. The resulting DDF curves ordinates for exceedance probabilities 1%, 2% and 5% are shown in Table 5. Last two rows in Table 5 show maximum daily rainfall for the basin and at the Valjevo station that were used for calculations.

Five meteorological models were made in HEC-HMS depending on design rainfall duration. For the durations of 3, 6, 9 and 12 hours constant intensity rainfall was assumed (block storms), while a synthetic hyetograph was developed by the alternating blocks method for the 24-hour rainfall duration.

Table 5 Design rainfall *P* of different exceedance probabilities *p* for durations t_k for the Obnica River Basin at h.s. Belo Polje

t_k (min)	P (mm)		
	p=1%	p=2%	p=5%
10	23.11	21.68	19.49
20	31.57	29.57	26.53
30	39.07	36.57	32.72
60	55.00	51.38	45.75
120	72.67	67.82	60.20
180	81.52	76.08	67.49
360	89.18	83.27	74.02
720	90.51	84.65	75.58
1440	90.69	84.99	76.38
max Pdaily Obnica	86.80	80.60	71.80
max Pdaily Valjevo	97.90	88.20	75.80

4.4. Results of model simulations with design storms

The comparative results of the runoff hydrograph peak flows simulated by the rainfall-runoff model using HEC-HMS and the design flows obtained by statistical analysis of annual maximum flows of the Obnica River at Belo Polje hydrologic station for 1954-2006 [5] are shown in Fig. 3. Table 7 also shows the values of simulated peak flows with exceedance probability of 1%, 2% and 5%, and the corresponding characteristic times of the synthetic unit hydrographs.

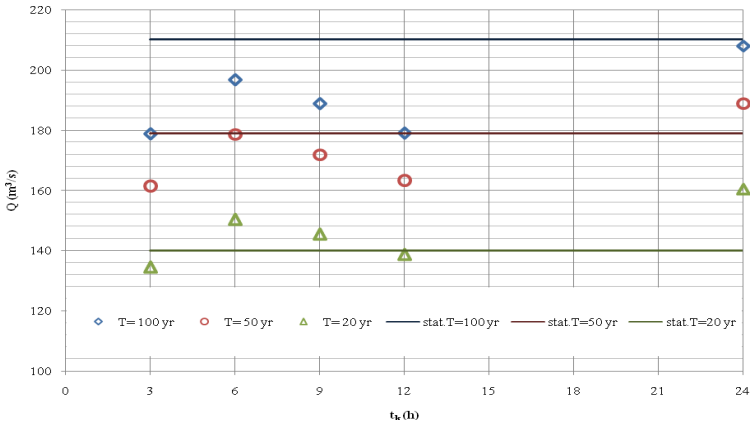

Fig. 3 Design floods of the Obnica River at Belo Polje based on design storms (markers) and obtained by statistical analysis (lines). The x-axis denotes design storm duration t_k.

Table 7 Design floods for different design storms and flood hydrograph parameters (basin lag t_p, time to peak T_p, recession time T_r, hydrograph base T_b)

Design storm type	Design floods			Synthetic unit hydrograph elements			
	$Q_{1\%}$ m^3/s	$Q_{2\%}$ m^3/s	$Q_{5\%}$ m^3/s	t_p h	T_p h	T_r h	T_b h
tk=3h, i=const.	178.7	161.5	134.5	10.2	11	38.5	49.5
tk=6h, i=const.	196.6	178.6	150.3	10.2	12.5	39.5	52
tk=9h, i=const.	188.8	171.9	145.4	10.2	14.5	40.5	55
tk=12h, i=const.	179	163.3	138.7	10.2	16	41.5	57.5
tk=24h, AB	208	188.9	160.4	10.2	11	40	51
Stat. analysis [3]	210	179	140				

Compared to the flood peaks estimated by statistical methods (Log-Pearson type 3 probability distribution [5]), it can be seen that the best agreement in the 1% design floods is obtained with synthetic design storm of 24 hours duration. Among the block storms of various durations, the 2% design flood closest to the statistical ones was obtained with the 6 hours block storm, while the 12 hour block storm is the closest to the 5% flood. In general, block storms of all durations performed well for higher (5%) probability of exceedance, while the 24-hour alternating block storm outperforms block storms for lower probabilities of exceedance (2% and 1%).

5. Concluding Remarks

By calibrating a flood hydrograph model based on synthetic unit hydrographs for a gauged basin (the Obnica River) using the HEC-HMS software and then applying the calibrated model to the design storms – a procedure typical for ungauged basins, it was possible to analyse the uncertainties in estimating design floods at the ungauged basins. The results have shown that the following conclusions can be made.

The highest values of design floods with return periods of 20, 50 and 100 years were obtained with the 24 hour temporally distributed synthetic design storm. Constant intensity storms of shorter durations fail to reproduce design floods of low frequency such as the 100-year flood. Among the block storms, the 6-hour design storm provides the highest design floods; this indicates that 6 hours is the critical storm duration for the Obnica River basin, what is in accordance with other studies [9] [18]. At the same time, it is obvious that the assumption on the constant rainfall intensity is not justified for the given catchment size and critical storm duration.

For application of the commonly used SCS curve number (CN) procedure the model calibration has shown that it would be of great importance to develop a unique method of estimating *CN* in Serbia based on the observed rainfall and flows. Curve number *CN* is usually estimated from the tables provided by SCS (NRCS) [16] based on different types of land cover and use. Such estimation needs to be compared to the neighbouring catchments (similar) where there are data on observed flows and rainfall.

Design flood hydrograph estimation using the design rainfall concept is affected by the selected hyetograph form, especially in terms of peak flow and time to peak. Also, realistic flood hydrographs specific for considered area can be determined only through

calibrating a rainfall-runoff model considering soil structure, moisture conditions and processes in the catchments. However, since this procedure is impossible at ungauged catchments, it is necessary to carefully select not only the elements of the synthetic unit hydrographs, but also to provide a set of design storms that can produce realistic design floods.

Acknowledgement. *The research presented in this paper is funded by Serbia's Ministry of Education, Science and Technological Development as a part of a scientific project titled "Assessment of Climate Change Impact on Water Resources in Serbia" (TR-37005).*

REFERENCES

1. Bhunya P. K, Panda S. N., and Goel M. K. (2011) "Synthetic Unit Hydrograph Methods: A Critical Review", The Open Hydrology Journal, 5, 1-8
2. Bossard M., Franec J., Otahel J. (2000) Corine Land Cover Techical Guide – Addendum 2000, Technical report No 40, Copenhagen (EEA)
3. Chow V., T., Maidment D., R., Mays L., W. (1988) Applied Hydrology, McGraw-Hill
4. Cunderlik J., Simonović S. (2004) Calibration, verification and sensitivity analysis of the HEC-HMS hydrologic model, CFCAS project: Assessment of Water Resources Risk and Vulnerability to Changing Climate conditions, Project report IV, University of Western Ontario, University of Waterloo, Upper Thames River Conservation Authority
5. Institit za vodoprivredu „Jaroslav Černi" (2009) Vodoprivredna Osnova Republike Srbije – Hdrometeorološke podloge
6. Kranse P., Boyle D. P., Base F. (2005) "Comparison of different efficiency criteria for hydrological model assessment, Advances in Geosciences", 5, pp 89-97
7. McCuen R. H. (2005) Hydrologic analysis and design, Pearson Education, Inc. Upper Saddle River, New Jersey
8. Mijalić M., Volf G., Ožanić N. (2009) "Određivanje Hidrograma otecanja korišćenjem HEC – HMS programa", Zbornik radova, Knjiga XII, Građevinski fakultet Sveučilišta u Rijeci, pp 55 - 86
9. Petrović J. (1996) Uporedna analiza maksimalnih proticaja na malim rekama metodama parametarske i statističke hidrologije, Magistarski rad, Građevinski fakultet, Beograd
10. Prohaska S. (2003) Hidrologija I deo, Rudarsko-geološki fakultet, Institut za vodoprivredu "Jaroslav Černi" i RHMZ Srbije, Beograd
11. Prohaska S., Bartoš Divac V. sa saradnicima (2014) Intenziteti jakih kiša u Srbiji, Monografija, Izdavač: Institut za vodoprivredu „Jaroslav Černi", Beograd, ISBN 978-86-82565-40-6, str. 1-481
12. Šraj M., Dirbek L., Brilly M. (2010) "The Influence of Effective Rainfall on Modelled Runoff Hydrograph", J. Hydrol. Hydromech, 58, 1, pp 3 – 14
13. US Army Corps of Engineers, Hydrologic Engineering Center (2008) HEC – HMS Applications Guide
14. US Army Corps of Engineers, Hydrologic Engineering Center (2000) HEC – HMS Technical Reference Manual
15. United States Department of Agriculture (1986). Urban hydrology for small watersheds, TR-55
16. Unated States Department of Agriculture, National resources conservation Service (2004) NEH 630 Chapter 9, Hydrologic Soil – Cover Complexes, 210 – VI – NEH
17. Yusop Z., Chan C. H., Katimon A. (2007) "Runoff Characteristics and Application of HEC – HMS for Modelling Stormflow Hydrograph in an Oil Palm Catchment", Water Science and Technology, Vol 56, No 8, pp 41 – 48
18. Zlatanović N. (2016) Metod distribuiranih brzina za određivanje vremena kašnjenja sintetičkog jediničnog hidrograma, Zbornik 17. savetovanja SDHI i SDH, pp. 458-469.

ODREĐIVANJE RAČUNSKIH PROTOKA MODELOM PADAVINE-OTICAJ NA MALIM SLIVOVIMA

U ovom radu je predstavljen model za simulaciju pika poplavnog talasa na malom slivu reke Obnice u Srbiji (površine 185 km^2) sa ciljem određivanja računskih velikih voda koristeći različite pristupe. Primenjen simulacioni model je napravljen u HEC-HMS programu (The Unated States Army Corps of Engineers (USACE) Hydrologic Center's Hydrologic Modeling System). Model je kalibrisan na osnovu osam snimljenih hidrograma i odgovarajućih kišnih epizoda i verifikovan za hidrograme i kišnie epizode koji nisu učestvovali u procesu kalibracije. Za simulaciju su korišćene računske kiše konstantnog inteziteta različitog trajanja kao i kiše trajanja 24 časa čiji je hijetogram formiran metodom alternativnih blokova. Svi simulirani protoci upoređeni su sa protocima dobijenim statističkom analizom maksimalnih godišnjih protoka. Rezultati pokazuju da se uključivanjem vremenske neravnomernosti u računske kiše trajanja 24 časa dobijaju vrednosti protoka koje su najbliže rezultatima statističke analize, dok to korišćenjem kiša konstantnog inteziteta nije bilo postignuto.

Ključne reči: *računske velike vode, računske kiše, padavine-oticaj, simulacija, HEC-HMS, hidrogram velikih voda*

FACTA UNIVERSITATIS
Series: **Architecture and Civil Engineering** Vol. 16, No 1, 2018, pp. 45-56
https://doi.org/10.2298/FUACE161226004J

PROPERTIES OF GEOPOLYMERS

UDC 691.1

Natalija Janošević, Snežana Đorić-Veljković, Gordana Topličić-Ćurčić, Jugoslav Karamarković

University of Niš, Faculty of Civil Engineering and Architecture, Niš, Serbia

Abstract. *Especially geopolymers are novel environmental friendly materials, with promises of considerable progress in the near future. These materials, with unique physical, chemical and mechanical properties can be used for many different applications. They are produced by using waste-products from the industry, and turning them into a high value construction material needed for infrastructure developments.*

Key words: *Geopolymers, novel materials, ceramics, concrete, fly ash, organic materials, ecological material*

1. INTRODUCTION

Geopolymers are materials based on exceptional physical, chemical and mechanical properties, new binder for fiber composites and new cement for concrete. With their exceptional physical characteristics, being fire, heat, acid and corrosion resistant, as well as having high compressive strength, geopolymers are used for many different applications. Some of them are fire resistant and thermal insulation materials, low tech and low energy material such as tiles, cements and concretes [1].

These novel materials are created in inorganic polymeric materials geopolymerisation process, in inorganic polymeric materials geopolymerisation process made from alumino-silicate materials with alkali metal silicates in highly alkaline conditions. The first geopolymer was made in 1978 by Joseph Davidovits, after catastrophic fires happened in France, in 1970s, and consecutive investigations for fire resistant and non-flammable material. Geopolymer as a term was created and applied in 1978 as French "géopolymères", mineral polymers resulting from geochemistry or geosynthesis.

Geopolymers are a class of inorganic polymeric, amorphous materials consisting of alumina, silica, and alkali metal oxides. They are typically synthesized by mixing an

Received December 26, 2016 / Accepted March 24, 2017
Corresponding author: Natalija Janošević
Faculty of Civil Engineering and Architecture, University of Niš, 18000 Niš, Aleksandra Medvedeva 14, Serbia
E-mail: janosevicnatalija@gmail.com

aluminosilicate source (metakaolin or fly-ash) with silica dissolved in highly caustic alkaline solutions. These materials are inorganic polymers made from dissolution of the aluminosilicate source, polycondensation and precipitation under ambient temperature. Advantages of geopolymers are the usage of cheap waste materials in their production (such as slag, fly ash, various clays and even agricultural wastes), lower CO_2 emission (the low carbon footprint) into the atmosphere during manufacture, ambient temperature production and high compressive and flexural strengths, in particular as compared to cements. All this characteristics are placing them in a category of new eco-friendly materials and also new elements of sustainable architecture [2, 3, 4, 5].

In Figure 1 four different species of concrete are presented: first - PFA Based geopolymer concrete made with pozzolan fly ash, second-Geopolymer concrete based on Kaolinit, third is Ground granulated blast furnace (GGBS) based geopolymer concrete, and fourth is traditional concrete.

Fig. 1 Range of geopolymer-concrete and ordinary-concrete [6].

2. GEOPOLYMERS DEVELOPMENTS

During 1930s and 1940s, sodium and potassium hydroxide were used to test ground slag with added Portland cement in iron blast furnace. This test was made to determine time needed for slag to set. In this kind of test for slag, Belgian scientist Purdon noticed that there was a rapid binder, with short time of hardening. Those types of reactions were used to make alkali-activated slag cements (Trief cements) for large scale construction in the 1950s [7].

During 1960s and 1970s, Victor Glukhovsky, a Ukrainian scientist at the KICE (Kiev Institute of Civil Engineering in the USSR), discovered that sodium alumino-silicate hydrates (zeolites) are created from rocks and clay mineral during alkali treatment. He called these materials soil silicate concretes and soil cements.

In 1972, at CORDI laboratory in Saint-Quentin a technology based on geosynthesis, natural kaolinite/quartz blended with mixed solid sodium hydroxide and water (Davidovits and Legrand, 1974) was developed. This kind of reaction was set relatively short, in hot pressed-thermosetting process for water evaporation at temperature 130-180°C with applied hydraulic pressure 10 - 30 bars [7]. A large contribution to the development and implementation of geopolymer composites was provided by the extensive research by Prof. Waltraud M. Kriven [8,9,10,11,12].

3. CHEMISTRY AND GEOPOLYMERIC SYSTEMS

The result of polycondensation of still hypothetical monomers (geopolymers precursors) - alumino-silicate oxides with alkali metal silicates under highly alkaline conditions can be considered a geopolymerisation. The Si and Al dissolution from the starting Si-Al materials in alkali silicate solution enhances the formation of geopolymers precursors. In the difference of the alkali silicate solution concentration and size-of the alkali silicate solution concentration and size of particle Si-Al, there are differences in extents of dissolution. Alkali hydroxide is essential for the catalysis of the polycondensation reaction, enabling dissolution to proceed with the reaction [1]. In Figure 2 the synthesis of the poly (sialatesiloxo) type geopolymers is schematically presented [1].

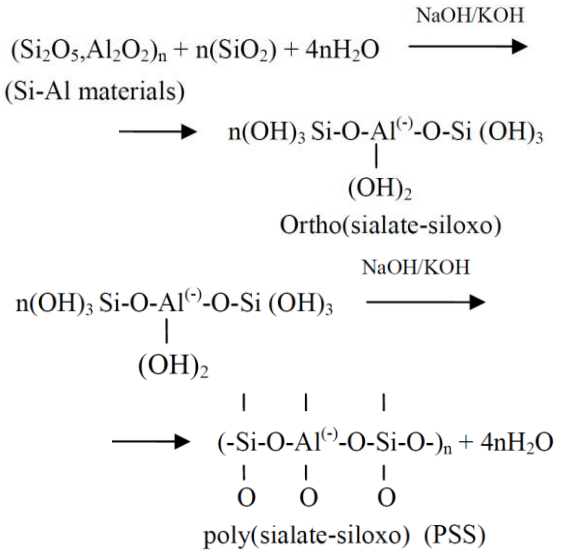

Fig. 2 The scheme of the synthesis of the poly (sialatesiloxo) type geopolymers [1].

Synthesis, curing and hardening occur for geopolymers at atmospheric pressure. Reaction time is substantially short resulting in amorphous to semi-crystalline three-dimensional matrices, depending on the temperature of curing, setting and hardening processes. Any Si-Al material can become the candidate source for geopolymerisation.

It is important to note that the SiO_2/Al_2O_3 ratio in the initial materials of geopolymerisation is critical for the obtained polymers, as it causes important structural differences that specify their physical and mechanical properties.

Furthermore, the M_2O/SiO_2 ratio in the alkali metal (M) silicate solution and the H_2O/M_2O ratio in the geopolymer composition are crucial for the geopolymers curing and formation. Alkali content has to sufficiently balance the charge requirements within the geopolymeric structure, without providing excess of charge that can form alkali carbonate by atmospheric carbonation and disrupt consequently the polymerisation process. Water content in geopolymeric synthesis is essential both in facilitating mixing procedure and in providing a mechanism for ion transportation. The excess of water affects negatively geopolymerisation causing the leaching of the more soluble compounds and their transportation away from the reaction occurring zone [1].

4. CREATION OF GEOPOLYMERS

The geopolymerization reaction occurs with highly strained AlO_5^{2-} coordination polyhedra in the amorphous metakaolin which contains a lone pair of electrons and is susceptible to dissolution by the highly caustic sodium metasilicate solution (water glass) of standard composition $Na_2Ox2SiO_2\,x11H_2O$ [5].

Tetrahedra AlO_4 which attract charge balancing Group I cations that are formed in the highly alkaline solution of the Al^{3+} and then react with SiO_2 to form an amorphous 3D network (Fig. 3).

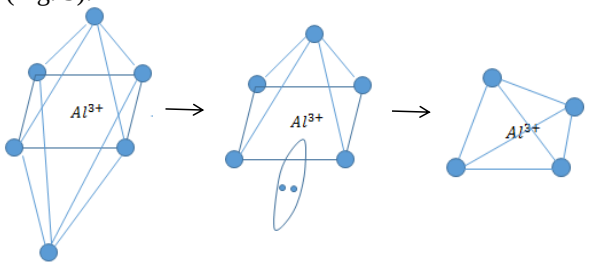

Fig. 3 a) Crystalline kaolin b) Amorphous metakaolin c) Aluminate tetrahedron [5].

Dehydration of crystalline kaolinite, where the Al^{3+} is in 6-fold coordination, comes to dissolution of the aluminosilicate source (e.g. metakaolin on Figure 3. b) and in amorphous metakaolin that make a highly strained 5-fold coordinated Al^{3+} [5].

5. ATOMIC STRUCTURE AND MICROSTRUCTURE OF GEOPOLYMERS

At room temperature corner-shared tetrahedral units which contain amorphous atomic structure of two compounds (Figure 4), SiO_2 and AlO_4 are formed.

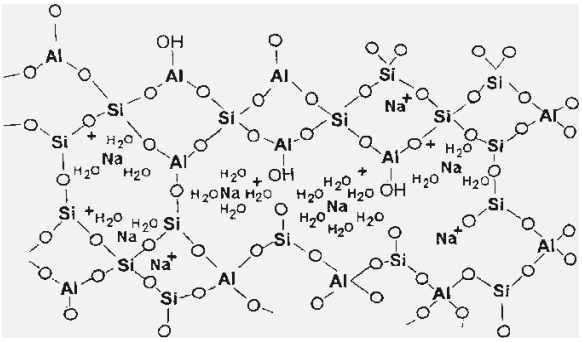

Fig. 4. Currently accepted atomic model of geopolymer structure [13].

The geopolymers microstructure can be nanoparticulate (approximately 20-40 nm in diameter) presented in Figure 5, and nanoporous (approximately 6.8 nm in diameter) presented in Figure 6.

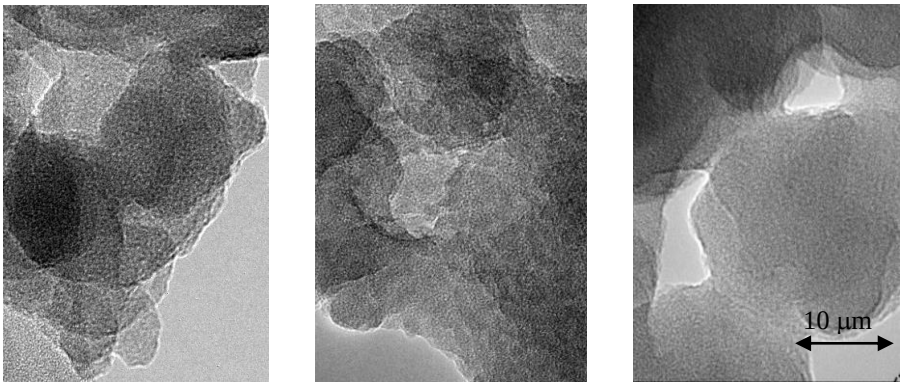

(a) Na GP (b) K GP (c) Cs GP

Fig. 5 High resolution transmission electron microscopy (HRTEM) of geopolymeric precipitates [5].

It should be noted that the pure geopolymer is impermeable, although it is nanoporous. In the Table 1 is presented Summary properties of Porosimetry of pure geopolymer.

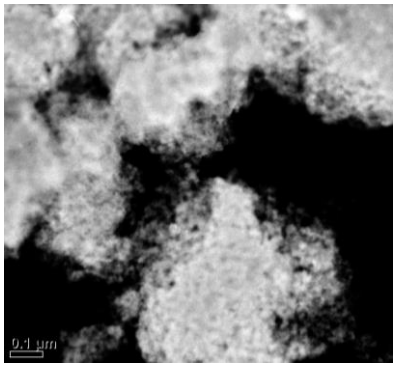

Fig. 6 High angle annular Dark Field TEM micrograph of KGP showing nanoporosity [5].

There are numerous variants of the geopolymers that refer to alkali-activated alumino-silicates, but which are made from impure forms of alumino-silicate sources in industrial waste products such as slag or fly ash. These compositions tend to lie off the stoichiometric 1:1:4:11 compositions measured by TEM/EDS of metakaolin-derived geopolymers that is presented in Figure 7. As occur in cements, these composites tend to have significantly lower mechanical properties due to the presence of calcium silicate hydrate (C-S-H or N-A-S-H) binder phases [5].

Table 1. Porosimetry of pure K-GP measured by Porotech, Inc. [5].

Average logarithmic pore radius	0.4362 nm
Average pore radius	3.3711 nm
Porosity over weight	0.3165 cm^3/g
Porosity over volume	0.4106 cm^3/cm^3
Meso- and macro-pore surface over weight	190.5778 m^2/g
Meso- and macro-pore surface over volume	247.2794 m^2/cm^3
Total pore surface over weight	274.6912 m^2/g
Total pore surface over volume	356.4186 m^2/cm^3
Density of solid phase	2.0481 g/cm^3

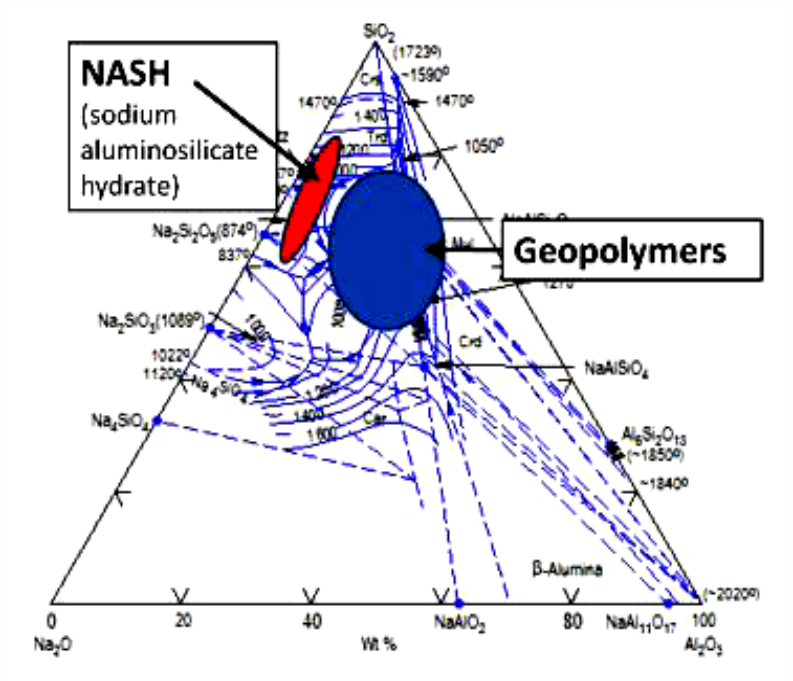

Fig. 7 Schematic comparison of alkali activated cements compounds such as sodium aluminosilicate hydrate (NASH) and stoichiometric geopolymers [5].

6. TYPES OF GEOPOLYMERS

6.1. Phosphate-based geopolymer

Phosphate-based geopolymers in short period of time became conventional polymers. They contain naturally occurring mineral phases, and they are synthesized at room temperature and set rapidly. They represent variety of mineral geopolymer, formed by an acid-base reaction between a metal oxide and an acid phosphate, where Si is totally or

partially replaced by phosphorus. Any divalent or trivalent oxide that is diffluent may be used to form phosphate geopolymers [7].

The main difference between phosphate geopolymers and polysilicate polymers is in their synthesis, because phosphate geopolymers are fabricated by acid-base reactions.

Applications of those polymers are in wide range of construction materials, oil and cements, dental cements, even radioactive waste stabilization.

6.1.1. Phosphate geopolymers

Phosphate geopolymers are synthesized in acid-base reaction between an acid phosphate and an inorganic oxide (divalent and trivalent metals). The reaction product is an anhydrous poly (phosphate) or a poly (hydrophosphate) that consolidates into a ceramic [7].

The following are the most common examples

$$2CaO + Ca(H_2PO_4)_2 + H_2O \rightarrow$$
$$CaO + 2CaHPO_4 \cdot H_2O \rightarrow Ca_3(PO_4)_2 + 2H_2O \quad (3)$$

$$MgO + KH_2PO_4 + 5\ H_2O \rightarrow MgKPO_4 \cdot 6H_2O \quad (4)$$

If the rate of this reaction is controlled, ceramics can be formed even at room temperature. Ceramics also can be formed in reaction with trivalent oxides, but only at higher temperature [14].

An example is berlinite ($AlPO_4$), formed by the reaction between alumina and phosphoric acid:

$$Al_2O_3 + 2H_3PO_4 \rightarrow 2AlPO_4 + 3H_2O \quad (5)$$

6.2. Organo-mineral geopolymers

6.2.1. Silicone

The siloxane (Si-O-Si) structure in organo-silicones is similar to the chains, rings, and networks of silicon and oxygen found in silica and the silicate minerals, for example in quartz. In the 1960s, studies shown that it is possible to pass from the polymeric silicate to the polymeric covalent molecules of an organosiloxane by replacing the bridging oxide ions of the silicate anions with methyl groups. The result of structures in this replacement are the silicate and aluminosilicate molecules: monomers, dimers, trimers, rings, chains, sheets and frameworks of corner-sharing silicate [SiO_4] groups [7].

6.2.2. Hybrid organo-mineral geopolymers

By incorporating the geopolymer into the organic polymer structure and adapting the chemical composition of the components, the new class of compounds was obtained.

The resulting hybrid material has improved fire resistance and excellent mechanical properties. The new developments are focusing on improving the mechanical and physical properties of the geopolymer itself, because a homogeneous mixture without phase separation requires a new approach in studies [7].

6.2.3. Kerogen geopolymer (Humic-acid based)

Kerogen-geopolymer is the final alternating product in Earth and the most stable material within all geopolymeric materials. Some geopolymeric materials due to their unique geopolymeric structure can last for a long time [7].

Geopolymers are the materials which can be classified into two major groups: organic containing geopolymers and pure inorganic geopolymers. The key parameter in the strength and durability of material with a large volume of inorganics is the small content of organics. Unique geopolymer that contains a high content of organics is the kerogen. Kerogen geopolymers occur in numerous forms: with more or less organics and opposite. It is evident that both inorganics and organics are required in a mix at a certain ratio, which will result in a geopolymeric structure.

It is the most abundant form of organic carbon on Earth, about 1000 times more abundant than coal, which forms primarily from terrigenous remains of higher plants. This geopolymeric structure is similar to human bone and teeth, typical inorganic-organic composites that show extreme durability and mechanical strength [6].

7. PROPERTIES OF GEOPOLYMERS

The physical, chemical and mechanical properties of geopolymeric materials indicate that they offer a wide range of industrial applications, although the formation of geopolymers is not still completely understood. The Si/Al molar ratio and curing, setting and hardening conditions in the geopolymeric structures determines the properties and the application fields of geopolymers [1].

Geopolymers are fire resistant up to 1400°C, heat resistant, and acid resistant materials. Also, they exhibit high early compressive strength, important fracture toughness, long-term durability, low apparent porosity or nano-porosity and freeze-thaw resistance.

Geopolymeric cements and concretes present ideal mechanical properties in comparing to Portland cement. Their compressive and tensile strengths are twice to three times bigger and the Moh's hardness ranges from 4 to 7.

Geopolymers are introduced into the construction materials and road building industrial sectors. Regarding their properties, geopolymers have a wide range of important industrial uses as pure, with fillers or reinforced materials [1].

In order to improve their mechanical properties, such as flexure, tension, shear and flexural fatigue at high temperatures, geopolymers are reinforced by different types of fabrics (carbon, glass, minerals or steel) to produce binders for advanced composite materials. Fiber reinforced geopolymeric binders and concretes are used as fire safety advanced materials into the transportation (air, sea, rail, car, etc.), nuclear and pharmaceutical industrial areas.

8. APPLICATION OF GEOPOLYMERS

Composite geopolymers are used for the production of electronic devices, moulds for thermoplastic material and metals casting, cutting tools, containers for hazardous chemicals and radioactive wastes, components for high performance engines, lightweight materials and prototype automobile components [1].

For construction applications all new materials must meet a set of high standards and procedures which is extremely expensive and time-consuming for manufacturers. Beside the lack of knowledge, especially on the long term behaviour of geopolymers, an important reason for the slow development of markets for geopolymers is a conservative view of new materials. However, a geopolymer industry is developing and an increasing number of geopolymer supplier companies are established based on research activities in universities and research institutes. Although there is no firm data on the market size, geopolymer concrete is now used in the transport sector in the USA and more recently in Australia. The short setting time of geopolymer cement makes it an ideal solution for repairing highways and airport runways [15].

Figure 8 shows the example of construction Queensland's University GCI building in Australia made from geopolymer concrete. It has 3 suspended floors built from structural slag/fly ash-based geopolymer concrete. This geopolymeric concrete has been branded by Australian architect Wagner and it is named as Earth Friendly Concrete (EFC) [16]. Three floors in this building were made from 33 structural pieces of floor construction. In Figure 9 is presented one of the structural floor panel made from geopolymer concrete (EFC) [17].

Recently, geopolymers are examined as potential technological solutions for the management of toxic and radioactive waste materials. Selecting an Al–Si material allowing acceptable levels of mechanical properties to be obtained is the key to produce cheaper geopolymer concretes . Production of cheaper concrete can be done by using low concentrations of alkali atoms and silicate units. The effect of carbon taxes on the cement and concrete industry also will help the geopolymer industry to enhance its competitiveness with Portland cements [18].

Another promising application of geopolymers is advanced fire resistant geopolymer composites. Geopolymers reinforced with carbon or glass fibres exhibit extraordinary mechanical properties. At elevated temperatures geopolymers are ideal materials for aerospace applications. In 1994, a geopolymer matrix composite was successfully used in a Formula 1 racing car by replacing titanium parts in exhaust system with geopolymeric composite. Subsequently these composites have been widely adopted in racing cars where their thermal properties are effective. Carbon fibre reinforced geopolymer composites do not burn or release any smoke after exposure to severe heat flux, which makes them appropriate materials for aircraft cabin fire protection, substituting for ordinary polymer matrix composites. The US Air Force now uses bombers equipped with geopolymer composites as fire resistant materials [15].

Fig. 8 Queensland's University building [16]. **Fig. 9** Construction of floor [17].

It should be noted that several advantages of geopolymers are related to the following.

(1) The low cost production, considering that they are based on alumino-silicate materials, which both occur naturally in abundance on the Earth as clay minerals and derive from industrial wastes as fly ash, blast-furnace slag [18].
(2) The energy-effectiveness of the production procedure since geopolymers are cured and hardened at relatively low temperature. The energy consumed for geopolymeric tiles fabrication is less than 16% of that of conventional ceramic bodies.
(3) The environmental contribution provided that:
   (a) a number of waste materials can be transferred into added value innovative products.
   (b) greenhouse gas emissions are essentially reduced during geopolymeric materials production (the geopolymeric cement manufacture emits 80% less CO_2 than that of Portland cement).
   (c) geopolymeric composites can be utilized for safe stabilization and immobilization of radioactive and toxic wastes [1].

9. CONCLUSION

A brief history of geopolymers and highlights of research activities in this area have been presented. Geopolymer technology has a history of a more than half a century. Desirable properties, abundant raw materials and successful applications of geopolymers promise considerable progress in large scale production of geopolymers in the near future.

In the last two decades, considerable research has been carried out through the world, providing a large volume of useful data and important findings on geopolymerisation and the properties of geopolymers.

Geopolymer concrete offers environmental protection by means of upcycling low-calcium fly ash and blast furnace slag, waste-products from the industries, into a highvalue construction material needed for infrastructure developments.

A large contribution to the development and implementation of geopolymer composites has been provided by the extensive research by Prof. Waltraud M. Kriven [10,11,12].

Geopolymer concrete has excellent compressive strength and is suitable for structural applications. The main factors that influence the properties of the fresh concrete and the hardened concrete have been identified. Simple guidelines for the design of mixture proportions are included. The elastic properties of hardened geopolymer concrete and the behavior and strength of reinforced geopolymer concrete structural members are similar to those in the Portland cement concrete. Fly ash-based geopolymer concrete also shows excellent resistance to sulfate attack and fire, good acid resistance, undergoes low creep, and suffers very little drying shrinkage.

A lack of information on some aspects of geopolymerisation is apparent and the incoming researches should focus on these gaps. Despite the current status and wide acceptance of Portland cement, the desirable properties of geopolymers, their environmental benefits, suggest that geopolymer technology should make significant progress in the near future.

It is very important to evolve the knowledge on this topic, considering there are a lot of possibilities of applying these novel materials in our area, further exploration of geopolymer usage is important. Also, it should be very useful to explore the possibilities for applying geopolymers in our region. One of the aspects of geopolymer research can be focused on the fractal analysis of geopolymer microstructure, which would significantly contribute to understanding and analysis of these new materials' properties.[19,20,21].

REFERENCES

1. Dimitrios Panias, Ioanna Giannopoulou, "Geopolymers: a new generation of inorganic polymeric novel materials", National Technical University of Athens, Proc. of 1st International Conference on Advances in Mineral Resources Management and Environmental Geotechnology, AMIREG 2004, June 2004, pp.407-412
2. Zoran Grdić, Gordana Topličić-Ćurčić, "Ekološki materijali – komponenta održive arhitekture", Zbornik radova Građevinskog fakulteta u Nišu, br. 25, pp. 87-94, Niš, 2010.
3. Gordana Topličić-Ćurčić, Zoran Grdić, Nenad Ristić, Iva Despotović, "Enviromental building materials and their application in civil engineering", International symposium about research and application of modern achievements in civil engineering in the field of materials and structures, DIMKS, XXV Kongres, Tara, 20 – 21. oktobar 2011, pp. 487 – 495.
4. Gordana Topličić-Ćurčić, Dušan Grdić, Nenad Ristić, Zoran Grdić, "Ceramic facade cladding as an element of sustainable development", Facta Universitatis, Series: Architecture and Civil Engineering vol. 13, no 3, 2015, pp. 219 – 231,
5. Waltraud M. Kriven, "For NSf proposal with Ange", private conversation, December 2015
6. http://blogs.qub.ac.uk/geopolymer/geopolymer-background/
7. Joseph Davidovits, "Geopolymer Chemistry & Applications", Institut Géopolymère, November 2015
8. "Instrinsic Microstructure of Geopolymers and Geopolymer-based Materials," W. M. Kriven, J. Bell, M. Gordon and Gianguo Wen, in "Geopolymer, Green Chemistry and Sustainable Development Solutions," edited by Joseph Davidovits. Proc. World Congress Geopolymer, 2005, St. Quentin, France. Published by the Geopolymer Institute, St. Quentin, France, pp 179-183 (2005)
9. S.S. Musil, W.M. Kriven, "In Situ Mechanical Properties of Chamotte Particulate Reinforced, Potassium Geopolymer," J. Am. Cer. Soc., 97(3) 907-915 (2014)
10. Daniel R. Ribero, Waltraud M. Kriven, "Properties of Geopolymer Composites Reinforced with Basalt Chopped Strand Mat or Woven Fabric," J. Am. Ceram. Soc., 99 [4] 1192-1199 (2015)
11. Brayden E. Glad, Waltraud M. Kriven, "Highly Porous Geopolymers Through Templating and Surface Interactions," J. Am. Ceram. Soc. 98 [7] 2052-2059 (2015)
12. Ruy A. Sa Ribeiro, Marilene G. Sa Ribeiro, Kaushik Sankar, Waltraud M. Kriven, Potassium-based Geopolymer Reinforced with Bamboo Fibers," J. Am. Ceram. Soc., 100 [1] 49-55 (2017)
13. Joseph Davidovits, "Geopolymers-Inorganic polymeric new material, Reprint of Journal of Thermal Analyses (1991)" , Institut Géopolymère, 1997
14. A.S. Wagh, and S.Y. Jeong, "Chemically Bonded Phosphate Ceramics: I. A Dissolution Model of Formation", J. Ceramic Society, 2003
15. Behzad Majidi, "Geopolymer Technology, from Fundamentals to Advanced Applications: A Review", Materials Technology, vol. 24, no.2, pp. 79-87 June 2009
16. https://www.geopolymer.org/news/worlds-first-public-building-with-structural-geopolymer-concrete/
17. http://www.architectureanddesign.com.au/awards-1/2013-awards-finalists/innovation-of-the-year/suspended-geopolymer-concrete-floor-panels
18. Vijaya Rangan, "Geopolymer concrete for environmental protection", The Indian Concrete Journal April 2014
19. Vojislav V. Mitica,Vesna Paunovica,Ljubisa Kocic, Fractal approach to $BaTiO_3$-ceramics micro-impedances, Ceramics International, Ceramics International 41 (2015) 6566–6574
20. V.V. Mitić, Lj. Kocić , V. Paunović, F. Bastić, D. Sirmić, The Fractal Nature Materials Microstructure Influence on Electrochemical Energy Sources, Science of Sintering, 47(2015) 195-204
21. A. Terzić, V. V. Mitić, Lj. Kocić, Z. Radojević, S. Pašalić, Mechanical Properties and Microstructure Fractal Analysis of Refractory Bauxite Concrete, Science of Sintering, 47 (2015) 331-346.

SVOJSTVA GEOPOLIMERA

Geopolimeri su novi ekološki materijali, koji imaju potencijala za veliki napredak u bliskoj budućnosti. Ovi materijali,sa jedinstvenim fizičkim, hemijskim i mehaničkim svojstvima mogu biti iskorišćeni na mnogo načina. Proizvedeni su korišćenjem industrijskih otpadnih materijala, a mogu se pretvoriti u visoko kvalitetne konstruktivne materijale potrebne za razvoj infrastrukture.

Ključne reči: *geopolimeri, novi materijali, keramika, beton, leteći pepeo, organiski materijali, ekološki materijali*

FACTA UNIVERSITATIS
Series: **Architecture and Civil Engineering** Vol. 16, No 1, 2018, pp. 57-66
https://doi.org/10.2298/FUACE170125005G

POTENTIAL OF USAGE OF SELF COMPACTING CONCRETE WITH ADDITION OF RECYCLED CRT GLASS FOR PRODUCTION OF PRECAST CONCRETE ELEMENTS

UDC 691.32

Dušan Grdić, Nenad Ristić, Gordana Topličić – Ćurčić, Dejan Krstić

University of Niš, The Faculty of Civil Engineering and Architecture, Niš, Serbia

Abstract. *The electronic and electric waste (e-waste) quantities have been sharply increasing since the beginning of the 21st century. A significant portion of e-waste is composed of glass originating from the cathode ray tubes of the TV-set screens and computer monitors (CRT glass) which, due to the complexity of the recycling process and its chemical composition is very hazardous and represents a huge environmental problem. One of the modes of recycled CRT glass application is for making of self-compacting concrete (SCC). The paper investigated various properties of fresh and hardened SCC where CRT glass played the role of powdery mineral admixture. SCC made in such a way, with satisfactory physical-mechanical characteristics is suitable for production of various precast concrete elements. In order to monitor the durability of experimental concrete in actual conditions, several curbs were experimentally placed in the course of reconstruction of a street in Niš.*

Key words: *E-waste, environment, CRT glass, SCC concrete, precast concrete*

1. INTRODUCTION

Electronic industry is one of the most important and fast growing industries in the world. Its growth and development in the recent decades created numerous jobs, accelerated technological development and simultaneously contributed to generation of considerable e-waste due to phasing out of electronic devices. E-waste, as it is termed in literature, increases considerably faster than other solid waste in the world [1].

Computer monitors and TV sets with cathode ray tubes have not been sold in Europe since 2011. However, these devices are still present in the households, and it is estimated that the landfills in Europe annually receive between 50000 tons and 150000 tons of obsolete CRT screens. Fernanda Andreola et al [2] anticipated that the quantity of collected CRT glass at the annual level will not be reduced in the future period.

Received January 25, 2017 / Accepted May 18, 2017
Corresponding author: Dušan Grdić
Faculty of Civil Engineering and Architecture, University of Niš, 18000 Niš, Aleksandra Medvedeva 14, Serbia
E-mail: dusan.grdic@gaf.ni.ac.rs

The CRT waste recycling process is very important, in environmental terms. There are two possible systems of cathode tube recycling – open and close loop recycling (Figure 1). The close loop recycling comprises recycling of old screens and production of new CRT devices. Regarding that in Europe there are no more factories producing new screens with cathode tubes, most often the CRT waste is exported to the countries where CRT screen factories still exist. The open loop recycling uses old CRT screens for production of new and different products [3]. A large number of scientific papers studies the potential of application of CRT glass in production of: ceramic tiles, artificial marble, glass jewelry, decorative crystals, etc.

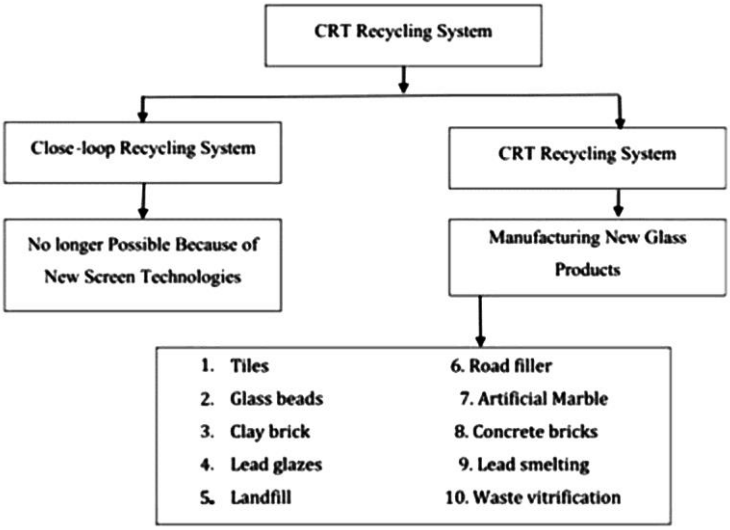

Fig. 1 The appearance of open and close loop of CRT glass recycling [3]

One of the possible directions of cathode glass usage considers the civil engineering industry, whereby glass would be used as substitution for a share of the aggregate or for a portion of filler in self-compacting concrete (SCC).

Emam Ali and Sherif Tersawy [4] examined properties of fresh and hardened SCC whereby the fine aggregate fraction was partially replaced by glass container cullet. Fine aggregate mass was replaced with 0%, 10%, 20%, 30%, 40% and 50% of CRT glass. The test results indicated that Slump Flow increased with the increase of glass share in the concrete mixture. On the other hand, the increase of glass admixture caused certain reduction of compressive strength, splitting tensile strength and static modulus of elasticity.

Kou and Poon [5] also examined properties of SCC where a portion of the river aggregate and crushed granite of grain size up to 10 mm was replaced by recycled glass containers. The river aggregate was replaced in the range between 0 and 30% with an increment of 10%, while granite was varied in the range between 5% and 15% with an increment of 5%. The results of their research indicate that the increase of the glass share in concrete mixture results in reduction of shrinkage and increase of concrete resistance to chloride action.

Miao Liu [6] in his paper used white and green glass container glass cullet as replacement for portions of both cement and fine aggregate in SCC. The glass admixture resulted in an increase of water/powder ratio and in decrease of required quantity of superplasticizer. The presence of glass was not reflected on the passing ability (L-box test), but it caused reduction of mechanical characteristics of concrete. The final conclusion of the study is that SCC with good physical-mechanical properties can be made if cement and fine aggregate are replaced with recycled glass in the quantity of up to 10%.

Ana Mafalda Matos et al [7] substituted 50% of limestone filler with recycled glass and monitored its effects on mechanical properties and durability of SCC made in this way. It was established that recycled glass increases concrete resistance to penetration of chlorides, reduces water absorption and has mechanical characteristics similar to the reference batch where filler was not substituted by recycled glass.

2. MATERIALS USED IN THE EXPERIMENT

For making of SCC three fractions of river aggregate were used (0/4 mm, 4/8 mm and 8/16 mm) originating from the South Morava river screening plant "Šilo Prom" d.o.o. Belotinac which conforms to all the quality standards prescribed by SRPS EN 206-1:2011[10] and EN 12620:2010 [11] standards. Also, pure Portland cement CEM I 42,5R manufactured by "CRH" Novi Popovac was used, which meets all the quality requirements prescribe by the SRPS EN 197-1:2013 standard [12]. Sika Viscocrete 5380 was used as the chemical admixtures in the mixture as superplasticizer.

Fig. 2 System for lining out and separation of integral parts of a monitor using hot wire.

The "Jugo - Impex" E.E.R. d.o.o. company deals with collection and recycling of cathode ray tubes of old TV sets and computer monitors. The cathode ray tubes in this company are dismantled to component elements using the state-of-the-art automatic high speed CTR separator. The mentioned separator consists of the lining out device (Figure 2, left), hot wire for separation of components (Figure 2, right) and the vacuum system for collection of fluorescence and dust [8]. The recycling center, for the needs of this research donated a certain amount of cathode ray glass which was further pulverized in the Laboratory of building materials using laboratory mill. After milling, the glass was passed through the 0,125 mm sieve. The composition of oxides in the clear glass is as usual, the ratio being $N_2O : CaO : SiO_2 = 1 : 1 : 6$, which was confirmed by a chemical

analysis (SiO_2 – 72,61%, Na_2O – 13,12%). There is a minor presence of other oxides (Al_2O_3, MgO, K_2O, SO_3).

3. EXPERIMENTAL SECTION

3.1. Concrete mixture composition

Concrete mixture composition is presented in table 1. The self-compacting concrete was made with: 400 kg cement, 1616 kg of the river aggregate with three fractions and 156 kg of recycled CRT glass, having fineness of 0,125 mm which served as a powder mineral admixture. Water/cement ratio was 0,45. The cathode ray tube glass had a share of 5,5% in volume of 1 m^3 of concrete.

Table 1 Concrete mixture composition

Type of material	Aggregate 0/4 mm	Aggregate 4/8 mm	Aggregate 8/16 mm	Filer	Cement	Water	Superplasticizer
Volume Percentage in1m^3[%]	29,62	11,58	20,11	5,5	12,70	18,15	0,45
Specific density [kg/m^3]	2620	2650	2650	2840	3150	1000	1100
Mass 1 m^3 [kg]	776	307	533	156	400	181,5	4,95

3.2. Fresh concrete tests results

The test results of fresh concrete are presented in table 2. Density of fresh concrete was tested according to SRPS EN 12350-6:2010 standard [13]. Entrained air content was tested according to SRPS EN 12350-7:2010 standard [14]. A concrete mixture can be considered SCC if it has flowability, viscosity, passing ability and segregation resistance. [9]. In order to verify the previously mentioned properties, the following fresh concrete tests were performed: slump and T_{500} spreading tests (SRPS EN 12350-8:2012 [15]), L – box test (SRPS EN 12350-10:2012 [16]) and test of stability on the sieve (SRPS EN 12350-11:2012 [17]).

Table 2 Fresh concrete tests results

Concrete characteristics	Measurement unit	Test result
Density	kg/m^3	2390
Air content	%	0,8
Spreading T_{500}	s	4,5
Slump test	mm	660
L-box test H1/H2	(mm/mm)	0,95
Segregation	%	12,8

After lifting of the filled cone, the time required for the concrete to spread over the diameter of 500 mm is measured, as well as the final diameter of the circle after the concrete has finished spreading (Figure 3, left). The L-box aims at checking the concrete

tendency to flow between the rebars during placing (Figure 3, right). SCC resistance to segregation is checked by measuring the time of concrete mass passage through the 5 mm sieve for the duration of 120 seconds.

Fig. 3 Slump flow test and L – box test

3.3. Hardened concrete test results

Water saturated concrete density test was performed on the hardened concrete cubes (SRPS EN 12390-7:2010 [18]) having sides of 15 cm at the age of 2, 7, 28 and 90 days. Compressive strength testing was performed according to SRPS EN 12390-3:2010 standard [19], while simultaneously the ultrasound velocity through concrete was monitored (SRPS EN 12504-4:2008 [20]) as well as the rebound number (SRPS EN 12504-2:2008 [21]). Flexural tensile strength was tested on the prisms having dimensions 10x10x40 cm at the age of 28 and 90 days according to SRPS EN 12390-5:2010 standard. [22]. According to SRPS EN 12390-6:2012 standard [23] tensile splitting test was performed on the specimens having cylindrical form, having diameter of ∅15 cm and height of 30 cm. „Pull – off" bond strength test was performed on the cubes having sides of 15 cm at the age of 28 and 90 days, in all according to SRPS EN 1542:2010 standard [24]. Static modulus of elasticity was tested on the cylindrically shaped specimens according to SRPS IS0 6784:2000 standard [25]. The Boehme abrasion resistance was tested on the sample cubes having sides of 7.07 cm according to SRPS B.B8.015:1984 standard [29].

The test of resistance to simultaneous action of frost and salt was performed according to SRPS U.M1.055:1984 standard [26]. According to SRPS U.M1.016:1992 standard [27] was performed M-200 test of resistance to frost action. In figure 4 (left) is presented the appearance of the samples after 25 cycles of successive freezing and de-freezing. Determination of pressurized water penetration was tested on the cubes having 15 cm sides according to SRPS U.M1.015:1998 standard [28]. The review of test results of hardened concrete is provided in table 3. In figure 4 (right) is presented the specimen after the penetration test using water under pressure of 7 bars.

Table 3 Review of the hardened concrete test results

Property:	Age:	Test results:
Water saturated density [kg/m^3]	2 days	2390
	7 days	2388
	28 days	2385
	90 days	2370
Compressive strength [MPa]	2 days	38,7
	7 days	47,7
	28 days	59,0
	90 days	72,2
Static modulus of elasticity [GPa]	28 days	29,9
	90 days	33,3
Flexural strength [MPa]	28 days	6,4
	90 days	7,7
Tensile strength [MPa]	28 days	4,2
	90 days	5,5
Tensile– Pull-off strength [MPa]	28 days	4,2
	90 days	5,1
Ultrasound impulse velocity [m/s]	28 days	4691
	90 days	4748
Rebound number	28 days	51,3
	90 days	56,5
Bohme abrasion resistance [cm^3/50 cm^2]	90 days	9,5
Pressurized water penetration [mm]	-	0
Resistance to simultaneous action of frost and defrosting salt [mg/mm^2]	-	0,11
Frost resistance (reduction of compressive strength M200) [%]	-	15,62

Fig. 4 Appearance of the specimens after the tests of resistance to simultaneous action of frost and salt (left) and the appearance of the specimen after water permeability test

3.4. Production and fitting of curbs made of SCC with recycled CRT glass admixture

In the period when the laboratory tests of SCC with recycled CRT glass admixture were being conducted, there was ongoing reconstruction of Dragiše Cvetkovića street in Niš. In cooperation with the company "Put Inženjering d.o.o." several curbs were made of the experimental concrete B 120/180-200, suitable for the reconstructed street. (Figure 5).

Fig. 5 Production of curbs made of SCC with CRT glass admixture

After the conducted appropriate curing of concrete, the curbs were fitted in the mentioned street (Figure 6). Since then, active monitoring of experimental curbs has been performed, for the purpose of observing their durability in real conditions.

Fig. 6 Fitting of curbs in Dragiše Cvetkovića street

4. DISCUSSION OF RESULTS

Based on the measured spreading of 660 mm, concluded that SCC with recycled cathode ray tube glass admixture belongs to the spreading class SF2 (of 660mm to 750 mm). The time measured for T_{500} test is 4,5s, so it can be concluded that SCC has satisfactory flowability. The percentage of passage through the 5 mm sieve (sieve stability test) amounted to 12,8% which indicates that experimental concrete has satisfactory resistance to segregation. The L-box test, determined that the concrete belongs to the PA2 class (≥0,80).

The obtained early compressive strength values at the age of 2 and 7 days were very high. The compressive strength at the age of 28 days was 59 MPa, while after 90 days the increase of the strength was 22%. This increase can be partially attributed to the puzzolanic activity of the milled CRT glass. The values of tensile splitting strength and tensile flexural strength were at the satisfactory level. The average value of penetration of water under pressure of 7 bars was 0 mm, which proved that SCC is water impermeable. After 25 cycles of simultaneous action of frost and defrosting salt, it was determined that there occurred the flaking of the surface layer of concrete, but that it was less than 0,2 mg/mm^2. On the basis of SRPS U.M1.055:1984 standard [26] it can be concluded that SCC has the damage degree MS1 and that it is resistant to this action. Reduction of compressive strength after 150 cycles of alternating freezing and de-freezing amounted to 10,20% in comparison to the reference batch, i.e. 15,62% after 200 cycles which proved that concrete had M-200 frost action resistance. Boehme abrasion resistance was 9,5 cm^3/50 cm^2 which is a satisfactory result.

4. CONCLUSION

Waste glass of cathode ray tubes of TV sets' screens and computer monitors represents an environmental issue, because waste disposal sites of such waste may pollute the environment. The paper investigates various properties of fresh and hardened SCC with the admixture of recycled cathode ray tube glass. It was determined that experimental SCC has excellent fresh concrete properties in terms of flowability, filling ability and segregation resistance.

The obtained values of compressive and tensile strength were high which is in agreement with the results in the paper [7]. On the basis of the obtained results of water permeability testing, resistance to frost action and simultaneous resistance to frost and defrosting salt action, and to abrasion resistance it can be concluded that SCC with CRT has satisfactory durability. For this reason it can be considered suitable for making of precast concrete elements such as interlocking paving elements and concrete curbs whose cross section does not exceed 300 cm^2. The monitoring of the experimentally fitted curbs in Dragiše Cvetkovića street in Niš, made with the experimental concrete, exhibited no deficiency regarding durability in comparison with the classical curbs fitted in the same street.

Based on the previous assertions, it can be generally concluded that the SCC concrete made with recycled cathode ray glass, as powder mineral admixture, can be successfully used for production of precast concrete elements.

Acknowledgement. *The work reported in this paper is a part of investigation within the research project TR 36017 "Utilization of by – product and recycled waste materials in concrete composites in the scope of sustainable construction development in Serbia: investigation and environmental assessment of possible applications" supported by Ministry for Science and Technology, Republic of Serbia. This support is gratefully acknowledged.*

REFERENCES

1. C. P. Baldé, F. Wang, R. Kuehr, J. Huisman, "The global e-waste monitor – 2014", United Nations University, IAS – SCYCLE, Bonn, Germany, 2015.
2. F. Andreola, L. Barbieri, A. Corradi, I. Lancellotti, "CRT glass state of the art: A case study: Recycling in ceramic glazes", Journal of the European Ceramic Society, vol. 27, issues 2–3, pp. 1623-1629, 2007.
3. N. Singh, J. Li, X. Zeng, "Global responses for recycling waste CRTs in e- waste", Waste Management, vol. 57, pp. 187-197, November 2016.
4. E. Emam Ali, S. H. Al – Tersawy, "Recycled glass as a partial replacement for fine aggregate in self compacting concrete", Construction and Building Materials, vol. 35, pp. 785-791, 2012.
5. S. C. Kou, C. S. Poon, "Properties of self – compacting concrete prepared with recycled glass aggregate", Cement and Concrete Composites, vol. 31, pp. 107-113, 2008.
6. M. Liu, "Incorporating ground glass in self – compacting concrete", Construction and Building Materials, vol. 25, pp. 919-925, July 2010.
7. A. M. Matos, T. Ramos, S. Nunes, J. Sausa-Coutinho, "Durability Enhancement of SCC with Waste Glass Powder", Materials Research, pp. 67-74, 2016.
8. "Uputstvo za upotrebu automatskog separtora CRT-a visoke brzine - Loyalty Equipment – Making Co. Ltd., Sichuan, China", Jugo – Impex E.E.R. d.o.o.
9. Z. Grdić, "Tehnologija betona", Građevinsko – arhitektonski fakultet Univerziteta u Nišu, pp. 261 – 274, 2011.
10. SRPS EN 206-1:2011 Beton – Deo 1: Specifikacije, performanse i usaglašenost, Institut za standardizaciju Srbije, 2011.
11. EN 12620:2010, Agregati za beton, Institut za standardizaciju Srbije, 2011.
12. SRPS EN 197-1:2013 Cement – Deo 1: Sastav, specifikacije i kriterijumi usaglašenosti za obične cemente, Institut za standardizaciju Srbije, 2013.
13. SRPS EN 12350-6:2010 Ispitivanje svežeg betona – Deo 6: Zapreminska masa, Institut za standardizaciju Srbije, 2010.
14. SRPS EN 12350-7:2010 Ispitivanje svežeg betona – Deo 7: Sadržaj vazduha, Institut za standardizaciju Srbije, 2010.
15. SRPS EN 12350-8:2012 Ispitivanje svežeg betona – Deo 8: Samougrađujući beton – Ispitivanje rasprostiranja sleganjem, Institut za standardizaciju Srbije, 2012.
16. SRPS EN 12350-10:2012 Ispitivanje svežeg betona – Deo 10: Samougrađujući beton – Ispitivanje pomoću L – kutije, Institut za standardizaciju Srbije, 2012.
17. SRPS EN 12350-11:2012 Ispitivanje svežeg betona – Deo 11: Samougrađujući beton – Ispitivanje segregacije pomoću sita, Institut za standardizaciju Srbije, 2012.
18. SRPS EN 12390-7:2010 Ispitivanje očvrslog betona – Deo 7: Zapreminska masa očvrslog betona, Institut za standardizaciju Srbije, 2010.
19. SRPS EN 12390-3:2010 Ispitivanje očvrslog betona – Deo 3: Čvrstoća pri pritisku uzoraka za ispitivanje, Institut za standardizaciju Srbije, 2010.
20. SRPS EN 12504-4:2008 Ispitivanje Betonskih konstrukcija – Deo 4: Određivanje brzine ultrazvučnog impulsa, Institut za standardizaciju Srbije, 2008.
21. SRPS EN 12504-2:2008 Ispitivanje Betonskih konstrukcija – Deo 2: Ispitivanje bez razaranja – Određivanje veličine odskoka, Institut za standardizaciju Srbije, 2008.
22. SRPS EN 12390-5:2010 Ispitivanje očvrslog betona – Deo 5: Čvrstoća pri savijanju uzoraka za ispitivanje, Institut za standardizaciju Srbije, 2010.
23. SRPS EN 12390-6:2012 Ispitivanje očvrslog betona – Deo 6: Čvrstoća pri cepanju zatezanjem uzoraka za ispitivanje, Institut za standardizaciju Srbije, 2012.
24. SRPS EN 1542:2010 Proizvodi i sistemi za zaštitu i sanaciju betonskih konstrukcija – Metode ispitivanja – Merenje prionjivosti "pull-off" metodom, Institut za standardizaciju Srbije, 2010.
25. SRPS ISO 6784:2000 Beton – Određivanje statičkog modula elastičnosti pri pritisku, 2000.
26. SRPS U.M1.055:1984 Beton – ispitivanje otpornosti površine betona na dejstvo mraza i soli za odmrzavanje, Službeni list SFRJ, br 48, 1984.

27. SRPS U.M1.016:1992 Beton – ispitivanje otpornosti betona prema dejstvu mraza, Službeni list SRJ, br 46, 1992.
28. SRPS U.M1.015:1998 Beton – Očvrsli beton, određivanje prodiranja vode pod pritiskom, Savezni zavod za standardizaciju br. 6/2-02-1/13, 19. januar 1998. godine.
29. SRPS B.B8.015:1984 Ispitivanje otpornosti prema habanju brušenjem, Institut za standardizaciju Srbije, 1984.

MOGUĆNOST PRIMENE SAMOUGRAĐUJUĆEG BETONA SA DODATKOM RECIKLIRANOG CRT STAKLA ZA IZRADU BETONSKIH PREFABRIKATA

Količine elektronskog i električnog otpada (e-otpad) su u značajnom porastu od početka 21. veka. Nezanemarljivu količinu e-otpada čini staklo od katodnih cevi televizijskih ekrana i kompjuterskih monitora (CRT staklo) koje zbog složenosti procesa reciklaže i svog hemijskog sastava ugrožava životnu sredinu i predstavlja veliki ekološki problem. Jedan od vidova primene recikliranog CRT stakla jeste njegova upotreba za spravljanje samougrađujućeg betona (SCC). U radu su ispitana različita svojstva svežeg i očvrslog SCC betona kod koga je katodno staklo imalo ulogu praškastog mineralnog dodatka. Ovako spravljen SCC beton sa zadovoljavajućim fizičko – mehaničkim karakteristikama pogodan je za izradu različitih betonskih prefabrikata. U cilju praćenja trajnosti eksperimentalnog betona u realnim uslovima ogledno je postavljena nekolicina betonskih ivičnjaka od predmetnog betona tokom renoviranja jedne ulice u Nišu.

Ključne reči: *E-otpad, životna sredina, CRT staklo, SCC beton, betonski prefabrikati*

FACTA UNIVERSITATIS
Series: **Architecture and Civil Engineering** Vol. 16, No 1, 2018, pp. 67-80
https://doi.org/10.2298/FUACE170206006T

AN ALTERNATIVE APPROACH TO FINITE DEFORMATION

UDC 539.371

Marina Trajković-Milenković[1], Otto T. Bruhns[2]

[1]University of Niš, The Faculty of Civil Engineering and Architecture, Niš, Serbia
[2]Institute of Mechanics, Ruhr-University Bochum, Germany

Abstract. *In elastoplasticity formulation constitutive relations are usually given in rate form, i.e. they represent relations between stress rate and strain rate. The adopted constitutive laws have to stay independent in relation to the change of frame of reference, i.e. to stay objective. While the objectivity requirement in a material description is automatically satisfied, in an Eulerian description, especially in the case of large deformations, the objectivity requirement can be violated even for objective quantities. Thus, instead of a material time derivative in the Eulerian description objective time derivatives have to be implemented. In this work the importance of the objective rate implementation in the constitutive relations of finite elastoplasticity is clarified. Likewise, it shows the overview of the most frequently used objective rates nowadays, their advantages and shortcomings, as well as the distinctive features of the recently introduced logarithmic rate.*

Key words: *finite deformations, objective rates, logarithmic rate, elastoplasticity, finite deformation decomposition*

1. EULERIAN DESCRIPTION OF FINITE DEFORMATION

The process of deformation of a deformable body *B* from its reference, B_0, to a current configuration, B_t, represents the change in shape and position of the observed body, as it is shown in Fig. 1. While the former leads to a varying distance between the arbitrary pairs of particles of the body *B* (here particles P and Q), the latter reflects a rigid body motion, i.e. translation and rotation. In this article an Eulerian description is adopted. Therefore, in order to define the position of the particle of interest, instead of material coordinates as independent variables spatial coordinates are used.

The distance between particles P and Q in the reference configuration, represented by a material vector d**X**, is changing during the process of deformation in a corresponding space vector d**x** according to law

Received February 6, 2017 / Accepted April 7, 2017
Corresponding author: Marina Trajković-Milenković
Faculty of Civil Engineering and Architecture, University of Niš, 18000 Niš, Aleksandra Medvedeva 14, Serbia
E-mail: trajmarina@gmail.com

$$d\mathbf{x} = \mathbf{F} \cdot d\mathbf{X}, \tag{1}$$

where **F** is a two-point tensor, called a *deformation gradient*. Its determinant, entitled the *Jacobian determinant* or shortly *Jacobian*, meets the rule

$$J = \det(\mathbf{F}) > 0. \tag{2}$$

In large deformation problems rotation plays an important role. A *polar decomposition theorem* elucidates this role. It postulates a unique multiplicative decomposition of the deformation gradient into a positive definite symmetric 2^{nd}-order Eulerian tensor **V** or Lagrangian tensor **U** known as *left* or *right stretch tensor*, respectively, and a proper orthogonal *rotation tensor* **R**, i.e.

$$\mathbf{F} = \mathbf{V} \cdot \mathbf{R} = \mathbf{R} \cdot \mathbf{U}. \tag{3}$$

In the Eulerian description the *left polar decomposition* is to be applied; it assumes that the deformation is composed of the rigid body motion, represented by the rotation tensor **R**, and the stretching, defined by the Eulerian left stretch tensor **V**, which follows the rotation.

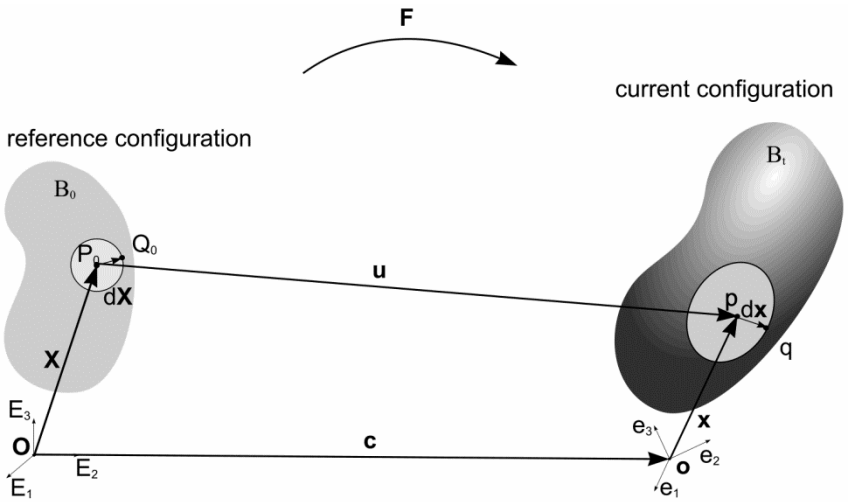

Fig. 1 Reference and current configuration of a deformable body

The squares of the left and right stretch tensors are called *left* and *right Cauchy-Green tensors* and are determined as

$$\mathbf{B} = \mathbf{V}^2 = \mathbf{F} \cdot \mathbf{F}^{\mathrm{T}} \quad \text{and} \quad \mathbf{C} = \mathbf{U}^2 = \mathbf{F}^{\mathrm{T}} \cdot \mathbf{F}, \tag{4}$$

are more convenient for numerical purpose. Relations between Cauchy-Green tensors are given as

$$\mathbf{B} = \mathbf{R} \cdot \mathbf{C} \cdot \mathbf{R}^{\mathrm{T}} \quad \text{and} \quad \mathbf{C} = \mathbf{R}^{\mathrm{T}} \cdot \mathbf{B} \cdot \mathbf{R}. \tag{5}$$

2. ANALYSIS OF MOTION

Since most of formulations of finite elastoplasticity are given in a rate form, which is well-suited for the numerical implementation of the latter into finite element based programs, it is necessary to express the previously introduced quantities as functions of time.

A velocity of the observed material point can be defined in the Eulerian description by the following relation

$$\mathbf{v}(t) = \dot{\mathbf{x}} = \frac{\mathrm{d}\mathbf{x}}{\mathrm{d}t}, \tag{6}$$

while its increment is given as

$$\mathrm{d}\mathbf{v}(\mathbf{x},t) = \frac{\partial \mathbf{v}(\mathbf{x},t)}{\partial \mathbf{x}} \cdot \mathrm{d}\mathbf{x} = \nabla \mathbf{v} \cdot \mathrm{d}\mathbf{x}, \tag{7}$$

i.e.

$$\mathrm{d}\mathbf{v} = \mathrm{d}\dot{\mathbf{x}} = \mathbf{L} \cdot \mathrm{d}\mathbf{x}. \tag{8}$$

Here **L** represents the *velocity gradient*. It actually maps the material line element d**x** to its rate in the current configuration. Unlike the deformation gradient, that describes a local deformation state of the particle P and is related to the reference configuration, the velocity gradient defines a *rate of change* of a local deformation state of the particle P and it is *not* related to the reference configuration. As a function of the deformation gradient the velocity gradient can be expressed in the form

$$\mathbf{L} = \dot{\mathbf{F}} \cdot \mathbf{F}^{-1}. \tag{9}$$

It can be decomposed into its symmetric part, related to stretching, and skew-symmetric part, related to rotation,

$$\mathbf{L} = \mathbf{D} + \mathbf{W}, \tag{10}$$

where the *rate of deformation tensor* or the *stretching tensor* **D** and the *vorticity tensor* or the *spin tensor* **W** are given respectively as

$$\mathbf{D} = \frac{1}{2}(\mathbf{L} + \mathbf{L}^{\mathrm{T}}) \quad \text{and} \quad \mathbf{W} = \frac{1}{2}(\mathbf{L} - \mathbf{L}^{\mathrm{T}}), \tag{11}$$

(see e.g. Malvern, 1969, and Mićunović, 1990).

One of the key tasks in defining a reliable model of elastoplastic material behaviour is the choice of a suitable strain rate measure that will be implemented in the constitutive laws. The stretching tensor **D** can be one of these strain rate measures. But, in spite of its name as the rate of deformation tensor, until recently it has been considered that the stretching tensor cannot be defined either as a Lagrangian or as an Eulerian strain rate tensor and therefore it has not been recognized as a rate of deformation (see Ogden, 1984). However, Xiao et al. (1997, 1998b) have proved that the stretching tensor **D** can be exactly integrated to give the Hencky strain tensor **h,** defined in the Eulerian description by the relation

$$\mathbf{h} = \frac{1}{2}\ln \mathbf{B} = \ln \mathbf{V}. \tag{12}$$

How to define the natural deformation rate **D** as a direct flux of the Hencky (logarithmic) strain **h** will be explained in Section 3.3.

3. OBJECTIVITY OF A TENSOR FIELD

The deformation of the body can be observed by one or several physical observers and, thus, it can be described in different ways. For example, we have two observers that are recording the process of deformation. One observer is labelled with star and another one without star. Consequently their records are designated on the same way. The transformation between the coordinate systems associated to the space position of both observers is described by the relation

$$\mathbf{x}^* = \mathbf{Q}(t)\cdot\mathbf{x} + \mathbf{c}(t), \tag{13}$$

where **Q** is a proper orthogonal tensor of relative rotation and **c** is a vector of relative translation of one observer relatively to another**.** Observations can be recorded in different time and therefore, using the time distance in records *a*, the time difference can be specified as

$$t^* = t - a. \tag{14}$$

Physical phenomena do not depend on the choice of the observer, which is not necessarily the case of their kinematical description. That reflects on the mathematical formulation of physical laws such as constitutive models.

According to Ogden (1984), scalar a_0, vector $\boldsymbol{\alpha}_0$ or 2nd-order tensor field $\mathbf{A}_0$ defined in the Lagrangian configuration, are objective if they conform to these transformation rules

$$\begin{aligned} a_0^*(\mathbf{X},t^*) &= a_0(\mathbf{X},t) \\ \boldsymbol{\alpha}_0^*(\mathbf{X},t^*) &= \boldsymbol{\alpha}_0(\mathbf{X},t) \\ \mathbf{A}_0^*(\mathbf{X},t^*) &= \mathbf{A}_0(\mathbf{X},t). \end{aligned} \tag{15}$$

Since the following relation holds

$$\dot{\mathbf{A}}_0^*(\mathbf{X},t^*) = \dot{\mathbf{A}}_0(\mathbf{X},t), \tag{16}$$

the conclusion we arrive to is that the material time derivative of the transformed Lagrangian 2nd-order tensor satisfies the objectivity requirement.

The Eulerian scalar quantity *a*, vector $\boldsymbol{\alpha}$ or 2nd-order tensor **A,** contrarily to the Lagrangian quantities**,** are objective if they transform according to the following rules

$$\begin{aligned} a^*(\mathbf{x},t^*) &= a(\mathbf{x},t) \\ \boldsymbol{\alpha}^*(\mathbf{x},t^*) &= \mathbf{Q}(t)\cdot\boldsymbol{\alpha}(\mathbf{x},t) \\ \mathbf{A}^*(\mathbf{x},t^*) &= \mathbf{Q}(t)\cdot\mathbf{A}(\mathbf{x},t)\cdot\mathbf{Q}(t)^{\mathrm{T}}. \end{aligned} \tag{17}$$

The last relation clearly shows that the transformation of the Eulerian quantities is dependent of the rotation tensor **Q** and accordingly of the change of frame.

The material time derivative of an objective Eulerian 2nd-order tensor changes as

$$\dot{\mathbf{A}}^{*} = \frac{\mathrm{d}}{\mathrm{d}t}(\mathbf{Q}\cdot\mathbf{A}\cdot\mathbf{Q}^{\mathrm{T}}) = \dot{\mathbf{Q}}\cdot\mathbf{A}\cdot\mathbf{Q}^{\mathrm{T}} + \mathbf{Q}\cdot\dot{\mathbf{A}}\cdot\mathbf{Q}^{\mathrm{T}} + \mathbf{Q}\cdot\mathbf{A}\cdot\dot{\mathbf{Q}}^{\mathrm{T}} \neq \mathbf{Q}\cdot\dot{\mathbf{A}}\cdot\mathbf{Q}^{\mathrm{T}}. \tag{18}$$

The last relation shows that the material time derivative of an objective 2nd-order tensor does not obey the transformation rule $(17)_3$, and, therefore, it can be concluded that *the material time derivative in the Eulerian description is not an objective quantity*. Therefore, instead of the material time derivative an *objective time derivative* has to be used in order to preserve the objectivity requirement in the Eulerian description. Then, the following relation holds

$$\dot{\mathbf{A}}^{*} = \mathbf{Q}\cdot\overset{\diamond}{\mathbf{A}}\cdot\mathbf{Q}^{\mathrm{T}}, \tag{19}$$

where $\overset{\diamond}{\mathbf{A}}$ is the objective time derivative of the objective Eulerian quantity **A**.

3.1. Corotational and convective frame

One of the observers, *O*, can be detected at the fixed point of space **o**, while the second, observer O^{*}, is located on the moving body at point $\mathbf{o}^{*}$ and it moves and rotates together with the deformable body (see Fig. 2). The point **o** is the origin of a fixed *background frame*, while $\mathbf{o}^{*}$ is the origin of a so-called *co-deforming frame*. In such a way, relation (13) shows the transformation between the background and the co-deforming frame. That means that the pair (**x**, *t*) represents the point in the Galilean space-time, occupied by the particle P, observed by *O* from the background frame, while the pair ($\mathbf{x}^{*}$, *t*) represents the *same* point in the space observed by O^{*} from the transformed moving frame. It will be assumed that both observers record the position of the particle at the same time; thus the time difference *a* vanishes.

From relations (13) and (14) the transformation between the frames can be defined as

$$\mathbf{x}^{*} = \mathbf{K}(t)\cdot\mathbf{x} + \mathbf{c}(t) \qquad \text{with} \qquad t^{*} = t, \tag{20}$$

where the time dependent tensor **K** is not the proper orthogonal but a general asymmetric 2nd-order tensor determined by the following 1st-order differential system with a prescribed initial value

$$\dot{\mathbf{K}} = \boldsymbol{\Psi}\cdot\mathbf{K}, \qquad \mathbf{K}|_{t=0} = \mathbf{1}. \tag{21}$$

In the previous relation **1** is the unit 2nd-order tensor while $\boldsymbol{\Psi}$ is the asymmetric 2nd-order tensor given by

$$\boldsymbol{\Psi} = \boldsymbol{\Omega} + \boldsymbol{\Gamma}, \tag{22}$$

where $\boldsymbol{\Omega}$ is the antisymmetric part and $\boldsymbol{\Gamma}$ is the symmetric part of $\boldsymbol{\Psi}$. The skew-symmetric tensor $\boldsymbol{\Omega}$ is called the *spin*.

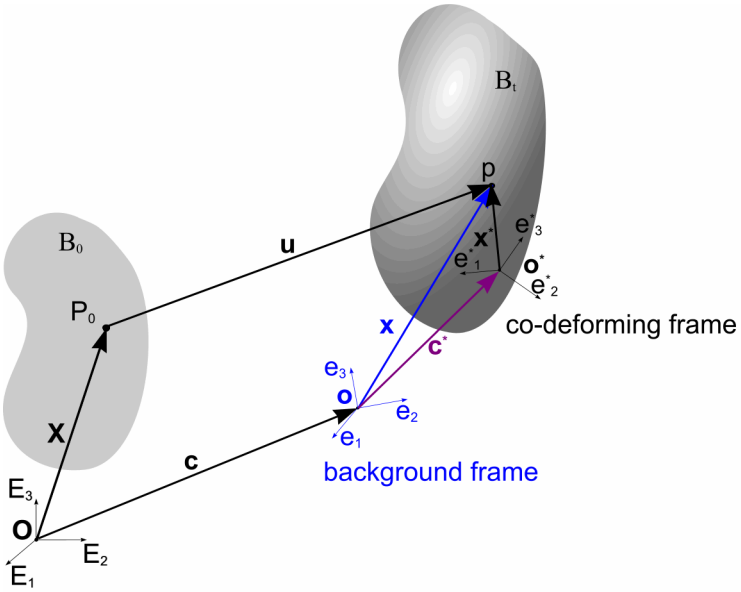

Fig. 2 Background and co-deforming frame

Transformation of an objective Eulerian tensorial quantity **A**, defined in the background frame, to $\mathbf{A}^*$ in the co-deforming frame can be determined by the transformation rule

$$\mathbf{A}^* = \mathbf{K} \cdot \mathbf{A} \cdot \mathbf{K}^{\mathrm{T}}. \tag{23}$$

Accordingly, the material time derivative of the transformed quantity $\mathbf{A}^*$ can be presented as

$$\dot{\mathbf{A}}^* = \frac{\mathrm{d}}{\mathrm{d}t}(\mathbf{K} \cdot \mathbf{A} \cdot \mathbf{K}^{\mathrm{T}}) = \dot{\mathbf{K}} \cdot \mathbf{A} \cdot \mathbf{K}^{\mathrm{T}} + \mathbf{K} \cdot \dot{\mathbf{A}} \cdot \mathbf{K}^{\mathrm{T}} + \mathbf{K} \cdot \mathbf{A} \cdot \dot{\mathbf{K}}^{\mathrm{T}} = \mathbf{K} \cdot \overset{\diamond}{\mathbf{A}} \cdot \mathbf{K}^{\mathrm{T}}, \tag{24}$$

where the objective time derivative, introduced in the previous Section, is determined by the tensor $\boldsymbol{\Psi}$ as

$$\overset{\diamond}{\mathbf{A}} = \dot{\mathbf{A}} + \mathbf{A} \cdot \boldsymbol{\Psi} + \boldsymbol{\Psi}^{\mathrm{T}} \cdot \mathbf{A}. \tag{25}$$

The kinematical property of relation (24) can be understood in such a way that the material time derivative of the counter part of the Eulerian quantity **A** in the co-deforming frame is the co-deforming counter part of the objective time derivative of the same quantity **A** in the background frame.

The objective rates of the symmetric Eulerian 2nd-order field have been so far given in a general form. Since the objective rates play an essential role in modelling of various material behaviours in the Eulerian description, the type of the objective rate should be carefully chosen. Depending on the choice of the tensor $\boldsymbol{\Psi}$ the objective rates can be generally classified in two categories of *corotational* and *non-corotational objective rates* (cf. Bruhns et al., 2004).

Every time the symmetric part of $\boldsymbol{\Psi}$, given by relation (22), vanishes, i.e. $\boldsymbol{\Psi}$ becomes equal to the spin $\boldsymbol{\Omega}$, the frame determined by Eqs. (20) and (21) is a *spinning* or *corotating frame* and $\mathbf{K}$ is equal to the rotation tensor. Otherwise, $\boldsymbol{\Psi}$ determines a *convective frame*. While the former experiences only constant rotation the latter can deform and rotate continuously during the deformation process. As for the convective frame, the coordinate system in $\mathbf{o}^*$ is no longer a Cartesian coordinate system and when it undergoes the change of frame, a physical or kinematical quantity can lose some important features. For example, the eigenvalues of the quantity of interest can be modified during the process of deformation. If we want to preserve the physical or kinematical features of a physical or a kinematical tensor, the tensor $\boldsymbol{\Psi}$ *must be* a skew-symmetric tensor, which means that $\boldsymbol{\Psi} = \boldsymbol{\Omega}$. That leads to $\mathbf{K} = \mathbf{Q}$, i.e. $\mathbf{K}$ is the proper orthogonal rotation tensor. For details see Bruhns et al. (2004) and Xiao et al. (2005).

Integration of (24) leads to the *generalised objective time integration* of the objective rate

$$\mathbf{A} = \mathbf{K}^{-1} \cdot \int_t \mathbf{K} \cdot \overset{\diamond}{\mathbf{A}} \cdot \mathbf{K}^{\mathrm{T}} \mathrm{d}t \cdot \mathbf{K}^{-\mathrm{T}}, \tag{26}$$

and it is applied in the co-deforming frame. This relation is found to be useful for the numerical implementation of the objective time derivatives in the constitutive relations of elastoplasticity.

3.2. Non-corotational rates

The objective non-corotational rate of the objective Eulerian quantity can be generally defined as

$$\overset{\triangledown}{\mathbf{A}} = \dot{\mathbf{A}} + \mathbf{A} \cdot \boldsymbol{\Psi} + \boldsymbol{\Psi}^{\mathrm{T}} \cdot \mathbf{A}. \tag{27}$$

With the specific choice of $\boldsymbol{\Psi}$ as

$$\boldsymbol{\Psi} = \mathbf{W} + m\mathbf{D} + c\,\mathrm{tr}(\mathbf{D})\mathbf{1}, \tag{28}$$

a broad class of objective non-corotational rates can be defined from (27):

$$\overset{\triangledown}{\mathbf{A}} = \dot{\mathbf{A}} + \mathbf{A} \cdot (\mathbf{W} + m\mathbf{D} + c\,\mathrm{tr}(\mathbf{D})\mathbf{1}) + (\mathbf{W} + m\mathbf{D} + c\,\mathrm{tr}(\mathbf{D})\mathbf{1})^{\mathrm{T}} \cdot \mathbf{A}, \tag{29}$$

where m and c are real numbers. For certain values of m and c in the last relation, well known rates can be obtained:
the (upper) Oldroyd rate

$$\overset{\triangledown\,\mathrm{Ol}}{\mathbf{A}} = \dot{\mathbf{A}} - \mathbf{L} \cdot \mathbf{A} - \mathbf{A} \cdot \mathbf{L}^{\mathrm{T}} \quad \text{for} \quad m = -1 \text{ and } c = 0, \tag{30}$$

the Cotter-Rivlin rate

$$\overset{\triangledown\,\mathrm{CR}}{\mathbf{A}} = \dot{\mathbf{A}} + \mathbf{L}^{\mathrm{T}} \cdot \mathbf{A} + \mathbf{A} \cdot \mathbf{L} \quad \text{for} \quad m = 1 \text{ and } c = 0, \tag{31}$$

the Truesdell rate

$$\overset{\triangledown\,\mathrm{Tr}}{\mathbf{A}} = \dot{\mathbf{A}} - \mathbf{L} \cdot \mathbf{A} - \mathbf{A} \cdot \mathbf{L}^{\mathrm{T}} + \mathrm{tr}(\mathbf{D})\mathbf{A} \quad \text{for} \quad m = -1 \text{ and } c = 0.5. \tag{32}$$

3.3. Corotational rates

The symmetric part of tensor $\boldsymbol{\Psi}$ may vanish, as it was pointed out in Section 3.1. It turns out that $\boldsymbol{\Psi} = \boldsymbol{\Omega}$. The rotating, or co-deforming, frame is then determined by the skew-symmetric 2nd-order Eulerian tensor $\mathbf{Q}$ instead of the general asymmetric 2nd-order tensor $\mathbf{K}$, introduced earlier. The skew-symmetric spin tensor $\boldsymbol{\Omega}$, determining the rotating frame, is defined by:

$$\boldsymbol{\Omega} = \dot{\mathbf{Q}}^{\mathrm{T}} \cdot \mathbf{Q} = -\mathbf{Q}^{\mathrm{T}} \cdot \dot{\mathbf{Q}} = -\boldsymbol{\Omega}^{\mathrm{T}}. \tag{33}$$

The rotating frame becomes the *corotating frame* and the general objective time derivative $\overset{\lozenge}{\mathbf{A}}$ becomes the corotational rate $\overset{\circ}{\mathbf{A}}$, defined as

$$\overset{\circ}{\mathbf{A}} = \dot{\mathbf{A}} + \mathbf{A} \cdot \boldsymbol{\Omega} - \boldsymbol{\Omega} \cdot \mathbf{A}. \tag{34}$$

The following relation describes transformation of the objective Eulerian 2nd-order tensor quantity from the background to the corotating frame

$$\mathbf{A}^{*} = \mathbf{Q} \cdot \mathbf{A} \cdot \mathbf{Q}^{\mathrm{T}}, \tag{35}$$

while the material time derivative of the transformed quantity $\mathbf{A}^{*}$ in the corotating frame turns into

$$\dot{\mathbf{A}}^{*} = \mathbf{Q} \cdot \overset{\circ}{\mathbf{A}} \cdot \mathbf{Q}^{\mathrm{T}}. \tag{36}$$

One comes to the conclusion that the corotational rate of the objective Eulerian tensor $\mathbf{A}$ corresponds to the material rate of $\mathbf{A}$ in the corotating frame (cf. Xiao et al., 1998a). The last relation does not hold for tensors that are not objective.

Different corotational rates can be obtained for different choices of the spin tensor $\mathbf{Q}$. Although the chosen spin relation (36) satisfies transformation rule $(17)_3$, the corresponding corotational rate does not need to be an objective quantity. That means that the most important demand of objectivity of the corotational rate (cf. Truesdell et al., 2004) may be violated. Bearing in mind the fact that the objective corotational rate has the crucial importance in a material behaviour description, especially of an inelastic behaviour, the significance of the proper choice of the objective rate and their defining spin tensors is again pointed out.

For different choices of a single antisymmetric real function, named a *spin function*, Xiao et al. in (1998a) and (1998b) define a general class of spin tensors and corresponding general class of objective corotational rates. In the spin function $h(z)$, z represents the ratio between n distinct eigenvalues of the left and right Cauchy-Green tensors, where $n \leq 3$ (for detailed definition of the spin function see Xiao el al. 1998b).

The choice of the spin function as

$$h(z) = h^{\mathrm{J}}(z) = 0 \tag{37}$$

yields the spin tensor

$$\boldsymbol{\Omega}^{\mathrm{J}} = \mathbf{W}, \tag{38}$$

which, implemented in (34), defines the well-known *Zaremba-Jaumann* rate

$$\overset{\circ}{\mathbf{A}}{}^{\mathrm{J}} = \dot{\mathbf{A}} + \mathbf{A}\cdot\mathbf{W} - \mathbf{W}\cdot\mathbf{A}. \tag{39}$$

The Jaumann rate was the first introduced in the rate formulation of inelastic material behaviour. Since it can be easily implemented and numerical calculations are not so time-consuming it has been widely accepted and used. It is, as well, incorporated in several commercial finite element codes. Implementation of the Jaumann rate in constitutive theories gives appropriate results for the case of small deformations. However, this rate may not be an adequate choice for the case of finite deformations (Lehmann, 1972; Dienes, 1979; Simo & Pister, 1984; Khan & Huang, 1995; Bažant & Vorel, 2014). It has been shown that for the pure elastic deformation constitutive model based on the Jaumann rate gives an unstable response at simple shear, known as *shear oscillatory phenomenon.*

In order to overcome the deficiencies encountered with the Jaumann rate implementation in finite deformation formulation, numerous alternative corotational rates have been developed (cf. Xiao et al., 2000).

One of them is the *polar* or *Green-Naghdi* rate. If the spin function takes the form

$$h(z) = h^{\mathrm{R}}(z) = \frac{1-\sqrt{z}}{1+\sqrt{z}}, \tag{40}$$

the *polar spin* $\boldsymbol{\Omega}^{\mathrm{R}}$ will be obtained

$$\boldsymbol{\Omega}^{\mathrm{R}} = \dot{\mathbf{R}}\cdot\mathbf{R}^{\mathrm{T}}, \tag{41}$$

which, substituted in (34), defines the *Green-Naghdi rate*

$$\overset{\circ}{\mathbf{A}}{}^{\mathrm{GN}} = \dot{\mathbf{A}} + \mathbf{A}\cdot\boldsymbol{\Omega}^{\mathrm{R}} - \boldsymbol{\Omega}^{\mathrm{R}}\cdot\mathbf{A}. \tag{42}$$

Even though the introduction of the aforementioned rates solves the problem of the unrealistic harmonic stress responses obtained for the Jaumann rate, Simo & Pister (1984) have showed that for the case of pure elastic deformation, where the recoverable elastic-like behaviour was expected, none of the constitutive relations, based on formerly used objective rates, can fulfil Bernstein's integrability condition to give an elastic relation, i.e. path-dependent and dissipative processes are detected for all rates.

Recently the new spin function, so-called *logarithmic spin function,* has been introduced as

$$h(z) = h^{\mathrm{R}}(z) = \frac{1+\sqrt{z}}{1-\sqrt{z}} + \frac{2}{\ln(z)}. \tag{43}$$

It leads to the *logarithmic spin tensor*

$$\boldsymbol{\Omega}^{\mathrm{Log}} = \dot{\mathbf{R}}^{\mathrm{Log}}\cdot(\mathbf{R}^{\mathrm{Log}})^{\mathrm{T}}, \tag{44}$$

whose implementation in (34) gives the *logarithmic corotational rate* or *Log-rate* of $\mathbf{A}$

$$\overset{\circ}{\mathbf{A}}{}^{\mathrm{Log}} = \dot{\mathbf{A}} + \mathbf{A}\cdot\boldsymbol{\Omega}^{\mathrm{Log}} - \boldsymbol{\Omega}^{\mathrm{Log}}\cdot\mathbf{A}. \tag{45}$$

The previously defined symmetric stretching tensor **D** is a natural characterization of the rate of change of the local deformation state, thus we want to present it as a direct flux of a strain measure. What is more, we are interested in finding out which Eulerian strain measure **e** and which corotational time derivative satisfy the following relation

$$\overset{\circ}{\mathbf{e}} = \mathbf{e} + \mathbf{e}\cdot\boldsymbol{\Omega} - \boldsymbol{\Omega}\cdot\mathbf{e} = \mathbf{D}, \tag{46}$$

where with **e** a general Eulerian strain measure has been designated.

In Xiao et al. (1997) and (1998a) the authors have proved that among all strain measures and among all corotational rates the spatial logarithmic strain measure **h** and the logarithmic rate are the unique choice that satisfies the above demand, i.e.

$$\overset{\circ}{\mathbf{h}}{}^{\mathrm{Log}} = \dot{\mathbf{h}} + \mathbf{h}\cdot\boldsymbol{\Omega}^{\mathrm{Log}} - \boldsymbol{\Omega}^{\mathrm{Log}}\cdot\mathbf{h} = \mathbf{D}. \tag{47}$$

In (44) it can be recognized that the logarithmic spin is determined by the proper orthogonal *logarithmic rotation* tensor $\mathbf{R}^{\mathrm{Log}}$ that is defined by the linear tensorial differential equation

$$\dot{\mathbf{R}}^{\mathrm{Log}} = -\mathbf{R}^{\mathrm{Log}}\cdot\boldsymbol{\Omega}^{\mathrm{Log}}, \qquad \mathbf{R}^{\mathrm{Log}}|_{t=0} = \mathbf{1}. \tag{48}$$

The corotating frame obtained from the background frame by the rotation $\mathbf{R}^{\mathrm{Log}}$ is named a *logarithmic corotating frame*. The material time derivative of an objective Eulerian quantity **A**, in the logarithmic corotating frame, is exactly the logarithmic rate of the same quantity, i.e.

$$\frac{\mathrm{d}}{\mathrm{d}t}(\mathbf{R}^{\mathrm{Log}}\cdot\mathbf{A}\cdot(\mathbf{R}^{\mathrm{Log}})^{\mathrm{T}}) = \mathbf{R}^{\mathrm{Log}}\cdot\overset{\circ}{\mathbf{A}}{}^{\mathrm{Log}}\cdot(\mathbf{R}^{\mathrm{Log}})^{\mathrm{T}}. \tag{49}$$

Applying the last assertion to **h** and the stretching **D**, the following relation will be obtained

$$\frac{\mathrm{d}}{\mathrm{d}t}(\mathbf{R}^{\mathrm{Log}}\cdot\mathbf{h}\cdot(\mathbf{R}^{\mathrm{Log}})^{\mathrm{T}}) = \mathbf{R}^{\mathrm{Log}}\cdot\mathbf{D}\cdot(\mathbf{R}^{\mathrm{Log}})^{\mathrm{T}}, \tag{50}$$

that is, *in the logarithmic corotating frame stretching* **D** *is a true time rate of* **h**. Integration of (49) leads to the corotational integration

$$\mathbf{A} = (\mathbf{R}^{\mathrm{Log}})^{\mathrm{T}}\cdot\int_t \mathbf{R}^{\mathrm{Log}}\cdot\overset{\circ}{\mathbf{A}}{}^{\mathrm{Log}}\cdot(\mathbf{R}^{\mathrm{Log}})^{\mathrm{T}}\,\mathrm{d}t\ \cdot\mathbf{R}^{\mathrm{Log}}, \tag{51}$$

and it is performed in the logarithmic corotating frame. The last relation is a particular form of the generalised objective time integration given by (26). This relation will be of tremendous importance in numerical calculations.

Following the theoretical postulates given in Bruhns et al. (1999) in Trajković-Milenković (2016) it is numerically proved that the implementation of the Log-rate in the constitutive relations of finite elastoplasticity successfully solved the aforementioned problems observed with all other corotational and non-corotational rates. On several benchmark examples it has been proved that the material behaviour prediction based on

the logarithmic rate is stable and completely in accordance with experimental tests, in opposition to actually popular objective rates.

Unlike to the Jaumann rate and the Green-Naghdi rate, which are already incorporated in the commercial finite element codes through the built-in subroutines and their application is completely optimized, the logarithmic rate has to be implemented in the software using the special user subroutine which allows user to define his own material model. This kind of subroutine offers the user a lot of possibilities but it will be called in each time step and for each integration point and, therefore, the numerical calculation can be time-consuming, which could be from the numerical point of view the only disadvantage of using the logarithmic rate.

4. Decomposition of Finite Deformation

Elastoplasticity represents a combination of two completely different types of material behaviour, namely elasticity and plasticity. A great number of the modern theories of elastoplasticity are confined to the description of a rate-independent behaviour of elastoplastic materials, i.e. viscous effects are ignored. Before 1960, most contributions in the rate-independent elastoplasticity theory were dedicated to the field of small deformations. Some of the basic ideas of the theories for small deformations can be fully or partially applied for the case where finite deformations are occurring (cf. Naghdi, 1990, and Xiao et al., 2006).

One of those ideas is the composite structure of elastoplasticity. It means that a total deformation, or total deformation rate, of elastoplastic material can be decomposed into its *elastic*, or reversible, and *plastic*, or irreversible, part and then a separate constitutive relation for each part has to be established. Taking into consideration the incremental essence of elastoplastic behaviour of material, we are more interested in the strain rate than the strain itself. The rate of infinitesimal strain $\boldsymbol{\varepsilon}$ can be additively decomposed in the following form:

$$\dot{\boldsymbol{\varepsilon}} = \dot{\boldsymbol{\varepsilon}}^e + \dot{\boldsymbol{\varepsilon}}^p. \tag{52}$$

Even though the researchers agree with the aforementioned statement for the case of small deformations, the decomposition of finite deformation into its reversible and irreversible part causes the disagreement within the members of the plasticity community dividing them into several various schools of plasticity.

The first belongs to the group which follows the idea that the classical Prandtl and Reuss formulation (52) can be extended to the finite deformation description using the *additive decomposition of the natural deformation rate* to its elastic and plastic part, i.e.

$$\mathbf{D} = \mathbf{D}^e + \mathbf{D}^p. \tag{53}$$

It has been thought that the above decomposition of the stretching can hold only for certain restrictive cases of deformation and materials, such as small elastic and finite plastic deformations in metals (Simo & Hughes, 1998). Such an opinion is coming from the fact that in order to fulfil the objectivity requirement the rate type model must involve the objective rate, instead of the material time derivative, and the use of the Jaumann and some other well-known objective rates in the context of decomposition (53) produce

irregular results, such as the shear oscillation phenomenon and the residual stresses occurrence for elastic closed strain path as well as non-integrability problem (see Trajković-Milenković, 2016, for details and relevant references). Thus, this decomposition has been rejected for a long time as inappropriate for a general purpose. This held true until recently when an implementation of the newly discovered logarithmic rate solved the existing problems (Xiao et al., 1997b, and Bruhns et al., 1999) which has been also numerically proved in Trajković-Milenković (2016).

The second approach is the most common in the finite deformation theories; that is the *multiplicative decomposition of the deformation gradient*, given by

$$\mathbf{F} = \mathbf{F}^e \cdot \mathbf{F}^p, \tag{54}$$

where $\mathbf{F}^e$ and $\mathbf{F}^p$ represent elastic and plastic part of the deformation gradient, respectively.

An *intermediate* stress-free configuration achieved by an elastic unloading from the current configuration is introduced by this formulation. Therefore, while the mapping from the reference to the current configuration is described by the deformation gradient $\mathbf{F}$, the mapping from the reference to the intermediate configuration can be described by its plastic part $\mathbf{F}^p$ and from the intermediate to the current configuration by its elastic part $\mathbf{F}^e$. An arbitrary rigid body rotation $\mathbf{Q}$ superimposed on the intermediate configuration has no influence on the decomposition (54), thus the determination of the elastic and plastic part of deformation gradient is not unique, i.e.

$$\mathbf{F} = \mathbf{F}^e \cdot \mathbf{F}^p = \bar{\mathbf{F}}^e \cdot \bar{\mathbf{F}}^p, \qquad \text{with} \qquad \bar{\mathbf{F}}^e = \mathbf{F}^e \cdot \mathbf{Q} \qquad \text{and} \qquad \bar{\mathbf{F}}^p = \mathbf{Q}^{\mathrm{T}} \cdot \mathbf{F}^p. \tag{55}$$

In addition, according to Naghdi (1990), multiplicative decomposition (54) has several shortcomings. The first "lies in the fact that the stress at a point in an elastic-plastic material can be reduced to zero without changing plastic strain only if the origin in stress space remains in the region enclosed by the yield surface." This is usually not the case, except of some special cases such as isotropic hardening. However, it is observed, that the yield surface may move in the stress space during deformation. Furthermore, "even if the stress can be reduced to zero at each material point, the resulting configuration will not, in general, form a configuration for the body as a whole, but only a collection of local configurations."

A further physically admissible decomposition is established by Green & Naghdi (1965) postulating the *additive decomposition of the Green strain*, the Lagrangian strain measure. The authors introduce a strain-like variable of Lagrangian type, called plastic strain $\mathbf{E}^p$, as a primitive variable. The total Green strain is decomposed using the form

$$\mathbf{E} = \mathbf{E}^e + \mathbf{E}^p, \tag{56}$$

where only for the case of small deformations $\mathbf{E}^e$ can be denoted as elastic strain. Having well understood the limited applicability of the additive separation of $\mathbf{E}$ for large deformations, they do not interpret the difference $\mathbf{E} - \mathbf{E}^p$ as an elastic strain or part, but as an alternative convenient variable used for well motivated purposes.

5. CONCLUSION

Since the introduction of the logarithmic rate has successfully eliminated the aforestated shortcomings of the proposed decomposition of finite deformation, our recommendation would be the implementation of the self-consistent Eulerian finite elastoplasticity theory, based on the logarithmic rate and the additive decomposition of the natural deformation rate. As well, it will be the base of our future work. The implementation of the proposed theory into commercial finite element codes will be used for numerical calculations of homogeneous and non-homogeneous problems in order to show the advantage of the suggested approach. The obtained results will later be published elsewhere.

REFERENCES

1. Malvern, L. E., 1969, *Introduction to the mechanics of a continuous medium*, Prentice-Hall, Inc., Englewood Cliffs, New Jersey, 713 p.
2. Mićunović, M., 1990, *Primenjena mehanika kontinuuma*, Naučna knjiga, Beograd, 332 p.
3. Ogden, R. W., 1984, *Non-linear elastic deformations*, Dover Publications, Inc. Mineola, New York, 532 p.
4. Xiao, H., Bruhns, O.T. & Meyers, A., 1997, *Hypo-elasticity model based upon the logarithmic stress rate*, in: J. Elasticity, 47, pp. 51-68.
5. Xiao, H., Bruhns, O.T. & Meyers, A., 1998a, *On objective corotational rates and their defining spin tensors*, in: Int. J. Solids Structures, 35(30), pp. 4001-4014.
6. Xiao, H., Bruhns, O.T. & Meyers, A., 1998b, *Strain rates and material spins*, in: J. Elasticity, 52, pp. 1-41.
7. Bruhns, O.T., Meyers, A. & Xiao, H., 2004, *On non-corotational rates of Oldroyd's type and relevant issues in rate constitutive formulations*, in: Proc. Roy. Soc. A, 460, pp. 909-928.
8. Xiao, H., Bruhns, O.T. & Meyers, A., 2005, *Objective stress rates, path-dependence properties and non-integrability problems*, in: Acta Mech., 176, pp. 135-151.
9. Lehmann, T., 1972, *Anisotrope plastische Formänderungen*, in: Romanian J. Techn. Sci. Appl. Mechanics, 17, pp. 1077-1086.
10. Trajković-Milenković, M., 2016, *Numerical implementation of an Eulerian description of finite elastoplasticity*, PhD Thesis, Ruhr University Bochum, Germany, 125 p.
11. Dienes, J. K., 1979, *On the analysis of rotation and stress rate in deforming*, in: Acta Mech., 32, pp. 217-232.
12. Simo, J. C. & Pister, K. S., 1984, *Remarks on rate constitutive equations for finite deformation problems: computational implications*, in: Comput. Meths. Appl. Mech. Engrg., 46, pp. 201-215.
13. Khan, A. S. & Huang, S., 1995, *Continuum theory of plasticity*, John Wiley& Sons, Inc., New York, 421p.
14. Bažant, Z. & Vorel, J., 2014, *Energy-Conservation Error Due to Use of Green-Naghdi Objective Stress Rate in Commercial Finite-Element Codes and Its Compensation*, in: ASME J. Appl. Mech., 81(2).
15. Xiao, H., Bruhns, O. T. & Meyers, A., 2000, *The choice of objective rates in finite elastoplasticity: general results on the uniqueness of the logarithmic rate*, in: P. Roy. Soc. A, 456, pp. 1865-1882.
16. Naghdi, P. M., 1990, *A critical review of the state of finite elasoplasticity*, in: Z. Angew. Math. Phys., 41, pp. 315-394.
17. Xiao, H., Bruhns, O. T. & Meyers, A., 2006, *Elastoplasticity beyond small deformations*, in: Acta Mech., 182, pp. 31-111.
18. Simo, J. C. & Hughes, T. J. R., 1998, *Computational inelasticity*, Springer-Verlag New York, Inc., 392 p.
19. Bruhns, O. T., Xiao, H. & Meyers, A., 1999, *Self-consistent Eulerian rate type elastoplasticity models based upon the logarithmic stress rate*, in: Int. J. Plasticity, 15, pp. 479-520.
20. Green, A. E. & Naghdi, P. M., 1965, *A general theory of an elasto-plastic continuum*, in: Arch. Ration. Mech. An., 18, pp. 251-281.
21. Truesdell, C., Noll, W. & Antman, S., 2004, *The Non-Linear Field Theories of Mechanics*, Volume 3 of The non-linear field theories of mechanics, Springer.
22. Bernstein, B., 1960, *Hypoelasticity and elasticity*, in Arch. Rat. Mech. Anal., 6, pp. 90-104.
23. Zaremba, S., 1903, *Sur une forme perfectionée de la théorie de la relaxation*, in Bull. Intern. Acad. Sci. Cracovie, pp. 594-614.

ALTERNATIVNI PRISTUP KONAČNIM DEFORMACIJAMA

U savremenoj formulaciji elastoplastičnog ponašanja materijala konstitutivne relacije su uglavnom date u formi izvoda, tj. predstavljaju vezu između izvoda napona i izvoda deformacije kako u formulaciji plastičnog tako i elastičnog dela deformacije. Usvojene konstitutivne relacije moraju ostati nezavisne u odnosu na promenu koordinatnog sistema, tj. da ostanu objektivne. Dok je preduslov objektivnosti u materijalnoj deskripciji automatski zadovoljen, u Ojlerovoj deskripciji, posebno u slučaju velikih deformacija, objektivnost može biti narušena čak i za objektivne promenljive. Stoga, umesto materijalnog izvoda, u konstitutivnim relacijama datim u Ojlerovoj deskripciji moraju se implementirati objektivni izvodi. Ovaj rad doprinosi pojašnjenju važnosti implementacije objektivnih izvoda u konstitutivnim relacijama konačne elastoplastičnosti i daje pregled danas najčešće korišćenih objektivnih izvoda, njihovih prednosti i nedostataka, kao i izuzetnih karakteristika nedavno uvedenog logaritamskog izvoda.

Ključne reči: *konačne deformacije, objektivni izvodi, logaritamski izvod, elastoplastičnost, dekompozicija velikih deformacija*

FACTA UNIVERSITATIS
Series: **Architecture and Civil Engineering** Vol. 16, No 1, 2018, pp. 81-91
https://doi.org/10.2298/FUACE170407007S

ALGORITHM FOR DETERMINATION OF S-N CURVES OF THE STRUCTURAL ELEMENTS SUBJECTED TO CYCLIC LOADING

UDC 624.042

Nenad Stojković[1], Dragoslav Stojić[2], Srđan Živković[2], Gordana Topličić-Ćurčić[2]

[1]College of Applied Technical Sciences Niš, Serbia
[2]Faculty of Civil Engineering and Architecture, University of Niš, Serbia

Abstract. *Fatigue life prediction of structural elements subjected to cyclic loading is usually performed using S-N curves, obtained from the experimental data from fatigue tests. However, in some cases the samples do not exhibit failure, due to reaching the predetermined number of cycles, failure of a non-relevant segment or terminating the test because of some other reason. These samples are usually referred to as runouts, and the data obtained from them could be used for determination of S-N curves as well. In this paper, the algorithm based on Maximum Likelihood method is proposed for the determination of S-N curves from experimental data that contain runouts. Following the algorithm, a MATLAB code was written and the verification was performed using the experimental data from the literature. The results showed that it could be successfully used for taking into account the runouts in the process of determination of S-N model parameters. It was concluded that the inclusion of runouts could significantly influence the predicted fatigue life, especially at the lower stress levels.*

Key words: *Fatigue, S-N curve, Algorithm, Maximum Likelihood method*.

1. INTRODUCTION

Most of the engineering structures in practice are subjected to changing load. This type of loading is usually represented as a cyclic loading, defined by the load amplitude, mean value and frequency. It causes the structures to undergo fatigue, which is defined as progressive and localized structural damage that occurs when a material is subjected to cyclic loading. The fatigue failure is usually different from the failures of structures subjected to static loading. They occur after certain time, i.e. the number of cycles, under loads lower than the ultimate load obtained from the static tests (sometimes significantly lower).

Received April 7, 2017 / Accepted September 21, 2017
Corresponding author: Nenad Stojković
College of Applied Technical Sciences Niš, Serbia
E-mail: svnenad@yahoo.com

The prediction of number of cycles to failure, referred to as fatigue life, is divided into two categories: high-cycle fatigue (HCF) and low-cycle fatigue (LCF). The difference between these two categories is that the first is associated with purely elastic behavior while the second involves plastic behavior. Because of this, the methods for fatigue life prediction associated with HCF and LCF are known as stress-life and strain-life, respectively. In order to select appropriate method for prediction of fatigue life it is very important to define the limit between these two fields. Although it is considered in the case of metals that the structures are subjected to HCF load when failures occur after more than 10^4 cycles, a clear limit could not be strictly defined. The difficulties in distinction between HCF and LCF are elaborated in [1].

Fatigue life prediction of structural elements is based on the experimental data obtained from the repeated fatigue tests. Identical specimens are subjected to cyclic loading at different stress levels and constant load ratio R, i.e. the ratio between the minimum and the maximum load in the cycle. The endured number of cycles at the moment of failure is recorded. If the specimen at a certain stress level does not reach the failure until predetermined number of cycles (usually 10^6-10^7), it is considered to have infinite fatigue life. On the other hand, sometimes the tests could be terminated due to some other reasons, such as failure of secondary element that is not of interest, technical issues etc. These specimens are referred to as "runouts". They are usually censored and in such cases fatigue life prediction is based solely on the failed samples data. The discrete experimental data are approximated by S-N curves, often called Wöhler curves. These curves are mathematically represented by S-N models which contain parameters that need to be determined by fitting the equations to experimental data. There are several methods for determination of model parameters, such as regression analysis [2], maximum likelihood method [3], as well as some specific methods [4,5]. For obtaining the model parameters using regression analysis only the data from the failed samples could be used. Other methods could take into account runouts as well. However, besides the regression analysis, which is available in commercial software, other methods require high computational skills and complicated algorithms. In this paper the algorithm was developed for the determination parameters of S-N model using the maximum likelihood method, based on which a MATLAB code is written. It is verified using the experimental data from the literature. The results showed that it could be successfully used for taking into account the runouts in the process of determination of S-N model parameters.

2. DETERMINATION OF PARAMETERS OF S-N MODEL

S-N curves are the most widely used tool for fatigue life prediction of structures. Although the fatigue life is a dependent variable of S-N models, experimental data are usually given on the graphs where X axis is fatigue life, and Y axis is maximum stress or stress amplitude. Depending on the nature of experimental results, the relationship between stress level and fatigue life could be represented by normal or logarithmic scale. Linear dependence of logarithm of fatigue life and stress level is given by the following expression:

$$\log N = a + bS \,, \tag{1}$$

where N is the fatigue life, S is the stress level and *a* and *b* are parameters to be defined by fitting S-N model to the experimental data. If the data show linear dependence between logarithms of fatigue life and stress level, the S-N curve is represented with the following equation:

$$\log N = a + b \log S \,, \tag{2}$$

or, rewritten in the power law form:

$$N = cS^b \,, \tag{3}$$

where $c = 10^a$. S-N model given by the Equation (3) is known in the literature as Basquin's model [6].

2.1. Maximum Likelihood Method

General and, in most cases, satisfactory assumption of the statistical analysis of fatigue data is that fatigue lives could be represented by normal distribution. If only the data of failed specimens are available, it is simple to calculate the mean value of the fatigue life at a certain stress level. However, if the dataset contains runouts, it could not be analyzed using simple procedures. In such cases, maximum likelihood method is often utilized.

Maximum likelihood method is well known for a long time, and its wide use started in the early twenties of the 20th century. The basic principle of this method is that from the number of possible parameter values, the most likely value is the one that gives the highest probability of obtaining the observed results. The disadvantage of this method is that it requires relatively complicated calculations. For the purpose of simplifying the calculations, it is convenient to use logarithms of the probabilities ($\log p_i$) instead of the probabilities themselves (p_i).

Starting from the assumption of linear dependence of the logarithm of stress level and logarithm of fatigue life (Eq. 2 and 3), the probability of certain fatigue data could be calculated as a function of the variable *t*, given by the following expression:

$$t = \frac{x - \mu}{\sigma} \,, \tag{4}$$

where μ and σ are assumed to be mean and standard deviation values of the observed results $x = \log N$ or $\log S$. For the assumed parameters of S-N model, these values are simple to be determined. The most probable set of parameters is the one which maximizes the value of likelihood function that is equal to the sum of the probabilities of each observed experimental data [3]:

$$L(\theta) = \sum_{i=1}^{n} L(\theta)_i = \sum_{i=1}^{n} \log p_i \,, \tag{4}$$

where $L(\theta)$ is total likelihood of the assumed set of parameters θ, $L(\theta)_i$ is the contribution of each experimental data, and $n = n_f + n_r$ the total number of data which is equal to the sum of number of failed specimens and runouts.

There is the difference between the contributions to the likelihood of failed specimens and runouts. The explanation lies in the fact that the failed specimens are represented by the probability of failure occurrence at the observed number of cycles, given by the probability density function (Eq. 6), while the runouts are represented by the probability

that the specimen will survive more than observed endured number of cycles, which is given by the cumulative distribution function (Eq. 7).

$$p^{fail} = (2\pi)^{0,5} \cdot \exp(-t^2/2)dt \tag{6}$$

$$p^{runout} = \int_t^{\infty} (2\pi)^{0,5} \cdot \exp(-u^2/2)du \tag{7}$$

The likelihood contributions, expressed from the Eq. (6) and (7) are given by the following equations:

$$L(\theta)_i^{fail} = -t^2/2 - \log\sigma \tag{8}$$

$$L(\theta)_i^{runout} = \log_e\left[\int_t^{\infty} (2\pi)^{0,5} \cdot \exp(-u^2/2)du\right] \tag{9}$$

2.2. Algorithm for determination of the parameters of S-N curves

The first step in the process of determination of S-N curves is the selection of a mathematical model. In this paper, the model that represents linear dependence between logarithm of stress level and logarithm of fatigue life, most frequently given by Eq. (2) and (3) was used. By making simple mathematical modifications it could be rewritten in the following form:

$$N = N_d (S/S_d)^k, \tag{10}$$

where k is the slope of S-N curve, S_d is endurance limit and N_d is number of cycles for which the endurance limit was defined, which in this case is equal to 2 million cycles. The parameters from the Eq. (10) are illustrated in Fig. 1.

After the selection of appropriate mathematical model, initial values of model parameters k and S_d, as well as standard deviation σ, have to be assumed. Although the recommendation for the calculation of these initial values is given in [3], in this paper they are set to be equal to the values obtained by performing regression analysis using only the failed specimen data. For this, a separate subroutine was written according to the procedure given in [2]. In the next step, using the assumed parameters, the fatigue lives are being calculated for each stress level from experimental dataset. Calculated values represent the assumed mean values of the fatigue lives at each stress level (μ_i). After obtaining σ and μ_i, using Eq. (4-10), it is relatively simple to calculate the value of likelihood $L(\theta)$. The values of likelihood are being calculated for a set of values of parameters k and S_d, that are in the range of predetermined minimum and maximum values. These values are chosen to be on the distance of ±25% from the initial values of parameters. Thereafter, the values of parameters that correspond to the maximum value of likelihood are used to calculate a new set of likelihood values using a number of standard deviation values, defined in the same way as in the case of parameters k and S_d. The maximum of the new set of likelihood values, and corresponding parameters and standard deviation represent the results of the first iteration. In each subsequent iteration, the minimum and maximum values of model parameters and the standard deviation are taken to be equal to the values of the array elements that were distanced ±2 index positions from

the values that correspond to the output values of the previous iteration. The iterative procedure is terminated when the relative difference of the maximum likelihood values of two consecutive iterations is less than or equal to 0,1%. The algorithm of the described procedure is given in Fig. 2.

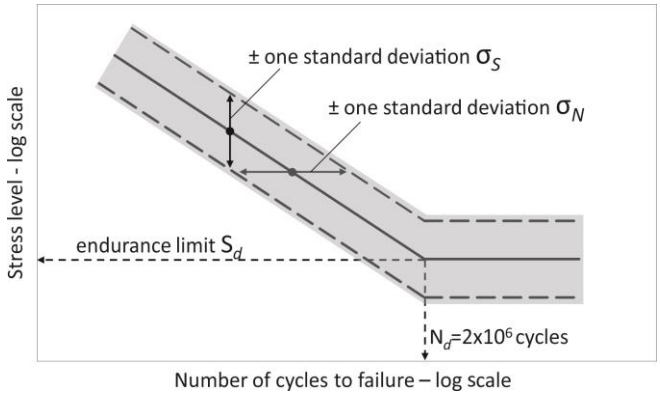

Fig. 1 Typical S-N curve given by Eq. (10) [3]

3. VERIFICATION AND VALIDATION OF THE PROPOSED ALGORITHM

As it was already pointed out, the aim of this paper was to develop an algorithm for the determination of the parameters of S-N model that could take into consideration both failed specimens and runouts. The functioning of the algorithm is verified by using the experimental data published in [7] (taken from [8]). The selected data represent the results of the experimental investigation of the fatigue life of the nickel based superalloy obtained by subjecting specimens to the cyclic load in the load controlled regime. The dataset consists of 22 failures and 4 runouts which is relatively large number of data for fatigue investigation. Thus, it is considered to be appropriate for the verification of the proposed algorithm. The results are shown in Table 1. In the case of runouts, i.e. the specimens 3,6,9 and 12, the results in the table represent the endured number of cycles. All other numbers of cycles represent the fatigue lives of corresponding specimens.

In order to verify the functioning of the MATLAB code, six sets of data were created by making some alterations of the original dataset. These alterations are summarized in Table 2. The first dataset, consisting only of failed specimens, was used to obtain S-N curve which will serve as the basis for alterations of the data. After analyzing the first set, four other sets were created by adding one data point, marked with diamonds in Fig. 3 and 4. The data points are added to the stress level of 80MPa, with the numbers of cycles that are equal to the predicted fatigue life of the first dataset, changed by 2σ, -1σ, $+1\sigma$ and $+2\sigma$ in cases 2, 3, 4 and 5, respectively. The values obtained in this way are shown in Table 3. The sixth set of data is equal to original experimental data.

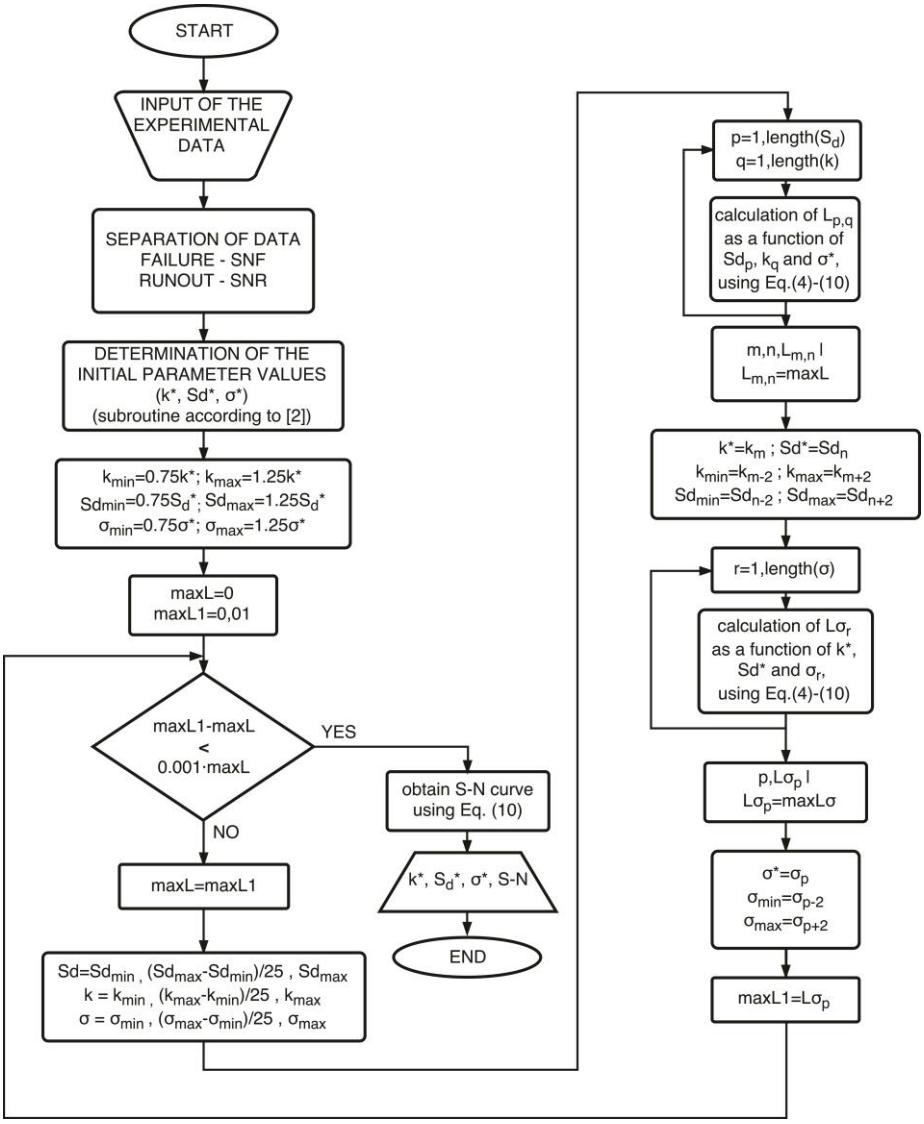

Fig. 2 Simplified algorithm for determination of the parameters of S-N model

Table 1 Fatigue test results from [7]

No.	S[MPa]	N [cyc.]	Status
1.	80.3	211629	failed
2.	80.6	200027	failed
3.	80.8	57923	runout
4.	84.3	155000	failed
5.	85.2	13949	failed
6.	85.6	112968	runout
7.	85.8	152680	failed
8.	86.4	156725	failed
9.	86.7	138114	runout
10.	87.2	56723	failed
11.	87.3	121075	failed
12.	89.7	122372	runout
13.	91.3	112002	failed
14.	99.8	43331	failed
15.	100.1	12076	failed
16.	100.5	13181	failed
17.	113.0	18067	failed
18.	114.8	21300	failed
19.	116.4	15616	failed
20.	118.0	13030	failed
21.	118.4	8489	failed
22.	118.6	12434	failed
23.	120.4	9750	failed
24.	142.5	11865	failed
25.	144.5	6705	failed
26.	145.9	5733	failed

Table 2 The analyzed datasets

Case	S[MPa]
1.	Only the data of failed specimens.
2.	The same as the first case with added data point at 80MPa and number of cycles equal to $N(1) - 2\sigma$
3.	The same as the first case with added data point at 80MPa and number of cycles equal to $N(1) - \sigma$
4.	The same as the first case with added data point at 80MPa and number of cycles equal to $N(1) + \sigma$
5.	The same as the first case with added data point at 80MPa and number of cycles equal to $N(1) + 2\sigma$
6.	Entire dataset given in Table 1.

Table 3 Calculated additional data points

Case.	S[MPa]	N [cyc.]
2.	80	32129
3.	80	63280
4.	80	245486
5.	80	483511

The parameters of S-N curves, obtained from datasets 1-6, as well as standard deviations, are given in Table 4. The S-N curves are plotted and compared in Fig. 3 and 4.

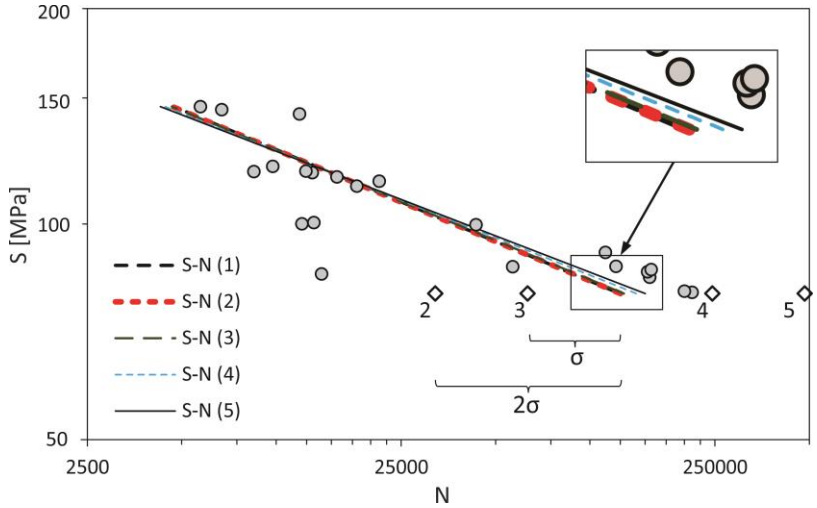

Fig. 3 The influence of the additional data points on the slope of S-N curve (cases 1-5)

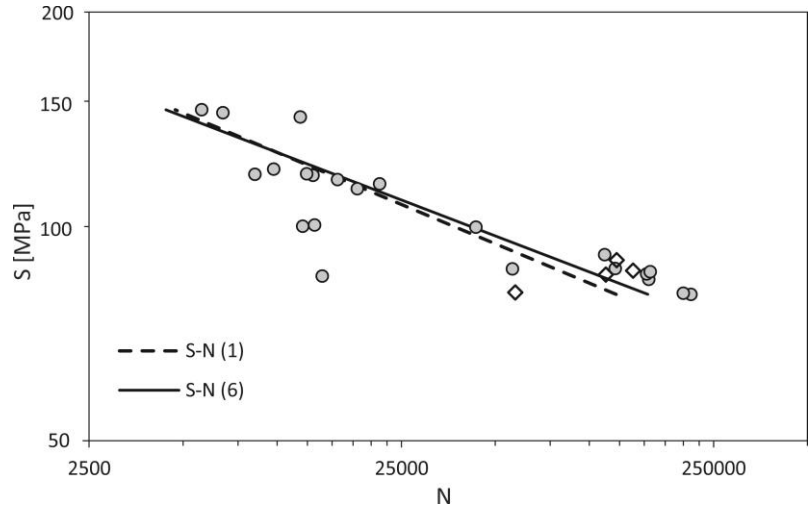

Fig. 4 Comparison of S-N curves obtained by excluding and including runouts in the determination of model parameters

From the calculation results, given in Table 4, it is clear that the inclusion of the runouts in the analysis has a greater influence on the S-N curve if the specimens endured larger number of cycles before the tests were stopped. The slope of the curve as well as the endurance limit exhibited changes with the increase of the endured number of cycles of additional data point. In the second case (Fig. 3), the data point is located relatively far away from the curve S-N (1), obtained by using only the failed specimen data. Moreover, it is located out of the 95% confidence limit (1.96σ). In accordance with this fact, the influence of the additional data point on the S-N curve is negligible. This was shown in Fig. 3, where curves S-N (1) and S-N (2) almost coincide. From the practical point of view, considering the curve S-N (1) and the corresponding standard deviation, the specimen was not expected to fail after 32 thousand cycles, which was only confirmed by the observed specimen. Similar influence on the S-N curve was seen in the case of the third dataset, though in this case there is certain difference between the curves S-N (1) and S-N (3). Here, it was also not expected that the specimen would fail after 63 thousand cycles, but the probability of failure was much greater than in the second case. In the fourth and fifth case, there is a clearly visible change in the slope of the S-N curve, which is justified by the fact that the additional samples were not expected to endure that many cycles. Finally, in Fig. 4, the influence of the real runouts on the slope of the S-N curve, as well as the predicted endurance limit, was illustrated. It could be noticed that the datasets 5 and 6 show almost the same change of the slope of the S-N curve although the runouts in the sixth dataset are much closer to the curve S-N (1). This could be attributed to the fact that there are more runouts in this dataset.

Table 4 The results of calculation using MATLAB code written according to the algorithm given in Fig. 2

Case	S_d [MPa]	k	σ^*
1.	48.042	-5.446	0.2944
2.	48.196	-5.472	0.2811
3.	48.658	-5.523	0.2792
4.	50.430	-5.756	0.2839
5.	51.667	-5.923	0.2857
6.	52.198	-5.952	0.2891

*The standard deviation values are given as log$N$

When analyzing the influence of runouts, one must have in mind that the plots in Fig. 3 and 4 were created using logarithmic scales for both the x-axis and the y-axis. Thus, even a small change in the slope could represent a big difference in fatigue life, especially at lower stress levels. For example, at the stress level of 80MPa, the curve S-N (6) predicts the failure after about 150 thousand cycles, which is 25% more than the number of cycles predicted by the curve S-N (1) (120 thousand cycles). This fact has to be considered when deciding whether to censor runouts or not.

Since the S-N model used in reference [8] assumed a nonlinear relationship between logarithms of stress and fatigue life, the S-N curve given in it was not adequate for the validation of the results of the proposed algorithm. Another dataset that contained runouts, taken from reference [9], was used to validate the algorithm predictions. Although the size of the dataset was relatively small, due to the similarity of the adopted S-N models and methods for the determination of parameters, it was considered suitable for the purpose of validation.

The comparison of S-N curves from [9], obtained by performing three different analyses, and S-N curve obtained by using proposed algorithm is given in Fig. 5. All of them represent the linear relationship between logarithms of stress and fatigue life. The curves from reference [9] provided the fatigue life predictions in which runouts were treated by:

- not including them in analysis,
- considering them as failures,
- analyzing them using the procedure based on maximum likelihood method, different than the one proposed here.

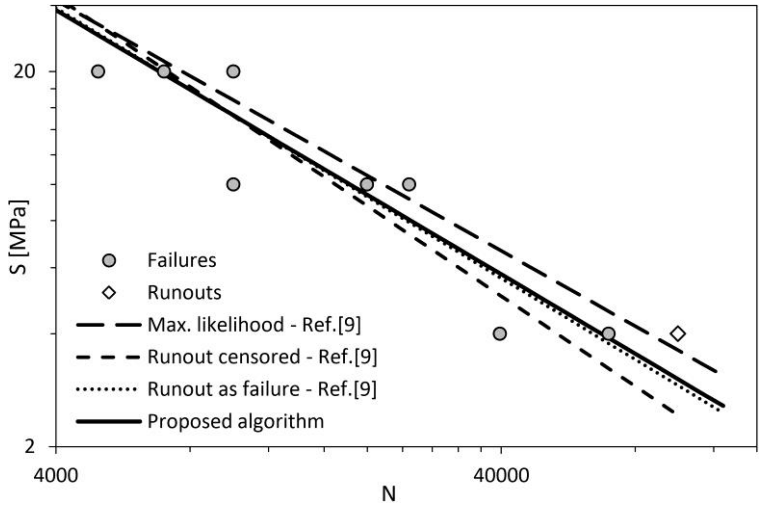

Fig. 5 Comparison of S-N predictions from Ref. [9] and predictions obtained using proposed algorithm

From the Fig. 5, it is clear that censoring of the runout gave a big difference in the fatigue life prediction, compared to the other analyses. Considering that the fatigue life of the runout is equal to or greater than the endured number of cycles, it makes sense that it should be considered at least as a failure, which is represented by the dotted curve. However, having in mind that this sample did not fail suggests that the curve should be shifted a bit to the right in this region. This was achieved by utilization of the maximum likelihood method. However, the S-N curve obtained using proposed algorithm is more logical that the one given in reference [9]. A considerable difference between the curves obtained by considering runouts as failures and analyzing them using maximum likelihood method is very non-conservative and not realistic since it is not known if the sample would fail in the next cycle. Thus, it could be concluded that the proposed algorithm gave very good fatigue life predictions.

4. CONCLUSION

In this paper, the algorithm for determination of the parameters of the S-N curve for prediction of the fatigue life of structures or elements subjected to cyclic loading is given. The algorithm is derived based on the maximum likelihood method. This method allows the

inclusion of runouts in the process of determination of model parameters. Based on the proposed algorithm, a MATLAB code is written and verified by using the experimental data from the literature. The results obtained from different sets of data showed that the MATLAB code gives the appropriate change of slope, as well as the predicted endurance limit, when runouts are included in the analysis. The results obtained by analysis of the real experimental data showed that censoring runouts could give significant difference in fatigue life prediction. The comparison of S-N curves obtained by using the proposed algorithm with the curves from the literature obtained by utilizing the maximum likelihood method showed that it gives very good predictions of the fatigue life. Having in mind all written above, in order to predict more accurate fatigue life, it is advisable to include runouts in the analysis of the experimental data, for which the proposed algorithm could serve as a good tool.

REFERENCES

1. T. Nicholas, High Cycle Fatigue: A Mechanics of Materials Perspective, Elsevier Ltd., Oxford, 2006.
2. S. Peter, E. Ostertagová, "Evaluation of Fatigue Tests by Means of Mathematical Statistics", Procedia Engineering, vol. 48, pp.636–642, 2012, doi: 10.1016/j.proeng.2012.09.564.
3. J. E. Spindel, E. Haibach, "The method of maximum likelihood applied to the statistical analysis of fatigue data", Internationla Journal of Fatigue, vol. 1(2), pp.81-88, 1979. doi: 10.1016/0142-1123(79)90012-4.
4. J. M. Whitney, "Fatigue characterization of composite materials, in Fatigue of Fibrous Composite Materials", ASTM STP 723, American Society for Testing Materials, pp. 133-151, 1981.
5. G. P. Sendeckyj, "Fitting models to composite materials, in Test Methods and Design Allowables for Fibrous Composites", ASTM STO 734, American Society for Testing Materials, West Conshohocken, pp.245-260, 1981.
6. O. H. Basquin, "The exponential law of endurance tests", in Proceedings of the American Society for Testing Materials, vol. 10, pp.625-630.
7. W. Nelson, "Fitting of Fatigue Curves with Nonconstant Standard Deviation to Data with Runouts", Journal of Testing and Evaluation, vol. 12, pp. 69-77, 1984, doi: 10.1520/JTE10700J
8. F. G. Pascual, W. Q. Meeker, "Regression Analysis of Fatigue Data with Runouts Based on a Model with Nonconstant Standard Deviation and a Fatigue Limit Parameter", Journal of Testing and Evaluation, vol. 25, pp.292-301, 1997.
9. S. Sarkani, T. A. Mazzuchi, D. Lewandowski, D. P. Kihl, "Runout Analysis in Fatigue Investigation", in Proceedings of the 11th International Conference on Fracture, Turin, Italy, March 2005, pp.5789-5794.

ALGORITAM ZA ODREĐIVANE S-N KRIVIH ELEMENATA KONSTRUKCIJA IZLOŽENIH CIKLIČNOM OPTEREĆENJU

Predviđanje veka trajanja elemenata konstrukcije ili same konstrukcije pri dejstvu cikličnog opterećenja najčešće se vrši pomoću S-N krivih, dobijenih na osnovu eksperimentalnih podataka ispitivanja uzoraka cikličnim opterećenjem do loma. Međutim, prilikom ispitivanja se može desiti da uzorak izdrži unapred određeni broj ciklusa bez loma, kao i da se ono iz određenog razloga prekine. Takvi uzorci se nazivaju preživelim, a podaci dobijeni na ovaj način takođe mogu biti od značaja za određivanje S-N krive. U ovom radu je prikazan algoritam za određivanje parametara S-N krive metodom maksimalne verodostojnosti, kojim se uzimaju u obzir i podaci o preživelim uzorcima. Na osnovu algoritma je napisan MATLAB program, čija je verifikacija urađena na eksperimentalnim podacima iz literature. Rezultati su pokazali da se pri proračunu parametara S-N krive pomoću razvijenog algoritma mogu na odgovarajući način uzeti u obzir i podaci o broju ciklusa koje su nepolomljeni uzorci preživli. Takođe, pokazano je da njihovo uključivanje u proračun može značajno uticati na predviđeni vek trajanja, pogotovo pri nižim nivoima opterećenja.

Ključne reči: *Zamor, S-N kriva, algoritam, metoda maksimalne verodostojnosti*.

FACTA UNIVERSITATIS
Series: **Architecture and Civil Engineering** Vol. 16, No 1, 2018, pp. 93-111
https://doi.org/10.2298/FUACE170420008C

FRAGILITY AND RELIABILITY ANALYSES OF SOIL - PILE - BRIDGE PIER INTERACTION

UDC 624.21:699.841

Mladen Ćosić[1], Radomir Folić[2], Boris Folić[3]

[1]Institute for Testing of Materials - IMS, Belgrade, Serbia
[2]University of Novi Sad, Faculty of Technical Sciences, Novi Sad, Serbia
[3]University of Belgrade, Innovative Centre, Faculty of Mechanical Engineering, Belgrade, Serbia

Abstract. *The purpose of this paper is to present the methodology for performance-based seismic evaluation of soil-pile-bridge pier interaction using the incremental nonlinear dynamic analysis (INDA). The system's input signal was treated through the generated artificial accelerograms which were subsequently processed by soil layers and for the bedrock. The INDA analysis was post processed separately for the pier and for the pile, so that the constructed PGA=f(DR) curves are in the capacitive domain. For these curves the authors identified the performance levels, while the regression analyses were conducted based on the specific DR and PGA parameters. Fragility curves were constructed based on the solutions of regression analysis and the probability theory of log-normal distribution. Based on the results of fragility analysis, reliability curves were also constructed. The methodological procedure for seismic performance analysis presented in this study provides an integrated quantitative-qualitative consideration and evaluation of the complex soil-foundation-structure interaction (SFSI).*

Key words: *incremental nonlinear dynamic analysis, pile performance, fragility, reliability, artificial accelerograms.*

1. INTRODUCTION

Due to the complexity of phenomena involved in the wave propagation in soil-structure interaction (SSI), mathematical modelling of this problem is based on a multidisciplinary approach to the engineering seismology and earthquake engineering. The soil-structure interaction can be considered by conducting tests on actual models and/or in the laboratory, using analytical and numerical methods. The development of

Received April 20, 2017 / Accepted September 7, 2017
Corresponding author: Radomir Folić
Faculty of Technical Sciences, Dositeja Obradovića Sq. 6, 21000 Novi Sad, Serbia
E-mail: folic@uns.ac.rs

modern codes for designing structures has been enhanced by taking into account the earthquake action, the level of security against premature collapse and non-ductile behaviour. However, given the stochastic nature of earthquakes and the complexity of the soil-structure interaction phenomenon, mathematical models and analyses dealing with this problem should be improved continuously. The soil-foundation-structure interaction (SFSI) is considered for both shallow and deep funding such as piles. The contemporary Performance-Based Earthquake Engineering (PBEE) methodology provides a more complete and sophisticated understanding and treatment of the SFSI through hazard analysis, structural analysis, damage analysis and loss analysis [1], [2]. Using the PBEE methodology, the analysis of structural response under seismic actions may be considered in time (TDA - time domain analysis), frequency (FDA - frequency domain analysis) and capacitive (CDA - capacity domain analysis) domains, analyzing the structure's bearing capacity and deformation in a particular case of piles.

The PBEE-based pile performance research methodology and the EQWEAP procedure developed for that purpose is described in [3], while the use of incremental dynamic analysis (IDA) for analyzing groups of piles is discussed in [4] and [5]. Seismic performances are considered in several ways: by applying the deterministic concept with a single earthquake scenario, based on parametric analysis and the probabilistic concept. The paper [6] presents a 3D finite element incremental dynamic analysis study of caisson foundations carrying single-degree of freedom (SDOF) structures on clayey soil. The emphasis is given to the interplay between the nonlinearities developed above (superstructure) and, mainly, below ground surface, either of material (soil plasticity) or of geometric (caisson–soil interface gapping and slippage) origin. The pile performance analysis by establishing a correlation between the engineering demand parameters (EDP) and the intensity measure (IM) is presented in [7]. The general approach of modelling the dynamic interaction of piles groups in the soil using the hybrid techniques by connecting the finite element method (FEM) and the boundary element method (BEM) is discussed in [8], while the various aspects of mathematical and numerical modelling of the complex soil-piles interaction are presented in [9]. General approaches to analyzing the seismic performance of piles with the emphasis on various mathematical soil-pile interaction models are presented in [10], while the interaction effects in evaluations of the system ductility demand ratio (DDR) are discussed in [11]. Modelling the piles and soil using 3D finite elements and taking into account the influence of plastic nonlinear soil behaviour in seismic performance assessment is presented in [12]. Analysis of seismic response of pile groups using the 3D solid FEM for piles and the soil is discussed in [13], while the method of 3D continuum for analyzing the seismic response is presented in [14]. The seismic performance analysis of the pile to pile cap connection is discussed in [15] using the FEM method and the study of this phenomenon was based on the damage to actual connections.

A large body of scientific research which is devoted to modelling the behaviour and analyzing the response of soil-pile systems is considered in the time domain of nonlinear dynamic analysis (NDA) or the capacitive domain of nonlinear static pushover analysis (NSPA). There is a considerably fewer number of soil-pile interaction studies based on the incremental dynamic analysis (IDA). Therefore, the concept of this work is focused on modelling the aspects of soil-pile interaction based on the INDA analysis, the application of which is discussed in the section of numerical simulation where the results are also presented. In order to understand and complete the methodology of these analyses, in

addition to the incremental nonlinear dynamic analysis, the following was also considered: numerical modelling of soil-pile interaction and the generation of artificial accelerograms. Results of numerical simulations were presented and 300 NDA analyses were statistically processed.

2. Numerical Modelling of the Soil-pile Interaction

In creating the mathematical and corresponding numerical soil-pile interaction model there are several phases: concretization, abstraction and discretization. The specific problem is defined in the concretization phase by considering separately the domains of soil, piles and the structure above ground level. Through the phase of abstraction, the actual physical soil-pile model is replaced by specific mathematical and numerical model, respectively, while in the discretization phase the predefined domains are transformed into subdomains. There are several approaches to modelling and analyzing the soil-pile interaction based on the finite element method, taking into account the development of geometric and material nonlinearity; they are the following:

- piles: 1D finite elements; soil: implicitly, based on the elements of interaction,
- piles: 1D finite elements; soil: 2D and 3D finite elements,
- piles: 2D finite elements; soil: implicitly, based on the elements of interaction,
- piles: 2D finite elements; soil: 2D finite elements,
- piles: 3D finite elements; soil: implicitly, based on the elements of interaction,
- piles: 3D finite elements, soil: 3D finite elements.

From the continuous numerical model, the soil-pile interaction system is translated into a discrete numerical model, while the principle of discretization allows modelling the sub domains behaviour at a very high level. The principle of approximation used in this study is based on modelling the pile and structure by liner finite elements, while the soil was modelled implicitly through replacement elements. Figure 1a shows the actual pile model in the soil and with the structure above ground level (bridge pier). Figure 1b shows the numerical pile model formed from linear finite elements, and with the structure above ground level.

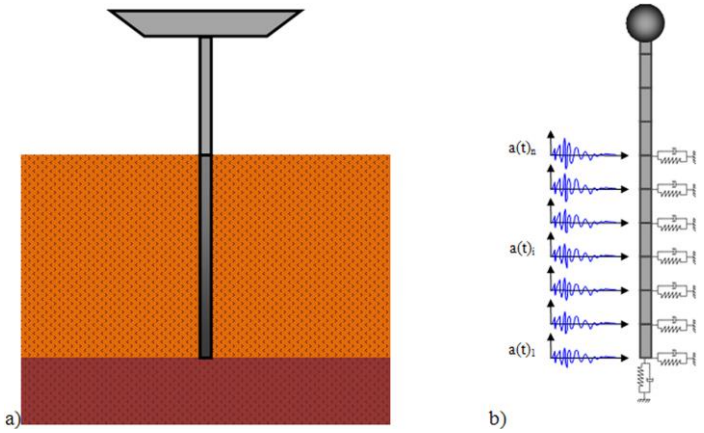

Fig. 1 a) the realistic model of pile in the soil, bridge pier and soil, b) the numerical model of pile, bridge pier and implicit modelling of soil action

The linear finite elements for modelling the pile and the bridge pier are based on the principle of propagation of nonlinear deformation along the element, where at the cross section level a specific fibre discretization is implemented. The cross-section is generally considered through three sub domains: unconfined concrete, confined concrete and steel. The stress-strain state at the cross section level is determined by integrating the nonlinear single-axis stress-strain state of each single fibre [16]. The above described linear finite elements are implemented into the SeismoStruct software [17]. According to Mander [18], the constitutive model of behaviour for the unconfined and confined domains of concrete is a nonlinear constant confinement concrete model, in which four parameters define mechanical properties. The first parameter f_{ck} is the concrete compressive strength, as defined by a 150x300mm cylindrical sample at age of 28 days according to EC 2 [19]:

$$\begin{aligned} f_{ck,c} &= f_{ck}\left(1+5\frac{\sigma_2}{f_{ck}}\right) \quad \text{for} \quad \sigma_2 \le 0.05 f_{ck} \\ f_{ck,c} &= f_{ck}\left(1.125+2.5\frac{\sigma_2}{f_{ck}}\right) \quad \text{for} \quad \sigma_2 > 0.05 \mathrm{f_{ck}} \end{aligned}, \tag{1}$$

where σ_2 is the effective lateral compressive stress due to confinement, and γ_c is the bulk density of concrete. The second parameter is f_{ctk} the strength of concrete under axial tension:

$$f_{ctk} = k_t \sqrt{f_{ck}}\,, \tag{2}$$

where k_t=0.5 for axial tension, and k_t=0.75 for bending tension. The third parameter $\varepsilon_{c,max}$ is the concrete strain under maximum compressive stress, while the fourth parameter k_c is the factor related to the ratio between the confined and unconfined compressive stress in concrete.

The constitutive model of behaviour of steel reinforcement is a bi-linear elastic-plastic model with kinematic strain hardening in the nonlinear deformation zone [20], where the following applies for the elastic domain:

$$\sigma_s = E_s(\varepsilon_s - \varepsilon_{s,p})\,, \tag{3}$$

where σ_s is the stress in steel reinforcement, E_s is the modulus of elasticity of steel reinforcement, ε_s is the strain of steel reinforcement, $\varepsilon_{s,p}$ is the plastic strain of steel reinforcement. The law of flow rule is defined by:

$$\dot{\varepsilon}_{s,p} = \gamma \mathrm{sign}(\sigma_s - q)\,, \tag{4}$$

while the law of isotropic and kinematic hardening by:

$$\dot{q} = \gamma H \mathrm{sign}(\sigma_s - q)\,, \quad \dot{\alpha} = \gamma\,, \tag{5}$$

where the condition for yielding is:

$$\begin{aligned} f(\sigma_s, q, \alpha) &:= |\sigma_s - q| - [\sigma_{s,y} + K\alpha] \le 0 \\ E_\sigma &= \{(\sigma_s, q, \alpha) \in \Re \times \Re^+ \times \Re \,|\, f(\sigma_s, q, \alpha) \le 0\} \end{aligned}, \tag{6}$$

while the Kuhn-Tucker complementary conditions:

$$\gamma \geq 0, \qquad f(\sigma_s, q, \alpha) \leq 0, \qquad \gamma f(\sigma_s, q, \alpha) = 0, \tag{7}$$

and the condition of consistency:

$$\gamma \dot{f}(\sigma_s, q, \alpha) = 0. \tag{8}$$

Defining the mechanical properties of the constitutive model of steel reinforcement behaviour requires the following three parameters. The first is E_s the modulus of elasticity of steel reinforcement, the second is $\sigma_{s,y}$ the stress at the yield point of reinforcement steel and the third is μ_s the ratio of post-elastic stiffness $E_{s,p}$ and the initial elastic stiffness E_s (strain hardening parameter), where:

$$E_{s,p} = \frac{\sigma_{s,ult} - \sigma_{s,y}}{\varepsilon_{s,ult} - \dfrac{\sigma_{s,y}}{E_s}}, \tag{9}$$

where $\sigma_{s,ult}$ is the maximum stress value in steel reinforcement and $\varepsilon_{s,ult}$ is the maximum value of strain of steel reinforcement, while γ_s is the specific weight of steel reinforcement.

The finite element type by which the pile and pier are modelled is the inelastic displacement-based frame element [21]. This type of finite element has six degrees of freedom $\theta_{A,y}$, $\theta_{A,z}$, $\theta_{B,y}$, $\theta_{B,z}$, Δ_a, θ_T, with the corresponding internal forces and moments $M_{A,y}$, $M_{A,z}$, $M_{B,y}$, $M_{B,z}$, N, M_T. Geometric nonlinearity is introduced by applying the effects of large displacement and rotation and through the P-Δ effects. The equilibrium and compatibility conditions are established on the deformed configuration using the co-rotational formulation [22].

The nonlinear dynamic soil-pile interaction (SPI) is modelled using the constitutive model of behaviour for the lateral analysis of piles, where the formation of gaps under cyclic soil deformation is also taken into account [23]. Effects of cyclic degradation/hardening of soil stiffness and strength are also taken into account; in addition, actions in the direction pile axis are also separately modelled, which are orthogonal to the effects that are introduced by applying this model of interaction. The hysteretic constitutive model consists of four major parts: backbone curve, standard reload curve (SRC), general unload curve (GUC) and direct reload curve (DRC). The backbone curve is an adaptive polygonal curve defined by four segments [24]:

$$p(y) = \sum_{i=1}^{j} (p_i - p_{i-1}) + \alpha_j K_0 (y - y_j), \quad j = \max(\mathrm{i}), \quad \forall y_i \leq y, \quad j \geq 0, \tag{10}$$

where: p is the soil response, y is the relative displacement, α_j is the stiffness reduction coefficient in the last curve segment and K_0 is the initial stiffness. Defining the mechanical properties of the constitutive model of the soil-pile interaction behaviour requires nineteen parameters: K_0 initial stiffness, F_c soil strength ratio at the first turning point $0 \leq F_c < 1$, F_y yielding soil strength, P_0 initial force ratio at zero displacement $0 \leq P_0 \leq 0.9$, P_a minimum force ratio at baseline $0 \leq P_a \leq P_0$, $P_a \leq \beta_n F_y$ and $P_a \leq F_c$, α stiffness ratio after first turning point $0.001 \leq \alpha \leq 1$, α_n unloading stiffness factor, β yielding stiffness ratio, β_n ultimate soil strength ratio $\beta_n < 1$ for $\beta < 0$, $\beta_n = 1$ for $\beta = 0$, $\beta_n > 0$ for $\beta > 0$, Flg flag settings combination indicator adjustment factor 1 out of 31 combinations in defining the constitutive model, e_{p1} is DRC starting stiffness ratio, p_1 gap force parameter $0 \leq p_1 \leq 1$, p_2 soil cave-in parameter, p_k and e_k are stiffness degradation/hardening parameters, p_s and e_s are strength degradation/hardening

parameters, k_s slope of the S-N curve and f_0 soil stress corresponding to point S_1 in S-N curve. The hysteretic damping ratio ξ_h of the model ranges from 0, for a perfectly elastic response, to the largest possible amount of energy dissipation per cycle under two-way cyclic loading [24]:

$$\xi_h = \begin{cases} \dfrac{1}{2\pi}\left[2-\dfrac{K_s}{K_0}\right] & \text{for } \phi \le \dfrac{\phi_1}{1-\phi_1} \\ \dfrac{1}{2\pi}\left[2-\dfrac{K_s}{K_0}-\left(\dfrac{K_s}{K_0}\right)\left(1-\dfrac{1+\phi}{\phi/\phi_1}\right)^2\left(\dfrac{1}{\alpha_1}-1\right)\right] & \text{for } \phi > \dfrac{\phi_1}{1-\phi_1} \end{cases}, \tag{11}$$

where $\varphi_i = p_i/p_f$, and K_s is the secant stiffness.

3. GENERATION OF ARTIFICIAL ACCELEROGRAMS

Generation is a procedure of creating artificial accelerograms based on defined procedures in the frequency domain [25]. This is a highly favourable procedure of creating accelerograms, considering that a ground motion record (GMR) can be created for the designed range of responses determined either by the deterministic or probabilistic concept. Also, this accelerogram is scaled and matched to the given response spectrum.

The procedure of generating artificial accelerograms is conducted by determining the spectral density function based on the response spectrum; in this specific case a pseudo response spectra has been used [26]. This function is used to derive the sinusoidal signal amplitude the phase angle of which is generated by a random number function in the range between $0 \div 2\pi$ according to uniform distribution. Sinusoidal signals are compressed in order to generate accelerograms. In order to determine the other properties of the artificial accelerogram, such as duration of recording, it is necessary to obtain additional information about the expected earthquake based on the response spectrum. Any periodic function can be developed into a sine wave [27]:

$$x(t) = A_0 + \sum_i A_i \sin(\omega_i t + \phi_i), \tag{12}$$

where A_i is the amplitude, and φ_i is the phase angle. The amplitude A_i is correlated with the function of spectral density $G(\omega)$:

$$A_i = \sqrt{2\int_0^{\omega_i} G(\omega_i)d\omega}, \tag{13}$$

while the relation between the response spectrum and the function of ground motion spectral density is given through:

$$G(\omega_n) = \frac{1}{\omega_n\left[\dfrac{\pi}{4\xi_s}-1\right]}\left\{\left(\frac{\omega_n S_v}{r_{s,p}}\right)^2 - \int_0^{\omega_n} G(\omega)d\omega\right\}^{1/2}, \tag{14}$$

where:

$$\xi_s = \frac{\xi}{1-e^{-2\xi\omega_n t}},\ r_{s,p} = [2\log\{2n(1-e^{-\delta_y(s)\sqrt{\pi\log 2n}})\}]^{1/2},\ \delta_y(s) = \left(\frac{4\xi t}{\pi}\right)^{1/2},\ n = \frac{-\omega_n t}{2\pi\log 0.368}, \quad (15)$$

where S_v is spectral velocity and ξ is the damping coefficient. The accelerogram generated by the above described procedure still fails to present the amplitude of the actual accelerogram model. To this end, it is necessary to define the acceleration envelope for the preliminary generated accelerogram:

$$X(t) = a(t) = I(t)\sum_i A_i \sin(\omega_i t + \phi_i). \quad (16)$$

In addition to the stationary envelope, trapezoidal and exponential envelopes have also been used, as well as a model of complex envelope where both the initial and final domains, and in particular the domain of strong motion, are separately defined.

Upon the generation of artificial accelerograms for representing the record of the free field motion, further analyses are conducted in order to generate accelerograms for soil layers and bedrock motion. In this specific case, the soil is considered as a single-layer system, but given the number of input accelerograms in numerical analyses for simultaneous performance of numerical integration in time, the single-layer system is considered as a multi-layer system with the same geo-technical properties. For each individual layer accelerograms are generated taking that waves are propagating similar to the single-layer system. Generally, the mathematical formulation of the transverse wave propagation in a single-layer system *s* and the bedrock *r* is as follows [28]:

$$u_s(z_s,t) = A_s e^{i(\omega t + k_s^* z_s)} + B_s e^{i(\omega t - k_s^* z_s)}, \quad u_r(z_r,t) = A_r e^{i(\omega t + k_r^* z_r)} + B_r e^{i(\omega t - k_r^* z_r)}, \quad (17)$$

where ω is the angular frequency and k^* is the complex wave number. By resolving equation (17), the following is obtained:

$$A_r = \frac{1}{2}A_s\left[(1+\alpha_z^*)e^{ik_s^* H} + (1-\alpha_z^*)e^{-ik_s^* H}\right],\ B_r = \frac{1}{2}A_s\left[(1-\alpha_z^*)e^{ik_s^* H} + (1+\alpha_z^*)e^{-ik_s^* H}\right], \quad (18)$$

$$A_s = \frac{2A}{(1+\alpha_z^*)e^{ik_s^* H} + (1-\alpha_z^*)e^{-ik_s^* H}}. \quad (19)$$

The accelerogram for bedrock is generated by applying the transfer function *F(ω)*, which is the ratio between the amplitudes for the terrain surface and the bedrock:

$$F(\omega) = \frac{1}{\cos k_s^* H + i\alpha_z^* \sin k_s^* H}. \quad (20)$$

4. INCREMENTAL NONLINEAR DYNAMIC ANALYSIS

The soil-pile interaction responses are considered in the capacity analysis domain using a series of nonlinear dynamic analysis (NDA), or incremental nonlinear dynamic analysis (INDA). Accelerograms are scaled successively from the initial minimum scaling

factor $F_{s,0}$ through the ultimate scaling factor $F_{s,n}$ for state of collapse. First, it is the scaling to a specific initial value, so that the structure's response to a given scaled level of earthquake is in the linear-elastic domain. This is achieved by scaling the accelerogram to a sufficiently low value of acceleration [29]:

$$PGA_{s,1} = F_{s,1} PGA_{us}\,, \tag{21}$$

where PGA_{us} is the maximum acceleration of original un-scaled accelerogram, $F_{s,1}$ is the start scaling factor for the NDA analysis, and $PGA_{s,1}$ is the maximum acceleration of the scaled accelerogram scaled to the initial minimum acceleration value. The scaling is continued by increasing $PGA_{s,i}$ in a successive manner:

$$PGA_{s,i} = PGA_{s,i-1} + 0.1 + 0.05(i-1) \quad \text{for} \quad i = 1,...n\,, \tag{22}$$

and when it is observed that the difference in the structure's response for two consecutive scaling values is without any major changes, then the scaling factor is increased. In the case when the difference in the structure's response to the two subsequent scaling values is significant, then the scale factor is reduced. If the NDA analysis for the $PGA_{s,i}$, shows that the maximum drift value is:

$$DR_{\max} \to +\infty\,, \tag{23}$$

then the scaling is done according to:

$$PGA_{s,i+1} = PGA_{s,i-1} + \frac{(PGA_{s,i} - PGA_{s,i-1})}{3}\,, \tag{24}$$

while the following applies to the scale factors:

$$F_{s,1} < F_{s,i} < F_{s,n}\,. \tag{25}$$

The required number of nonlinear dynamic analyses (NDA) within a single incremental nonlinear dynamic analysis (INDA) is defined by [30]. Figure 2 shows the pushover INDA curve *IM=f(EDP)* constructed based on the interpolation of discrete values $I_i(EDP_i, IM_i)$ from the NDA analyses for scaling accelerograms from the elastic, through non-linear and up to the collapse domain. Values of the engineering demand parameter EDP and the intensity measure IM are given on the abscissa and the ordinate, respectively.

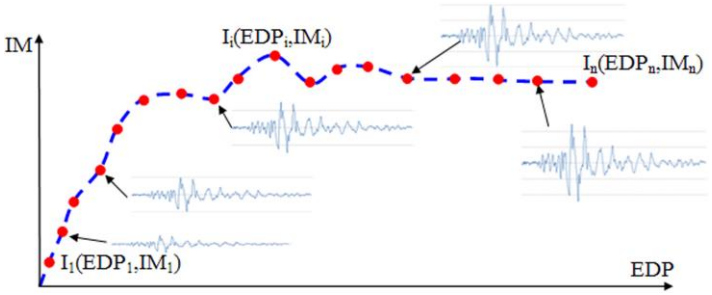

Fig. 2 The INDA pushover curve *IM=f(EDP)* with discrete values from the NDA analyses and scaled accelerograms [25]

The INDA analysis used in this study is equivalent to the term of the existing IDA (incremental dynamic analysis) analysis INDA≡IDA, provided if the IDA analysis is a complete nonlinear analysis with the development of both geometric and material nonlinearities in the system. In the procedure of determining the acceleration, velocity and displacement of the soil-pile interaction, in terms of earthquake actions, the differential equations of motion are the following:

$$[M]\{a\}+[C]\{v\}+[K]\{d\}=\{Q\}\,. \tag{26}$$

Solving equation (26) is carried out by a step by step numerical integration using the Hilber-Hughes-Taylor (HHT) method in its modified form [31]:

$$[M]\{a\}_{i+1}+(1+\alpha)[C]\{v\}_{i+1}-\alpha[C]\{v\}_i+(1+\alpha)[K]\{d\}_{i+1}-\alpha[K]\{d\}_i=\{Q\}_{i+\alpha}\,, \tag{27}$$

and for a given moment of time:

$$t_{i+1}=t_i+\Delta t\,, \tag{28}$$

where $[M]$ is the mass matrix, $\{a\}$ is the acceleration vector, $[C]$ is the damping matrix, $\{v\}$ is the velocity vector, $[K]$ is the stiffness matrix, $\{d\}$ is displacement vector and $\{Q\}$ is the vector of externally generated forces. Displacement and velocity vectors are expressed by:

$$\{d\}_{i+1}=\{d\}_i+\Delta t\{v\}_i+\frac{\Delta t^2}{2}[(1-2\beta)\{a\}_i+2\beta\{a\}_{i+1}]\,, \tag{29}$$

$$\{v\}_{i+1}=\{v\}_i+\Delta t[(1-\gamma)\{a\}_i+\gamma\{a\}_{i+1}]\,, \tag{30}$$

while for the vector of externally generated forces the following applies:

$$\{Q\}_{i+\alpha}=\{Q\}(t_{i+\alpha})\,, \tag{31}$$

where:

$$t_{i+\alpha}=(1+\alpha)t_{i+1}-\alpha t_i=t_{i+1}+\alpha\Delta t\,. \tag{32}$$

The HHT method becomes unconditionally stable if parameters α, β and γ are selected according to the following relations:

$$\alpha\in\left[-\frac{1}{3},0\right],\quad \beta=\frac{1}{4}(1-\alpha)^2\,,\quad \gamma=\frac{1}{2}-\alpha\,. \tag{33}$$

Correction of the system's stiffness matrix is carried out after each step, and it is based on the Newton-Raphson's incremental-iterative method.

5. Numerical Simulation Results and Discussion

Numerical simulations of nonlinear pile behaviour in interaction with the soil were carried out using the finite element method in the SeismoStruct software [17]. In the pre-processing stage, the numerical parameters of the model were defined separately for each domain according to the previously presented mathematical formulation. The pile and pier diameter is d_p=1.8m, the pile length is L_p=15m, while the bridge pier height is L_b=10m. The pier and pile are of circular cross-section with radially disposed reinforcement consisting of 25 rods of Ø40mm diameter. The cross-section is discretized to 300 fibres, and a total of 10 integration

sectors were considered. The mass applied to the pier top is m=816t. The constitutive concrete model is defined for the C 25/30 strength class, according to EC 2 [19]: f_{ck}=25MPa, f_{ctk}=0, $\varepsilon_{c,max}$=2.1$^0/_{00}$ and γ_c=24kN/m³ for the unconfined and confined concrete domain, k_c=1 for the unconfined concrete domain and k_c=1.2 for the confined concrete domain. The real value of the concrete strength under the pressure of $f_{ck,calc}$=30MPa for the confined concrete domain is higher than the nominal value of f_{ck}=25MPa, since it is multiplied with k_c. For the purposes of this research the effects of tensile stress in the concrete were annulled f_{ctk}=0, while the global coefficient k_c is used as the ratio of unconfined and confined compressive stress in concrete. The constitutive model of steel reinforcement is also defined according to EC 2 [19]: E_s=200GPa, $f_{s,y}$=435MPa, μ_s=0.01 and γ_s=78.5KN/m³. The following are the parameters of the constitutive model of soil-pile interaction: K_o=15000KN/m³, P_0=0, P_a=0, α=0.5, α_n=1, β=0, β_n=1, Flg=31, e_{p1}=1, p_1=1, p_2=0, p_k=1, e_k=1, p_s=1, e_s=1 and k_s=0.1. Parameters F_c and F_y are determined in the function of changes along the soil depth, so that these values were separately identified for the 16 link elements used for modelling the soil-pile interaction based on the *p-y* curves. Thus, at the soil depth of h=1m: F_c=0.338 and F_y=118.2KNm, while on the soil depth of h=5m: F_c=0.645 and F_y=1298.2KNm.

The artificial accelerograms were generated using the Simqke software [32] for the horizontal elastic response spectra according to EC 8 [33] for type C soil, where the shear wave velocity $v_{s,30}$=290m/s, the peak ground acceleration PGA=0.35g, the soil coefficient S=1.2, damping ratio ζ=5%, and the number of cycles of improving the fitting of the response spectra of the generated accelerograms n_f=100. The n_f value greatly influences the generation of artificial accelerograms, as its increase severely influences the frequency content of accelerograms [25]. On the other hand the increase of this value results in a somewhat higher number of local acceleration peaks which values tend to the absolute value of peak acceleration. Two groups were considered, each with five artificial accelerograms. The first group consists of accelerograms of shorter total time of acceleration recording t_{acc}=20s and a shorter time of stationary domain, where the times of stationary domain initiation and finalization are $t_{s,i}$=2s and $t_{s,f}$=10s, respectively (Figure 3a). The second group consists of accelerograms with longer total time of acceleration recording t_{acc}=40s and a longer time of stationary domain, where the times of stationary domain initiation and finalization are $t_{s,i}$=2s and $t_{s,f}$=15s, respectively (Figure 3b). Accelerograms were sampled at a time interval of Δt=0.01s, so that sampling frequency is f_s=100Hz. For all generated artificial accelerograms, PGA is obtained to be 0.437g.

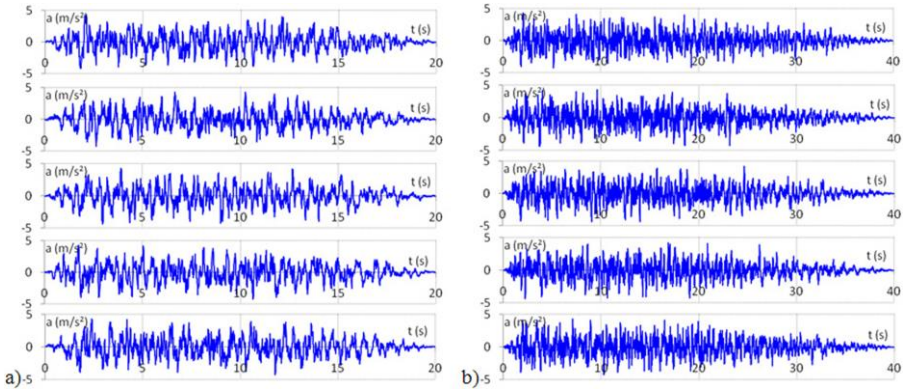

Fig. 3 The generated artificial accelerograms for:
a) $t_{s,i}$=2s, $t_{s,f}$=10s, t_{acc}=20s, b) $t_{s,i}$=2s, $t_{s,f}$=15s, t_{acc}=40s

After the accelerograms were generated, they were further processed in the Shake software [34], in order to generate independent accelerograms along the soil depth $a(t)_i$ (Figure 4). The soil domain is discretized to 15 soil layers of 1m thickness, while the bedrock domain is considered separately, so that for each INDA analysis 16 simultaneous accelerograms were used in the processing phase. A total of 160 accelerograms were generated in this manner. In INDA analyses, these accelerograms were simultaneously scaled, so that for a single INDA analysis all 16 accelerograms were scaled with the same scale factor. First, accelerograms were scaled to the initial value of $PGA_{s,1}$=0.1g for h=0 and then incrementally scaled to ΔPGA=0.1g. Given the differences among the accelerograms and the scale factors according to Figure 4, the ultimate scale factors among the accelerograms for a single INDA analysis are also different. Due to the large number of generated accelerograms, they are not presented in this paper; instead, only the values of *PGA* changes along the soil depth were provided. For each INDA analysis, accelerograms were scaled to *PGA*=3g, so the total of 300 NDA analysis were carried out. By processing the INDA analyses the discrete values $I_i(EDP_i,IM_i)$ were obtained, which were then interpolated and represent the system response in the capacitive domain. For the EDP parameter, a global drift (*DR*), while for the IM parameter a *PGA* was selected. Figures 5 and 6 are depicting the *DR-PGA* ratio curves for the pier top and the pile head, respectively.

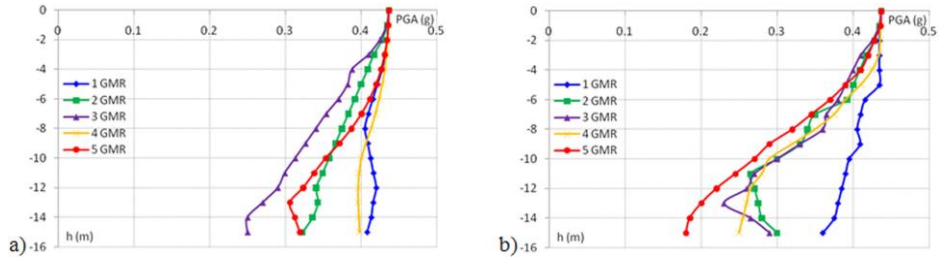

Fig. 4 Changes of the *PGA* along the soil depth for the generated artificial accelerograms: a) the first group, b) the second group

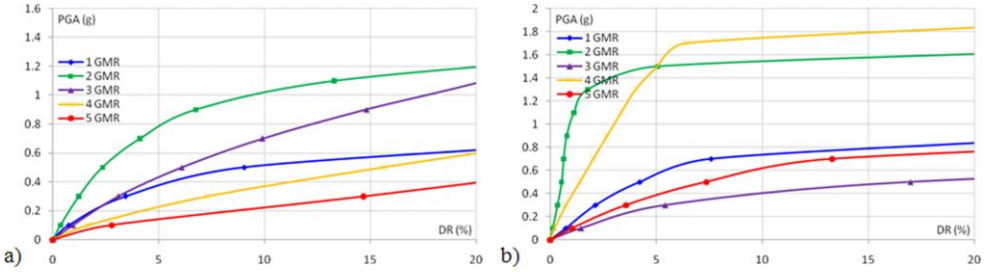

Fig. 5 The *DR-PGA* curve for the pier top: a) the first group of accelerograms, b) the second group of accelerograms

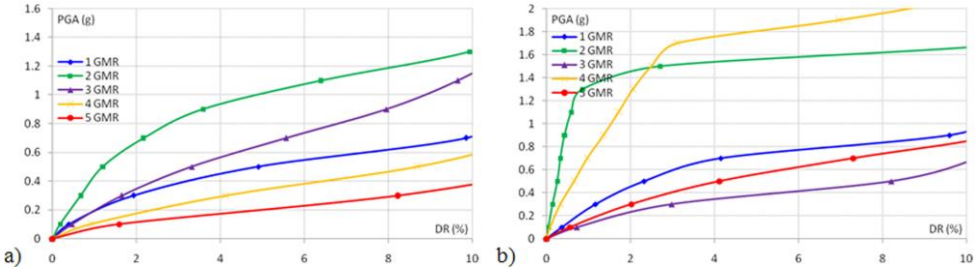

Fig. 6 The *DR-PGA* curve for the pile head: a) the first group of accelerograms, b) the second group of accelerograms

Generally, it can be concluded that there is a discrepancy in the soil-pile system response for two different groups of accelerograms, first with t_{acc}=20s and second with t_{acc}=40s total acceleration recording time. A difference also exists when considering the pier and pile response, where slightly higher *PGA* values were registered for the pile, as compared to the pier. The drift interval value for the pier is considered in the range of *DR*=[0÷20]%, while for the pile this range was *DR*=[0÷10]%. The limit states of the soil-pile system were determined by considering the structural performance level (SPL): immediate occupancy (IO), collapse prevention (CP) and the global dynamic instability (GI). The issue of determining the limit states of the system can be resolved via the EDP or IM parameters, by calculating the corresponding parameter IM for the given EDP. For the purpose of the present study, the appropriate limit state for the IM parameter has been established based on the EDP parameter according to codes. The IO performance level is determined by considering the *PGA* value for the global drift DR_{IO} of reinforced concrete systems according to SEAOC [35] and FEMA 356 [36]:

$$0.5\% \le DR_{IO} \le 1\%,\ PGA_{IO} = DR_{IO} \cap (PGA = f(DR)),\ DR_{IO} = \frac{D_{IO}}{H}, \qquad (34)$$

where D_{IO} is the displacement for the IO performance level and H is the height. The CP performance level is determined when the tangent slope to the *PGA=f(DR)* curve is equal to 20% of the initial elastic slope DR_e of this curve or when *DR*=10%:

$$DR_{CP} = \min \begin{cases} 20\% DR_e \\ 10\% \end{cases}, \quad PGA_{CP} = DR_{CP} \cap (PGA = f(DR)), \quad DR_{CP} = \frac{D_{CP}}{H}, \quad (35)$$

where D_{CP} is the displacement for CP performance level. The GI performance level is determined for the condition that the *PGA=f(DR)* curve asymptotically approaches the horizontal line:

$$DR_{GI}, PGA_{GI} : \frac{PGA_i - PGA_{i-1}}{DR_i - DR_{i-1}} \to 0,\ PGA_{GI} = DR_{GI} \cap (PGA = f(DR)),\ DR_{GI} = \frac{D_{GI}}{H}, \quad (36)$$

where D_{GI} is the displacement for the GI performance level. Based on the above set criteria for determining the performance level, statistical analyzes were conducted for each *PGA=f(DR)* curve. Results of these analyzes are shown in Table 1, sorted separately

for the pier and pile. Tags in the table are as follows: PGA_m mean value of the maximum acceleration values, PGA_{med} median value of the peak acceleration values, PGA_{min} minimum value of peak accelerations, σ standard deviation, v variance. Discrete values of specific PGA_i performance levels for the soil-pile interaction, separately with respects of the pier and pile, respectively, are shown in Figures 7 and 8. The number of discrete values (samples) is shown on the abscissa, while the PGA_i values, as determined according to the previously described methods, are shown on the ordinate.

Table 1 Discrete DR_i and PGA_i values of specific performance levels for the soil-pile interaction

pier									
performance level		IO_{min}		IO_{max}		CP		GI	
DR_m (%)	PGA (g)	0.5	0.11	1	0.23	8.32	0.75	-	0.96
DR_{med} (%)	PGA (g)	0.5	0.06	1	0.11	10	0.65	-	0.87
DR_{min} (%)	PGA (g)	0.5	0.02	1	0.04	1.4	0.24	18.6	0.39
σ		0.132		0.305		0.446		0.473	
v		0.017		0.093		0.199		0.223	
pile									
performance level		IO_{min}		IO_{max}		CP		GI	
DR_m (%)	PGA (g)	0.5	0.22	1	0.36	6.71	0.88	-	1.03
DR_{med} (%)	PGA (g)	0.5	0.11	1	0.20	7.35	0.80	-	0.90
DR_{min} (%)	PGA (g)	0.5	0.03	1	0.07	0.9	0.36	-	0.36
σ		0.290		0.387		0.420		0.535	
v		0.084		0.150		0.176		0.287	

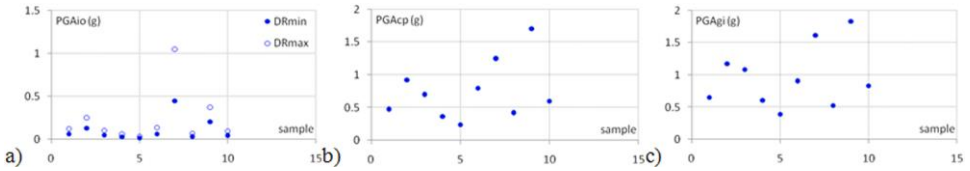

Fig. 7 Discrete *PGA* values of specific performance levels for the pier: a) IO, b) CP, c) GI

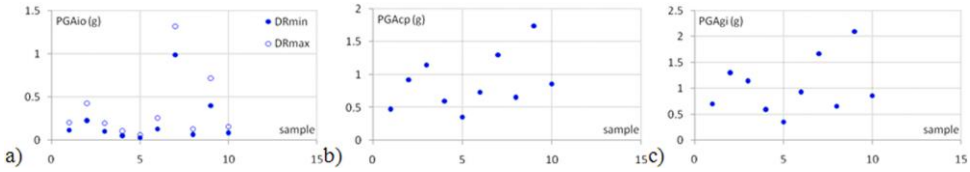

Fig. 8 Discrete *PGA* values of specific performance levels for the pile: a) IO, b) CP, c) GI

The determination of the PGA_{IO} intensity measure for the IO performance criterion is always a function of fixed value of DR_{IO}. However, the PGA_{CP} intensity measure for the CP performance criterion can be oscillating to a significant degree. In this specific case, a lower drift value has been realized of DR_{min}=0.9% for the CP performance level, as compared to the drift value of DR_{min}=1% for the IO_{max} performance level at the pile head.

The consequence of this situation is that the pile can much faster develop the state of pre-collapse in the second group of accelerograms. The determination of the GI performance level is much more complicated as compared to the previous IO and CP performance levels, since, in certain situations, the *PGA*=*f*(*DR*) curve does not need to approach the horizontal line asymptotically. More precisely, it is obligatory that the *PGA*=*f*(*DR*) curve is horizontal; in many cases, however, this condition is optional, unless the sign of inclination of the *PGA*=*f*(*DR*) curve changes from positive to negative value. This condition is achieved only in one case, in DR_{min}=18.6% and *PGA*=0.39g for the pier, while in other cases the GI performance level is determined based on the maximum drift value.

Unlike the previously presented deterministic methods of evaluation of performance levels and the conditions of the soil-pile interaction system, based on the theory of probability it is possible to consider the system's fragility. The probabilistic concept in the analysis of the soil-pile interaction system is based on a qualitative consideration of the damage level according to HAZUS [37]: slight, moderate, extensive and complete. These damage levels are defined as a function of the system ductility μ, so that the level of slight damage is equivalent to $1<\mu<2$, the level of moderate damage is equivalent to $2<\mu<4$, the level of extensive damage is equivalent to $4<\mu<7$, while the level of complete damage is equivalent to $\mu>7$ [38]. The intensity parameter IM is commonly considered by identifying the appropriate response spectra with the variation of standard deviation $\pm\sigma$, which is a function of uncertainty of the seismic demand that is imposed to the structure. However, in this study, a variation of seismic demand is applied which is a function of scaling the IM parameter, i.e. the *PGA*, according the INDA analysis. In this sense, it is possible to consider a much wider range of seismic demand variations *PGA*=[0÷1]g without any further extrapolation. The relation between μ and *PGA* was determined based on regression analysis for the linear function of $\ln\mu=k\cdot\ln PGA+n$, so that the following was obtained for the pier (Figure 9a):

$$\ln\mu = 1.325\cdot\ln PGA + 3.644\,, \tag{37}$$

while for the pile (Figure 9b):

$$\ln\mu = 1.272\cdot\ln PGA + 2.877\,. \tag{38}$$

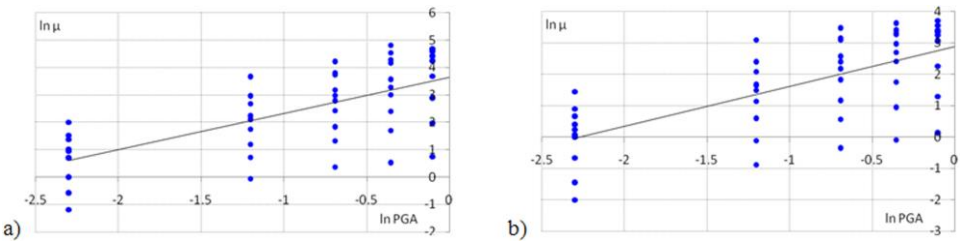

Fig. 9 Regression analysis for the *DR* and *PGA* relation: a) pier, b) pile

The fragility curve was constructed in relation to the *PGA* intensity measure by using the log-normal distribution, the probability density function of which is:

$$f(PGA,m,\sigma)=\frac{1}{PGA\sigma\sqrt{2\pi}}e^{-\frac{(\ln(PGA)-m)^2}{2\sigma^2}}, \tag{39}$$

where m is the mean PGA value. The cumulative distribution function on the occurrence of damage is determined by [39]:

$$P=F(PGA,m,\sigma)=\frac{1}{2}\mathrm{erfc}\left(-\frac{\ln PGA-m}{\sqrt{2}\sigma}\right)=\Phi\left(\frac{\ln PGA-m}{\sigma}\right), \tag{40}$$

where *erfc* is the complementary error function and Φ is the cumulative distribution function. The discrete probability functions for the pier and pile are shown in Figures 10a and 10b, respectively. A lower level of damage is typical up to PGA=0.2g for the pier model, while for the pile, this value is up to PGA=0.3g. The cumulative probability distribution function of damage for the seismic soil-pile interaction is shown in Figures 11a and 11b for the pier and pile, respectively. The upper limit of the complete damage level is considered for μ_{sup}=20, whereby the changes of this limit significantly affect the cumulative probability distribution function of complete damage. By comparing the obtained solutions for the pier and pile, it can be concluded that the pier is more sensitive to the changing levels of intensity measures PGA. The consequence of this is that the same PGA level results in larger damage to the pier, where the development higher intensity damage is also more likely. Typical values for seismic intensity measures PGA=[0.1÷0.5]g and the corresponding probabilities of fragility P_i for seismic soil-pile interaction are shown in Table 2. Values of fragility probability beneath the diagonal in Table 2 are typically equivalent to 1 or very close to this value, while those above the diagonal are typically equivalent to 0 or very close to this value. The values on the diagonal itself and near to it in Table 2 are declining. If, for example, the value of PGA=0.1g, then it can be concluded that at all fragility levels of the pier are higher than that of the pile. Thus, for the level of slight damage, the probability of pier and pile fragility are equal to P=0.88 and P=0.04, respectively, while for the level of extensive damage this value is P=0 for both the pier and the pile. On the other hand, for PGA=0.3g, the probability of pier and pile fragility for the level of slight damage are P=1, while for the level of extensive damage is P=0.99 and P=0.03, respectively.

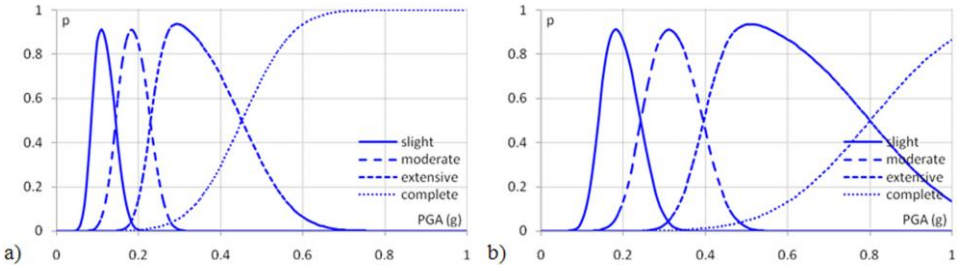

Fig. 10 Discrete probability functions: a) pier, b) pile

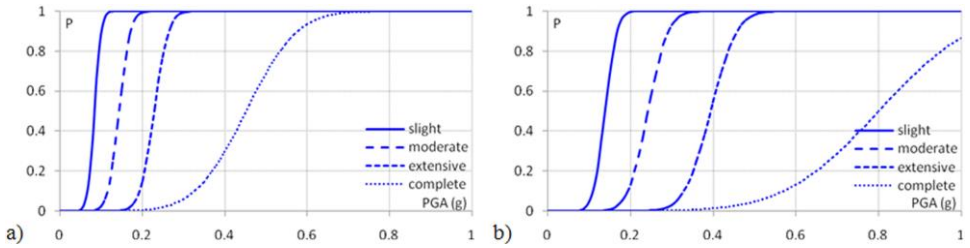

Fig. 11 Fragility curves for seismic soil-pile interaction: a) pier, b) pile

Table 2 Probability of fragility P_i for the typical seismic intensity measure PGA_i of the soil-pile interaction

		pier				pile			
damage		slight	moderate	extensive	complete	slight	moderate	extensive	complete
PGA=0.1g	P_i	0.88	0.02	0	0	0.04	0	0	0
PGA=0.2g	P_i	1	0.99	0.15	0	0.99	0.13	0	0
PGA=0.3g	P_i	1	1	0.99	0.06	1	0.93	0.03	0
PGA=0.4g	P_i	1	1	1	0.29	1	1	0.55	0.01
PGA=0.5g	P_i	1	1	1	0.69	1	1	0.98	0.05

Evaluation of the system performance is also performed by analyzing the system reliability state. When applying this analysis a more complete answer is obtained regarding the system state, and it is based on the previously considered fragility analysis. System reliability R is defined by [40]:

$$R = \Phi^{-1}(1-P)\,. \tag{41}$$

A negative R coefficient value indicates a possible failure and system unreliability, while a positive R coefficient value indicates that the failure probability is approximately equal to 0, i.e. that the system is reliable to a significant degree. When the R coefficient value is ≈6, then the system reliability is ≈100%, while in the case when R≈0, the system failure probability is P=50%. Reliability curves for the seismic soil-pile interaction are shown in Figures 12a and 12b for the pier and pile, respectively. Comparing the solutions obtained for the pier and pile, it can be concluded that the pier is more sensitive to the changing levels of intensity measure *PGA*, so that higher levels of uncertainty can be expected at lower *PGA* values, as compared to the pile. Typical values of seismic intensity measure of *PGA*=[0.1÷0.5]g and the corresponding values of reliability coefficient R_i for the seismic soil-pile interaction are shown in Table 3. Values of reliability probability beneath the diagonal in Table 3 are typically negative, while those above the diagonal are typically positive. The values on the diagonal itself and near to it in Table 3 are increasing. For P>50%, pier reliability at slight level of damage is *PGA*≤0.08g, at moderate level of damage is *PGA*≤0.14g, at extensive level of damage is *PGA*≤0.22g and at complete level of damage is *PGA*≤0.45g. For P>50%, pile reliability at slight level of damage is *PGA*≤0.13g, at moderate level of damage is *PGA*≤0.24g, at extensive level of damage is *PGA*≤0.39g and at complete level of damage is *PGA*≤0.8g.

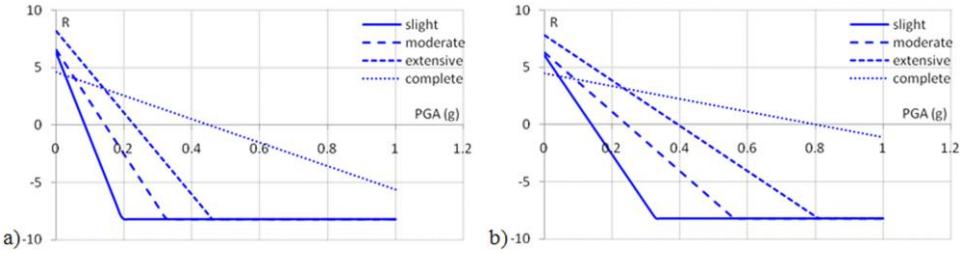

Fig. 12 Reliability curves for the seismic soil-pile interaction: a) pier, b) pile

Table 3 Values of reliability coefficient R_i for typical seismic intensity measures PGA_i of the soil-pile interaction

		pier				pile			
damage		slight	moderate	extensive	complete	slight	moderate	extensive	complete
PGA=0.1g	R_i	-1.17	2	4.60	3.61	1.70	3.71	5.85	3.90
PGA=0.2g	R_i	-8.22	-2.54	1.04	2.59	-2.65	1.12	3.86	3.35
PGA=0.3g	R_i	-8.22	-7.09	-2.52	1.56	-7.01	-1.48	1.87	2.79
PGA=0.4g	R_i	-8.22	-8.22	-6.08	0.54	-8.22	-4.07	-0.12	2.23
PGA=0.5g	R_i	-8.22	-8.22	-8.22	-0.49	-8.22	-6.67	-2.11	1.68

6. SUMMARY AND CONCLUSIONS

In this study, a numerical model has been developed for the soil-pile-bridge pier interaction in order to evaluate the system's seismic performance. The pier and pile were modelled according the principles of concretization, abstraction and discretization in numerical analysis using the finite element method. Effects representing the influence of soil were introduced by applying the principle of implicit modelling the nonlinear dynamic soil-pile interaction. The input signal to the system is treated through the generated artificial accelerograms, which were further processed by layers of soil and bedrock. The system response is analyzed in the capacitive domain using the incremental nonlinear dynamic analysis (INDA). The INDA analysis was processed in a successive manner by scaling the nonlinear dynamic analysis (NDA) according the defined scaling criteria.

The NDA and INDA analyses were post processed according to the global drift *DR* and the corresponding *PGA* values separately for the pier and separately for the pile, so that curves *PGA=f(DR)* were constructed in the capacitive domain. The IO, CP and GI performance levels were determined for these curves, and based on specific *DR* and *PGA* parameters regression analyses were carried for the linear function $\ln\mu=k\cdot\ln PGA+n$. The fragility curves were constructed based on the solutions of regression analysis and the probability theory of log-normal distribution for the *PGA* intensity measures. The intensity parameter *IM* is typically considered by identifying the corresponding response spectra with the variation of standard deviation $\pm\sigma$, which is a function of uncertainty of seismic demand that is imposed to the structure. However, in this study the authors applied a variation of seismic demand in a function of scaling the *IM* parameter, or *PGA* according to the INDA analysis. In this sense, it is possible to consider a much wider range of variation in seismic demand *PGA*=[0÷1]g without any further extrapolation. By

comparing the obtained solutions of the fragility curve for the pier and pile, it can be concluded that the pier is more sensitive to the changing levels of intensity measure *PGA*, than the pile. Thus, the same *PGA* level results in larger damage to the pier, where the development of higher intensity damage is also more likely. Based on the solutions obtained in fragility analysis, reliability curves were also constructed. By comparing the obtained solutions for the pier and pile, it can be concluded that the pier is more sensitive to the changing levels of intensity measure *PGA*, so that it can develop higher levels of uncertainty at lower *PGA* values, as compared to the pile. The methodological procedure for seismic performance analysis presented in this study provides an integrated quantitative and qualitative consideration and evaluation of the complex soil-foundation-structure interaction (SFSI).

REFERENCES

1. H. Krawinkler, Challenges and progress in performance-based earthquake engineering, International Seminar on Seismic Engineering for Tomorrow - In Honor of Professor Hiroshi Akiyama, Tokyo, Japan, 1999.
2. J. Moehle, H. Krawinkler, A framework methodology for performance-based earthquake engineering, The 13th World Conference on Earthquake Engineering, Paper No. 679, Vancouver, Canada, 2004.
3. D. Chang, T. Yang, C. Yang, Seismic performance of piles from PBEE and EQWEAP analyses, Geotechnical Engineering Journal of the SEAGS & AGSSEA, 41(2) (2010) 1-8.
4. M. Cubrinovski, B. Bradley, Assessment of seismic performance of soil-structure systems, The 18th NZGS Geotechnical Symposium on Soil-Structure Interaction, Auckland, New Zealand, 2008.
5. M. Cubrinovski, B. Bradley, Evaluation of seismic performance of geotechnical structures, International Conference on Performance-Based Design in Earthquake Geotechnical Engineering, Tsukuba, Japan, 2009.
6. A. Zafeirakos, N. Gerolymos, V. Drosos, Incremental dynamic analysis of caisson-pier interaction, Soil Dynamics and Earthquake Engineering, 48 (2013) 71-88.
7. B. Bradley, M. Cubrinovski, R. Dhakal, Performance-based seismic response of pile foundations, Geotechnical Earthquake Engineering and Soil Dynamics IV, ASCE Geotechnical Special Publication 181, Sacramento, USA, 2008.
8. F. Chen, H. Takemiya, J. Shimabuku, Seismic Performance of a Wib-Enhanced Pile Foundation, The 13th World Conference on Earthquake Engineering, Paper No. 1273, Vancouver, Canada, 2004.
9. B. Folic, R. Folic, Design methods analysis of seismic interactions soil-foundation-bridge structures for different foundations, NATO Advanced Research Workshop 983188: Coupled Site and Soil-Structure Interaction Effects with Application to Seismic Risk Mitigation, Borovets, Bulgaria, 2008.
10. W. Finn, Characterizing pile foundations for evaluation of performance based seismic design of critical lifeline structures, The 13th World Conference on Earthquake Engineering, Paper No. 5002, Vancouver, Canada, 2004.
11. H. Ghalibafian, C. Ventura, R. Foschi, Effects of nonlinear soil-structure interaction on the inelastic seismic demand of pile-supported bridge piers, The 14th World Conference on Earthquake Engineering, Beijing, China, 2008.
12. M. Alfach, Influence of soil plasticity on the seismic performance of pile foundations - a 3D numerical analysis, Jordan Journal of Civil Engineering, 6(4) (2012) 394-409.
13. T. Maki, S. Tsuchiya, T. Watanabe, K. Maekawa, seismic response analysis of pile foundation using finite element method, The 14th World Conference on Earthquake Engineering, Beijing, China, 2008.
14. T. Thavaraj, W. Finn, G. Wu, Seismic response analysis of pile foundations, Geotechnical and Geological Engineering, 28(3) (2010) 275-286.
15. M. Teguh, C. Duffield, A. Mendis, G. Hutchinson, Seismic performance of pile-to-pile cap connections: an investigation of design issues, Electronic Journal of Structural Engineering (EJSE), 6(1) (2006) 8-18.
16. SeismoStruct: User Manual, 254p, 2012, URL: http://www.seismosoft.com
17. SeismoStruct, URL: http://www.seismosoft.com
18. J. Mander, M. Priestley, R. Park, Theoretical stress-strain model for confined concrete, Journal of Structural Engineering, 114(8) (1988) 1804-1825.
19. Eurocode 2, Design of Concrete Structures - Part 1-1: General Rules and Rules for Buildings, European Committee for Standardization, Brussels, Belgium, 2003.
20. J. Simo, T. Hughes, Computational Inelasticity, Springer-Verlag, New York, USA, 1998.

21. J. Hellesland, A. Scordelis, Analysis of RC bridge columns under imposed deformations, IABSE Colloquium, Delft, Holland, 1981, pp. 545-559.
22. C. Fellipa, Nonlinear Finite Element Methods, University of Colorado, Boulder, USA, 2007.
23. N. Allotey, M. El Naggar, A numerical study into lateral cyclic nonlinear soil-pile response, Canadian Geotechnical Journal, 45(9) (2008) 1268-1281.
24. N. Allotey, El M. Naggar, Generalized dynamic winkler model for nonlinear soil-structure interaction analysis, Canadian Geotechnical Journal, 45(4) (2008) 560-573.
25. M. Ćosić, S. Brčić, Ground motion processing methodology for linear and nonlinear seismic analysis of structures, Journal of Construction (seriban), 66(11-12) (2012) 511-526.
26. Y. Fahjan, Selection, scaling and simulation of input ground motion for time history analysis of structures, Seminar on Earthquake Engineering and Historic Masonry, University of Minho, Braga, Portugal, 2010.
27. D. Gasparini, E. Vanmarcke, Simulated Earthquake Motions Compatible with Prescribed Response Spectra, Massachusetts Institute of Technology, Boston, USA, 1976.
28. S. Kramer, Geotechnical Earthquake Engineering, Prentice Hall, Upper Saddle River, USA, 1996.
29. D. Vamvatsikos, A. Cornell, Applied incremental dynamic analysis, Earthquake Spectra, 20(2) (2004) 523-553.
30. M. Ćosić, About the required number and size of increments in incremental nonlinear dynamic analysis, GNP 2010, Civil Engineering - Science and Practice, Žabljak, Montenegro, 2010.
31. H. Hilber, T. Hughes, R. Taylor, Improved numerical dissipation for time integration algorithms in structural dynamics, Earthquake Engineering and Structural Dynamics, 5(3) (1977) 283-292.
32. Simqke: URL: http://dicata.ing.unibs.it/gelfi/software/simqke/simqke_gr.htm
33. Eurocode 8, Design of Structures for Earthquake Resistance - Part 1: General Rules, Seismic Actions and Rules for Buildings, European Committee for Standardization, Brussels, Belgium, 2004.
34. Shake: URL: http://www.proshake.com
35. SEAOC Blue book: Recommended Lateral Force Requirements and Commentary, Report prepared by Structural Engineers Association of California, Sacramento, USA, 1999.
36. FEMA 356, Pre-Standard and Commentary for the Seismic Rehabilitation of Buildings, American Society of Civil Engineers, Federal Emergency Management Agency, Washington D.C., USA, 2000.
37. HAZUS, Earthquake Loss Estimation Methodology, National Institute of Building for the Federal Emergency Management Agency, Washington D.C., USA, 1997.
38. E. Choi, R. DesRoches, B. Nielson, Seismic fragility of typical bridges in moderate seismic zones, Engineering Structures, 26(2) (2004) 187-199.
39. N. Johnson, K. Samuel, N. Balakrishnan, Continuous Univariate Distributions, Vol. 1, Wiley-Interscience, New York, USA, 1994.
40. F. Nateghi-a, V. Shahsavar, Development of fragility and reliability curves for seismic evaluations of a major prestressed concrete bridge, The 13th World Conference on Earthquake Engineering, Paper No. 1351, Vancouver, Canada, 2004.

ANALIZA POVREDLJIVOSTI I POUZDANOSTI INTERAKCIJE TLO - ŠIP - STUB MOST

U radu je prikazana procedura evaluacije seizmičkih performansi interakcije šip-tlo inkrementalnom nelinearnom dinamičkom analizom (INDA - Incremental Nonlinear Dynamic Analysis). Ulazni signal u sistemu je tretiran preko generisanih veštačkih akcelerograma, a koji su dodatno procesirani po slojevima tla do osnovne stene. Postprocesiranje INDA analiza izvršeno je posebno za stub, a posebno za šip, tako da su konstruisane krive PGA=f(DR) u kapacitativnom domenu. Za ovako konstruisane krive određeni su performansni nivoi, a na osnovu određenih DR i PGA parametara sprovedene su regresione analize. Krive povredljivosti su konstruisane na osnovu rešenja regresione analize i teorije verovatnoće log-normalne raspodele. Takođe, konstruisane su i krive pouzdanosti na osnovu rešenja analize povredljivosti. Metodološki postupak za analizu seizmičkih performansi, prezentovan u ovom istraživanju, omogućava integrisano kvantitativno-kvalitativno razmatranje i evaluaciju kompleksne interakcije konstrukcija-tlo (SFSI - Soil-Foundation-Structure Interaction).

Ključne reči: *inkrementalna nelinearna dinamička analiza, performanse šipova, povredljivost, pouzdanost, veštački akcelerogrami.*

FACTA UNIVERSITATIS
Series:**Architecture and Civil Engineering** Vol. 16, No 1, 2018, pp. 113-123
https://doi.org/10.2298/FUACE170425009D

ROCK RAMP IMPACT ON THE RIVERINE HYDRAULIC

UDC 627.514.61

Yonko Dobrev[1], Slaviša Trajković[1], Milan Gocić[1], Dragan Milićević[1], Nikolay Lissev[1]

[1]Faculty of Hydraulic Engineering, University of Architecture, Civil Engineering and Geodesy - Sofia, Bulgaria
[2]University of Niš, Faculty of Civil Engineering and Architecture, Niš, Serbia

Abstract. *The following case study is part of a wider research of the impact of rock ramps on river environment. It aims to give a quantitative assessment of the velocity reduction in upstream section of a rock ramp. The alteration of the flow velocities is one of the most considerable factors for the habitat modification. The creation of still water environment in upstream impoundment might affect the physical properties of the habitat. Thus a mutation of the hydrobionts diversity may occur. By means of one – dimensional numerical model a comparative analysis of velocity fields is executed. Two cases are examined: before and after construction of a rock ramp with step – pools. The model proofs a significant flow velocity reduction in upstream section, which might have a negative environmental impact.Another point of interests of the study is the high flow river capacity. The flooded areas and the water level variation are evaluated at $Q_{50\%}$, $Q_{5\%}$ and $Q_{1\%}$. The results can be used for assessment of the structure reliability and for analysis of both: saturation of riparian zone and alteration of floodplain ecology.*

Key words*: Rock ramp, Water intake, River environment, Numerical modelling*

1. INTRODUCTION

The fragmentation of the longitudinal river corridor by weirs, dams, hydropower facilities and culverts represents a major global human impact on running waters (Broadhurst et al., 2012, Stoller et al., 2016). While the obvious and often irreversible impacts of large impoundments are now well recognized, there is also growing awareness of the pivotal role of the flow regime as a key 'driver' of the river ecology and their associated floodplain (Baki et al., 2014, 2015, 2016).

Received April 25, 2017 / Accepted June 14, 2017
Corresponding author: Milan Gocić
Faculty of Civil Engineering and Architecture, University of Niš, 18000 Niš, Aleksandra Medvedeva 14, Serbia
E-mail: mgocic@yahoo.com

The impact from alterations to natural hydrology, changes to stream geomorphology, disruption of localised erosion and sedimentation processes, evaporative water loss, creation of still water environments, impediment of larval drift and extractive water use have had a severe negative impact on the abundance and diversity of native fish populations and the quality of aquatic habitats throughout the world (Ghimire and Jones, 2014, Cassan and Laurens, 2016).

Many fish species display a preference for particular types of habitat such as pools, riffles or backwater areas (Matthews, 1985, Angermeier, 1987, Pusey et al., 1993). The richness of the fauna often increases as habitat complexity increases, with depth, velocity and cover being the most important variables governing this relationship (Gorman and Karr, 1978, Felley and Felley, 1987, Pusey et al., 1995).

The Marica River is located in South Bulgaria and is a part of the European network Natura 2000 for protection of the habitats. In some areas, it is included in the network for protection of the birds. Its waters are used intensively for public water supply, irrigation and industry.

In the last decades, as a result of the increased anthropogenic impact in the river basin, considerable river bed degradation has been observed. In certain areas, there is coastal erosion that puts at risk a number of facilities and farmlands. The main reasons for this negative trend are sand and gravel extraction, river modification, and disturbed sediment balance in the river basin.

As a consequence of the above mentioned problems, water level decreases constantly and many of the water intake structures are left above the water level. The challenge is to find an engineering solution, which will stabilize the river bed and increase the water level, without considerable fragmentation of the river ecosystem.

2. DESCRIPTION OF THE FACILITY

The Marica River is the largest river in Bulgaria with a catchment area about 53 000 km^2 (Fig. 1). It rises from Marichini lakes in Rila mountain. Its mean annual flow varies from 0.628 m^3/s at altitude of 1900 m to 107.92 m^3/s at the border between Bulgaria and Turkey.

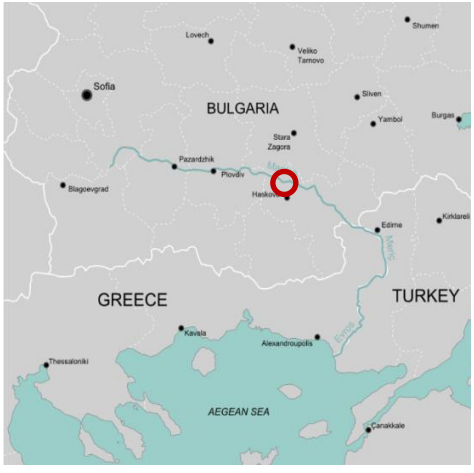

Fig. 1 Location of the Marica River and the examined section

The examined section of the Marica River is a part of the European ecological network Natura 2000 for the habitats and birds protection, which presumes significant requirements for design and construction of weirs or dams in the Management Plan of the River basin. The midstream represents a modified river section for protection of harmful effects of water. During the last decades, due to the active anthropogenic impact considerable erosion process occurred (Fig. 2).

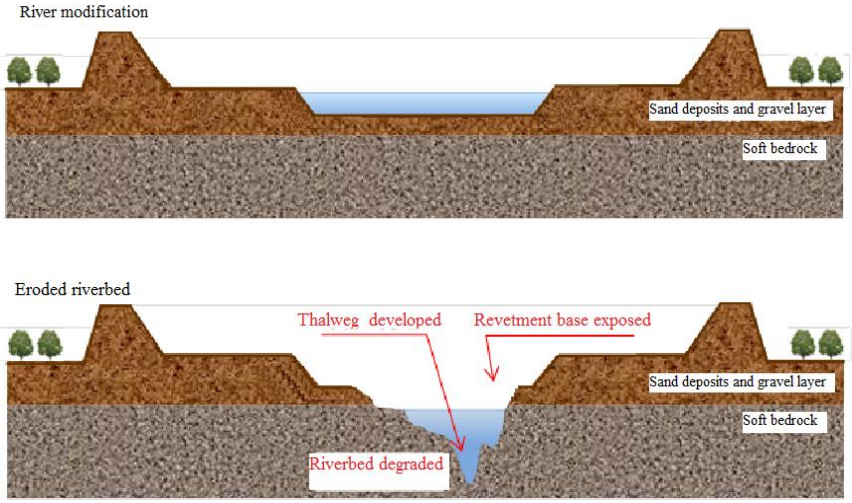

Fig. 2 River bed degradation

A scenario with rock ramp construction is investigated, as an erosion control structure with a low ecological impact. There are different types of block ramps: on the one hand the block ramps formed by a block carpet, where the entire flume width is covered by blocks, and on the other hand the block ramps formed by different configuration of clusters (Fig. 3). Each ramp type establishes different hydraulic conditions and thus needs to be investigated separately (Tamagni, 2013).

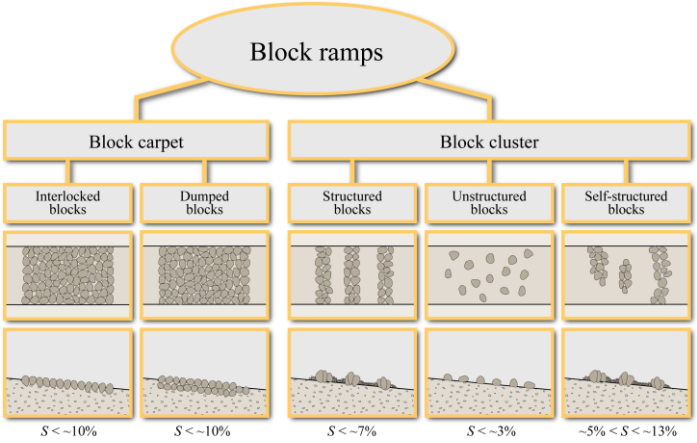

Fig. 3 Classification of block ramps (Tamagni, 2013)

The proposed facility (step – pool rock ramp) aims to increase the water level, providing water discharge for the diversion canal, and to limit the erosion process in the river bed (Fig. 4). At the same time it offers an opportunity for migration of different fish species at different water discharges.

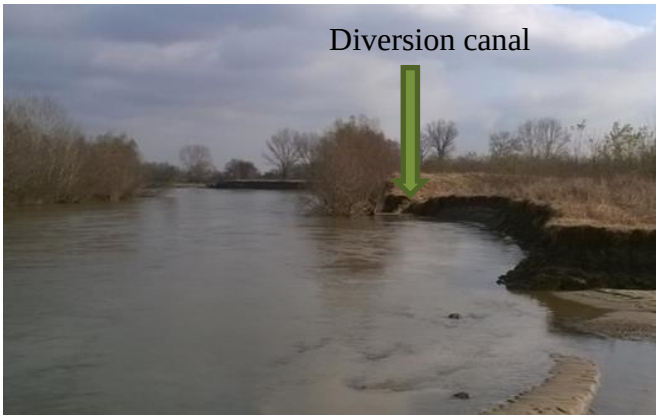

Fig. 4 River bed erosion and collapsed water intake

The rock ramp (Fig. 5) consists of a low-flow channel designed to maintain biologically adequate depth and velocity conditions for upstream and downstream migration during periods of small discharges (Studer and Schleiss, 2009, 2011). Under low-flow conditions, downstream sections are unlikely to influence flow depths on the ramp. Therefore, hydraulics could be determined using normal depth calculations which provide a quick determination of the low-flow channel width and ramp length meeting low-flow fish passage depth and velocity conditions (Mooney, 2007).

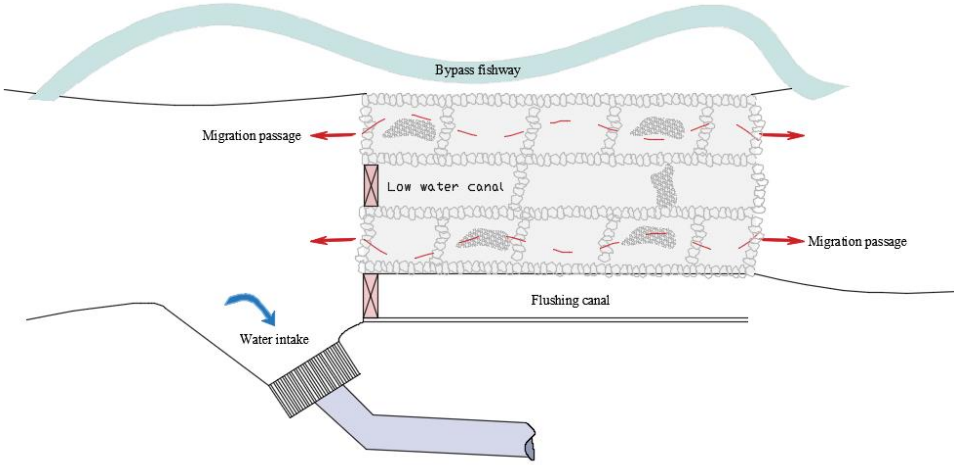

Fig. 5 Plan of a water intake with rock ramp

In the zone of the water intake is located the flushing channel for the deposited sediments. Its additional purpose is to release part of the high flow discharges.

The fish migration might occur through the bypass fish way or through the rock ramp body. The position and the size of the step – pools are from great importance. There are various configurations and arrangements of rock that can be utilized provided the rock is large enough to be essentially immobile and the drops are low enough to allow aquatic life to migrate upstream (Tamagni et al., 2010). The variety of flow conditions in the step – pools is an important issue, which solution could be proofed by 3D model.

Within the framework of this study is examined a solution with the construction of a rock ramp (2.4 m high, 1:30 longitudinal slope). The effects of this measurement should be stabilization of the river bed, groundwater accumulation, as well as water supply for wetlands and floodplains due to rising water levels. Access to the flood plains is essential to the reproduction of numerous species that spawn in such habitats when food resources are abundant. Effective management of floodplain barriers is required to ensure that ecological functioning is maintained. The proposed concept aims to ensure a water discharge for the intake structures under the following conditions:

- flow characteristics and dynamics preservation,
- preservation of river continuum,
- reliable erosion protection,
- high water flow conveying.

Qualitative assessment of the flow characteristic and dynamic preservation rate could be given after comparative analysis of the velocity fields for both cases: before and after the rock ramp construction. The rivers in their upper and middle streams are composed of small sections (meso-scale habitats) with different physical characteristics (rapids, still water etc.), which represent a wide range of microhabitat variables as water depth, flow velocity, substrate, and shading. Usually, if a weir is constructed the upstream zone gets more homogenous, the flow velocity decreases significantly, the water depth increases and substrate gets more monotonous. In many cases that causes a considerable habitat modification, which leads to distribution shifts of the typical fish species, macrozoobenthos and macrophytes to fatally block or delay upstream fish migration.

The water continuum preservation is a very complicated issue, because it requires a complex evaluation. On one hand the river ecosystem fragmentation causes disturbance of the migration of species, which depend on longitudinal movements along the stream continuum during certain phases of their life cycle. This requires detailed information for the hydrobionts, their migration behaviour and capacity. On the other hand the disturbance of the sediment balance and the nutrient distribution as a consequence of the weir or dam construction might lead to upstream habitat modification and to downstream erosion processes and nutrient demand.

3. Numerical Model

The main abiotic factors that have an impact on the specifics of the flow and thus on the physical characteristics of the habitats are: flow velocity, water depth and water level variation.

The two basic purposes of the modelling procedure are to determine the flow velocity alteration in the upstream river section as a consequence of the rock ramp construction and to verify the river capacity during peak water discharge.

3.1. Description of the model

The study is conducted using a numerical 1D model HEC – RAS (Hydrologic Engineering Center - River Analysis System) version 5.0, developed by the U.S. Army Corps of Engineers. The HEC – RAS system contains the following river analysis components for: (1) steady flow water surface profile computations; (2) one-dimensional and/or two-dimensional unsteady flow simulation; (3) quasi unsteady or fully unsteady flow movable boundary sediment transport computations; and (4) water quality analysis. The component for steady flow, which is used in this case, is intended for calculating water surface profiles for steady gradually varied flow, where the following flow condition is assumed (Brunner, 2016):

- steady flow,
- hydrostatic pressure distribution,
- velocity vector is in flow direction only,
- no channel geometry alteration in time.

The basic computational procedure is based on the solution of the one dimensional energy equation (Bernoulli equation) by means of the standard step method. The energy losses are evaluated by friction (Manning's equation) and contraction/expansion (coefficient multiplied by the change of velocity head).

For this case study purposes a georeferencing model with 111 profiles was created, which covered more than 6000 m long river section. The profiles and the areas with different Manning coefficient were defined (Richardson et al., 2001, Rice et al., 1998) in ArcMap 10.4. Two scenarios were considered – before and after construction. The calculations were performed for water discharges with the following probabilities: 1%; 5%; 25%; 50%; 75%; 95%;

3.2. Results

3.2.1. Velocity field's alteration

It is obvious from the results that the velocity variation curves follow the same trends in both cases: before and after construction (Fig. 6). The difference between the values varies from 30% to 60% in some sections. As it was expected, the zone with the lowest velocities is in the area before the rock ramp, where the differences in values are the highest. The final assessment, how the flow velocity reduction and the increased water depth will modify the habitats, must be given after detailed analysis of their physical properties and the behaviour of the hydrobionts, which is not part of this study.

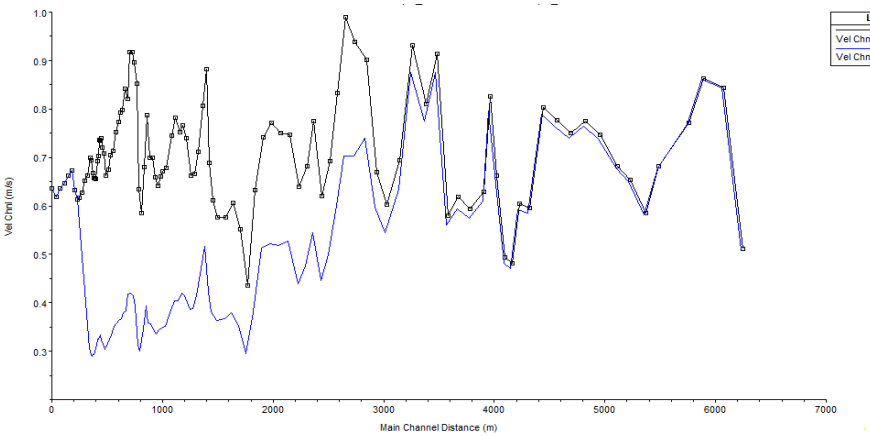

Fig. 6A Flow velocity curves before and after construction for $Q_{25\%}$

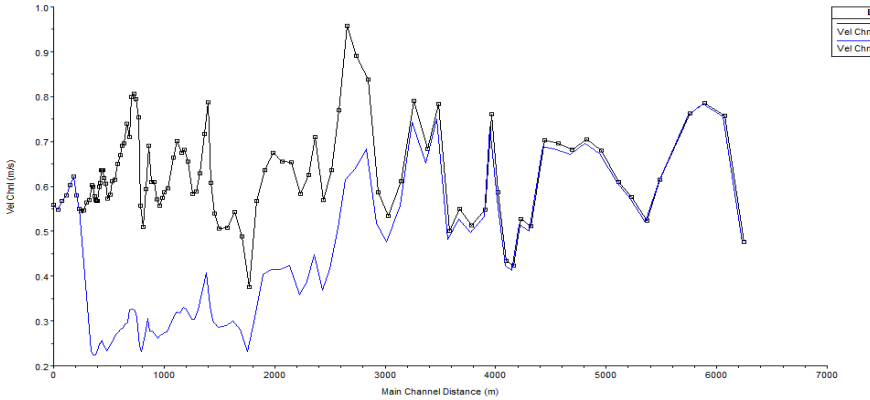

Fig. 6B Flow velocity curves before and after construction for $Q_{50\%}$

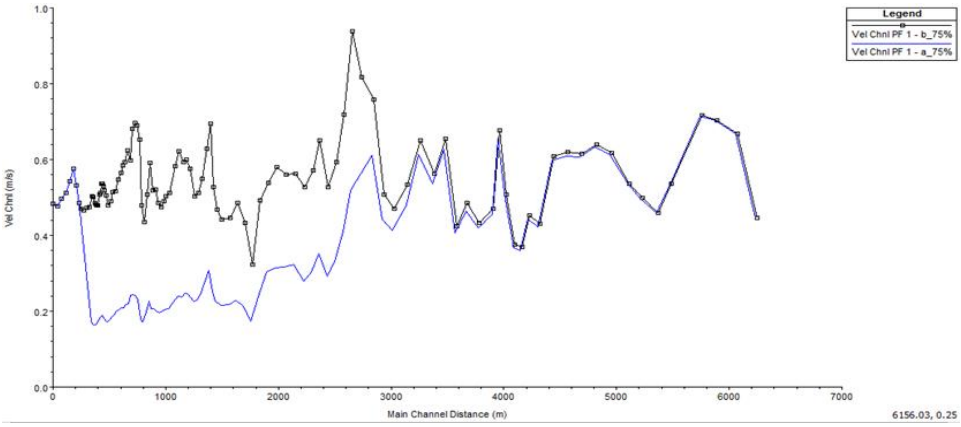

Fig. 6C Flow velocity curves before and after construction for $Q_{75\%}$

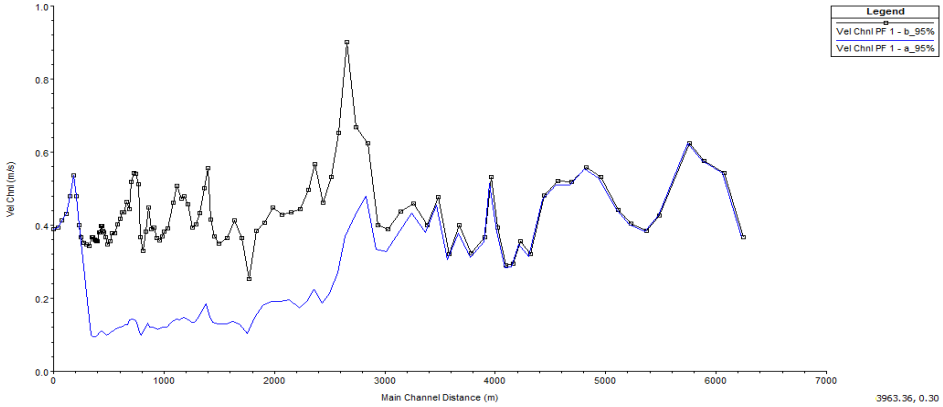

Fig. 6D Flow velocity curves before and after construction for $Q_{95\%}$

3.2.2. High flow river capacity

The structure reliability analysis is performed for water discharges $Q_{1\%}$ and $Q_{5\%}$, according to the Bulgarian legislation. The results indicate an insignificant flow modification caused by the rock ramp construction. The reason could be explained with the shape of the river bed cross section, which could be interpreted as a compound trapezoid. With higher water discharge than $Q_{5\%}$ the rock ramp is fully submerged and water level reaches the levees toe. This can be seen from the rating curves comparison (Fig. 7) and from the flooded areas map (Fig. 8). With water discharge $Q_{1\%}$ flow over the levees crown is not to be expected.

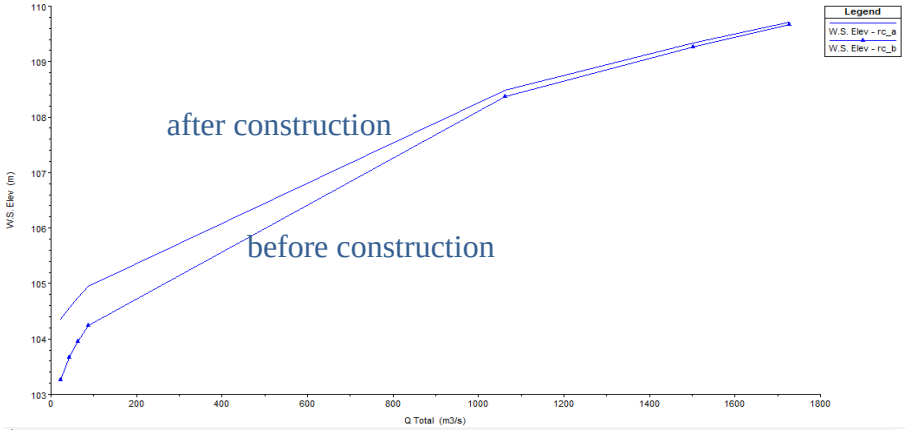

Fig. 7 Rating curves before and after construction

Fig. 8A Flooded areas at $Q_{50\%}$

Fig. 8B Flooded areas at $Q_{5\%}$

Fig. 8C Flooded areas at $Q_{1\%}$

4. CONCLUSIONS

The flow velocity alteration in upstream section of weir or dam is an important prerequisite for analysis of the river ecosystem modification. The excessive decrease might lead to changing of the physical, chemical and biological properties of the habitat.

The designed rock ramp causes a significant velocity reduction in upstream section, in some areas with more than 50%. The velocity curve profile gets flatter after the facility construction, which means reduction of the flow patterns diversity. It is important to note, however that one – dimensional modelling estimates mean values of velocities in every cross section, which might be an effective starting point for further investigations. Flow variety might be examined more precisely by means of more dimensional models.

With regard to the high water conveying, an insignificant water level increase by reason of the rock ramp construction is observed. At $Q_{50\%}$ the Northeast bank gets partly submerged, due to its flatter topography. The influence of the rock ramp on the water level decreases with increasing the flow discharge.

REFERENCES

1. Angermeier, P.L. (1987) Spatiotemporal variation in habitat selection by fishes in a small Illinois stream. Pages 52-60 in D. C. Matthews and W. J. Heins (eds.) Community Ecology of North American Stream Fishes. University of Oklahoma Press, London.
2. Baki, A.B.M., Zhu, D.Z., Rajaratnam, N. (2014) Mean Flow Characteristics in a Rock-Ramp-Type Fish Pass, Journal of Hydraulic Engineering 140 (2), 156-168.
3. Baki, A.B.M., Zhu, D. Z., Rajaratnam, N. (2015), Turbulence Characteristics in a Rock-Ramp-Type Fish Pass, Journal of Hydraulic Engineering, 141(2), doi:10.1061/(ASCE)HY.1943-7900.0000962.
4. Baki, A.B.M., Zhu, D. Z., Rajaratnam, N. (2016) Flow Simulation in a Rock-Ramp Fish Pass, Journal of Hydraulic Engineering 142(10), doi:10.1061/(ASCE)HY.1943-7900.0001166.
5. Broadhurst, B.T., Ebner, B.C., Clear, R.C. (2012) A rock-ramp fishway expands nursery grounds of the endangered Macquarie perch (Macquaria australasica), Australian Journal of Zoology, 60(2), 91-100.
6. Brunner, G. W. (2016) HEC - RAS River Analysis System, Hydraulic Reference Manual. U.S Army Corps of Engineers.
7. Cassan, L., Laurens, P. (2016) Design of emergent and submerged rock-ramp fish passes, Knowledge and Management of Aquatic Ecosystems, 417(45), doi: 10.1051/kmae/2016032.
8. Felley, J.D., Felley, S.M. (1987) Relationships between habitat selection by individuals of a species and patterns of habitat segregation among species: fishes of the Calcasieu drainage. Pages 61-68 in D.C. Matthews and W.J. Heins (eds.) Community Ecology of North American Stream Fishes. University of Oklahoma Press, London.
9. Ghimire, S., Jones, G. (2014). Restoration of a gauging weir to aid fish passage. Journal of Hydro-environment Research 8, 43-49.
10. Gorman, O.T., Karr, J.R. (1978) Habitat structure and stream fish communities. Ecology 59:507-515. Schlosser, I.J. 1982. Fish community structure and function along two habitat gradients in a headwater stream. Ecological Monographs 52, 395-414.
11. Matthews, W.J. (1985) Critical current speeds and microhabitats of the benthic fishes, Percina roanoka and Etheostoma flabellare. Environmental Biology of Fishes 12, 303-308.
12. Mooney, D.H.J. (2007). Rock Ramp Design Guidelines. Denver: U.S Department of the Interior Bureau of Reclamation Technical Service Center.
13. Pusey, B.J., Arthington, A.H., Read, M.G. (1993) Spatial and temporal variation in fish assemblage structure in the Mary River, south-east Queensland: the influence of habitat structure. Environmental Biology of Fishes 37, 355-380.
14. Rice, C.E., Kadavy, K.C., Robinson, K.M. (1998) Roughness of Loose Rock Riprap on Steep Slopes. Journal of Hydraulic Engineering, 124(2), 179-185.

15. Richardson, E.V., Simons, D.B., Lagasse, P.F. (2001) Hydraulic Design Series No. 6, River Engineering for Highway Encroachments, Highways in the River Environment,. U.S. Department of Transportation Federal Highway Administration, Publication No. FHWA NHI 01-004. p. 6.1-74.
16. Stoller, J., Hayes, D., Murry, B. (2016) Effects of a rock-ramp fishway on summer fish assemblage in a Lake Huron tributary, Fisheries Management and Ecology, 23(5), 407-417.
17. Studer, M., Schleiss, A. (2009) Velocity and Water Depth Analysis on Different Types of Block Ramps. Proceedings of the 33rd IAHR Congress: Water Engineering for a Sustainable Environment, 710-717.
18. Studer, M., Schleiss, A. (2011) Analyse von Fliessgeschwindigkeiten und Abflusstiefen auf verschiedenen Typen von Blockrampen. WasserWirtschaft 101(1–2), 67–71.
19. Tamagni, S. (2013) Unstructured block ramps. *Mitteilungen* 223, Versuchsanstalt für Wasserbau, Hydrologie und Glaziologie (VAW), R. M. Boes, Hrsg., ETH Zürich, 1-4.
20. Tamagni, S., Weitbrecht, V., Boes, R. (2010) Design of unstructured block ramps: a state-of-the-art review. In: Dittrich A, Koll K, Aberle J, Geisenhainer P (eds) River Flow 2010 Proceedings of the International Conference on Fluvial Hydraulics. Bundesanstalt für Wasserbau, Karlsruhe, pp 729–736.

UTICAJ KAMENE RAMPE NA HIDRAULIKU REKE

Studija slučaja prikazana u ovom radu je deo šireg istraživanja o uticaju kamenih rampi na životnu sredinu reke. Ona ima za cilj da da kvantitativnu procenu smanjenja brzine u uzvodnoj deonici kamene rampe. Promena brzine toka je jedan od najznačajnijih faktora za modifikaciju staništa. Formiranje mirne vodene sredine u uzvodnom usporu može uticati na fizička svojstva staništa. Tako može doći do promene biodiverziteta organizama koji žive u vodenoj sredini. Primenom jednodimenzionalnog numeričkog modela izvršena je komparativna analiza polja brzina u zoni kamene rampe. Ispitana su dva slučaja: pre i posle izgradnje kamene rampe sa stepenik – bazen strukturom. Model dokazuje značajnost smanjenja brzine toka vode u uzvodnoj deonici, što može imati negativan uticaj na životnu sredinu.Još jedan aspekt interesovanja ove studije je kapacitet reke sa kamenom rampom za prijem velikih voda. Poplavljena područja i varijacije nivoa vode su procenjeni za proticaje Q50%, Q5% i Q1%. Rezultati mogu da se koriste za procenu pouzdanosti strukture i za analizu kako zasićenja priobalja, tako i promene ekologije u poplavljenom području.

Ključne reči: *kamena rampa, zahvat vode, životna sredina reke, numeričko modelovanje.*

FACTA UNIVERSITATIS
Series: **Architecture and Civil Engineering** Vol. 16, No 1, 2018, pp. 125-134
https://doi.org/10.2298/FUACE170712010V

SENSITIVITY ANALYSIS OF TIMBER-CONCRETE COMPOSITE STRUCTURES

UDC 624.016

Nikola Velimirović[1,2], Dragoslav Stojić[1]

[1]University of Niš, Faculty of Civil Engineering and Architecture, Niš, Serbia
[2]University of Niš, Faculty of Science and Mathematics

Abstract. *The sensitivity analysis could be defined as a study of how the variability of the output parameter of the considered model can be distributed to its sources, actually, on the variability of the various input model parameters. It helps to identify the most important design parameters of a particular structure and to focus on them during the design and optimization process. This paper is focused on the application of stochastic sensitivity analysis of maximum equivalent stress and maximum mid-span deflection of timber-concrete composite beam. All input parameters were considered to be random variables. Latin Hypercube Sampling numerical simulation method was employed. The estimation of the sensitivity was derived from Spearman rank-order correlation coefficient.*

Key words: *sensitivity analysis, timber-concrete composite, simulation method, Spearman rank-order correlation*

1. INTRODUCTION

The design of building structures is a comprehensive process in which the most favorable design solution should be proposed. The design parameters that describe the proposed geometry of the structure, the material properties and the all influences on the structures should be considered during the design process. In order to more efficiently develop design proposals it is a great benefit to be able to identify the most important input parameters that have the greatest impact on a particular output parameter, such as, load-carrying capacity or deformation.

The sensitivity analysis could be defined as a study of how the variability of the output parameter of the considered model can be distributed to its sources, actually, on the variability of the various input model parameters [1]. It provides us with the ability to

Received July 12, 2017 / Accepted August 15, 2017
Corresponding author: Nikola Velimirović
Faculty of Civil Engineering and Architecture, University of Niš, 18000 Niš, Aleksandra Medvedeva 14, Serbia
E-mail: velimirovic.nikola@gmail.com

identify the most important design parameters of a particular structure and helps to focus on them during the design and optimization process. It is desirable to perform the sensitivity analysis at an earlier design stage, when it is possible to change the most important design parameters.

The sensitivity analysis can generally be divided into two basic categories: the deterministic and the stochastic sensitivity analysis. The deterministic sensitivity analysis is often referred to as design sensitivity, because it is often used in the design of structures. It uses a design model that allows a successive change in the value of the input parameters of the design model, considering the effect of their change on the desired output parameter. The basic principle of this analysis is that the estimation of the variability of the output design parameter is based on the variation of only one input parameter, while the other design parameters have a constant value. This study represents the simplest way of considering the relative impact of different input design parameters that vary within its range by comparing the obtained results from the observed output parameter in each calculation step. Although this study is easy to apply in practice and it provides a quick overview of the performance of the design model, it neglects the correlation among the input design parameters that certainly exist in real conditions. Also, it cannot perceive significant information about the character of the variability of the input design parameters. However, the stochastic sensitivity analysis provides much more complex information about the design parameters because they are considered as the random variables with a certain distribution. Unlike the deterministic sensitivity analysis, the variability of a particular output parameter due to a single input parameter is evaluated by varying all other design parameters at the same time. The influence of other design parameters is relevant for consideration, because in real conditions overall characteristics of structure depend on the correlation of all design parameters.

2. STOCHASTIC SENSITIVITY ANALYSIS BASICS

The methodology of conducting a stochastic sensitivity analysis is the same for different fields of its application, but the difference is in defining the basic steps that may vary from case to case. Based on the review and analysis of available literature [2,3,4,5], we have defined the basic steps in the stochastic sensitivity analysis:

1) Defining the design model of the structure based on the selected input design parameters that we want to include in the analysis as well as defining the output parameters taking into account the questions that should be answered by this sensitivity analysis
2) Characterization of the input design parameters defining the distribution and characteristics of each random variable
3) Generating a sample of the input design parameters through the use of an appropriate random sampling method
4) Conducting a series of numerical simulations over a design model in order to calculate the output parameter
5) Evaluation of the impact and relative importance of each input design parameter on the observed output parameter

In order to conduct the stochastic sensitivity analysis, it is necessary to use numerical simulation methods. They are mainly based on calculating a deterministic problem several

times, each time with a different set of input data. The generated samples of the input design parameters present input data sets for numerical simulations and can be represented by the matrix *N*x*M*. Each row in this matrix represents the input data of the independent numerical simulation. Matrix element x_{ij} represents the individual sample of each input design parameter.

$$\begin{bmatrix} x_{11} & x_{12} & \dots & x_{1m} \\ x_{21} & x_{22} & \dots & x_{2m} \\ \dots & \dots & \dots & \dots \\ x_{n1} & x_{n2} & \dots & x_{nm} \end{bmatrix} \rightarrow \begin{bmatrix} y_1 \\ y_2 \\ \dots \\ y_n \end{bmatrix} \tag{1}$$

The Monte Carlo sampling method is the most common method for the generation of such a matrix. The Latin Hypercube Sampling (LHS) method [6], which is applied in this paper, represents advanced and more efficient form of the Monte Carlo sampling method. This method is very popular, because its efficient method of spreading domains allows obtaining a large amount of information on variability and sensitivity based on a relatively small sample. The LHS method generates samples of input design parameters, taking into account the predetermined probability distribution for each of the input parameter. This method ensures that each input parameter has full coverage of its range.

In general, we can distinguish two types of stochastic sensitivity analysis: methods based on variance analysis and methods based on regression and correlation. Methods based on variance analysis perform the distribution of the total variance of the output parameter to the input parameter variance, while the methods based on regression and correlation use the regression of the output parameter to the input parameters [7].

In this paper, the estimation of the sensitivity will be derived from Spearman rank-order correlation coefficient (ρ) [8] which is defined as follows:

$$\rho_i = 1 - \frac{6\sum d_i^2}{n(n^2-1)} \tag{2}$$

where d_i is a difference between each pair of ranges of the corresponding variables X_j and Y, and n denotes the number of pairs of samples.

Spearman rank-order correlation coefficient ρ_i indicates the strength of a monotone connection between the variables and can have a value of +1 to -1. The value +1 indicates the perfect link of ranks, while the value -1 shows the perfect negative link of ranks. On the other hand, when the value of the coefficient ρ_i is equal to zero, this indicates the absence of a connection between the ranks.

3. Application of Sensitivity Analysis in the Design of Timber-concrete Composite Beams

Timber-concrete composite (TCC) structure is a structural system in which the timber beam is connected to the concrete flange using different types of shear connectors. In this paper we will consider a simply supported TCC beam of span 4m. The concrete flange is made of concrete strength class C25/30 and the timber beam is made of Spruce, sawn soft-wood strength class C27. The dimensions of the considered beam have been adopted

to present the usual dimensions of TCC floors (Figure 1). Based on the literature review about TCC floors, we have adopted the width of the concrete slab (b_c) to be 70 cm, while its height (h_c) is 7 cm. The width of the timber beam (b_t) is 10 cm, and its height (h_t) is 20 cm.

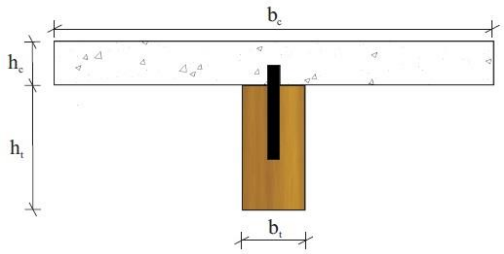

Fig. 1 Timber-concrete composite cross section

The observed TCC beam is loaded with imposed load of 3 kN/m^2 which is recommended for residential and office buildings, based on Eurocode 1 [9]. In our case, the connection between the timber and concrete part was achieved by the glued-in steel rods ϕ20/150 *mm*, made of the steel grade S235 and placed on every 24 cm. Steel rods are installed at right angles to the beam in the previously drilled holes and coated with an epoxy resin [10].

3.1. Numerical model of timber-concrete composite beam

In recent years, numerical models of structures are increasingly used in design process to simulate their behavior. Generation of the numerical model of the TCC beam was carried out using the finite element method in the software package ANSYS Workbench 15.0. This analysis uses the symmetry of the beam and the load. Therefore, the 3D model of the half of the beam is generated, which is shown in Figure 2. The concrete is modeled using the finite elements SOLID 258. The timber is modeled as an orthotropic material, using SOLID158 elements. The steel used for shear connectors is modeled using SOLID158 elements, as well.

The TCC beam is modeled considering the different friction coefficients between the contact surfaces of the constituent elements. The following friction coefficients between the materials were used: timber-concrete 0.5 [11], timber-steel 0.57 [12] and steel-concrete 0.9 [13]. The contact elements TARGE170 and CONTA174 were used to model the contact between the different parts of this TCC beam.

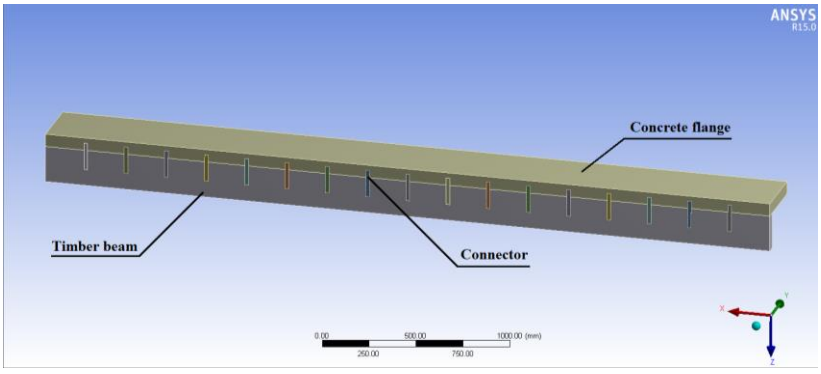

Fig. 2 3D model of the half of TCC beam

3.2. Selection and characterization of the input design parameters

Taking into account all the parameters that make the previously generated numerical model, would make the sensitivity analysis too cumbersome. Therefore, we have selected a number of design parameters that are shown in Table 1. The characterization of the selected input parameters will be determined based on the JCSS Probabilistic Model Code [14]. Table 1 gives an overview of the selected probability distribution, mean value and coefficients of variation for each of the selected input parameters involved in this sensitivity analysis.

Table 1 Input design parameters involved in this analysis

Design parameter	Quantity	Dimension	Distribution	Mean	Coefficient of variation
Concrete flange width	b_c	*mm*	Normal	700	0.02
Concrete flange height	h_c	*mm*	Normal	70	0.02
Timber beam width	b_t	*mm*	Normal	100	0.01
Timber beam height	h_t	*mm*	Normal	200	0.01
Diameter of the connector	d_s	*mm*	Normal	20	0.02
Number of connectors	n_s	*kom*	Uniform	17	
Concrete Young's modulus	E_c	*MPa*	Lognormal	31000	0.05
Density of the concrete	ρ_c	kg/m^3	Normal	2300	0.04
Timber Young's modulus	E_{tx}	*MPa*	Lognormal	12000	0.13
Density of the timber	ρ_t	kg/m^3	Normal	450	0.1
Steel Young's modulus	E_s	*MPa*	Lognormal	210000	0.13

3.3. Sensitivity analysis of the output parameter

The results of the conducted sensitivity analysis can be presented in different ways, but in engineering the common way is using the bar chart. Input parameters with a higher correlation coefficient have a greater influence on the observed output parameter, while the input parameters with a correlation coefficient whose value is close to zero have a low impact on the observed output parameter. The positive sensitivity of an input parameter indicates that as the value increases, the value of the observed output parameter increases as well. However, the negative sensitivity shows that with the increase in its value, the value of the considered output parameter decreases.

3.3.1. Sensitivity analysis of maximum equivalent stress

Firstly, we will present the results of the stochastic sensitivity analysis of the maximum equivalent stress σ_e, given in Table 2.

Table 2 Spearman rank-order correlation coefficients of the maximum equivalent stress

	b_t	d_s	n_s	h_c	h_t	b_c	E_c	E_s	E_t	ρ_c	ρ_t
ρ	0.05	-0.49	-0.57	-0.06	-0.12	0.2	-0.01	0.47	0.04	0.21	-0.01

Also, these results could be presented using the bar chart, as it shown in figure 3.

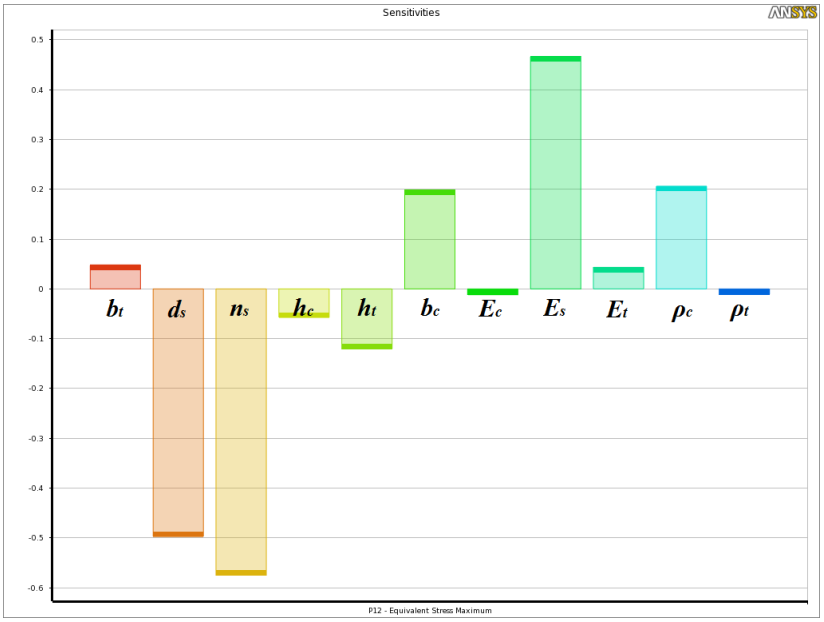

Fig. 3 Sensitivities of the maximum equivalent stress

Considering the results of the conducted stochastic sensitivity, it is noticeable that the parameters which describe shear connectors, such as the number of rods (n_s), the diameter of connector (d_s) and the Young's modulus of the steel (E_s) have the dominant influence on the maximum equivalent stress. Also, from the given results, it can be concluded that the increase in the values of the input design parameters b_t, b_c, E_s, E_t and ρ_c directly affects the increase in the maximum equivalent stress of the observed TCC beam. Also, as the values of the design parameters (d_s, n_s, h_c, h_t, E_c and ρ_t) increase, the maximum equivalent stress of the observed TCC beam reduces.

3.3.2. Sensitivity analysis of the maximum mid-span deflection

The results of the stochastic sensitivity analysis of the maximum deflection of the observed TCC beam, given in Table 3.

Table 3 Spearman rank-order correlation coefficients of maximum mid-span deflection

	b_t	d_s	n_s	h_c	h_t	b_c	E_c	E_s	E_t	ρ_c	ρ_t
ρ	-0.03	-0.04	-0.22	-0.24	-0.42	0.31	-0.28	-0.07	-0.61	0.29	0.07

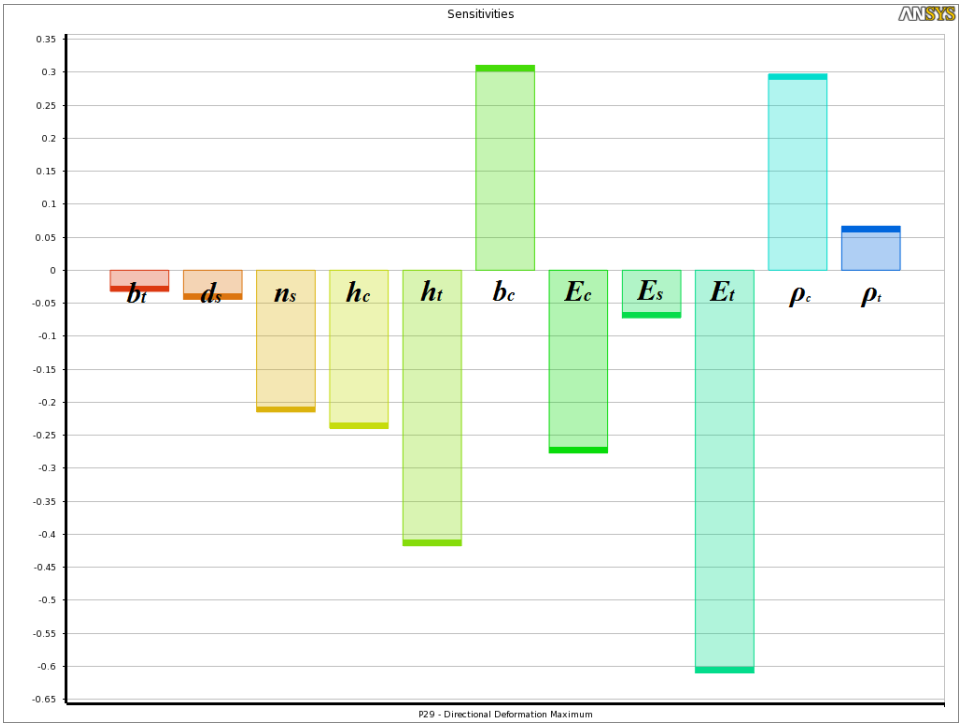

Fig. 4 Sensitivities of the maximum mid-span deflection

In Figure 4, we graphically presented the results of the stochastic sensitivity analysis of the maximum mid-span deflection of the TCC beam. It is interesting to note that the parameters which describe shear connectors, the diameter of the rod (d_s), the number of connectors (n_s) and the Young's modulus of the steel (E_s) do not have a dominant influence on the maximum mid-span deflection of the TCC beam. Based on the results of conducted sensitivity analysis, it can be concluded that the increase in the values of the design input parameters b_c, ρ_c and ρ_t directly affects the increase in the maximum mid-span deflection of the beam. Also, as the value of the design input parameters (b_t, d_s, n_s, h_c, h_t, E_c, E_s and E_t) increases, the maximum deflection of the observed beam decreases.

3.4. Response surface method

In order to better understand the correlation among the input parameters and the output parameter the Response surface method (RSM) is employed. This method provides a more precise description of correlation among design parameters [15].

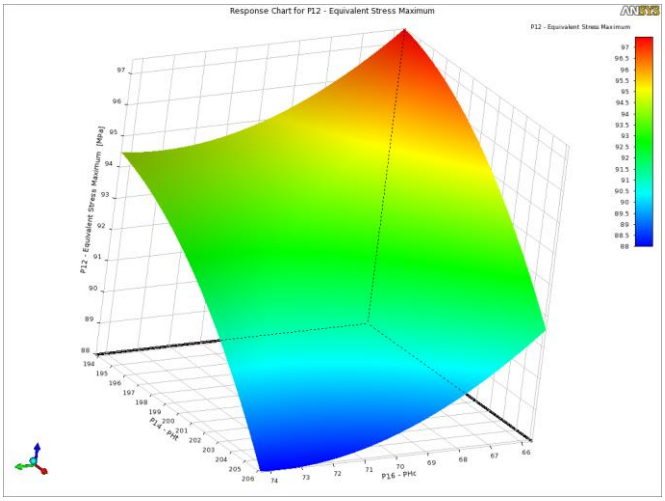

Fig. 5 Response surface for maximum equivalent stress

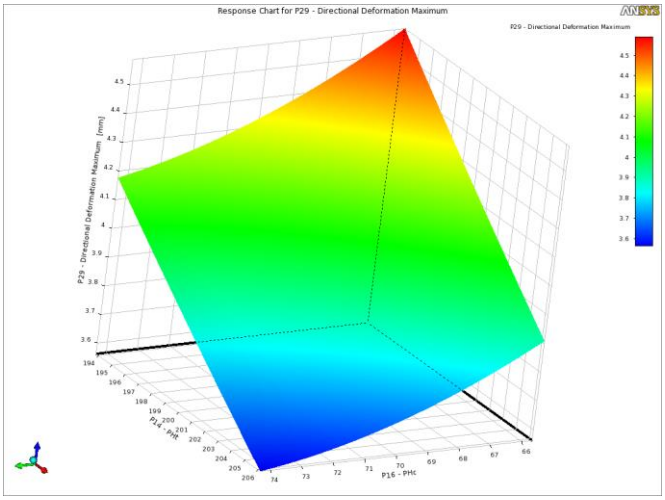

Fig. 6 Response surface for maximum mid-span deflection

RSM is based on the basic assumption that the influence of the input parameters on the output parameter can be approximated by the polynomial function. In the most cases, square function is used:

$$Y = c_0 + \sum_{i=1}^{n} c_i X_i + \sum_{i=1}^{n} \sum_{j=1}^{n} c_{ij} X_i \cdot X_j \tag{3}$$

where c_0 is constant, c_i is linear coefficient and c_{ij} is a square coefficient. Regression is usually applied for the evaluation of these coefficients using the least square method.

4. CONCLUSION

The sensitivity analysis can generally be divided into two basic categories: the deterministic and the stochastic sensitivity analysis. Although the deterministic sensitivity analysis is easy to apply in practice and it provides a quick overview of the performance of the design model, it neglects the correlation among the input design parameters that certainly exist in real conditions. However, the stochastic sensitivity analysis provides much more complex information about the design parameters because they are considered as random variables with a certain distribution. The characterization of the selected input parameters was determined based on the JCSS Probabilistic Model Code. Unlike the deterministic sensitivity analysis, the variability of a particular output parameter due to a single input parameter is evaluated by varying all other design parameters at the same time. This paper was focused on the application of the stochastic sensitivity analysis on the maximum equivalent stress and the maximum mid-span deflection of the timber-concrete composite beam. The generation of the numerical model of the TCC beam was carried out using the finite element method in the software package ANSYS Workbench 15.0. The conducted analysis used the symmetry of the beam and the load. The sensitivity of considered output parameter was derived from Spearman rank-order correlation coefficient. Considering the results of the conducted stochastic sensitivity analysis, it is noticeable that the parameters which describe shear connectors, the number of rods (n_s), the diameter of connector (d_s) and the Young's modulus of the steel (E_s) have the dominant influence on the maximum equivalent stress, but do not have a dominant influence on the maximum mid-span deflection of the TCC beam. Based on the results of the conducted sensitivity analysis of the mid-span deflection, it can be concluded that the increase in the values of the design input parameters b_c, ρ_c and ρ_t directly affects the increase in the maximum mid-span deflection of the beam. Also, as the value of the design input parameters (b_t, d_s, n_s, h_c, h_t, E_c, E_s and E_t) increases, the maximum deflection of the observed beam decreases. In order to better understand the correlation among the input parameters and the output parameter, the Response surface method was employed.

REFERENCES

1. A. Saltelli, M. Ratto, T. Andres, F. Campolongo, J. Cariboni, D. Gatelli, M. Saisana, and S. Tarantola, "Global Sensitivity Analysis – The Primer", John Wiley and Sons, 2008.
2. A. Saltelli, S. Tarantola, F. Campolongo and M. Ratto, "Sensitivity analysis in practice: a guide to assessing scientific models", Wiley; 2004.
3. J.C. Helton, J.D. Johnson, C.J. Sallaberry and C.B. Storlie, "Survey of sampling-based methods for uncertainty and sensitivity analysis", Reliability Engineering and System Safety 91, 1175–1209, 2006.
4. W. Tian, "A review of sensitivity analysis methods in building energy analysis", Renewable and Sustainable Energy Reviews 20, 411–419, 2013.
5. P. Heiselberg, H. Brohus, A. Hesselholt, H. Rasmussen, E. Seinre and S. Thomas, "Application of sensitivity analysis in design of sustainable buildings", Renewable Energy, 34:2030–6, 2009.
6. A. Olsson, G. Sandberg and O. Dahlblom, "On Latin hypercube sampling for structuralreliability analysis", Structural Safety, 25, 47–68, 2003.
7. Z. Kala, "Sensitivity analysis of stability problems of steel plane frames", Thin-Walled Struct,49(5):645–51, 2011.
8. W. Pirie, "Spearman Rank Correlation Coefficient", Encyclopedia of Statistical Sciences, 2004.
9. CEN, "Eurocode 1: Actions on structures - Part 1-1: General actions - Densities, self-weight, imposed loads for buildings", Brussels, Belgium, 2002.
10. V. Rajčić, "Eksperimentalna ispitivanja spregnutih nosača drvo-lagani beton“, Građevinar 53, 1-8, 2001.

11. J.-W. Van de Kuilen, M. Dejong, "3D-numerical modelling of DVW reinforced joints", In: Proceedings of 8th WCTE Finland, 2004.
12. A. Dias, J.W.G. Kuilen, H. Cruz and S. Lopes, "Non-linear FEM models for timber–concrete joints made with dowel type fasteners", In: Proceedings of 8th WCTEFinland, 2004.
13. A. Dias, H. Cruz, S. Lopes and J.W.G. Kuilen, "Experimental shear-friction test on dowel type fastener timber–concrete joints", In: Proceedings of 8th WCTE Finland, 2004.
14. JCSS, "Probabilistic Model Code", Joint Committee on Structural Safety, 2001.
15. A. Haldar and S. Mahadevan, "Probability, Reliability and Statistical Methods in Engineering Design", Wiley, New York, 2000.

ANALIZA OSETLJIVOSTI SPREGNUTIH KONSTRUKCIJA TIPA DRVO-BETON

Analiza osetljivosti se može definisati kao studija o tome kako varijabilnost izlaznog parametra modela može biti raspodeljena na njene izvore, odnosno na varijabilnosti različitih ulaznih parametara tog modela. Ona pomaže u identifikaciji najvažnih projektnih parametara određene konstrukcije, kako bi se projektovanje i optimizacija konstrukcije fokusirala na njih. Ovaj rad predstavlja primenu stohastičke analize osetljivosti maksimalnog ekvivalentnog napona i maksimalnog ugiba u sredini raspona spregnute grede tipa drvo-beton. Svi ulazni parametri su posmatrani kao slučajne promenljive. U radu je korišćena Latin Hypercube Sampling numerička simulaciona metoda. Ocena osteljivosti je izvršena pomoću Spirmanovog koeficijenta korelacije rangova.

Ključne reči: *analiza osetljivosti, spregnute konstrukcije tipa drvo-beton, simulaciona metoda, Spirmanov koeficijent korelacije rangova*

FACTA UNIVERSITATIS
Series: **Architecture and Civil Engineering** Vol. 16, No 1, 2018, pp. 135-147
https://doi.org/10.2298/FUACE170830011M

NUMERICAL MODELING OF ULTRASONIC WAVE PROPAGATION – BY USING OF EXPLICIT FEM IN ABAQUS

UDC 624:517.957]:004.42

Nemanja Marković[1], Dragoslav Stojić[1], Radovan Cvetković[1], Vladimir Radojičić[2], Stefan Conić[1]

[1]Department for Materials and Structures, Faculty of Civil Engineering and Architecture, University of Niš, Serbia
[2]Faculty of Technical Sciences Priština, Serbia

Abstract. *Monitoring of structures implies integration of sensors and actuators, smart materials, data transfer as well as computer analyses and simulations with the purpose of damage detection, localization, assessment and prediction of the state of damage at the certain moment and in time. This paper presents the application of the explicit finite element method for modeling of the wave propagation. The examples of concrete plates and thin steel plates in which the propagation of the Lamb waves occur were analyzed. Explicit finite element method was shown to be very efficient even for the waves in ultrasound range. Efficiency, ease of the use and reliability of the wave propagation modeling by the explicit finite element method can contribute to the development of a new and the improvement of the existing methods for the monitoring of structures.The main purpose of this paper is to demonstrate a waveform propagation model using an explicit FEM in ABAQUS software.*

Key words: *explicit finite element method, structural health monitoring, wave propagation, piezoelectric sensors, damage detection*

1. INTRODUCTION

Computer-aided engineering (CAE) is the broad usage of computer software to aid in engineering analysis tasks, for mechanical, civil-engineering, air-industry etc. It includes Finite Element Analysis (FEA), Computational Fluid Dynamics (CFD), Multi-body dynamics (MBD) and optimization. As Moor's rule predicted, the computing power increases tenfold every five years. The CAE engineers have witnessed and enjoyed the great advances in computer architectures and software functionalities. With growing

Received August 30, 2017 / Accepted October 27, 2017
Corresponding author: Nemanja Marković
Faculty of Civil Engineering and Architecture, University of Niš, 18000 Niš, Aleksandra Medvedeva 14, Serbia
E-mail: nemanja.markovic@gaf.ni.ac.rs

computing power, expectations for more accurate predictive analysis have also risen. Simulation as an important design tool has been built into the manufacturing process. This represents a tough challenge to engineers as they try to assess the reliability of the results predicted by the computer simulation, even before the prototype test is conducted. Being overly reliant on simulation results can sometimes lead to wrong and costly decisions. In recent years, the concept of verification and validation has been proposed. Verification and validation is critical for certain types of simulation, whose errors could lead to major disasters. It is essential to determine how to systematically verify the numerical solution.

It is very difficult to write about when exactly the finite element method (FEM) was created. The first forms of this method are used for the purpose of civil engineering and airline industries and it can be said with some reserve that Hrennikoff A. and R. Courant are the initiators of the FEM. Today, computer simulations which are for the most part carried out by finite element method, are widespread in scientific research and practical application. The explicit finite element method has been successfully applied to various simulations such as wave propagation, nonlinear transient dynamics with small and large deformations. It is now widely adopted in the manufacturing process as well as in the research activity. As reported in journals and conferences, many problems have been solved by using explicit finite element method.

Monitoring of structures using piezoelectric (PZT) patches represents one of the modern methods of structural health monitoring, which are still in development. Application of PZT sensors/actuators has been excessively experimentally investigated under the static, dynamic, and cyclic loading on the structural elements and whole structures such as: beam elements [1÷3], columns [4÷6], reinforced concrete walls [7], frames [8], piles [9] and bridge structures [10]. PZT sensors have proven to be multifunctional devices which could be applied for various purposes, such as monitoring of vehicle induced impact forces on bridges [11], monitoring of the bond between reinforcement and casted concrete [12], detection of the damage of reinforcement inside a RC element [13], monitoring of the water content variation in concrete [14], vibration control of civil engineering structures [15], determination of early strength of concrete in-situ [16] as well as determination of compressive stresses due to the seismic actions on RC structures [17].

PZT patches are being used very successfully for monitoring and detection of the damage of steel and aluminum structures in aircraft industry, civil engineering, mechanical engineering etc. The use of Lamb waves induced by PZT patches bonded on the structure surface is of great importance in these types of structures for damage detection and localization and determination of damage size. For the purpose of damage detection, *Pitch-catch* [18], *Pulse-echo* [19] and *Time-reversal [20] methods were* experimentally and numerically analyzed.

Modeling of wave propagation in reinforced-concrete plate elements, using finite element method and commercial software package *ANSYS* was applied in [21]. Besides the use of commercial software package *ANSYS*, very successful modeling of wave propagation was performed in software *ABAQUS* [22] as well as in *LS-DYNA* [23]. FEM was successfully applied in modeling of three-dimensional propagation of PZT patch induced Lamb wave through reinforced composites [24] and homogenous plates [25]. FEM modeling of directed Lamb waves, induced by piezoelectric patches bonded on the steel plate, was utilized in [26]. There are many published papers showing the application of FEM modeling of wave propagation.

However, the use of propagation of waves induced by PZT actuators was analyzed also by the use of other methods. Spectral-element method was used for modeling of wave propagation in plate elements [27] as well as the local interaction simulation approach [28].

The aim of this paper is to review the efficiency of explicit FEM for the purpose of modeling wave propagation. This method can be used for general modeling of wave propagation, but in this paper, the wave propagation induced by PZT smart aggregate (SA) actuators embedded in reinforced concrete plate elements with a hole was analyzed.

2. THEORY OF LAMB WAVES

Lamb waves propagate in solid plates. They are elastic waves whose particle motion lies in plane direction. Lamb waves may propagate in free plates with parallel sides.

Basic concepts of the Lamb wave propagation presented in this paper were used from reference [29]. In thin isotropic and homogeneous plates the waves, regardless of the mode, can generally be described in a form of *Cartesian* tensor notation as [30]:

$$G \cdot u_{i,jj} + (\lambda + G) \cdot u_{j,ji} + \rho \cdot f_i = \rho \cdot \ddot{u}_i \qquad i, j = 1,2,3 \tag{1}$$

with the following designations: u_i is displacement, f_i is body force, ρ is density, G is shear modulus, and λ is Lame constant.

Using Helmholtz decomposition equation (1) can be decomposed into two uncoupled parts under the plane strain condition:

$$\frac{\partial^2 \phi}{\partial x_1^2} + \frac{\partial^2 \phi}{\partial x_3^2} = \frac{1}{c_L^2} \frac{\partial^2 \phi}{\partial t^2} \tag{2}$$

$$\frac{\partial^2 \psi}{\partial x_1^2} + \frac{\partial^2 \psi}{\partial x_3^2} = \frac{1}{c_S^2} \frac{\partial^2 \psi}{\partial t^2} \tag{3}$$

Where:

$$\phi = [A_1 \sin(px_3) + A_2 \cos(px_3)] \cdot \exp[i(kx_1 - \omega t)] \tag{4}$$

$$\psi = [B_1 \sin(qx_3) + B_2 \cos(qx_3)] \cdot \exp[i(kx_1 - \omega t)] \tag{5}$$

$$p^2 = \frac{\omega^2}{c_L^2} - k^2, \quad q^2 = \frac{\omega^2}{c_T^2} - k^2, \quad k = \frac{2\pi}{\lambda_{wave}} \tag{6}$$

with the following designations: A_1, A_2, B_1 and B_2 are four constants determined by the boundary conditions, k is wave number, ω is circular frequency and λ_{wave} is wavelength of the wave. Longitudinal velocity c_L and transverse (shear) velocity c_S are defined by:

$$c_L = \sqrt{\frac{E(1-\nu)}{\rho(1+\nu)(1+2\nu)}} = \sqrt{\frac{2G(1-\nu)}{\rho(1-2\nu)}} \tag{7}$$

$$c_S = \sqrt{\frac{E}{2\rho(1+\nu)}} = \sqrt{\frac{G}{\rho}} \tag{8}$$

If we assume plane strain conditions, the displacement in the wave propagation direction (x_1) and normal direction (x_3) can be described as:

$$u_1 = \frac{\partial \phi}{\partial x_1} + \frac{\partial \psi}{\partial x_3}, \quad u_2 = 0, \quad u_3 = \frac{\partial \phi}{\partial x_3} - \frac{\partial \psi}{\partial x_1} \tag{9}$$

However, the conditions which correspond to the propagation of Lamb waves:

$$u(x,t) = u_0(x,t), \quad t_i = \sigma_{ji} n_j, \quad \sigma_{31} = \sigma_{33} = 0 \quad \text{at} \quad x_3 = \pm d/2 = \pm h \tag{10}$$

where d is plate thickness and h is half plate thickness. By applying the boundary conditions defined by equation (10) to equation (9) we can obtain the general description of Lamb waves in an isotropic and homogeneous plate:

$$\frac{\tan(qh)}{\tan(ph)} = \frac{4k^2 qpG}{(\lambda k^2 + \lambda p^2 + 2Gp^2)(k^2 - q^2)} \tag{11}$$

Applying equation (6) and equations (7) and (8) into the equation (11), and considering trigonometric features of the above equation, equation (11) can be split into two parts with unique symmetric and anti-symmetric properties, respectively, implying that Lamb waves in a plate consist of symmetric and anti-symmetric modes [30]:

$$\frac{\tan(qh)}{\tan(ph)} = -\frac{4k^2 qp}{(k^2 - q^2)^2} \text{ - Symmetric modes} \tag{12}$$

$$\frac{\tan(qh)}{\tan(ph)} = -\frac{(k^2 - q^2)^2}{4k^2 qp} \text{ - Anti-symmetric modes} \tag{13}$$

Equations (12) and (13) are known as the Rayleigh-Lamb equations.

3. EXPLICIT FINITE ELEMENT METHOD

Since the process of explicit finite element method is explained in many publications so far, here we will give only a brief overview of the basic equations and rules. Starting with Newton's second law written in matrix form:

$$F = M \cdot A \tag{14}$$

with the following designations: F is body force, M is mass matrix, and A is acceleration.

Whereby members of the expression can be defined by the following expressions:

$$F_i^m = -\int_\Omega (\sigma_{ij} \Phi_{M,j}) d\Omega + \int_\Omega f_i \Phi_M d\Omega + \int_{\Gamma_S} g_i \Phi_M d\Gamma_S \tag{15}$$

$$M_{MN} = \int_\Omega (\rho \Phi_M \Phi_N) d\Omega \tag{16}$$

$$A_i^N = \ddot{u}_i^N(t) \tag{17}$$

Where: F_i^m is body force; σ_{ij} is stress; Φ_M, Φ_N are based functions; g_i represents the components of the tractions on part of the boundary Γ_S; M_{MN} is mass matrix; ρ is mass density; f_i represents the components of the body force; $\ddot{u}_i^N$, u is second derivation of displacement and displacement; A_i^N is acceleration; t is time; Ω is space domain; Γ_S is boundary domain.

More detailed explanation of the elements of equations can be found in [31]. System defined by equation (14-17) is a system of second-order ordinary differential equations in time, whether linear or nonlinear. For solving this system explicit scheme uses central difference method to approximate the acceleration, velocity and displacement. Assume that the time domain $[0,T]$ is uniformly divided into N equal subintervals $[t_n, t_{n+1}]$, with $0=t_0< t_1<\ldots t_N=T$, $t_{n+1}-t_n=\Delta t=T/N$. The displacement, velocity and acceleration as time derivatives are approximated by the finite difference method, expressed in the vector form as:

$$\begin{cases} \partial_t u_{n+1/2}^h = (u_{n+1}^h - u_n^h)/\Delta t \approx \dot{u}_{n+1/2}^h \\ \partial_{t^2} u_n^h = (\partial_t u_{n+1/2}^h - \partial_t u_{n-1/2}^h)/\Delta t = (u_{n+1}^h - 2u_n^h + u_{n-1}^h)/\Delta t^2 \\ \ddot{u}_n^h \approx (\dot{u}_{n+1/2}^h - \dot{u}_{n-1/2}^h)/\Delta t \end{cases} \tag{18}$$

$$\begin{cases} \partial_t u_{n+1/2}^h = \partial_t u_{n-1/2}^h + \partial_{t^2} u_n^h \Delta t \\ u_{n+1}^h = u_n^h + \partial_t u_{n+1/2}^h \Delta t \end{cases} \tag{19}$$

where u is displacement, $\dot{u}$ is velocity and $\ddot{u}$ is acceleration. Δt (*subinterval*) is equal to $t_{n+1}-t_n$ or T/N.

Approximated the acceleration by central difference method defined in (18) and (19), the finite element equation (14) is reduced:

$$\partial_{t^2} u_n^h = M^{-1} \cdot F_n \tag{20}$$

The explicit finite element procedure can be presented as an algorithm in Figure 1.

The implementation of equation (20) is conditionally stable and the time step Δt has to be smaller than the critical time step Δt_{crit} which in an undamped system depends on the higher frequency in the smallest element:

$$\Delta t \le \Delta t_{crit} = \frac{2}{f_{\max}} \tag{21}$$

For wave propagation modeling, as small deformations of elements is assumed, an approximation often used is that the critical time step is the transit time of a dilatational wave through the smallest element in the model:

$$\Delta t \le \Delta t_{crit} = \frac{\Delta L}{c_L} \tag{22}$$

where ΔL is the smallest element size, Δt is time step and Δt_{crit} is critical time step.

In this paper, the criterion for defining the time step is defined by the basis of equation (22). The size of the final element is adapted to satisfy the usual condition that a wavelength divided by a final element is greater than ten.

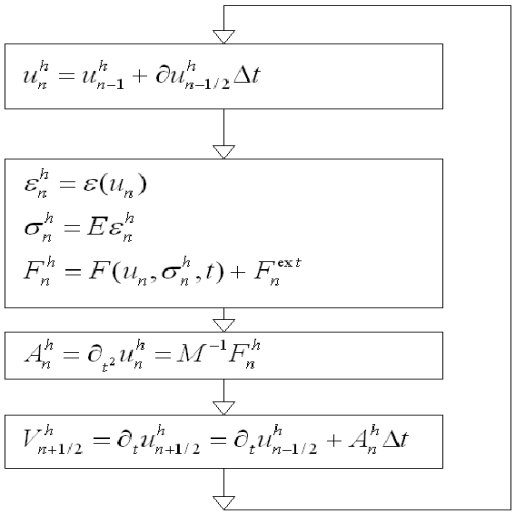

Fig. 1 Procedure of explicit finite element method

The diagonal mass matrix is an important feature that makes the explicit method efficient and practical. When using diagonal mass matrix, the step to calculate acceleration by applying Newton's second law in (20) is reduced to a simple division without the need of inverting the mass matrix. This reduces the time for model calculation and makes explicit finite element method a very efficient for modeling wave propagation.

4. NUMERICAL EXAMPLES

Application of explicit finite element method will be presented in the case of concrete plate and thin steel plate. Both plates are modeled with damage in the form of holes. The geometry of the plates, position of actuators and sensors, and position and size of damage are shown in Figure 2.

4.1. Numerical model 1 - Concrete plate

A *0.4x0.4x0.05m* concrete plate, with two PZT SA, which is numerically analyzed is presented in Figure 2. Damage is simulated as a hole with radius of *0.02m*. The modeling method, employing standard and explicit FEM represent the modeling procedure used in the paper [32] which was verified by the experiment on the concrete beams. The model of PZT SA was made in the software package ABAQUS/STANDARD taking into consideration electromechanical characteristics of PZT materials, using the combination of mechanical equilibrium and the equation of equilibrium of electrical flux.

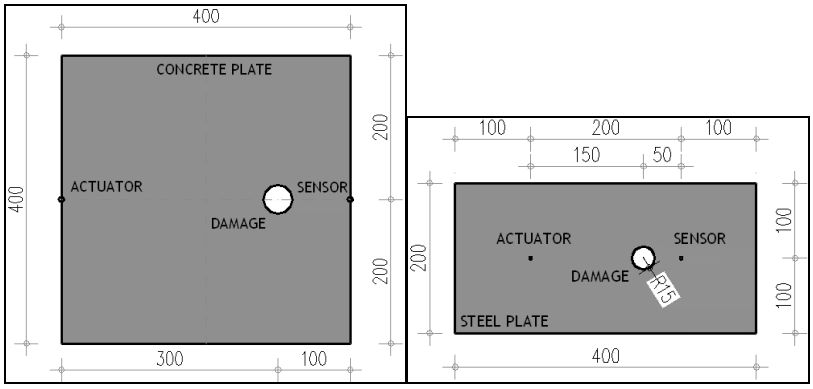

Fig. 2 Geometric characteristics of concrete and steel plate models

Displacement obtained as a consequence of imparting of electrical voltage on the PZT element was used as an input parameter for modeling of wave propagation, performed in ABAQUS/EXPLICIT software package. Function of displacement variation used in the analysis is *3.5 cycle Hanning windowed tone burst signal* defined with equation (23) with duration of $3.5e^{-5}$ *sec* and central frequency of *100kHz*.

$$P_t = \begin{cases} \left[1-\cos\left(\dfrac{2\pi f}{N}t\right)\right]\sin(2\pi ft); & for \quad 0 \le t \le \dfrac{N}{f} \\ 0; & for \quad t \ge \dfrac{N}{f} \end{cases} \tag{23}$$

Concrete plate was modeled as linear-elastic material with characteristics presented in Table 1. Material damping is modeled with Rayleigh damping model. For defined material Rayleigh damping, two damping factors must be specified: α_R for mass proportional damping and β_R for stiffness proportional damping. For a given mode I the fraction of critical damping can be expressed in terms of the damping factors:

$$\xi_i = \frac{\alpha_R}{2\omega_i} + \frac{\beta_R \omega_i}{2} \tag{24}$$

where ω_i is the natural frequency at this mode. Values of mass and stiffness proportional factors in presented concrete model are defined in Table 1.

Table 1 Material characteristics of linear-elastic concrete model

Concrete	Value
Density (ρ) [kg/m^3]	2400
Modulus elasticity (E) [Pa]	$30 \cdot 10^9$
Poissons ratio (ν)	0.2
Mass damping factor	0.01
Stiffness damping factor	$5 \cdot 10^{-8}$

4.1.1. Results and discussion

In Figures 3 and 4 the wave propagation through concrete plate induced by PZT actuator was shown. At the upper part of the Figure 3 the beginning of the wave propagation was shown, and at the lower part further wave propagation was shown. In these Figures, the wave propagates freely, limited only by geometry of the concrete plate.

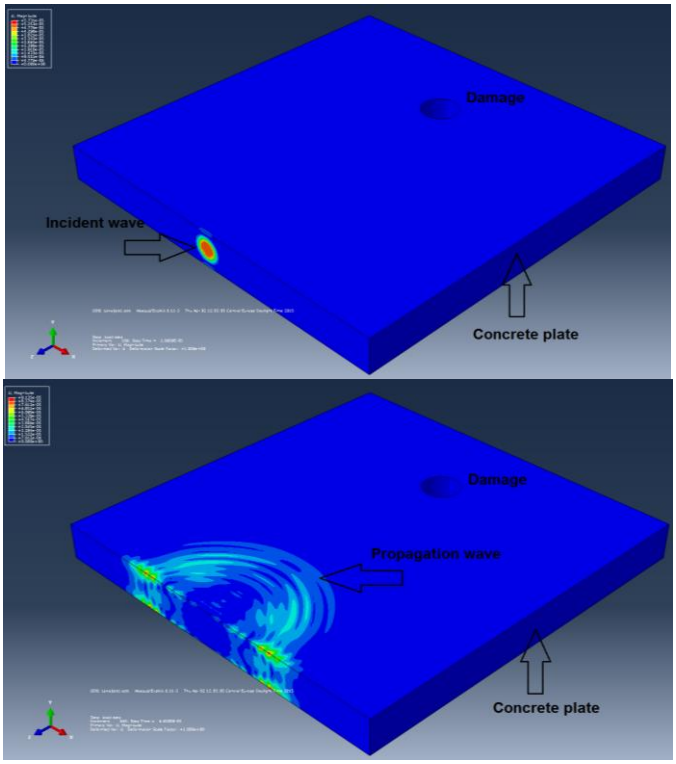

Fig. 3 Wave propagation at concrete plates at time points: 1.06 e^{-5} (s) and 6.65 e^{-5} (s).

The first reflection of the wave was shown in Figure 4a, where the waves were reflected off the sides and are propagating back toward the actuator. However, besides the waves reflected off the plate sides, the waves reflect of the damage as well. This was also shown in Figure 4b. This reflection has a direct influence on the reduction of the energy of the output signal in the sensor. By monitoring the energy of the output wave in sensor it is possible to monitor the damage initiation and propagation in concrete element.

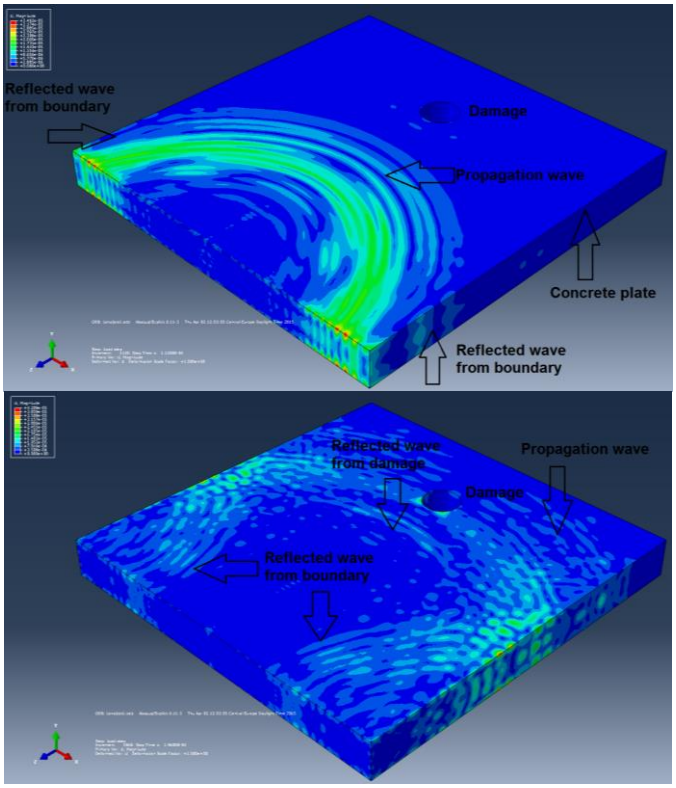

Fig. 4 Wave propagation at concrete plates at time points: 11.2 e^{-5} (s) and 19.6 e^{-5} (s).

4.2. Numerical model 2 - Steel plate

Since in this case the thickness of the steel plate is very small, the propagation of the Lamb waves occurred. This was not the case in the concrete plate. The modeling of the Lamb wave propagation was performed by the application of the explicit finite element method with the diagonal mass matrix using software package ABAQUS/EXPLICIT. The dimensions of the analyzed model were *0.4x0.2m*, with the hole diameter of *R=0.015m*. Mechanical properties of steel used for the modeling of the plate are shown in Table 2. Based on the Lamb wave propagation theory, the basic parameters for wave propagation modeling were calculated: longitudinal wave propagation speed *4943.3 (m/s)*, transversal wave propagation speed and wavelength *0.0494 (m)*. According to many authors' recommendations, the number of finite elements per one wavelength should be *7* to *20*, where the upper limit satisfies high frequency excitation incidents. In steel plate models *16* finite elements were used per one wavelength. The same input signal was used as in case of the concrete models, defined by the equation (31). The applied time increment satisfies the critical time increment condition given by the equation (30).

Table 2 Material characteristics of a linear-elastic steel model

Steel	Value
Density (ρ) [kg/m^3]	7850
Modulus elasticity (E) [Pa]	$210 \cdot 10^9$
Poisson's ratio (ν)	0.3

4.2.1. Results and discussion

In figures 5 and 6, the propagation of Lamb waves through thin steel plates is shown. Figure 5a shows the initial wave propagation from the position of the PZT actuator, bonded to the steel plate. Figure 5b shows the moment of wave reflection of the plate sides. All figures show the displacements perpendicular to the plate at the moment suitable for the visual inspection of the wave propagation through the plate.

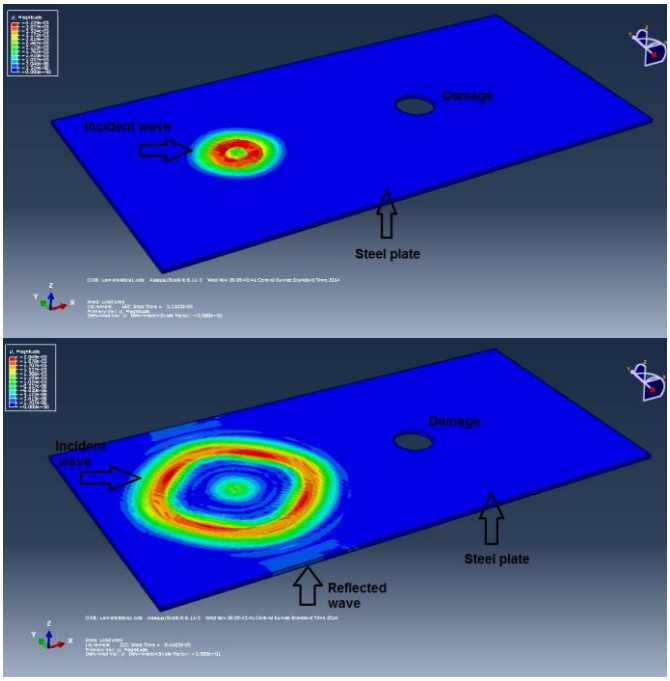

Fig. 5 Lamb wave propagation at steel plates at time points: 3.21 e^{-5} (s) and 6.01 e^{-5} (s).

In Figure 6a, the wave reaches the damaged part, which could be clearly seen together with the reflection of the plate sides. The damage reflects the waves which return toward the actuator and weakens the wave propagation toward the sensor (Figure 6b). Also, the transmitted wave has weaker intensity for the damaged plate compared to the undamaged one. The weakening of the propagating wave influences the output signal, as it was explained in the case of concrete plate, which can be used for monitoring the damage of the steel plates. In this paper, an undamaged model has not been analyzed. All of these notes refer to the application of the modeling process in the damage detection.

For better visual representation, the displacements shown for the case of Lamb wave propagation are scaled *50* to *100* times, depending on the figure.

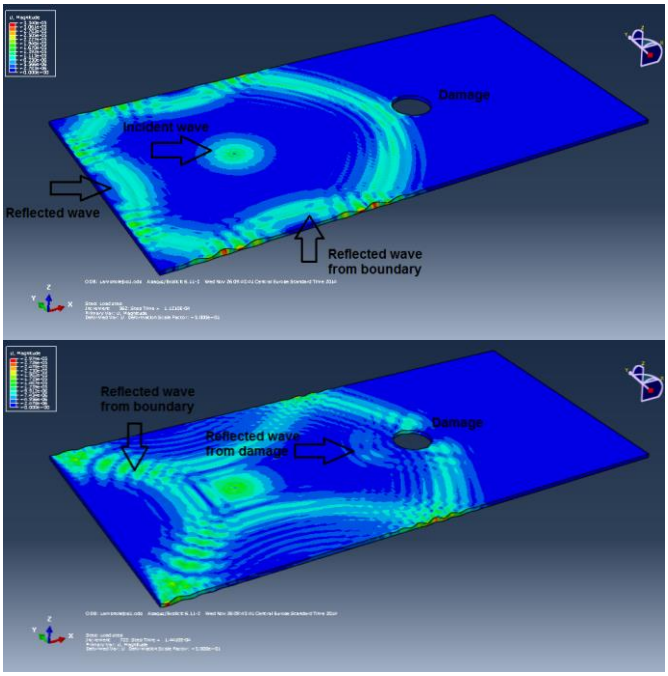

Fig. 6 Lamb wave propagation at steel plates at time points: 11.21 e^{-5}(s) and 14.43 e^{-5}(s).

6. CONCLUSIONS

1. Modern active structural health monitoring methods of structures certainly represent the future of the monitoring civil engineering buildings, and their development is ever more expected in the future. Numerical methods and computer modeling play an important part in the development of these methods.
2. This paper presents the explicit finite element method (EFEM) which is very efficient for modeling ultrasonic wave propagation through the concrete and steel plates. EFEM is the direct integration method using the principle of central differential and a diagonal matrix mass, which are the main characteristics of the efficiency of this method.
3. Original numerical models of wave propagation through the concrete plate elements made with EFEM are presented in the paper. Also, explicit finite element method was used for modeling Lamb wave propagation in thin steel plate with damage.
4. The paper analyzes obtained results and gives recommendations for using models for the purposes of structural health monitoring and non-destructive damage detection.
5. The explicit FEM proved to be very effective in modeling wave propagation. For thin plates, it can be used without major difficulties and for relatively large

geometric models that are often used in practice. However, for concrete plates that have a higher thickness and dimensions their application is limited to laboratory samples of smaller dimensions. By increasing the applied frequency, the dimension of the final element decreases, which very often leads to application of a model with more than a million FEs.

6. Finally, the authors recommend an explicit FEM implemented in the ABAQUS / EXPLICIT software for wave propagation modeling and consider it to be one of the most effective methods currently available.

REFERENCES

1. Song G., Gu H., Mo Y.L., Hsu T.T.C., Dhonde H., Concrete structural health monitoring using embedded piezoceramic transducers, Smart Materials and Structures, 2007, vol. 16, pp. 959-968.
2. Hu B., Kundu T., Grill W., Liu B., Toufing V., Embedded piezoelectric sensors for health monitoring of concrete structures, ACI Material Journal, 2013, vol. 110, pp.149-158.
3. Dumoulin C., Karaiskos G., Deraemaeker A., Monitoring of crack propagation in reinforced concrete beams using embedded piezoelectric transducers, VIII International Conference on Fracture Mechanics of Concrete and Concrete Structures – FraMCos-8, Toledo, Spain, March 2013.
4. Howser R., Moslehy Y., Gu H., Dhonde H., Mo Y.L., Ayoub A., Song G., Smart-aggregate-based damage detection of fiber-reinforced-polymer-strengthened columns under reverse cyclic loading, Smart Materials and Structures, 2011, vol. 20.
5. Moslehy Y., Gu Haichang, Belarbi A., Mo Y.L., Song G., Smart aggregate based damage detection of circular RC columns under cyclic combined loading, Smart Materials and Structures, 2010, vol. 19.
6. Gu H., Moslehy Y., Sanders D., Song G., Mo Y.L., Multi-functional smart aggregate-based structural health monitoring of circular reinforced concrete columns subjected to seismic excitation, Smart Materials and Structures, 2010, vol. 19.
7. Yan S., Sun W., Song G., Gu H., Huo L.S., Liu B., Zhang Y.G., Health monitoring of reinforced concrete shear walls using smart aggregates, Smart Materials and Structures, 2009, vol. 18.
8. Laskar A., Gu Haichang, Mo Y.L., Song G., Progressive collapse of a two-story reinforced concrete frame with embedded smart aggregates, Smart Materials and Structures, 2009, vol. 18.
9. Wang R.L., Gu H., Mo Y.L., Song G., Proof-of-concept experimental study of damage detection of concrete piles using embedded piezoceramic transducers, Smart Materials and Structures, 2013, vol. 22.
10. Soh C.K., Tseng K.K.H., Bhalla S., Gupta A., Performance of smart piezoceramic patches in health monitoring of a RC bridge, Smart Materials and Structures, 2000, vol. 9.
11. Song G., Olmi C., Gu H., An overheight vehicle-bridge collision monitoring system using piezoelectric transducers, Smart Materials and Structures, 2007, vol. 16, pp. 462-468.
12. Wu F., Chang F.K., debond Detection using Embedded Piezoelectric Elements for Reinforced Cocrete Structures – Part II: Analysis and Algorithm, Structural Health Monitoring, 2006, vol. 5(1), pp. 17-28.
13. Ervin B. L., Reis H., Longitudinal guided waves for monitoring corrosion in reinforced mortar, Measurement Science and Technology, 2008, vol. 19.
14. Liu T., Huang Y., Zou D., Teng J., Li B., Exploratory study on water seepage monitoring of concrete structures using piezoceramic based smart aggregates, Smart Materials and Structures, 2013, vol. 22.
15. Song G., Sethi V., Li H.N., Vibration control of civil structures using piezoceramic smart materials: A review, Engineering Structures, 2006, vol. 28, pp. 1513-1524.
16. Song G., Gu H., Mo Y.L., Smart aggregates: multi-functional sensors for concrete structures – a tutorial and review, Smart Materials and Structures, 2008, vol. 17.
17. Hou S., Zhang H.B., Ou J.P., A PZT-based smart aggregate for compressive seismic stress monitoring, Smart Materials and Structures, vol. 21.
18. Ihn J.B., Chang F.K., Pitch-catch Active Sensing Methods in Structural Health Monitoring for Aircraft Structures, 2008, vol. 7, pp. 5-19.
19. Giurgiutiu V., Structural Damage Detection with Piezoelectric Wafer Active Sensors, Journal of Physics: Conference Series 305, 2011.
20. Poddar B., Kumar A., Mitra M., Mujumdar P.M., Time reversibility of a Lamb wave for damage detection in a metallic plate, Smart Materials and Structures, 2011, vol. 20.

21. F. Song, G.L. Huang, J. H. Kim, S. Haran, On the study of surface wave propagation in concrete structures using a piezoelectric actuators/sensor system, Smart Materials and Structures, 2008, vol. 17, 8pp.
22. N. Marković, D. Stojić, T. Nestorović, Modeliranje Lamb talasa kod tankih čeličnih ploča u cilju detekcije oštećenja, Zbornik radova Građevinsko-arhitektonskog fakulteta u Nišu, 2014, vol. 29, pp. 1-14.
23. M. Yang, P. Qiao. Modeling and experimental detection of damage in various materials using the pulse-echo method and piezoelectric sensors/actuators. Smart Materials and Structures, 2005, vol.14, pp.1083-1100.
24. R. Weber, S. M. H. Hosseini, U. Gabbert. Numerical simulation of the guided Lamb wave propagation in particle reinforced composites. Composite Structures, 2012, vol. 94, pp. 3064-3071.
25. S. V. Ende, R. Lammering. Modeling and Simulation of Lamb Wave Generation with Piezoelctric Plates. Mechanics of Advanced Materials and Structures, 2009, vol. 16, pp. 188-197.
26. W. Zhou, H. Li, F. G. Yuan. Guided wave generation, sensing and damage detection using in-plane shear piezoelectric wafers. Smart Materials and Structures, 2014, vol.23, 10pp.
27. M. Rucka. Modelling of in-plane wave propagation in a plate using spectral element method and Kane-Midlin theory with application to damage detection. Archives of Applied Mechanics, 2011, vol. 81, pp.1877-1888.
28. B. C. Lee, W. J. Staszewski. Modelling of Lamb waves for damage detection in metallic structures: Part I. Wave Propagation. Smart Materials and Structures, 2003, vol. 12, pp. 804-814.
29. Z. Su, L. Ye, Identification of Damage Using Lamb Waves – From Fundamentals to Applications, Lecture Notes in Applied and Computational Mechanics, vol. 48. Springer, 2009, pp. 15- 58.
30. J. L. Rose, Ultrasonic Waves in Solid Media, Cambridge University press, New York, 1999.
31. Shen R. Wu, Lei Gu, Introduction to the Explicit Finite Element Method for nonlinear transient dynamics, Wiley, New Jersey, 2012.
32. N. Marković, T. Nestorović, D. Stojić, Numerical Modeling of Damage Detection in Concrete Beams using Piezoelectric Patches, Mechanics Research Communications, 2015, vol. 64, pp 15-22.

NUMERIČKO MODELIRANJE ULTRAZVUČNOG PROSTIRANJA TALASA – KORISTEĆI EKSPLICTINU MKE U ABAQUSU

Monitoring konstrukcija podrazumeva integrisanje senzora i aktuatora, pametnih materijala, prenosa podataka kao i kompjuterskih analiza i simulacija u cilju detekcije, lokalizacije, procene i predviđanja stanja oštećenja u datom trenutku i kroz vreme. U radu je prikazana primena eksplicitne metode konačnih elemenata za modeliranje propagacije talasa. Metoda je direktna integraciona metoda koja koristi dijagonalnu matricu masa. Analizirani su primeri betonskih ploča i tankih čeličnih ploča kod kojih se javlja prostiranje Lamb talasa. Eksplicitna metoda konačnih elemenata se pokazala veoma efikasnom čak i za talase u ultrazvučnom opsegu. Efikasnost, laka upotreba i pouzdanost modela propagacije talasa izvedenih eksplictinom metodom konačnih elemenata mogu doprineti u razvoju novih ili unapređenju postojećih metoda monitoringa konstrukcija.

Ključne reči: *eksplicitna metoda konačnih elemenata, monitoring konstrukcija, propagacija talasa, piezoelektrični senzori, detekcija oštećenja*

FACTA UNIVERSITATIS
Series: **Architecture and Civil Engineering** Vol. 16, No 1, 2018, pp. 149-157
https://doi.org/10.2298/FUACE170915012I

BATHYMETRIC SURVEYS OF SHPILJE RESERVOIR

UDC 55
502/504

Dragan Ivanoski, Slaviša Trajković, Milan Gocić

[1]University SS Cirilus and Methodius, Faculty of Civil Engineering, Skopje, Macedonia
[2]University of Niš, Faculty of Civil Engineering and Architecture, Serbia

Abstract. *Periodic bathymetric surveys are carried out to define quantity of sedimented material in reservoirs, as well as to determine the areas most endangered by the silting process. Such surveys in the Republic of Macedonia were started as an obligatory and regular practice in the seventies of the last century, immediately after the formation of the larger artificial lakes. These were carried out for almost all reservoirs in the country and it can be said that there is already a sufficient amount of data on some of them that can serve as a basis for high quality analyses of the silting trend of the reservoirs and of the extent to which erosion is affecting the basin area. This paper provides a review of the results from the latest field surveys and analyses of changes in the configuration of the Shpilje reservoir bottom, carried out in the period 2014 to 2016.*

Key words: *bathymetric surveys, reservoir volume, silting with sediments.*

1. INTRODUCTION

Intensive construction of dams in the Republic of Macedonia and creation of reservoirs for different purposes started in the second half of the last century. Up till now, 23 large dams and over 120 small dams have been built in the territory of the country. With the very formation of the reservoirs, there started systematic periodic hydrographic surveys for the purpose of defining the sedimentation trend, i.e., changes in the capacity of the reservoirs due to sedimentation of deposits. In addition, the spatial distribution and the effectiveness of the reservoirs in keeping the sediments were analyzed. Based on such analyses, instructions were given for protection against erosion in the reservoir basin areas.

Received September 15, 2017 / Accepted September 29, 2017
Corresponding author: Dragan Ivanoski
Faculty of Civil Engineering, University SS Cirilus and Methodius, Skopje, Macedonia
E-mail: ivanoski@gf.ukim.edu.mk

Turbulent social changes in the territory of former Yugoslavia caused a slowdown in monitoring of the sedimentation in the reservoirs of the Republic of Macedonia so that hydrographic, i.e., bathymetric surveys were not at all carried out in a period of about 20 years. Data for reservoirs are often limited due to the expense and time required for their acquisition via field survey (Revenga et al., 2005; Zhang et al., 2016; Palanques et al., 2014; Vörösmarty et al., 2001).

Bathymetric surveys can help to manage water and make decisions, especially when natural hazards such as droughts and floods occur (Ayana et al., 2015; Ortt et al., 2000; Gao, 2009)

To continue with the positive practice of monitoring the sedimentation process, efforts have been made for the last few years to resume surveys of reservoirs throughout the country. Among the first such surveys was the one done for the Shpilje reservoir or Debar Lake. Some of the results from the performed analyses are given further in this paper.

2. SURVEY OF THE BOTTOM TOPOGRAPHY OF SHPILJE RESERVOIR

Debar Lake or Shpilje reservoir represents an artificial lake located in the west part of Macedonia, south of the town of Debar, in the vicinity of the Macedonian-Albanian border. The lake covers an area of 13.2 km^2; it is 92 m deep and is situated at an altitude of 580m above the sea level. It was created with the construction of a 102 m high dam located at the merging point of the Crn Drim River and the Radika River. This dam was constructed in the period from 1966 to 1968. With its total capacity of 543 x 106 m^3 of accumulated water, Debar Lake has more water than any other individual artificial lake in Macedonia. Its basic purpose is production of electric power, irrigation, sport and recreation and lately, commercial fish breeding.

Fig. 1 Location of the Shpilje reservoir

The first hydrographic surveys of the Shpilje reservoir after it had been put into operation were carried out in 1986. Based on these surveys, a study was elaborated on the changes of the reservoir bottom and quantity of deposited sediments for the period starting with its putting into operation. An emphasis was also put on the most exposed zones of the reservoir regarding silting intensity and corresponding measures for protection were proposed. Since then, no surveys were done until 2014 when these were resumed. Surveys were carried out in the period from 16th to 25th June, 2014. For these surveys, measuring equipment owned by the Faculty of Civil Engineering in Skopje was used, while the surveys were done by an operational team from the public enterprise managing the reservoir.

The used measuring system consists of two parts: spatial geographic positioning system (GPS) and ultrasonic bathymeter (exo sonder) that functions at a frequency of 200 kHz. This system generates measuring points on the bottom of the reservoir in absolute x, y and z coordinates. The usual accuracy is 0.1 m along z-axis, i.e., along depth and several centimeters in horizontal plane (x and y coordinates).

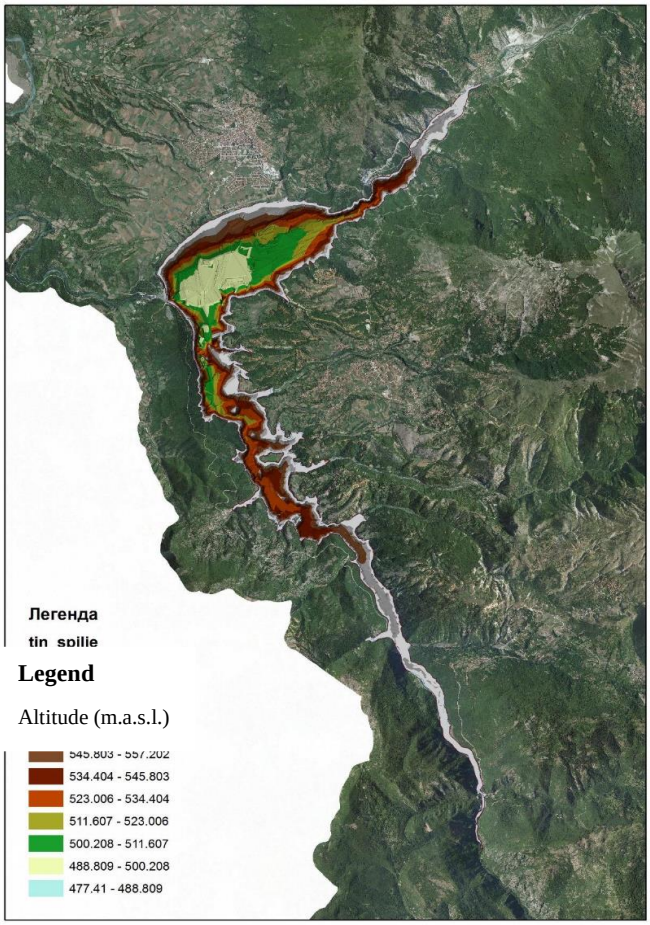

Fig. 2 Digital terrain model (DTM) of the Shpilje reservoir bottom

Based on the recorded water depths and known water level of the reservoir in the period when the measurements were performed, the absolute levels of the reservoir bottom were computed. These data were used to generate a digital terrain model (DTM) of the reservoir bottom (Figure 2).

3. Analysis of Results from Measurements

The surface areas of the water table were calculated using the previously generated DTM of the reservoir. For each water level, the surface area of the water table was computed starting from the lowest measured level of the terrain (492 m above the sea level) to the normal level (580 m above the sea level). The dependence of the water table surface area A(ha) on the water level Z (m above the sea level) is presented in Figure 3. For the purpose of comparison, the same figure also shows the initial distribution of the reservoir surface areas in the period when the structure was put into operation in 1969.

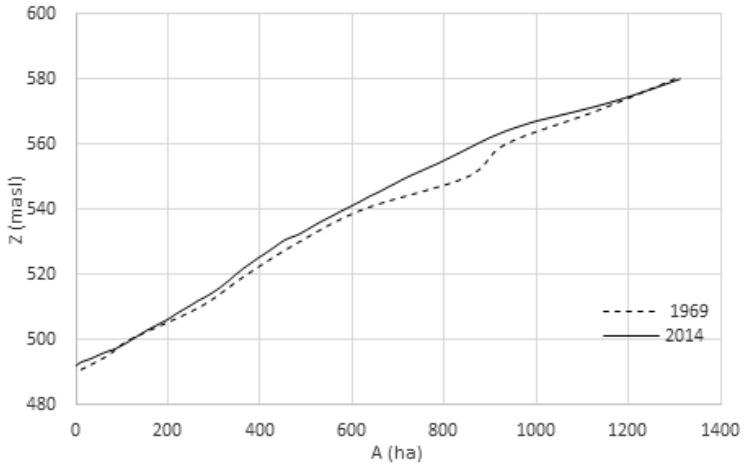

Fig. 3 Lines of Shpilje reservoir surface areas – initial conditions in 1969 and conditions in June 2014

The elementary volume, or the volume of the reservoir between any two adjacent water levels can be defined by integration of the surface below the curvature of surfaces, while the cumulatively summed up elementary volumes yield the volume curvature, $V = f(Z)$.

To compute the elementary volumes from the numerical data in this study, the method of smoothed contoured surfaces was used.

According to this method, the elementary volume is computed as follows:

$$DV = \frac{A_i + A_{i-1}}{2} \times (Z_i - Z_{i-1})$$

where:

DV – elementary volume between two successive surfaces of the water table (Ai и Ai-1)

Z – water level for the analyzed surfaces (m above the sea level)

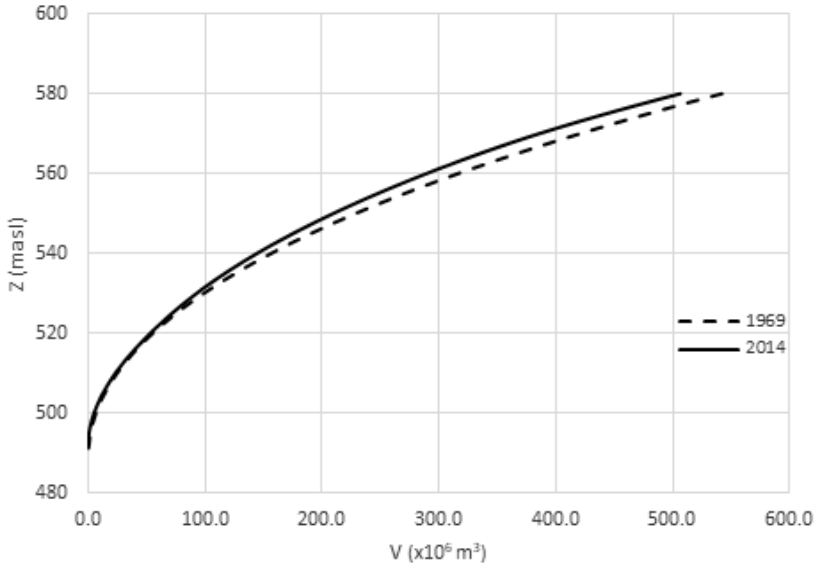

Fig. 4 Line of volumes of Shpilje reservoir – initial conditions in 1969 and conditions in 2014.

From the volumes line (Figure 4), the following data can be obtained:

In the case of a normal level of the reservoir Znl = 580.0 masl, the total volume of the reservoir amounts to:

$$Vnl = 506{,}32 \times 10^6 \text{ m}^3.$$

According to data available, the initial volume of the reservoir at normal level amounted to:

$$Viv = 543 \times 10^6 \text{ m}^3$$

In the period from the beginning of operation of the structure in 1969 until 2014 when the last measurements were done for the reservoir, a total of:

$$Vsed = 36.7 \times 10^6 \text{ m}^3 \text{ were deposited.}$$

To the minimal operational level of HPP Shpilje, Zmol = 562.5 masl, there corresponds a volume of:

$$Vmol = 311 \times 10^6 \text{ m}^3.$$

The present available storage capacity of the reservoir amounts to:

$$Vscp = Vnl - Vmol = 195.32 \times 10^6 \text{m}^3$$

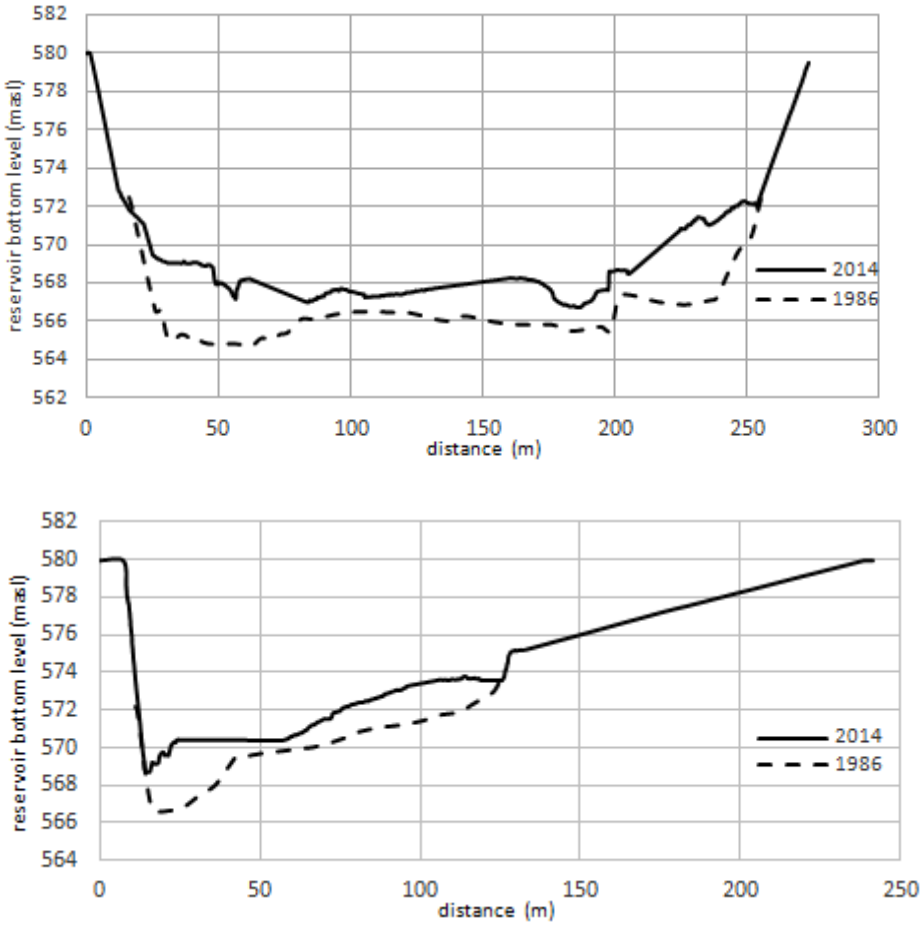

Fig. 5 Characteristic cross-sections along the Crn Drim and the Radika rivers

The analysis of distribution of sediments was done by comparison of the reservoir bottom configuration at selected cross-sections and longitudinal sections. The cross-sections of the reservoir were established upon previous survey of the bottom done in 1986. Longitudinal sections were also elaborated for the two arms of the reservoir, namely, along the Crn Drim River and the Radika River water courses, with presented conditions at the lowest points of the bottom recorded during the previous survey in 1986 and conditions recorded during the survey until 2014. This provides a clear high quality presentation of the distribution of sediments in the reservoir.

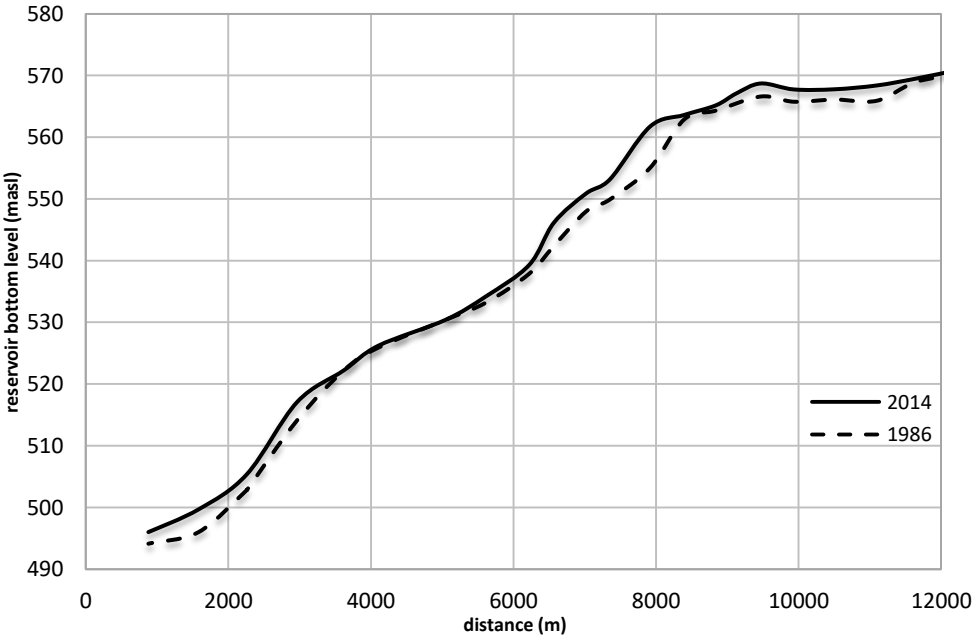

Fig. 6 Longitudinal section of the reservoir along the Crn Drim River water course

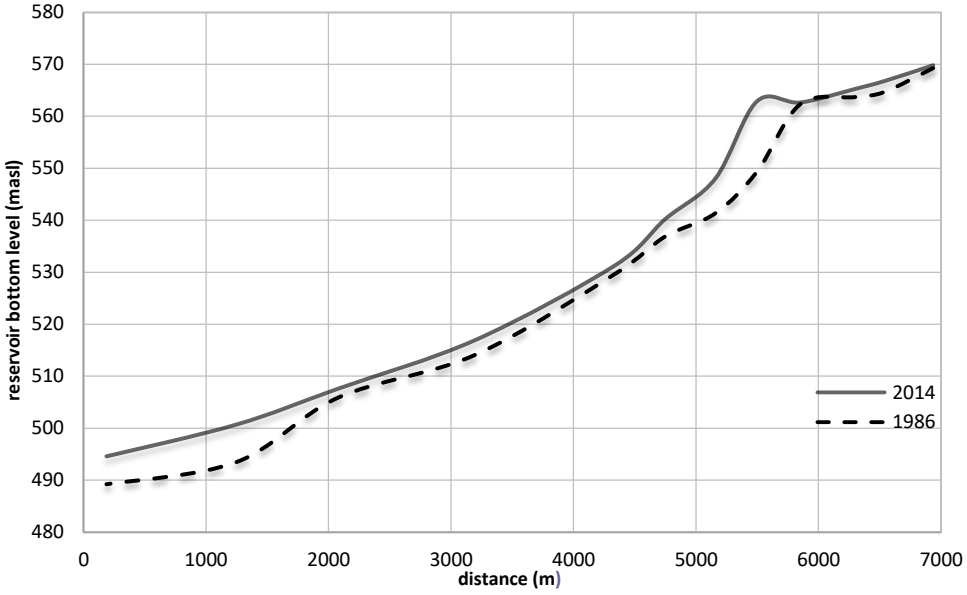

Fig. 7 Longitudinal section of the reservoir along the Radika River water course.

4. CONCLUSIONS

Based on the survey of the Shpilje reservoir bottom in 2014 and the performed analyses of the sedimentation process, the following conclusions are drawn:

- The sedimentation process in the reservoir takes place along the entire length of the reservoir, both along the Crn Drim River and the Radika River;
- As to the Crn Drim River arm, the most intensive silting is observed in areas where side tributaries empty into Crn Drim on the left and the right side of the reservoir.
- Along the Radika River arm, the most intensive silting is observed in the area where the Radika River empties into the reservoir. The configuration of the bottom of the reservoir in this area is extraordinarily variable and susceptible to dynamic processes of erosion and silting;
- Regarding the silting intensity, there stands out the zone of the reservoir between level 540 and 570 m above the sea level which corresponds with positions where the stated tributaries empty into the reservoir;
- In addition to the effect of the immediate basintributaries, it should also be mentioned that there is an intensive bank erosion and local collapses of the reservoir banks.

To reduce the production of eroded material in the Shpilje reservoir basin and the transfer of that material to the reservoir, the following measures have been proposed:

- Elaboration and proposal of possible forest-reclamation works for the purpose of reduction, i.e., elimination of erosion processes in the basins of the reservoir tributaries characterized by extensive erosion processes;
- Detailed checking of the already constructed anti-erosion structures in the basin of the lake and proposal of adequate measures for repair, reconstruction and possible construction of new structures that will control the transfer of eroded material into the reservoir;
- Construction of a sedimentation tank along the Radika River course, immediately upstream from the place where it empties into the lake. With this structure, the transfer of sediments to the reservoir will be controlled and certain income for the local community will be achieved by its regular cleaning and separation of the deposited material;
- Continuation of monitoring of the reservoir silting at each 5 to 10 years and after each big torrential downpours and taking corresponding anti-erosion measures accordingly.

REFERENCES

1. Ortt, R. A. Jr., Kerhin, R. T., Wells, D., Cornwell, J. (2000). Bathymetric survey and sedimentation analysis of Loch Raven and Prettyboy reservoirs. Maryland Geological Survey. Coastal and Estuarine Geology File Report no. 99-4, 56p.
2. Ayana, E.K., Philpot, W.D., Melesse, A.M., Steenhuis, T.S. (2015). Assessing the potential of MODIS/Terra version 5 images to improve near shore lake bathymetric surveys, International Journal of Applied Earth Observation and Geoinformation, 36, 13–21.
3. Gao, J. (2009). Bathymetric mapping by means of remote sensing: methods, accuracy and limitations, Progress in Physical Geography, 33(1), 103–116.

4. Revenga, C., Campbell, I., Abell, R., De Villiers, P., Bryer, M. (2005). Prospects for monitoring freshwater ecosystems towards the 2010 targets, Philosophical Transactions of the Royal Society B: Biological Sciences, 360, 397–413.
5. Zhang, S., Foerster, S., Medeiros, P., Araujo, J.C., Motagh, M., Waske, B. (2016). Bathymetric survey of water reservoirs in north-eastern Brazil based on TanDEM-X satellite data, Science of the Total Environment, 571, 575–593.
6. Palanques, A., Grimalt, J., Belzunces, M., Estrada, F., Puig, P., Guillén, J. (2014). Massive accumulation of highly polluted sedimentary deposits by river damming, Science of the Total Environment, 497-498, 369–381.
7. Vörösmarty, C., Askew, A., Grabs, W., Barry, R., Birkett, C., Döll, P., Goodison, B., Hall, A., Jenne, R., Kitaev, L. (2001). Global water data: a newly endangered species, Eos Transactions American Geophysical Union, 82, 54–58.

BATIMETRIJSKA MERENJA U AKUMULACIJI ŠPILJE

Periodična batimetriska merenja se izvode kako bi se definisala količina istaloženog materijala u akumulacijama, kao i određivanje najugroženijih područja usled procesa sedimentacije. Ovaj vid merenja u Republici Makedoniji započela su kao obavezna i redovna praksa sedamdesetih godina prošlog veka, neposredno nakon formiranja većih akumulacionih jezera. One su sprovodene na skoro svim akumulacijama u zemlji i može se reći da o nekima od njih već postoji dovoljno podataka koji mogu poslužiti kao osnova za kvalitetne analize trenda zapunjavanja jezera kao i stepena erozije u slivnom području. Ovaj rad pruža pregled rezultata najnovijih terenskih merenja i analiza promena u konfiguraciji dna akumulacije Špilje, sprovedene u periodu od 2014 do 2016. godine.

Ključne reči: *batimetriska snimanja, zapremina akumulacije, zapunjavanje sedimentima*

FACTA UNIVERSITATIS
Series: **Architecture and Civil Engineering** Vol. 16, No 1, 2018, pp. 159-173
https://doi.org/10.2298/FUACE170710013M

CONCRETING PROCESS PRODUCTIVITY ANALYSIS

UDC 693.5

Biljana Matejević, Milorad Zlatanović

University of Niš, Faculty of Civil Engineering and Architecture, Niš, Serbia

Abstract. *During constructing of any structure, there are a large number of factors impacting the total performance of the construction site. One of very important factors is productivity. Because of the specific nature and importance of concreting works, when constructing a building structure, it is necessary to pay a special attention to execution of these works. In this paper is analyzed the productivity in general sense, as well as productivity in civil engineering, with a focus on productivity in the course of concreting works. The importance of concreting works is emphasized, and the concreting works technology is described. A review and a description of the factors affecting the concreting process productivity are provided. A productivity analysis is performed on the concrete construction site based on the data obtained by recording the concreting process, and some of the results are provided.*

Key words: *civil engineering, productivity, concreting process, concreting technology, impact factors.*

1. INTRODUCTION

The parameter expressing the rate at which a work has been executed is called productivity. For the first time, the work productivity was mentioned in an article by the French mathematician Quesnay in 1766. A century later, in 1883, Littre defined productivity as a "faculty to produce". At the beginning of 20^{th} century the productivity was more precisely defined as a ratio of output and resources used for obtaining of the output. A formal definition of productivity was introduced in 1950 by Organization for European Economic Cooperation: Productivity is the ratio between the achieved production (output) and the resources invested in the production (input) according to the expression (1), where the invested resources can be: work, material, finances, etc.

Received July 10, 2017 / Accepted January 22, 2018
Corresponding author: Biljana Matejević
Faculty of Civil Engineering and Architecture, University of Niš, 18000 Niš, Aleksandra Medvedeva 14, Serbia
E-mail: biljana.matejevic@gaf.ni.ac.rs

$$\text{Productivity} = \frac{\text{Output}}{\text{Input}} \tag{1}$$

The term productivity is often confused with other terms such as production and speed. This is because it is supposed that, if there is an increase in production or speed, an increase of productivity would occur, which may but also may not be true. Productivity is related to the efficient usage of resources (input) in production (output), and production is an activity of creating something, so in other words, production is a measure of the produced quantity, irrespective of the input used for that. As a result, production can be high, but productivity needs not necessarily be high. On the other hand, speed indicates output produced in a unit of time, irrespective of used resources. Again, speed can be high, but productivity needs not be high.

Figure 1 shows in a popular way the productivity: The right things should be performed in a right way in order to keep the production/process/work… productive. If the right things are performed in a wrong way, one becomes ineffective, or if the wrong things are performed in a right way – inefficient. Ultimately, doing wrong things in a wrong way is inconsiderate.

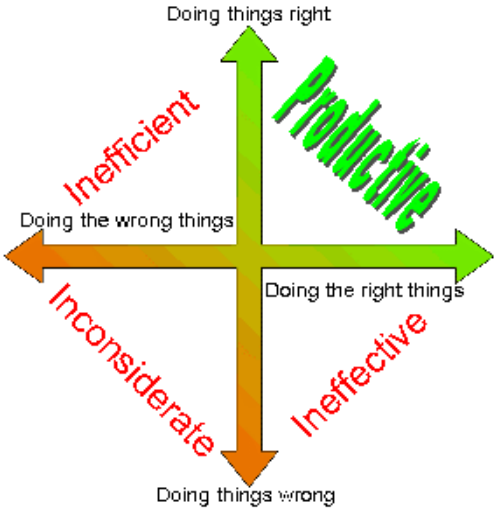

Fig. 1 Productivity (www.savjetnik.ba/šta-je-produktivnost/)

2. PRODUCTIVITY IN CIVIL ENGINEERING

Productivity is one of the most important factors which affect the total performances of any construction site, small or large. Production (output) is more often expressed through a unit of measure (volume, surface area, weight, etc.), and the input is mostly the time unit (hours, shifts, man-days, machinery-days, etc.). There is neither a universal nor a standard way for defining productivity of civil engineering processes, but in essence, the

work productivity in civil engineering is most often expressed as realized production in a unit of time.

There are several ways for expressing and measuring productivity in civil engineering. Productivity can be expressed as ratio between the achieved quantity product and labor expenditure. A considerably broader view can be taken, which entails not only labor bu any other input element. In comparison to the observed level, there are several types of productivity. If the productivity is related to one activity (one position of work) where there is one type of the achieved product, and thus one unit of measure, it is then a single factor productivity. Productivity, observed at a higher level, in comparison to more than one activity, or one group of works, is expressed through (multi factor productivity). Also the productivity expressed at the level of the entire construction site, with all the activities included, defines the total factor of productivity. Measuring and studying productivity has a great impact on the shortening of deadlines and reduction of projects cost, quality enhancement, provision of efficient work execution supervision, feedback, increased profit, etc.

3. CONCRETING WORKS IMPORTANCE

Concrete, as a building material has a very wide application in civil engineering industry, and for that reason it is a special subject of research. It owes its wide application to the relatively inexpensive natural materials: cement, aggregate and water, which are composite ingredients of a concrete mix. By adding water and determining the proper ratio of components and concrete making technology, the required physical-mechanical characteristics of concrete can be affected. The improved concrete technologies are based on the addition of admixtures which to a certain extent affect the concrete resistance to external effects. Various technologies are available for making and placing of concrete. The concreting process, starting from making of concrete in the concrete factory, over its transport to the construction site, and to the placing in a structure is the common construction process of a wide range of building structures. It can be rightly claimed that it is the most widely and most often used material in contemporary building construction According to data dating back to 2006, the total global concrete production was around 6 billion cubic meters, which represents around 1 cubic kilometer per resident of the planet (www.sr.wikipedia.org). Due to the specific characteristics of this building material and various influences (interruptions, downtime, irregularities, etc.) which occur during concreting, it is very important to pay a special attention to planning and execution of such works.

Concreting works constitute a major part of construction works, both of infrastructural and high-rise buildings. In case of the housing structures, in the skeletal construction system, the share of concreting works is considerable, from the aspect of quantities and costs. For instance, an average amount of concrete placed into a housing buildings having a basement, ground floor, 5 floors and an attic (P_0+P+5+$P_{k)}$, and gross surface area of 400 m^2 per floor, in the skeletal construction system, is around 1 250 m^3, of which around 860 m^3 is placed in the slabs (75 800 €), 220 m^3 into the vertical elements – columns, walls, lift shafts (22 200 €) and 170 m^3 into other smaller elements – window and door lintels, sidewalks, parapets, floors, etc. (17 350 €). The total cost of concreting works of 115 350 € represents around 38 % of the total cost of basic building works. For such structures, concrete works represent

critical activities in the dynamical plan of works execution. For this reason, it is important to perform a realistic planning of execution of these works by coordinating all influences and by providing the required productivity. It can be accomplished using the software package for net dynamic planning.

One of the most important developmental projects of the Republic of Serbia is the constructing of housing space which is an existential need across the entire territory of Serbia. Necessity to build housing space is an evident consequence of population migrations, formation of new, young households, and replacement of dilapidated and low quality (environmentally inappropriate and energy inefficient) housing stock. According to the analyses of the real estate market and other indicators, the number of required houses a year in Serbia is over 25 000, and currently there is over 300 000 households without the proper housing. (www.pks.rs/PrivredaSrbije).

4. CONCRETING PROCESS TECHNOLOGY

Nowadays, production of fresh concrete, in the conditions of contemporary technologies and increasing work division, is progressively performed in concrete plants. Concrete plants usually service a large number of constructions sites, if they are stationary, or only a specific construction site, which means that they are semi-stationary or mobile.

A technological system of a concrete plant consists of a silo for aggregate, silo for cement, water and admixture weighing systems. Optionally, such plant can have the additional silo which can store filler, micro-silicone or some other concrete admixtures. The weighing procedure depends on the manufacturer of a concrete plant, and considerably differs from one to another manufacturer.

The quality of concrete is specified based on the structural design, or technical conditions for concreting. The structural design defines the required concrete class (MB) as well as other concrete properties which determine the durability of the structures (frost and frost and salt resistance, water tightness, etc.) and concrete placing technology. In the design documents, the concrete class for a certain part of the building is specified, or the work item describes the required concrete class and other properties.

The quality control consists of the production control and control of compliance with the conditions of the conditions of structural and concrete designs. By controlling the concrete quality, it is verified that the required concrete class and other requisite properties have been achieved for a specific concrete batch. Acceptance criteria determine whether a specific batch will be accepted or rejected.

Quality control of the produced concrete is performed during concrete production and at the construction site (at the location where concrete is placed) in accordance with the regulations and provisions of PBAB (Code for Concrete Works). In addition to compressive strength, the concrete plant also performs control of particle size distribution and water content in the aggregate, fresh concrete consistency, start and completion of setting, and of cement and admixtures (Technical conditions for transported concrete SRPS U.M1.045).

On the constructions site, concrete consistency and workability ought to be tested (Technical conditions for transported concrete SRPS U.M1.045).

A special attention must be paid to the concrete transport and good coordination between a concrete plant and a construction site, to avoid unwanted changes in the fresh

concrete properties. Finished concrete must be transported to a construction site in suitable (workable) condition, considering that it has a limited placing time, so it is necessary to plan and organize its transport well. The most often and most appropriate way of fresh concrete transport from a concrete plant to a construction site is in mixer trucks, whose constant drum rotation during transport keeps concrete fresh. Since mixer trucks have different capacities (5 – 12 m^3), it is necessary to well coordinate the required number of vehicles with the transport needs in terms of quantity and time. Fresh concrete transport represents a very delicate operation in the framework of entire concreting works execution technology, for the following reasons: potential for segregation, leaking of cement paste from the vehicles, evaporation of water during prolonged transport (especially in summer time), time of transport in the function of the start of setting of cement in concrete and of consistency retention (especially in the summer period) – usage of retardant admixtures, change of consistency over time when plasticizers and suerplasticizers are used. During concrete transport, care must be taken that: concrete temperature during transport does not exceed permissible limits, coarse fractions do not crush the fine fractions because particle size distribution is changed, concrete does not become segregated, etc. In essence, transport should be organized so that there are no delays and interruptions during pouring into formwork. According to SRPS U.M1.045/87 concrete mixture must be poured out of a transport vehicle no later than 2 hours after water was added in a concrete plant, if the transporting vehicle has a truck mixer device, or alternately, 1 hour if the transporting vehicle does not have a truck mixer device. In case of cold and damp weather, and when setting retardant is used as admixture, the proper time can be longer. When weather is hot and when concrete is made with a larger share of cement, or when concrete hardening accelerator is used, the proper time can be shorter.

Transport of any quantity of concrete loaded in the transport vehicle is documented by a shipping note issued by a worker in the concrete plant. The shipping note – bill of lading consists of two copies, one staying at the constructions site, and the other, signed by a construction site representative is returned to the concrete plant. Data which need to be written on the shipping note are: name of the concrete manufacturer, date of delivery, name of the purchasing customer, name of the construction site, name of the structure, type and class of concrete, special properties of concrete, delivered quantity, type of used aggregate and cement, time of completion of a transport vehicle filling up, concrete consistency, concrete temperature, time of arrival of a transport vehicle to the construction site, starting and ending time of off loading of concrete.

There are several ways of transport and placement of concrete at a construction site, but one of the most often implemented is by using the concrete pumps, especially the truck mounted ones (concrete pump trucks). Concrete pump trucks have extendable booms which allow flexible placing of concrete at various points of a structure, horizontally, at a height or at a depth. Nowadays, the pumped concrete became an important link in the chain of contemporary civil engineering, and concrete pumps are the most developed special machines, and one quarter of total concrete is placed using them. Work with the pumps is simple and engages a small number of workers, and concrete placed by a pump must have appropriate characteristics such as the quality of fine particles, aggregate grain shape, consistency, quantity of entrained air, etc. Concrete placing using pumps is quick, has a good quality and provides high profit. A record was set in 2008 in terms of the height where concrete was pumped – 606 m, at the Burj Khalifa skyscraper in Dubai (www.wikipedia.org/wiki/Burj_Khalifa).

Concrete placement comprises spreading of fresh concrete or filling the formwork using the concrete pump, compacting of concrete using vibrators and finishing of top surfaces of elements. Prior to placing concrete, it is necessary to control the installed formwork and reinforcement. The formwork must be well engineered and secured to prevent its failing and concrete leaking. The basic principle of placing is that concrete placement must be finished before cement starts to set. Setting time depends on the type and quantity of cement, as well as of admixtures, so it necessary to place concrete in the formwork and compact it with vibrators in that time. The most favorable time for placing concrete is at the air temperature from $+14^{o}$C to $+20^{o}$C. Placing of concrete at external temperatures below $+5^{o}$C and above $+30^{o}$C is considered concreting under special conditions when it is necessary to implement special concrete protecting measures. Placing of concrete is as important as the proper transport and production. This procedure ensures a homogeneous compacted structure without cavities in concrete, which contributes to its water tightness and durability, and to obtaining of a required class of concrete. Concrete ought to be installed and compacted so that all the reinforcement is well encased in concrete within prescribed tolerances for concrete protective layer. A special attention must be paid to placing and compacting of concrete at locations where cross-section dimension change (e.g. where they are narrowed) next to apertures, where reinforcement bars are densely laid and where there are concreting breaks. Normal layer thickness should not exceed the height of the immersed vibrator, and vibration should be performed by immersing the vibrator vertically, so that the surface of the lower layer is re-vibrated. In case of the thicker layers, re-vibration of the surface layer is recommended in order to avoid plastic precipitation of concrete below the upper reinforcement bars. Rate of placing and compacting of concrete must be sufficiently high to avoid cold joints and sufficiently low to avoid excess precipitation or overloading of formwork and scaffolds.

Concreting procedures depend on the type of structure, type of concreting elements, type of concrete etc. Concreting of columns (figure 2) must be performed without breaks to the specified height. Free fall of poured concrete must not exceed 1.5 m to prevent concrete segregation.

Fig. 2 Concreting of reinforced concrete columns (photo by the author of the paper)

Concreting of walls is performed in layers 30 – 50 cm thick, with uniform placing of concrete along the entire length (figure 3). Very thin elements (less than 15 cm thick) and in the case of very dense reinforcement, loading must be performed through the openings in the formwork which are made from the sides.

Fig. 3 Concreting of reinforced concrete walls
(photo by the author of the paper)

Fig. 4 Concreting of reinforced concrete slab
(photo by the author of the paper)

Solid slabs are concreted in strips having a specified width (figure 4), and in case of „fert“ structure slabs with girders and ring beams, one must first concrete girders and ring beams, and the slab afterwards (figure 5).

Concreting process is finished by curing concrete, which can vary, depending on the type of concrete and weather conditions. The concrete curing process comprises protection of concrete from weather conditions (high and low temperature, strong wind, aggressive impacts, mechanical damage etc). In practice, usually the curing of concrete is not paid sufficient care which can cause very negative effects, especially in terms of the durability of surface layer of concrete. Preventing of rapid loss of water from the surface layer can be provided by wetting the concrete with water or by covering it using various materials, or coating or sprinkling in order to create membranes.

Fig. 5 Concreting of "fert" ceiling (photo by the author of the paper)

At the end of the concreting process, a final evaluation of concrete quality is give based on the documents of taking over of concrete, visual inspection and by reviewing the construction site documents. The final concrete quality evaluation proves safety and durability of the structure.

In figure 6 are provided concreting process phases, from concrete production to placing in a structure.

The technology of execution of the concreting works considered in this paper comprises making of concrete in a concrete plant, transport to the construction sited using truck mixer trucks, transport and placing using pump trucks and compacting using vibrators.

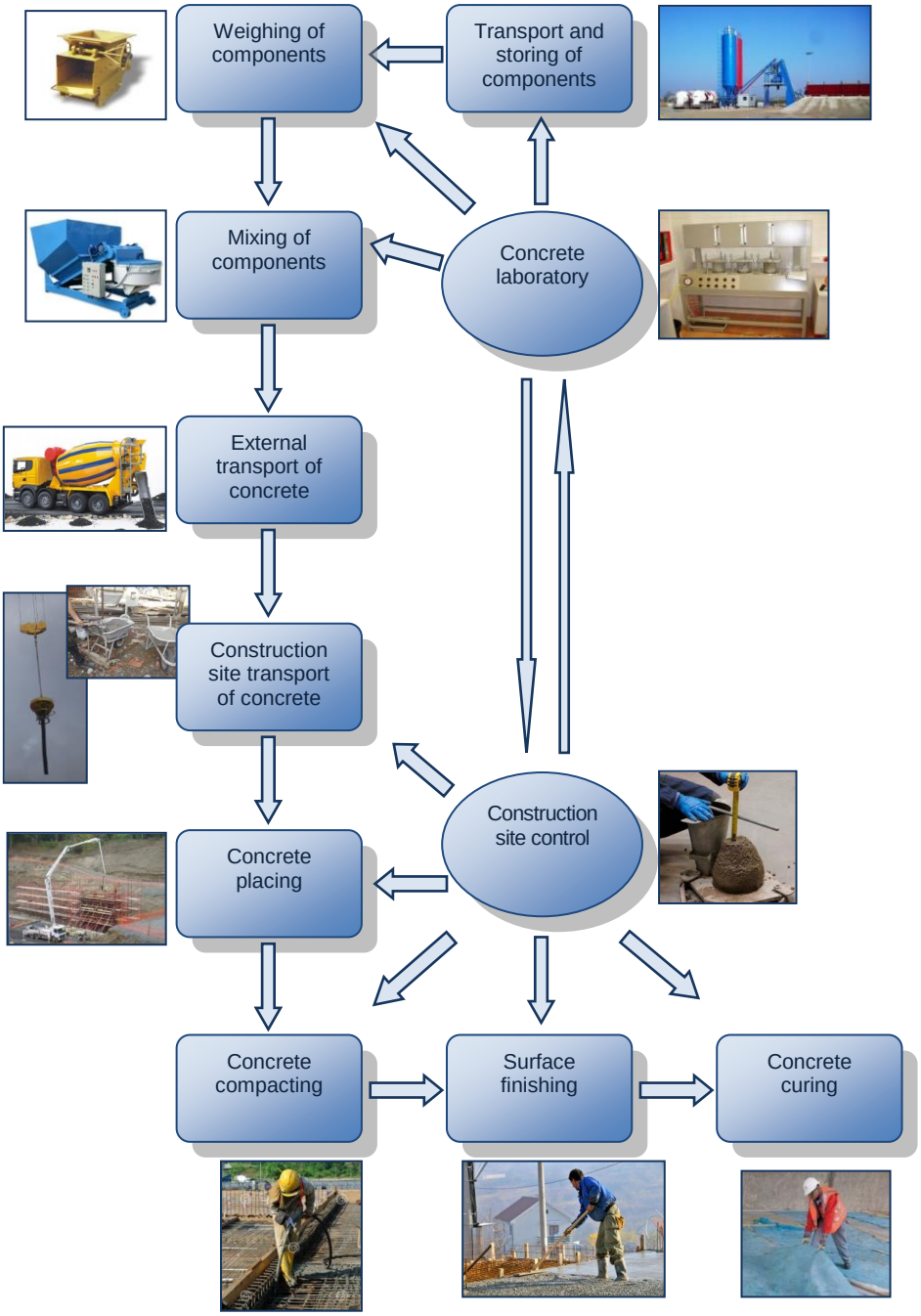

Fig. 6 The stages from production to concreting

5. CONCRETING PROCESS PRODUCTIVITY

There is a large number of factors which have a varying importance and impact in studying the concreting process productivity. Based on the previous considerations, it can be concluded that the concreting process productivity expressed as a ratio between the placed amount of concrete and time required for obtaining a unit of measure depends on the following factors:

- Concrete supply (truck mixer at the construction site, concrete factory, concrete plant, capacity, distance, ...);
- The structure (dimensions of the structure, accessibility for placing – position of the construction site, elements of the structure where concrete is installed: foundations, slabs, beams, columns, walls, ...);
- Concreting technology (truck pump, stationary pump, crane, hoist, carts, directly from the truck mixer,… vibrators, etc.);
- Machinery to be used (condition, capacity, availability, ...);
- Characteristics of the work crew engaged on placing concrete (number of workers, ability, skill, coordination of work crew, motivation, training level, working experience, ...);
- Weather conditions (time of year, air temperature, precipitations, ...);
- Construction site management etc.

5.1. Concrete supply

Concrete is produced in the concrete facilities of various capacities with automatic or semi-automatic control. For the classes of concrete lower than MB 25, for the first category concretes (B.I) and small quantities of concrete, it is permitted to use manual or machine making of concrete without previous tests. Therefore, the method of making and practical performance of concrete plant/truck mixer have a direct impact on the productivity of construction site concreting. Concrete factory position in respect to the construction site (distance, transport conditions: urban, extra-urban traffic, etc.) available number of truck mixers and their capacity have an impact on synchronization with the construction site demands which is directly related to the required time and productivity. Also, simultaneous supplying of several constructions site from the same concrete plant inexorably leads interruptions and reduction of productivity.

5.2. Structure

Concreting of various elements of the structure entails variations in productivity. Concreting the massive structures, with great thickness and a higher amount of concrete per unit of measure is not the same as concreting thinner elements such as, for instance, walls or slabs or placing concrete in some complex cross-section elements, etc. In figure 7 is presented average achieved productivity depending on the type of concreted element, based on the collected data from the construction site. The lowest productivity was achieved during concreting of columns and walls, and the highest during concreting of solid slabs.

Table 1 The average achieved productivity depending on the type of element

Type of element	Average achieved productivity (m^3/h)	Number of concreting
Slabs	24,27	40
Slabs and beams	19,12	38
Columns and walls	7,88	58

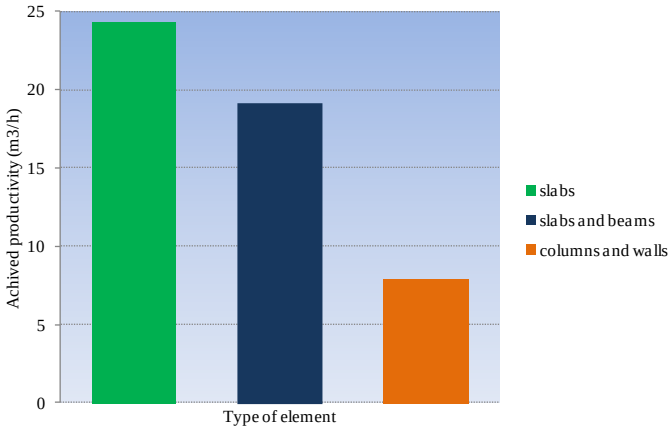

Fig. 7 The average achieved productivity depending on the type of element

The type of concrete element (reinforced or non-reinforced) also has an effect, as well as the type and class of concrete, composition of concrete, quantity of concrete, quantity of reinforcement and method of reinforcing, type of formwork etc. Figure 8 presents the increase of achieved productivity with an increase of the quantity of concrete to be placed. If the element is densely reinforced, the placing of concrete into the formwork and compaction will be more difficult. Height of the structure being concreted (reach of the pump pipeline, extensions, crane radius etc.) as well as the position of the construction site (accessibility of concrete pump approach, confined city conditions, ...) have a great impact on productivity.

Table 2 The average achieved productivity depending on the amount of concrete

Amount of concrete	Average achieved productivity (m^3/h)	Number of concreting
Less than 10 m^3	7,53	9
10-30 m^3	7,95	49
30-100 m^3	18,83	46
100-200 m^3	24,69	20
More than 200 m^3	28,13	12

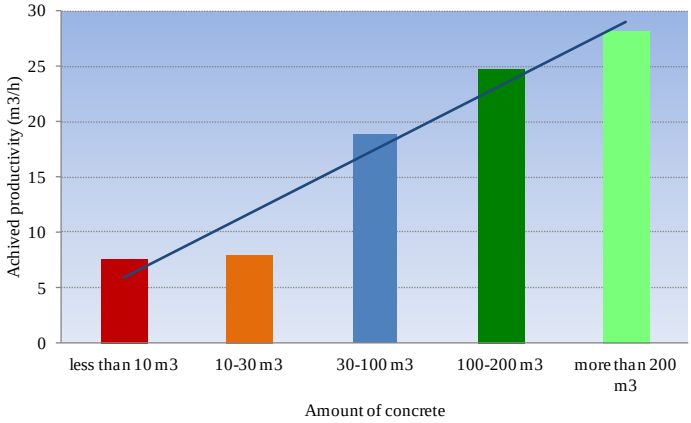

Fig. 8 The average achieved productivity depending on the amount of concrete

5.3. Concreting technology

Depending on the applied concreting technology, achieved productivity mostly varies. Different time is needed for placing a unit of measure of concrete if concrete is transported using a truck pump instead of, for instance, stationary pump. Concreting will last even longer if it takes a crane to transport concrete, some other hoist or carts, and it will require a considerably higher number of workers. The method of concrete compaction has an impact on the process duration. Placing using vibrators, formwork vibrators or vibrating rods and plates will affect engaging of different number of workers and achieving different productivity.

5.4. Machinery

Machinery affects the concreting process productivity to a great extent, considering that a larger share of concreting entails usage of machinery. It is comprised that a higher performance of machinery can largely increase productivity of the entire process. The age of the machinery, as well as its condition, regarding maintenance, contribute to a higher or lower efficiency (malfunctions, repairs, downtime, etc.). Availability of machinery also has an impact on the continuous flow of the works, that is, on avoiding interruptions and delays. In case of malfunctions, there should always be spare machinery at disposal. The availability can also refer to the occupancy of machine engaged at some other process which results in waiting for it to become available (for instance, concrete plant makes concrete for several construction site simultaneously, or a crane is engaged lifting some other materials apart from concrete, etc.).

5.5. Concreting work crew characteristics

Productivity can be increased by planning a sufficient number of workers, of appropriate qualifications and training level. It is clear that abilities, motivation and adequate skills possessed by the workers have a direct impact on the quality of works and achieved productivity. It is necessary that the workers have sufficient working experience and motivation for execution of the considered works. A formed work crew, if it is well

coordinated and with a sense of team work will enable the works to be executed very quickly, without delays due to misunderstanding or discrepancy between the skill level of the workers. Coordination level of a work crew is evaluated using marks from 1 (poorly coordinated and organized group) to 3 (excellent coordination) on the construction sites, and in figure 9 is presented the increased productivity resulting from the better coordination of a work crew. All these characteristics have an impact on productivity and relate both to manual laborers and machinery operators.

Table 3 The average achieved productivity depending on the crew organization

Evaluation of the crew organization	Average achieved productivity (m^3/h)	Number of concreting
1	6,03	7
2	7,52	33
3	9,44	18

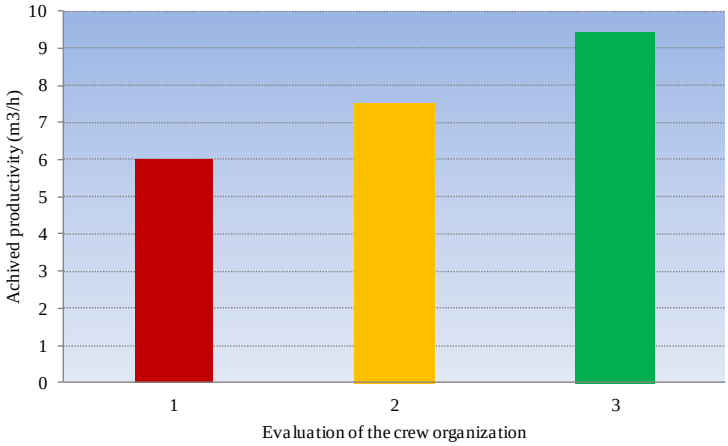

Fig. 9 The average achieved productivity depending on the crew organization

5.6. Weather conditions

Since the concreting works are executed mostly in the open air, as most of the works in civil engineering, weather conditions can exert a considerable impact to productivity. Concreting, as rule is executed at temperatures 5-30^{o}C. However, after adding various admixtures, it is possible to execute the works at lower or higher temperatures than these without consequences on the concrete quality. In those case high or low temperatures can have a negative impact on the working ability of the crew, and thus on the achievable productivity. Diagram in figure 10 displays the achieved productivity in comparison to three temperature ranges. The highest productivity was achieved at air temperatures 5-15^{o}C. Precipitations also affect the process, in a way that concreting has to be interrupted in case of heavy rain or showers, while working in drizzle is possible, but it affects the productivity. It is clear what effects the seasons in a year have, regarding the temperature but also shorter daylight time in late autumn and winter months. Periods within a day, i.e.

shifts in which the works are executed, as well as the shift length, have an impact on the realized productivity. Night work and longer duration of the shifts, as well as the work on Sundays and during holidays have a negative impact on the workers due to fatigue and lower motivation, and in case of machinery malfunction, repairs are more difficult to perform, etc.

Table 4 The average achieved productivity depending on the temperature range

Temperature range (^{o} C)	Average achieved productivity (m^3/h)	Number of concreting
5-15	22,93	30
15-25	20,74	25
25-35	21,35	23

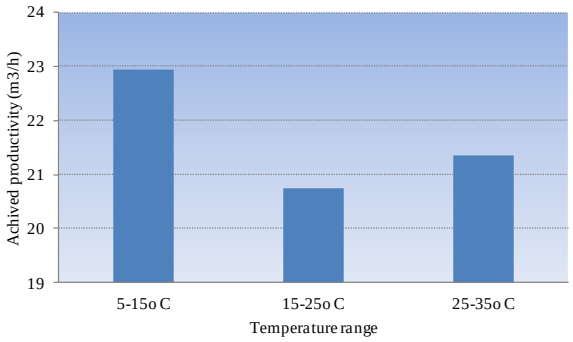

Fig. 10 The average achieved productivity depending on the temperature range

5.7. Construction site management

Concreting process productivity is also affected by the relations and of the participants in the process and the atmosphere among them. A professional, correct relationship and trust between managers on a construction site and workers is a very important factor for a good and timely achieving of goals. The experience and experience of the heads in managing a construction site and execution of works on the similar structures is significant, as well as motivation, influence, responsibility, etc. However, the most important for productivity of the concreting process is the construction site management model, i.e. management of the concrete works execution process.

6. CONCLUSION

The paper provides an analysis of concreting works productivity and describes the most influential factors on the concreting process itself. For reasons of specific character and importance of concreting works, it is necessary to pay a special attention to them during construction of any civil engineering structure. In order to finish the works in the planned deadline, required productivity of concreting works as critical activities in the dynamic work execution plan must be ensured. However, owing to a large number of

various influential factors, it is not always simple and easy to ensure uninterrupted and continuous works. Because of the limited time for placing of concrete, it is necessary to well synchronize concrete producer and the constructions site, in order to provide the continuity of concreting works. Concreting of various elements results in different productivity levels. Placing of large quantities of concrete, as well as a better organization and coordination of the crew result in higher productivity.

REFERENCES

1. A. Flašar, Proučavanje tehnoloških procesa u građevinarstvu, Fakultet Tehničkih nauka, Novi Sad, 1985.
2. A. M. Jarkas, "Analysis and measurement of buildability factors affecting edge formwork labour productivity", Journal of Engineering Science and Technology Review, vol. 3 (2010) 1, pp. 142-150
3. A. M. Jarkas, "Buildability Factors Influencing Concreting Labor Productivity", Journal of Construction Engineering and Management, 138 (2012) 1, pp. 89–97
4. B. Matejević, Model za prognoziranje produktivnosti procesa betoniranja, doktorska disertacija, Građevinsko-arhitektonski fakultet, Niš, 2016.
5. P. G. Prabhu, D. Ambika, "Study on behaviour of workers in construction industry to improve production efficiency", International Journal of Civil, Structural, Environmental and Infrastructure Engineering Research and Development (IJCSEIERD), 5 (2013), pp. 59-66
6. Pravilnik o tehničkim normativima za beton i armirani beton – BAB 87
7. M. E. Shehata, K. M. El-Gohary, "Towards improving construction labor productivity and projects' performance", Alexandria Engineering Journal, 50 (2011) 4, pp. 321-330
8. M. Soham, B. Rajiv, "Critical factors affecting labour productivity in construction projects: case study of south gujarat region of India", International Journal of Engineering and Advanced Technology, 2 (2013) 4, pp. 583-591
9. A. Soekiman, K. S. Pribadi, B.W. Soemardi, R. D. Wirahadikusumah, "Factors relating to labor productivity affecting the project schedule performance in Indonesia", Procedia Engineering, 14 (2001), pp. 865-873
10. Softconsulting (www.savjetnik.ba/šta-je-produktivnost/)
11. Tehnički uslovi za transportovani beton SRPS U.M1.045
12. H. R. Thomas, D. R. Riley, V. E. Sanvido, "Loss of labor productivity due to delivery methods and weather", Journal of Construction Engineering and Management, 125 (1999) 1, pp. 39-46.
13. H. R. Thomas, I. Zavrski, "Construction baseline productivity: Theory and practice", Journal of Construction Engineering and Management, 125 (1999) 5, pp. 295-303
14. www.sr.wikipedia.org
15. www.pks.rs/PrivredaSrbije
16. www.wikipedia.org/wiki/Burj_Khalifa

ANALIZA PRODUKTIVNOSTI PROCESA BETONIRANJA

Tokom izvođenja radova na izgradnji bilo kog objekta, javlja se veliki broj faktora koji imaju uticaj na ukupne performanse gradilišta. Jedan od veoma značajnih faktora je produktivnost. Zbog specifičnosti i značaja betonskih radova pri izgradnji građevinskog objekta potrebno je obratiti posebnu pažnju na izvođenje ovih radova. U ovom radu analizira se produktivnost: u opštem smislu, kao i produktivnost u građevinarstvu, sa posebnim osvrtom na produktivnost pri izvođenju betonskih radova. Ukazano je na značaj betonskih radova i opisana tehnologija izvođenja betonskih radova. Dat je pregled i opis faktora koji imaju uticaj na produktivnost procesa betoniranja. Izvršena je analiza produktivnosti na konkretnim gradilištima na osnovu podataka dobijenih snimanjem procesa betoniranja i dati su neki od rezultata.

Ključne reči: *građevinarstvo, produktivnost, proces betoniranja, tehnologija betoniranja, uticajni faktori.*

CIP - Каталогизација у публикацији
Народна библиотека Србије, Београд

71/72+62

FACTA Universitatis. Series, Architecture and Civil Enginering / editor-in-chief Dragoslav Stojić. - Vol. 1, No 1 (1994)- . - Niš : University of Niš, 1994- (Niš : Unigraf-X-copy). - 24 cm

Tri puta godišnje. - Tekst na engl. jeziku. -
Drugo izdanje na drugom medijumu:
Facta Universitatis. Series: Architecture and Civil Engineering (Online) = 2406-0860
ISSN 0354-4605 = Facta Universitatis. Series: Architecture and Civil Engineering
COBISS.SR-ID 98807559

FACTA UNIVERSITATIS

Series

Architecture and Civil Engineering

Vol. 16, Nº 1, 2018

Contents